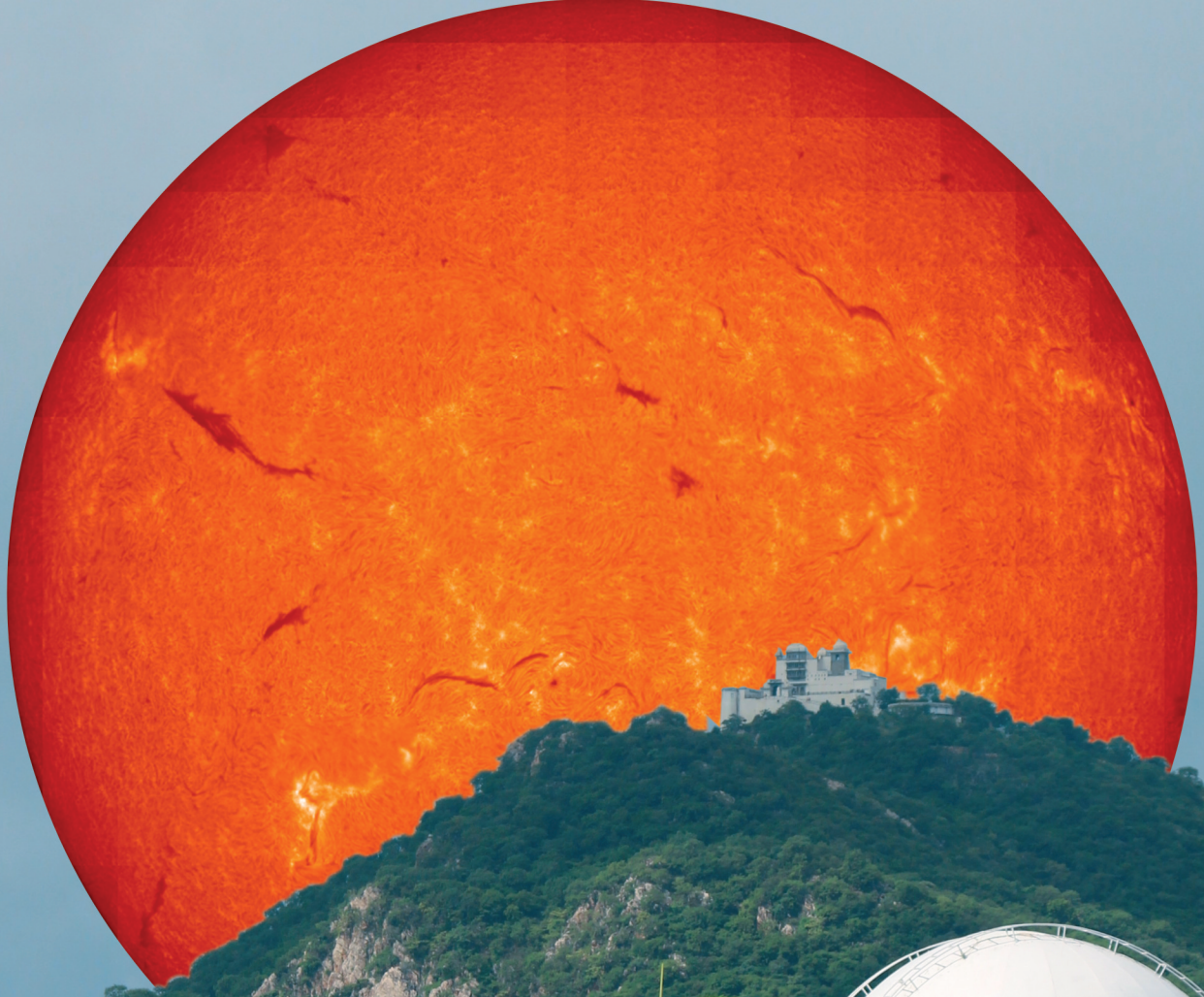




भौतिक अनुसंधान प्रयोगशाला, अहमदाबाद  
Physical Research Laboratory, Ahmedabad



वार्षिक प्रतिवेदन  
Annual Report

2014-2015

**Front cover page:** The Udaipur Solar Observatory (USO) on an island in Fatehsagar Lake, Udaipur. In the background is an H-alpha full-disk image of the Sun constructed from a mosaic of about 290 high resolution images taken sequentially with the newly installed Multi-Application Solar Telescope (MAST) at the USO.

**Inside back cover pages:** Events at PRL

**Back cover page:** High resolution G-band (right column) and respective H-alpha (left column) images of an active region on the Sun taken with MAST. Bottom photograph shows the MAST pointing towards the Sun as the Sun sets behind the Sajjangarh hill. The backdrop is a part of the H-alpha full-disk image shown on the front cover.

**Compiled & Layout by:**  
Office of the Dean, PRL.

**Published by:**  
Physical Research Laboratory, Ahmedabad.

**Printed by:**  
Creative Printers Private Limited, Ahmedabad.

वार्षिक प्रतिवेदन  
**Annual Report**  
**2014 - 2015**



**भौतिक अनुसंधान प्रयोगशाला, अहमदाबाद**  
**Physical Research Laboratory, Ahmedabad**



# PRL Council of Management

## Chairman

Professor U.R. Rao  
Antariksh Bhavan, New BEL Road  
Bengaluru-560231

Former Chairman, ISRO

## Members

Dr. K. Radhakrishnan  
Secretary, Department of Space, Govt. of India  
Antariksh Bhavan, Bengaluru-560231

Chairman, ISRO  
(Up to 31.12.2014)

Dr. A. S. Kiran Kumar  
Secretary, Department of Space, Govt. of India  
Antariksh Bhavan, Bengaluru-560231

Chairman, ISRO  
(From 14.01.2015)

Shri A. Vijay Anand, IRS  
Department of Space, Govt. of India  
Antariksh Bhavan, Bengaluru-560231

Additional Secretary & FA, DOS

Shri Sanjay S. Lalbhai  
Ahmedabad Education Society  
Ahmedabad

Nominee, Ahmedabad Education Society

Shri Kartikeya V. Sarabhai  
Director  
Centre for Environment Education  
Ahmedabad

Nominee, Karmakshetra Educational  
Foundation

Shri Mukesh Puri, I.A.S.  
Principal Secretary  
Higher & Technical Education  
Government of Gujarat, Gandhinagar

Nominee, Government of Gujarat

Professor J. N. Goswami  
Director  
Physical Research Laboratory, Ahmedabad

Ex-Officio  
(Up to 30.11.2014)

Professor Utpal Sarkar  
Director  
Physical Research Laboratory, Ahmedabad

Ex-Officio  
(From 01.12.2014)

## Member - Secretary

Shri Y.M.Trivedi  
Registrar  
Physical Research Laboratory, Ahmedabad

Ex-Officio  
(Up to 31.10.2014)

Wg. Cdr. (Retd.) Vibhas Gupta  
Registrar  
Physical Research Laboratory, Ahmedabad

Ex-Officio  
(From 01.11.2014)



# Contents

<b>Director's Foreword</b>	1
<b>Science Highlights</b>	3
<b>Awards and Honours</b>	9
<b>Human Resources Development</b>	12
<b>Theses Submitted</b>	13
<b>Colloquia/Public Lectures by Visitors</b>	14
<b>Invited Talks at Conferences / Symposia / Workshops</b>	16
<b>Lectures at Universities / Institutions</b>	20
<b>Science at PRL</b>	
<i>Astronomy and Astrophysics</i>	23
<i>Solar Physics</i>	35
<i>Planetary Sciences and PLANEX Program</i>	46
<i>Space and Atmospheric Sciences</i>	60
<i>Geosciences</i>	73
<i>Theoretical Physics</i>	92
<i>Atomic, Molecular and Optical Physics</i>	103
<b>Publications</b>	
<i>Publications in Journals</i>	114
<i>Publications in Proceedings of Conferences/Symposia/Workshops</i>	122
<i>Books Edited/Review Articles/Technical Notes</i>	126
<b>Promotion of Basic Sciences, Official Language and Outreach Activities</b>	127
<b>Facilities and Services</b>	131
<b>Honorary Fellows</b>	137
<b>Honorary Faculty</b>	138
<b>Academic Faculty</b>	139
<b>Technical Faculty</b>	142



# Director's Foreword

Science at PRL is thriving on nurturing excellence. A very high academic standard was set and maintained by our predecessors, which makes the task more challenging, but our scientists continue to maintain the high level, which is apparent from the nearly two hundred research publications, mostly in high impact peer reviewed journals, and the awards this year and recognitions they have received. In addition to publications in journals, one monograph and seven review articles have been published. Seven research scholars have submitted their theses during the year. Collectively, PRL Faculty members received invitations to give more than two hundred lectures at Conferences, Symposia and Workshops and also at Universities and other Academic Institutions. PRL also invited close to twenty faculty members from both within the country and abroad for scientific interactions. Several other meetings and workshops in the area of planetary and atmospheric sciences were also held during the year.

Honours and acclamation received by faculty members from different national and international academic fora reflects the mature state of scientific research done at PRL. The recognitions include the Axford Medal, ISRO Outstanding Achievement Award for the year 2012, INSA-Senior Scientist Position, Elsevier Reviewer Recognition Certificate, PRL Award, and the Eminent Mass Spectrometrists Award. PRL faculty members serve as Council Members of National and International Science Academies as well as in Council and Advisory Committees of several academic institutions, government departments such as SERB, CSIR and MOES. Several PRL research scholars received awards for their presentation in scientific meets that include the Justice Oak Best Thesis Award of the Astronomical Society of India.

Along with the ongoing research, several new research initiatives have been taken up during the last plan period. The Multi-Application Solar Telescope at Udaipur Solar Observatory has been operationalized and has started receiving the data and found to be working as expected.

Generous support received from the Department of Space has enabled PRL to initiate scientific programmes in frontier areas of research, that include search of exo-planets, laboratory studies of interstellar grains, laboratory synthesis of astro-molecules and experimental studies in the field of quantum optics. Significant progress has also been made in the areas of planetary sciences and exploration and PRL is developing several payloads for the upcoming Chandrayaan-2 and proposed Aditya missions.

Several new facilities, that include an Accelerator Mass Spectrometer and a Ground-based Radar will be operational within the next one year and provide new impetus for research in the fields of Atmospheric and Space Sciences, Geosciences and Planetary Sciences. A high end computing cluster "Vikram-100" is already operationalized. Plans for establishing a 2.5 meter telescope facility at Mt. Abu are nearing completion. This facility is expected to be realized within a time frame of three years. The quantum optics laboratory is already operational and spadework has started to house the Accelerator Mass Spectrometer and a laboratory for Astrochemistry in the Thaltej campus.

Research carried out at PRL during the year led to several very significant results. The recurrent nova V745 Scorpii, in its third outburst on 6 February 2014 was monitored from the Infrared Observatory at Mt. Abu. This observation revealed the generation of a powerful blast wave by the high velocity.

PARAS radial velocity (RV) measurements suggested a transiting Jupiter planet around a metal-rich red giant star. A significant clue about sunspot magnetic field was revealed for the first time by a study of the relative signs of chiral and shear components of the electric current in a sunspot. In the process of developing a modern polarimeter for the Multi-Application Solar Telescope, the liquid crystal variable retarders (LCVRs) used for the

polarimetry were successfully characterized. Along with this experimental activity, a new Milne-Eddington inversion code was developed for the MAST polarimetry. A new chromatographic procedure for simultaneous extraction of Si and Mg has been established. This experimental development is a major step in facilitating the simultaneous study of silicon and magnesium isotope systematics of differentiated meteorites to understand core formation process and time scales for formation of planetesimals and planets. The ASPEX experiment, selected for ISRO's Aditya-L1 mission and under development at PRL, consists of two particle analysers which use the unique location of the spacecraft at the L1 point to carry out systematic and continuous observations of particle fluxes. Evidence of the effect of tropospheric cyclonic system on upper atmospheric dynamics has been obtained from Gurushikhar, Mt. Abu during the cyclonic storm Nilofar using optical airglow emissions and outgoing longwave radiation as the tracers for upper atmospheric and tropospheric wave activity, respectively. The first ever pan-India seasonal and annual isotopic maps for precipitation across the country and the corresponding meteoric water lines are now available from IWIN Isotope Data and provide new insights about spatio-temporal variations in hydro meteorological processes operating in India. Carbon transfer from the atmosphere to the deep ocean is enhanced by cyclonic eddies in the ocean and using nitrogen isotopes, the enhancement in biological productivity was quantified in the Bay of Bengal. In addition, nitrogen isotopes were also used to quantify productivity variation in the equatorial Indian Ocean and the Southern Oceans. These values will serve as important inputs to Global Climate Models. Interpretation of new signals at colliders and their consequences to particle physics and cosmology produced several significant results. Major impact has been made on our understanding of the neutrinoless double beta decay. Important results have been reported in atomic physics, both theoretical and experimental. New research program has been initiated in areas of laser physics and astrochemistry.

On the academic front, the strength of faculty has reached nearly seventy five with the induction of new faculty members. They are engaged in scientific and technical activities together with twenty five supporting Technical Faculty and more than twenty five junior scientists, engineers and technicians. Nearly a hundred research scholars and post-doctoral fellows along with a significant number of project associates are currently associated with PRL.

The 9<sup>th</sup> UN CSSTEAP course on Space Sciences for the Asia-Pacific region hosted by PRL started on 01 August, 2014. Several university faculty members visited PRL for extended periods for collaborative studies as a part of our continuing effort to provide opportunities for academic interactions to interested faculty members from universities. PRL continues its academic association with Gujarat University, Ahmedabad, M. S. University of Baroda, Vadodara, M.L.S University, Udaipur, S. P. University, V. V. Nagar, Indian Institute of Technology, Gandhinagar, Pondicherry University, Pondicherry and Nirma University, Ahmedabad.

PRL continues to expand its HRD activities by inducting more number of college and university students from all over India for its summer programme and also through its association with similar programmes conducted jointly by the three Science Academies in India. More than 50 graduate students, several undergraduate students as well as an equal number of engineering students have participated this year in the PRL Summer Internship programme. PRL is entrusted to conduct the PLANEX and RESPOND programmes of the Department of Space and currently more than forty research groups at various universities and research institutions across the country are receiving funds and advice to carry out scientific investigations in the fields of Astronomy, Planetary and Space Sciences. Several interactive meetings of interested faculty members and scientists from universities and research institutes with technical personnel involved in Indian planetary missions were also held during the year.

"Science Day" celebration at PRL has now become a major event for the state of Gujarat with participation of selected students from across the state. PRL offers scholarships and incentives to students based on their performance in various science related activities conducted on that day. Starting last year, special events are also arranged for the accompanying teachers.

Continuous efforts are on to ensure the use of Hindi in administrative matters and official communications. The Hindi version of the PRL website is ready and operational. The Town Official Language Committee has recognized the various initiatives taken by PRL and the work done in implementation of Hindi in various domains.

Thanks to generous support from the Department of Space (DOS), implementation of the 12<sup>th</sup> Five Year Plan is proceeding well with several new facilities already in place and a few others expected to be at PRL soon. Collective efforts and coordination between academic and administrative personnel have ensured timely acquisition and the onus is now on Team PRL to deliver high quality science. The untiring effort put in by all members of the PRL family ensured that we have been able to do reasonable justice to the faith reposed in us by DOS and we need to give our best to achieve the next higher level of excellence.

I am grateful to all the members of the PRL Council for their encouragement, invaluable advice and whole hearted support for all the scientific activities pursued at PRL. In particular, I am indebted to Prof. U. R. Rao, Chairman, PRL Council, Dr. K. Radhakrishnan, Former Chairman, ISRO and Dr. A. S. Kiran Kumar, Chairman, ISRO for their sage advices, unstinted support and encouragement that resulted in a year of steady growth and progress at PRL.

**Utpal Sarkar**

**Director**

# SCIENCE HIGHLIGHTS

## Astronomy and Astrophysics

- Mt. Abu observations detected very high, variable optical polarization from blazar candidate CGRaBS J0211+1051 in Jan-Feb 2011 based on which we had proposed the source to be a low energy peaked blazar (LBL). Later, multi-wavelength data was used to estimate various parameters and to verify its classification vis-a-vis blazar sequence. The light curves show variations in the high-energy  $\gamma$ -rays to be correlated with X-ray, UV, and optical variations, indicating to their co-spatial origin. This multi-wavelength study enabled us to trace the low-energy (synchrotron) component of the spectral energy distribution, whose peak lies at  $\sim 1.35 \times 10^{14}$  Hz, confirming CGRaBS J0211+1051 to be an LBL. Some other parameters, such as the local magnetic field ( $\sim 5.93$  G) and black hole mass ( $\sim 2.4 \times 10^8 M_{solar}$ ), are also estimated.
- Based on the long-term trends in the light-curve (1971 to 2013) of S5 0716+71 we had predicted last year (Annual Report 2013-14, p26) that the source should start brightening towards the beginning of 2015. The inference was based on the possibility of the long-term systematic changes in the brightness of the source. According to this, the source brightens as the viewing angle decreases and vice versa, due to, perhaps, precession of the jet. Mt. Abu Observatory and other related data shows that source started brightening towards the end of 2014 and reached unprecedented levels (11.6 mag in R band) in January 2015. A sustained increase in average brightness over a few year period is required to confirm a precessing jet.
- Mt. Abu monitoring of the recurrent nova V745 Scorpii, in its third outburst on 2014 February 6, revealed the generation of a powerful blast wave by the high velocity ( $> 4000$  km/s) ejecta. The temperature of the shocked gas is raised to more than  $10^8$  K just after the onset of outburst. The shock, showing a decelerative Sedov-Taylor phase, causes  $\gamma$ -ray emission, just like five other known novae. The question whether all such novae are  $\gamma$ -ray emitters or such emissions are restricted only to symbiotic systems with a shocked red giant wind could be addressed by such study. Our analysis also suggests that the White Dwarf (WD) in V745 Sco is very massive and a potential progenitor for a future SN Ia explosion.
- Near-IR spectra, covering 50 days of the eruption of recurrent nova T Pyxidis were taken from Mt. Abu at 18 epochs. A major finding is the transition of the nova from the He/N to the Fe II class within a few days after the outburst as inferred from the appearance of prominent HeI lines soon after the onset of the eruption and certain carbon lines, near-IR hallmarks of the Fe II class. Based on the observation that the  $Br\gamma$  line is optically thick, lower limits on the emission measure and electron density in the ejecta are placed.
- Type 1a Supernova (SN) 2014J, brightest and closest in the last four decades, provided best opportunity to study a thermonuclear SN over a wide range of the electromagnetic spectrum. The best fit at maximum

using a Galactic type extinction law yields  $RV = 1.4 \pm 0.1$ , which is compatible with a power-law extinction expected from multiple scattering of light. Seventeen optical and 23 NIR spectra were obtained during -10 days to +10 days from the time of maximum B-band brightness. Carbon is not detected in the optical spectra, but C $\sim$ I 1.0693 micron line in NIR is identified. The velocities for O I, Mg II, Si II, S II, Ca II, and Fe II suggest that SN 2014J has a layered structure with little or no mixing.

- The compact objects in High Mass X-ray Binaries (HMXBs) show significant and rapid variation in the X-ray emission. One such HMXB, 4U 1700-37 was observed with Suzaku in 0.5-70 keV energy range. Though we did not find any signature of pulsations in the light curves, a quasi-periodic oscillation at  $\sim 20$  mHz was detected in the power density spectrum of the source. Iron emission lines at 6.4 and 7.1 keV and an absorption like feature at  $\sim 39$  keV were detected in the spectrum of the X-ray source. These findings suggest the compact object in the X-ray binary to be a neutron star. Considering the feature at  $\sim 39$  keV as cyclotron absorption line, the surface magnetic field of the neutron star was estimated to be  $\sim 3.4 \times 10^{12}$  G.
- Timing and spectral studies of binary X-ray pulsars provide important information regarding the geometry of the system and matter distribution in the vicinity of the neutron star. Time resolved spectroscopy of eclipsing HMXB pulsar OAO 1657-415 was carried out to investigate the cause of significant flux variability at the time scale of  $\sim 10$  ks. Presence of additional dense matter at various orbital phases was confirmed as the cause of the low-flux regions in the X-ray light curves. The presence of additional dense matter at different orbital phases of the pulsar is explained to be due to the inhomogeneously distributed clumps of matter around the neutron star. Investigation of iron emission line parameters at different orbital phases suggested the existence of neutral and ionized iron atoms in emission sites located within the accretion radius.
- A NuSTAR study of the black hole GRS 1915+105 during its plateau state revealed its power density spectrum showing strong QPO at  $\sim 1.5$  Hz with the spectrum dominated by the Comptonization component and almost no contribution from the disk. The spectrum was fitted with a cut-off power law and its reflection from the disk and the model counts were given as input to the simulation which considers the oscillation of spectral parameter(s) at a frequency equal to that of the QPO. We found that the oscillations of power law index can produce QPO nature. The Lense-Thirring precession model, considered as the most successful, was not able to explain our results of oscillating power law index at QPO-frequency. Our simulation results provide a crucial information on the oscillation of power law index which can help understand the mechanism of QPO generation.
- Using systematic 327 MHz observations and exploiting the IPS technique, the ratio of the rms electron density fluctuations to the background density in the solar wind (density modulation index,  $\epsilon_N \equiv \Delta N/N$ ) was studied.

This ratio is of vital importance in understanding several problems in heliospheric physics related to solar wind turbulence. We have inferred the dissipation scale of the turbulent cascade in the solar wind in the inner heliosphere, often referred to as the inner scale of turbulent fluctuations and shown that it depends on the kind of density model assumed for the solar wind and can be equal to the electron/proton gyro-radius.

- PARAS radial velocity (RV) measurements suggest a transiting Jupiter planet around a metal-rich red Giant star. Most of the exoplanets orbit around Sun-like dwarf stars and only a handful of them are found around Giant stars. Such evolved stars have typical radii of 2 to 10 solar radii. Hence, exoplanets in the close proximity usually get destroyed by strong tidal interactions and heat. Present result shows existence of a transiting Jupiter of mass 1.4 Jupiter with approximate period of 39 days around an evolved star of 1.5 Solar Mass with stellar radius of 2 to 4 solar radii. The planet has an orbital eccentricity of 0.05, semi-major axis of 0.255 AU and measured K-value (semi-amplitude) of 65m/s. Host star has Fe/H= 0.2, log(g) value of 3.5 - 3.7 confirming its giant phase.
- A Compton polarimeter as a focal plane instrument for Hard X-ray telescope is being developed. The basic instrument design consists of a 10 cm long plastic scintillator surrounded by a cylindrical array of 15 cm long CsI(Tl) scintillators. The plastic scatterer is read out by a PMT whereas the CsI(Tl) scintillators are readout by new generation Si-photomultipliers. Detailed characterization for each of the 16 CsI(Tl) scintillators is done, measuring their low energy threshold, which is a critical parameter for achieving the required sensitivity. The complete instrument is assembled and operational stability verified. Performance of the polarimeter has been tested with both unpolarized and polarized beam of radiation at various energies. The results are quite encouraging and agree well with the simulation results.

### Solar Physics

- Further evidence for flare-induced global oscillations in the Sun was obtained using full sun integrated Doppler and intensity measurements using respectively the GOLF and VIRGO instruments on board the Solar and Heliospheric Observatory (SOHO). This approach holds promise for detecting similar responses related to stellar flares.
- Enhanced power of photospheric oscillations was seen in localized regions surrounding a solar flare which seem to be driven by a magnetic-jerk like phenomenon caused by large amplitude changes in the magnetic field at those locations.
- A significant clue about sunspot magnetic field was revealed for the first time by a study of the relative signs of chiral and shear components of the electric current in a sunspot, which tends to support a monolithic flux tube model, as opposed to a "spaghetti" model consisting of a bunch of tiny magnetic flux elements held together by an as yet unidentified force.

- The physical processes involved in the initiation and eruption of a magnetic flux rope from a solar active region resulting in an Earth-directed coronal mass ejection (CME) were identified using a combination of photospheric vector magnetograms obtained from the Helioseismic and Magnetic Imager (HMI) and coronal images from AIA on board the Solar Dynamics Observatory (SDO). The availability of magnetic twist required for coronal observational signatures of flux rope dynamics was measured from the magnetic field observations at the photosphere, which in turn confirms that the observed geometrical evolution of this flux bundle is a signature of magnetic twist.
  - An extensive multi-wavelength study of an M4.0 flare showed impulsive energy release and non-thermal emission in a confined M4.0 flare triggered by rapidly evolving magnetic structures. Also, a large-scale implosion in coronal loops was seen during the pre-flare phase of an M6.2 flare which could be clearly identified with a confined eruption of a flux rope.
  - Using new observations from the Heliospheric Imager (HI) on board the twin STEREO spacecraft, the CME features were tracked in 3-D as enhanced density structures. In-situ plasma and compositional parameters provide evidence that the rear edge density structures correspond to a filament associated with the CME while the density enhancement at the front corresponds to the leading edge of the CME. Using a similar approach, the evolution and consequences of interacting CMEs of 2012 November 9-10 could be clearly recorded revealing the nature of their collision, significance of post-collision kinematics and its role in increasing the geo-effectiveness.
  - Using computations relying on the Implicit Large Eddy Simulation (ILES) property of non-oscillatory numerics, the repetitive formation and decay of current sheets in magnetic loops was monitored in numerical simulations and the creation of diverse magnetic structures could be demonstrated which were associated with different generic patterns of the footpoint motions.
  - Similar numerical simulations of viscous relaxation of an incompressible, thermally homogeneous magnetofluid having infinite electrical conductivity demonstrated the role of topological complexity in spontaneous development of current sheets, even in the absence of magnetic null-points.
  - In the process of developing a modern polarimeter for the Multi-Application Solar Telescope, the liquid crystal variable retarders (LCVRs) used for the polarimetry were successfully characterized. Along with this experimental activity, a new Milne-Eddington inversion code was developed for the MAST polarimetry.
- were identified based on excess/deficit of isotopes  $^{17}\text{O}$  and  $^{18}\text{O}$  amongst which four are formed in envelopes of red giant branch (RGB) or asymptotic giant branch (AGB) stars. A single grain was observed to be highly enriched in the heavy Oxygen isotopes and is likely to have formed either in stars with higher-than-solar metallicity or has a supernove (SNe) origin.
- A new chromatographic procedure for simultaneous extraction of Si and Mg has been established. This experimental development is a major step in facilitating the simultaneous study of silicon and magnesium isotope systematics of differentiated meteorites to understand core formation process and time scales for formation of planetesimals and planets.
  - Troilite-metal nodules occur rarely in L Chondrites and their origin is still not completely understood. We came across an unusually large ( $\sim 2$  cm) such nodule in the recently fallen Indian meteorite Katol (L6-7). Mineral, chemical and petrological studies using EPMA and ICP-MS on the complexly intergrown troilite-metal texture, have revealed that the nodule formation is a localised event by a high energy impact which caused local frictional heating at the structural and compositional discontinuities. Trapped, radiogenic and cosmogenic noble gases in this nodule indicate that it formed very early, most probably on the parent body.
  - Morphological and topographical analysis of lobate flow features (LFFs) emerging from the pole-facing walls of craters distributed within Alba Patera (between  $30^\circ$ - $60^\circ$  N and  $80^\circ$ - $140^\circ$  W) suggests evidence for young, less moderate glaciation, a process not well documented on Mars. Its radial/unidirectional flow indicated that the required amount of ice/snow should have been relatively less than that involved in emplacement of concentric crater flows (CCF) that completely filled the craters floor from all the sides. LFFs are suggested to have formed in an intermediate period, i.e. between CCF and gullies (within  $\sim 100$ - $10$  Ma), and their presence is abundant over the pole-facing wall of craters. The climate during the  $\sim 90$  Ma which supported LFF formation changed to a phase where ice accumulation is significantly reduced and is confined to the small alcoves at certain locations during the last 10 Ma.
  - Remote sensing investigations of the Lowell crater region in the north western quadrant of Orientale basin using high resolution datasets from NASA's LRO, Kaguya of JAXA and ISRO's Chandrayaan-1 missions have revealed topographical, morphological and spectral diversity of the region and age of selected units in the area. The rim-wall morphology and topography, pronounced asymmetry in the ejecta distribution and crater density in selected parts of the proximal ejecta blanket suggests that the Lowell crater formed due to an oblique impact ( $\sim 30^\circ$ - $45^\circ$ ) in the Montes Rook from the S-SW direction  $\sim 370$  Ma ago. The lithological assemblages of the various components of the Lowell crater indicate that it excavated a deep-seated pre-existing (pre/post Orientale) mafic pluton.

### Planetary Sciences and PLANEX Program

- The search for in-situ presolar silicate and oxide grains was carried out in a section of Isheyevo meteorite, with a focus towards lithic clasts with  $\delta^{15}\text{N}$  as high as 3000‰ (as determined earlier, elsewhere), using high spatial resolution ( $\sim 150$  nm) mapping with nanoSIMS. 6 grains

- A dual frequency microwave brightness index has been proposed for the estimation of regolith thickness using simulated passive microwave brightness temperature ( $T_B$ ) expected from Chandrayaan-2 at 1.25 GHz and 2.1 GHz bands. Inverted regolith thickness estimates using single (L-band) and dual frequency index agree with in-situ measurements at Apollo regions. For the Apollo 14 and Apollo 17 locations, inverted regolith thickness values differ from mare and highland region estimates. Impact basin ejecta (Apollo 14) and mare-highland transition region (Apollo 17) are areas where vertical variation of FeO and TiO<sub>2</sub> occurs along with lateral variations influencing the emitted brightness temperature from lunar regolith.
- The ASPEX experiment selected for ISRO's Aditya-L1 mission consists of two particle analysers which use the unique location of the spacecraft at the L1 point to carry out systematic and continuous observations of particle fluxes over an energy range spanning 100 eV to 5 MeV. The ASPEX payload consists of two components to cover the entire energy range the Solar Wind Ion Spectrometer (SWIS) covering the low energy range (100 eV to 20 keV) using an electrostatic analyser and the Supra Thermal Energetic Particle Spectrometer (STEPS) covering the high energy range (20 keV to 5 MeV) using solid state and scintillation detectors. The entire STEPS package and the processing electronics of SWIS package with software are under development in PRL.

### Space and Atmospheric Sciences

- Evidence of the effect of tropospheric cyclonic system on upper atmospheric dynamics has been obtained using optical airglow emissions and outgoing longwave radiation as the tracers for upper atmospheric and tropospheric wave activity, respectively. This has been achieved using OH, O<sub>2</sub> and Na emission intensities obtained from Gurushikhar, Mt. Abu during the cyclonic storm Nilofar, wherein ~ 4-hr periodicity was seen to be coherent in all these parameters.
- Two-dimensional gravity wave structure has been obtained in daytime using oxygen dayglow emissions at multiple wavelengths that originate at different altitudes. This feature, hitherto not reported before, has opened up a new dimension for upper atmospheric studies as it is now possible to investigate the altitude structure of the wave dynamics in the daytime due to different energy inputs.
- Aerosol optical depths simulated by global models are lower than the measured aerosol optical depths due to the absence of seasonal cycle in the models which is attributed to the lack of proper representation of aerosol emissions and not due to meteorology.
- The coarse mode aerosols (sizes greater than 0.6  $\mu\text{m}$ ) contribute ~50% to the columnar aerosol volume over Ahmedabad throughout the year because of the abundance of super-micron aerosols in contrast to Kanpur in the Indo-Gangetic Plains where sub-micron aerosols (sizes less than 0.6  $\mu\text{m}$ ) dominate.

### Geosciences

- A significant change in the  $\delta^{18}\text{O}$ -S relationship of the surface waters of the Bay of Bengal occurred during CE1994-2006. This was caused by river discharge containing glacier melt with highly depleted <sup>18</sup>O that mixes with the surface water of the Bay of Bengal. An estimated  $2.43 \times 10^{11} \text{ m}^3$  of Himalayan ice is likely to have melted during this period. This is a conservative estimate and is based on an increase in the fresh water contribution from Himalayan glaciers only to the Bay of Bengal. If Himalayan glaciers continue to melt at this rate, then the ice will disappear in 200-400 years.
- We estimated the increase in biological production in the surface Bay of Bengal induced by eddies. The highest surface productivity ( $2.71 \mu\text{MCD}^{-1}$ ) and chlorophyll a ( $0.18 \mu\text{g L}^{-1}$ ) were found within the eddy, and the lowest, at its outer edge.
- Significant stable isotopic differences between the summer and winter monsoons and their causes were documented.
- Dissolved Fe an important micronutrient controlling biogeochemistry of the oceans was measured in Indian Ocean using in-house developed very sensitive flow injection system. The Bay of Bengal waters are characterized by higher Fe resulting from particulate dissolution and shelf release in oxygen minimum zone. Atmospheric deposition contributes to the higher dissolved Fe in the surface water of the Arabian Sea. Hydrothermal activity contributes large amount of dissolved Fe to the Indian Ocean.
- Particulate matters contribute significantly to the dissolved Nd budget of the Arabian Sea. Particle – water interaction seems to have a dominant control on the Nd budget of the Arabian Sea with Nd contribution from fluvial particles increases towards northern Arabian Sea whereas Aeolian contribution decreases towards northern and eastern Arabian Sea.
- $\delta^{98}\text{Mo}$  gets modified during transport in the rivers and estuaries leading to its non-zero input to the ocean impacting the determination of paleo-redox condition.
- Ocean anoxia traced using  $\delta^{98}\text{Mo}$  of black shales indicate increasing oxic vs anoxic condition in the global ocean from the Proterozoic to the Early Cambrian.
- The vertical distribution of Dissolved Organic Carbon (DOC) in the Bay of Bengal has significant influence of fresh water discharge from several rivers and productivity with implications to the carbon budget of the region.
- The climatic history reconstructed from sediment cores from the Saurashtra peninsula shows that they responded in accordance with the global climatic events during the last two millennia.
- First ever Pan-India seasonal and annual isotopic maps for precipitation across the country and the corresponding meteoric water lines are now available from IWIN Isotope Data which provides new insights about spatio-temporal variations in hydro meteorological processes operating in India.

- A simple and user friendly technique, based on monitoring of absolute humidity along the backward wind trajectories, has been evolved to obtain first order information about probable vapour source region for precipitation at a given location.

### Theoretical Physics

- We have studied in detail the problem of parameter degeneracies which affect the sensitivity of neutrino oscillation experiments. In particular we consider the long baseline accelerator experiments T2K and NOVA and the atmospheric neutrino experiment of the India-Based Neutrino Observatory (INO) and show how the combination of different experiments help in resolving the degeneracies. We have also studied how addition of data from the above experiments help to economize the configurations of the LBNE experiment (which is recently renamed as DUNE) which is a 1300 km baseline beam based experiment being planned in US. We examined the hint of the leptonic CP phase from the data of the T2K experiment and examined if it can give any hint for the yet unknown neutrino oscillation parameters hierarchy and octant of the 2-3 mixing angle.
- We studied the implications for neutrinoless double beta decay in the context of TeV scale Left-Right symmetric models. In particular we consider scenarios in which the contributions due to light-heavy mixing or mixing between the left and right handed gauge bosons can make significant impact on the effective mass governing neutrinoless double beta decay.
- We also studied the production of heavy neutrinos at the Large Hadron Collider through the dominant s-channel production mode as well as the vector boson fusion process. We consider the TeV scale minimal linear seesaw model containing two heavy singlets with the opposite lepton number. This model is fully reconstructible from oscillation data apart from an overall normalization constant which can be constrained from the metastability of the electroweak vacuum and bounds coming from lepton flavour violation searches. The Dirac nature of heavy neutrinos in this model implies suppression of the conventional same-sign-dilepton signal at the Large Hadron Collider. We analyze the collider signatures with the trilepton final state and missing transverse energy as well as vector boson fusion type signals which are characterized by two additional forward tagged jets. Our investigation reveals that due to stringent constraints on light-heavy mixing coming from lepton flavor violation and metastability bounds, the model can be explored only for a light to moderate mass range of heavy neutrinos. We also note that in case of a positive signal, flavor counting of the final trilepton channel can give information about the mass hierarchy of the light neutrinos.
- Discovery of 125 GeV SM like Higgs boson with no significant hints of new physics summarise the first part of its run at Large hadron Collider (LHC). Stability of electro-weak vacuum, based on the present inputs from Higgs mass, Top mass together with strong coupling constant, can shed light on scale of new physics and that in turn also can constrain parameters. Although the concept of matrix copositivity and conditions has been developed for a long time in mathematics, very little exploration has been done to connect in physics context. Here we utilised this powerful tool to deduce the conditions that unambiguously ensure the boundedness of scalar potential.
- Propelled by the diverse experiments strongly indicating the existence of dark matter, particle physicists are busy accommodating them in our favourite new models as a new fundamental stable particle. While 'observing absence' being the signature of their presence at the Large Hadron Collider, extracting properties of new fundamental particles from such events are rather complex. Different constraint variables are developed that can be used for mass measurements and reconstruction of these events.
- By studying electric dipole moments (EDMs) of  $^{223}\text{Rn}$ ,  $^{199}\text{Hg}$  and  $^{225}\text{Ra}$ , the best limits on the tensor-pseudotensor coupling constant (CT) and nuclear Schiff moment (S) are inferred as  $\text{CT} < 2.09 \times 10^{-9}$  and  $\text{S} < 1.45 \times 10^{-12} |e| \text{fm}^3$  respectively. Combining these results with the nuclear models, it yielded limits on the strong CP-violating parameter  $\text{QCD} < 1.1 \times 10^{-9}$  and the combined up and down quark chromo-EDMs  $(\text{du-dd}) < 2.8 \times 10^{-26} |e| \text{cm}$ . These limits indicate possible signature of new physics beyond the standard model of particle physics. The clock frequency of the low-lying octupole transition in  $\text{Yb}^+$  is considered as suitable to replace the present primary frequency standard based on the ground state hyperfine transition of Cs atom. The quadrupole shift, one of the major systematic shifts, due to the gradient of stray electric field is determined and its implication on inferring possible temporal variation of fine structure constant is discussed.
- The frequency dependent scattering rate of generalized Drude model contains important information on the electronic structure and on scattering mechanism. In an important investigation, we study the frequency dependent scattering rate of cuprates (Mitrovi-Fiorucci/Sharapov-Carbotte scattering rate) in the pseudogap phase using the non-constant energy dependent Yang-Rice-Zhang (YRZ) density of states. First, with the energy dependent density of states, the scattering rate shows a depression at low energy coming from the opening of the pseudogap. Second, the evolution of  $1/\tau(\omega, T)$  with temperature shows the observed increase in scattering rate with temperature at lower frequencies and the temperature independence of scattering at higher frequencies. These signatures are qualitatively in accord with the experiments.
- A model is developed to capture "dance of pre-formed pairs" in the pseudogap state of high temperature cuprate superconductors. The model is a crude description of a hypothetical situation in which spin-driven spatial organisation of the pre-formed pairs is analysed. Within a mean-field theory (a slight

generalization of Bragg-Williams theory) we examined the behaviour of heat capacity and an “order parameter” which captures the short range correlations between the pre-formed pairs.

- We pursued the estimation of transport coefficients of hot and dense matter. In this context, we estimate dissipative properties viz: shear and bulk viscosities of hadronic matter using relativistic Boltzmann equation in relaxation time approximation within ambit of excluded volume hadron resonance gas model. We find that at zero baryon chemical potential the shear viscosity to entropy ratio decreases with temperature and reaches very close to Kovtun-Son- Starinets (KSS) bound. At sufficiently large baryon chemical potential this ratio shows same behavior as a function of temperature but goes below KSS bound. We further find that along chemical freeze out line  $\eta/s$  increases monotonically while the bulk viscosity to entropy ratio ( $\zeta/s$ ) decreases monotonically.

### Atomic, Molecular and Optical Physics

- PRL has proposed a satellite payload onboard Aditya L1 satellite to study the anisotropy of solar particles at the Lagrangian point L1. A Top-Hat-Analyzer - an electrostatic energy analyzer (ESA) for ion energies 200 eV - 20 keV was developed and tested in the lab. This ESA uses a resistive anode encoder (RAE), which is indigenously developed in the lab by depositing germanium tracks on a large area sapphire plate. The electronics for signal processing RAE signals also was indigenously developed. The ESA with RAE were successfully tested in the lab.
- New experimental cryo-facility to simulate icy astrochemical conditions as low as 10 K has been established in the laboratory. Using this new facility, chemistry occurring in icy mantles of cold dust grains are simulated. Synthesis of the basic unit of Polycyclic Aromatic Hydrocarbon (PAH), benzene, in dense medium via the propargyl radical is demonstrated experimentally for the first time in PRL. Propargyl radical pathway to benzene in dense medium was theoretically predicted in 1992 and now proven experimentally in 2014. This is the second known pathway for benzene synthesis on the cold dust grains and therefore insisting astronomers and astrophysicists to search for propargyl containing compounds in the interstellar medium. The study of infrared spectra of acetonitrile-water ice mixture revealed several new bands that can be used to detect such a dimer/cluster on Titan. Similarly, synthesis of ammonium dithiocarbamate from ammonia and carbon disulphide ices suggested the presence of complex thio compounds on Io and cometary ices.
- An accurate phase measurement from experimental low photon level interferograms has been demonstrated using a constrained optimization method that takes into account the expected redundancy in the unknown phase function. This approach is shown to have significant noise advantage over traditional methods, such as balanced homodyning or phase shifting that treat individual pixels in the interference data as independent of each other.
- Optical beams with phase singularity, although being classical, have properties of two mode entanglement in quantum states. This fact has been verified experimentally in our laboratory. Our experiment establishes an alternate form of Bell's inequality in terms of the Wigner distribution function which can be used for classical as well as quantum systems.
- We have demonstrated a new class of high power, continuous-wave, single-frequency coherent source in the ultraviolet wavelength range useful for quantum optics experiments.
- We have experimentally verified that the Boyd and Kleinman theory once predicted for optimum frequency doubling efficiency of continuous wave and long-pulsed lasers is also valid for ultrafast lasers under certain group velocity mismatch and spatial walk off effect.
- There is a continuing debate on the relative role of Indian Summer Monsoon (ISM) and the mid-latitude westerlies in driving the glaciation in Himalaya. Most studies suggest that on multi-millennial time scales, Himalayan glaciers responded to the enhanced ISM. In contrast, studies at PRL with robust chronometric controls, for the first time demonstrated that the mid-latitude westerlies drive the glaciations during global cooling events. This establishes a coupling between the northern latitude cooling and expansion of glaciers in Himalaya.
- Luminescence sensitivity of natural quartz varies over ten orders of magnitude. The reasons have been debated for long and a coherent explanation was not available. Using Fourier transform infra red spectroscopy and photoluminescence studies, it was observed that luminescence sensitivity of quartz was anti-correlated with the OH absorption signal. We suggested that the sensitivity is determined by silica-water impurity complexes. This study, when formalized, will have important ramification in sediment provenance studies.
- Marine inundations from Tsunamis are natural hazards. Recurrence intervals and magnitudes of inundations of large tsunamis are therefore needed. We provided the first chronometric data for past tsunamis along the Gujarat coast and suggested that besides the 1945 event, tsunami events around 6.6 ka and 35 ka occurred. The source region was estimated to be the Strait of Hormoz and the Chagos Archipelago.

# Awards and Honours

## Faculty

### U. R. Rao

1. D.Sc. (Hon. Causa), Vijayanagara Sri Krishnadevaraya University, Bellary, 2014.

### U. Sarkar

2. Elsevier most valued reviewers in appreciation of contributions to the quality of the Journal, Nuclear Physics B, August, 2014.

### J. N. Goswami

3. Axford Medal (first Indian Scientist to receive), for outstanding achievements in Geosciences, including planetary and solar system science, as well as unselfish cooperation and leadership in Asia and Oceania, Asia Oceania, Geosciences Society, 2014.
4. ISRO Outstanding Achievement Award for the year 2012, for significant contributions in Chandrayaan mission.
5. Life time achievements award at the 29<sup>th</sup> ISMAS Symposium on Mass Spectrometry held in Jodhpur, Rajasthan during 2 - 6 February, 2015.

### A. K. Singhvi

6. Invited member, Editorial board for journal EPISODES, International Union of Geological sciences (IUGS).
7. Invited member, Senior Advisory Board of Encyclopedia of Quaternary Science, Springer Verlag.

### R. Ramesh

8. Invited to the Editorial Boards of Journal of Climate Change and Current Science

### S.V.S. Murty

9. Member, Editorial Board, The Journal of Indian Geophysical Union.

### M. M. Sarin

10. Awarded INSA-Senior Scientist Position, January 2015.

### S. Ramachandran

11. Member, Editorial Board, Journal of Environmental Engineering and Science.

**D. Pallamraju**

12. Main Convener, General session on the Ionosphere and Atmosphere 10th annual Asia Oceania Geosciences Society (AOGS) Meeting, Sapporo, Japan, 28 July-01 August 2014.
13. Member, Editorial Board of Indian Journal of Radio and Space Physics (IJRSP) (2015 - 2017).
14. Member, National Science Steering Committee for the new ISRO Program "Solar Terrestrial Atmosphere Research Program (STARP)-India".

**Nandita Srivastava**

15. Working group leader jointly with Christian Moestl for working group on "Optimal combination of in-situ and remote sensing", Seventh solar information processing (SIP) workshop, La Roche den Ardenne, Belgium, August 18-21, 2014.
16. Established Scientist's Travel Award (ESTA) to attend the European Geosciences Union meeting, Vienna, April 2015.

**S. Goswami**

17. Joint Physics Coordinator, INO-ICAL collaboration.
18. Convener, INO-ICAL Conference Committee.
19. Joint Guest Editor, Advances in High Energy Physics.

**J. S. Ray**

20. Awarded "PRL Award" for the year 2013, Physical Research Laboratory, Ahmedabad, 12 August, 2014.

**S. K. Singh**

21. Awarded, "Eminent Mass Spectrometrist Award 2014", Indian Society for Mass Spectrometer, 29<sup>th</sup> ISMAS Symposium on Mass Spectrometry, Jodhpur, Rajasthan, February, 2 - 6, 2015.

**V. Sheel**

22. Main Convener, "Science and exploration of Mars and Venus", 11<sup>th</sup> annual Asia Oceania Geosciences Society (AOGS) meeting, Sapporo (Japan), 28 July-01 August, 2014: In Top 16 among 176 scientific sessions.
23. Empanelled as an expert in a committee to review "Centres of Excellence" at Sri Venkateswara University, Tirupati, constituted by the commissioner of technical education, Andhra Pradesh.
24. Convener (Indian-PI) of India-UK workshop on Indian megacities: developing effective environmental mitigation strategies, organised at Edinburgh, UK, February 18-20, 2015.

**R. D. Deshpande**

25. Expert Member, Board of Studies in Geology, M. S. University, Vadodara (for three years from November 2014).

**B. Joshi**

26. Awarded Research Professorship at School of Space Research, Kyung Hee University, Yongin, South Korea for the academic year 2014 - 2015.

**D. Chakrabarty**

27. Elected co-ordinator for Theme-3 electrodynamic processes in the near space environment: electrodynamic processes in the Ionosphere / Plasmasphere and its coupling with solar plasma variations and terrestrial forcing in the proposed Solar Terrestrial Atmospheric Research Program (STARP)INDIA.
28. Elected session chair in session ST10 (General session on the ionosphere and the atmosphere), AOGS, Sapporo, Japan, 28 July-01 August, 2014.

**Student****J. Sikdar**

29. First prize for best oral presentation at the 29<sup>th</sup> ISMAS Symposium on Mass Spectrometry held in Jodhpur, Rajasthan during 2 - 6 February, 2015.

**V. Panditi**

30. Justice Oak Best Thesis Award of the Astronomical Society of India, 2014.
31. Best thesis presentation award, Astronomical Society of India meeting, IISER, Mohali, March 2014.

**F. I. Laskar**

32. Best Ph.D. Thesis award in the Physical Sciences category, Gujarat Science Academy, 2014.

**R. A. Lagad**

33. 2<sup>nd</sup> prize, poster presentation, 29<sup>th</sup> ISMAS Symposium on Mass Spectrometry, Jodhpur, Rajasthan, 2-6 February, 2015.

**U. S. Banerji**

34. 2<sup>nd</sup> Prize, poster presentation, Expert Meet and National Conference on "Climate Change and Environmental Sustainability: Records from Poles to Tropics", Centre of Advanced Study in Geology, University of Lucknow, September, 9-10, 2014.

**S. Prabhakar**

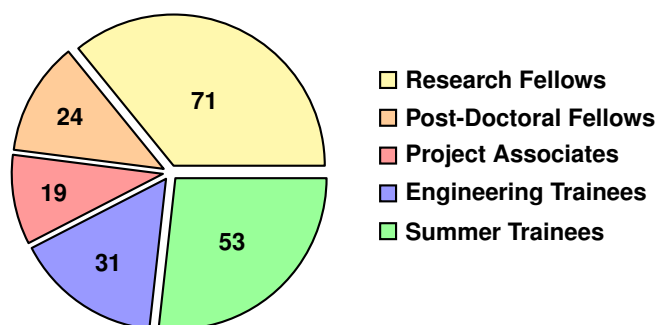
35. Best student paper award, Photonics 2014, IIT Kharagpur, December 13-16, 2014.

**A. N. Chaitanya**

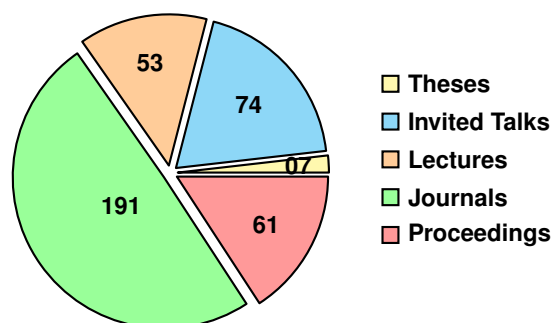
36. Student presentation prize from SPIE, USA, ICOP 2015, Kolkata, 20-22 February, 2015.
37. Best Student Paper Award at PHOTONICS 2014 Conference, IIT Kharagpur, December 13-16, 2014.
38. Awarded as one of the best posters at National Laser Symposium, Tirupati, 3-6 December, 2014.

# Human Resources Development

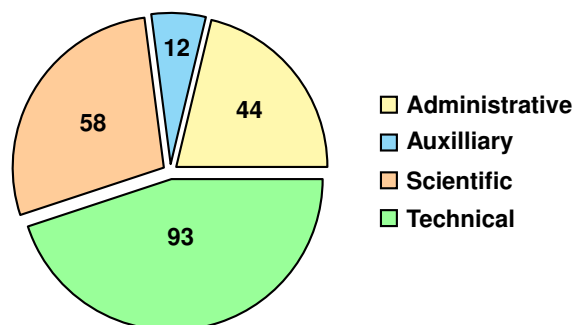
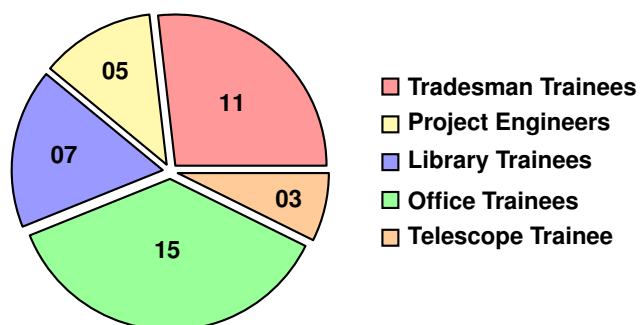
## Research & Internship Programmes



## Scientific Contributions



## Administrative and Auxiliary staff structure



The laboratory has a strong Human Resource Development (HRD) component with Doctoral, Post-Doctoral, visiting Scientist programs. In addition we have an Associate program for university teachers and project training for graduate and post graduate students in both engineering and computer applications. PRL organizes intensive summer programmes for students as well as college teachers every year. The purpose is to initiate them to current research activities being pursued at PRL which they can continue even after returning back to their colleges. It is also aimed at motivating them to take up research in basic sciences. The scientific output and staff details in numbers during the reporting year are presented in the above pie charts.

As a part of HRD activity under the PLANEX, following programmes were organized by PRL:

1. Workshop on Mars Orbiter Mission, PRL, Ahmedabad, August 20-21, 2014.
2. ISRO's Structured Training Programme (STP) Course on "Planetary Exploration", PRL, Ahmedabad, January 27-30, 2015.
3. 15<sup>th</sup> PLANEX Workshop on "Mars and Moon: Remote Sensing and Analogue Studies", PRL, Ahmedabad, January 4-10, 2015.
4. PLANEX Projects PIs Review meeting, PRL, Ahmedabad, March 27, 2015.

# Theses Submitted

## 1. Amrendra K. Pandey

“Dissociation Dynamics of Unstable Molecular Systems”, Mohanlal Sukhadia University, Udaipur, May, 2014.

## 2. Shashi Prabhakar

“Vortices of Light and their Interaction with Matter”, IIT Gandhinagar, July, 2014.

## 3. Tanushree Basak

“Astro-Particle Aspects of Dark Matter Phenomenology”, Mohanlal Sukhadia University, Udaipur, July, 2014.

## 4. Fazlul I. Laskar

“Effects of lower atmospheric and solar forcings on daytime upper atmospheric dynamics”, IIT, Gandhinagar, September, 2014.

## 5. Raja Bayanna Ankala

“Study of coupling between the layers of the solar atmosphere at high-resolution”, Mohanlal Sukhadia University, Udaipur, December, 2014.

## 6. Suruchi Goel

“The Study of Properties of Sunspots”, Mohanlal Sukhadia University, Udaipur, February, 2015.

## 7. Wageesh Mishra

“Evolution and consequences of coronal Mass ejections in the heliosphere”, Mohanlal Sukhadia University, Udaipur, March, 2015.

# Colloquia/Public Lectures by Visitors

## **Dr. Deshdeep Sahdev**

Department of Physics, IIT Kanpur

***Indigenous technology in a Globalized World: A Case Study or Resolving Atoms in our Backyards***

## **Prof. Ashok Das**

Professor Department of Physics and Astronomy, University of Rochester Rochester, USA

***Supersymmetry, shape invariance and the Legendre equation***

## **Dr.Ketan Patel**

Istituto Nazionale di Fisica Nucleare, Theoretical Physics Group, Padova, Italy

***The Flavour Puzzle and Grand Unification***

## **Dr. Manikandan Muthu**

IIT Madras, Chennai

***Haloarchaea - an Astrobiological relevance***

## **Dr. V.M.Datar**

Head Nuclear Physics Division, Bhabha Atomic Research Centre, Mumbai .

***Melting of shell effects and radiating dumbbells - two interesting problems in nuclear physics***

## **Dr.R.N.Singh**

INSA Senior Scientist CSIR - NGRI, Hyderabad.

***Bayesianism in Geosciences***

## **Prof.Rajiv V.Gavai**

Chairperson & Senior Professor Theoretical Physics at TIFR, Mumbai

***QCD Critical Point:A Synergy between Theory and Experiment***

## **Prof.Lokesh C. Tribedi**

Full Professor (H), Department of Nuclear and Atomic Physics,Tata Institute of Fundamental Research,

***Fast ion-molecule collisions: Interdisciplinary science***

## **Prof. K.P.J.Reddy**

Senior Professor Department of Aerospace Engineering, Indian Institute of Science, Bangalore.

***Shock Waves Research in IISc: Taking them to Commercial Arena***

## **Dr. Helen Mason**

Department of Applied Mathematics and Theoretical Physics, Cambridge, UK

***The Active Sun: what have we learnt from recent Space Observations?***

## **Prof. Sushil K. Dash**

Emeritus Professor Centre for Atmospheric Sciences, Indian Institute of Technology, Delhi.

***Indian summer monsoon and associated extreme events based on RegCM projections under CORDEX programme***

## **Prof.P.K.Manoharan**

Professor and head, Radio Astronomy Centre National Centre for Radio Astrophysics Tata Institute of Fundamental Research Udhagamandalam (Ooty) 643001

***Ooty Interplanetary Scintillation Observations and 3-D Heliosphere***

## **Prof.Sandip Pakvasa**

University of Hawaii, Honolulu

***Public Lecture - Galactic Neutrino Communication and Search for Extra Terrestrial Intelligence (SETI)***

## **Dr .M .S .Nandakumar**

Centro de Astrofisica da Universidade do Porto, Portugal

***The formation of high mass stars***

**Dr.Haranath Ghosh**

Assistant Professor RRCAT, Indore

***Fe-based superconductors ; 7 years after its discovery***

Vikram Professor, PRL.University of Colorado, Boulder, USA  
***Public Lecture-The Impacts of Extreme Space Weather on Society and the Economy***

**Prof.Rajat K.Bhaduri**

Visiting Professor IMSc, Chennai, India.

***Dark Matter (DM) and Dark Energy (DE) from a Bose-Einstein Condensate***

**Prof. B. Ananthanrayan**

Professor, Chairman, Centre for High Energy Physics, Indian Institute of Science, Bengaluru.

***Physics of light flavoured quarks***

**Prof. Daniel N. Baker**

Director, Laboratory for Atmospheric and Space Physics, Vikram Professor, PRL.University of Colorado, Boulder, USA

***New Results Concerning Earth's Van Allen Radiation Belts***

**Prof. Sourendu Gupta**

Department of Theoretical Physics, TIFR, Mumbai

***Hot stuff***

**Prof. Daniel N. Baker**

Director, Laboratory for Atmospheric and Space Physics,

**Dr. Girish S. Setlur**

Associate Professor, Department of Physics, IIT Guwahati

***Rabi Oscillations in Graphene***

# Invited Talks at Conferences / Symposia / Workshops

## Astronomy and Astrophysics

### P. Janardhan

1. "Declining Solar Polar Fields and their Signatures in the Solar Wind: Implications to near Earth Space", United Nations/Japan Workshop on Space Weather Science and Data Products from ISWI Instruments, Fukuoka, Japan, 2-6 March, 2015.

### A. Chakraborty

2. "PARAS: The first dedicated program on exoplanets in India", Geneva Observatory, Geneva, Switzerland, September, 2014.

### S. V. Vadawale

3. "Prospects of Hard X-ray Polarimetry with Astrosat-CZTI", International conference on X-ray Polarization in Astrophysics: A New window about to open?, Stockholm, Sweden, 25 - 28 August, 2014.
4. "Hard X-ray Polarimetry: Why and How?", Topical conference on Hard X-ray Astronomy: Astrosat and beyond, Goa, 24 - 26 September, 2014.

### T. Chattopadhyay

5. "Prospects of hard X-ray polarization of galactic X-ray binaries with Astrosat CZTI", Topical conference on Hard X-ray Astronomy: Astrosat and beyond, Goa, 24 - 26 September, 2014.

### S. Naik

6. "High Mass Neutron Star X-ray Binaries", Hard X-ray Astronomy: Astrosat and Beyond, Goa, 24-26 September, 2014.

### S. Ganesh

7. "PRL plans for ground based observations of Comet Siding Spring C/2013 A1 and its interaction with Mars", Meeting to discuss observations of Comet C/2013 A1 Siding Spring encounter, ISRO HQ, Bangalore, 13 October, 2014.
8. "Observations of cometary dust from Mount Abu", International Conference on Interstellar Dust, Molecules and Chemistry, Tezpur University, Assam, India, 15-18 December, 2014.

**Solar Physics****S. K. Mathew**

9. "Multi-Application Solar Telescope", Conference on coupling and dynamics of the solar atmosphere, IUCAA, Pune, India, 10-14 November, 2014.

**N. Srivastava**

10. "Solar optical instrumentation", DWIH Indo-German winter school on Astrophysics, TIFR, Mumbai, 3-7 November, 2014.
11. "CME-CME interaction: kinematics and consequences", Astronomical Society of India meeting, NCRA, Pune, 17-20 February, 2015.

**Planetary Sciences and PLANEX Program****K. K. Marhas**

12. "Nano-SIMS : an unique imaging tool using secondary ion emission", One day workshop on "Nanoprobe Techniques", IIT Delhi, 14 July, 2014.

**J. P. Pabari**

13. "Microwave Remote Sensing of Planetary Surfaces ", A. D. Patel Institute of Technology, Vitthal Udyognagar, Gujarat, India, 15 October, 2014.

**S. V. S. Murty**

14. "Atmospheres of terrestrial planets An overview", The Second Venus Workshop, NGRI, Hyderabad, 28-29 October, 2014.

**Space and Atmospheric Sciences****D. Chakrabarty**

15. "Effects of space weather processes on the equatorial electrojet current system", session ST03, AOGS, Sapporo, Japan, 28 July-01 August, 2014.

**D. Pallamraju**

16. "The CAWSES Program and Indian Perspective", 13<sup>th</sup> Solar Terrestrial Physics Meeting Xián, China, 12-18 October, 2014.

**L. K. Sahu**

17. "Variability of volatile organic compounds at continental sites and surrounding marine regions of India", International Global Atmospheric Chemistry (IGAC) India Working Group Workshop, IISc, Bangalore, 06 April, 2014.
18. "Variability of tropospheric ozone over an urban site in India: A study based on MOZAIC and CCM vertical profiles over Hyderabad", Scientific symposium on atmospheric composition observation by commercial aircraft, Toulouse, France, 12-15 May, 2014.
19. "Measurements of volatile organic compounds over India and surrounding oceanic regions: need for future studies", Japan Agency for Marine-Earth Science and Technology (JAMSTEC), Yokohama, Japan, 10 October, 2014.
20. "Measurements of volatile organic compounds and importance of model based study of trace gases over India", Meteorological Research Institute (MRI), Tsukuba, Japan, 14 October, 2014.
21. "PTR-TOF-MS measurements of VOCs at Ahmedabad during winter", India-UK seminar on Knowledge transfer on Indian mega-cities: developing effective environmental mitigation strategies, Edinburgh, UK, 18-20 February, 2015.

**R. Sekar**

22. "Results on E-region plasma irregularities based on rocket measurements", 40<sup>th</sup> COSPAR Scientific Assembly, Moscow, August, 2014.

**S. A. Haider**

23. "Predicted meteor showers at Mars during the encounter of comet C/2013 A1" (Paper #PS07-A009), 11<sup>th</sup> Asia Oceanic Geosciences Society (AOGS) meeting, Sapporo, Japan, 28 July-01 August, 2014.
24. "Ionosphere of Mars during disturbed condition (Paper # C3.2-0019-12), 40<sup>th</sup> COSPAR Scientific Assembly, Moscow, Russia, 02-10 August, 2014.
25. "Science and exploration of Indian Mars mission (Paper # B0.2-0021-14), 40<sup>th</sup> COSPAR Scientific Assembly, Moscow, Russia, 02-10 August, 2014.
26. "Meteoroid ablation in the atmosphere of Mars" (Paper # 3.2-008-14), 40<sup>th</sup> COSPAR Scientific Assembly, Moscow, Russia, 02-10 August, 2014.
27. "Chemistry and dynamics of the lower ionosphere of Mars (Paper #C4.3-0017-14), 40<sup>th</sup> COSPAR Scientific Assembly, Moscow, Russia, 02-10 August, 2014.
28. "Science and exploration on Mars: MAVEN/Mangalyaan", International Conference on Frontiers of Spectroscopy (ICFS), Banaras Hindu University, 10-12 January, 2015.
29. "Mars atmosphere and magnetosphere", ISRO-Structured Training Program (STP) Planetary Exploration, PRL, 27-30 January, 2015.

**S. Ramachandran**

30. "Aerosols and Monsoon Rainfall", International Workshop on "Assessing the impact of aerosols and changing climate on monsoon and extreme events", Ansal University, Gurgaon, 12-15 January, 2015.

**V. Sheel**

31. "Role of dynamics and biomass burning on CO and O<sub>3</sub> over Asia: MOZAIC vs. Models", MOZAIC-IAGOS Scientific symposium on atmospheric composition observation by commercial aircraft, Toulouse, France, 12-15 May, 2014.

**Geosciences****J. S. Ray**

32. "Learning from subduction zone: the story of Andamans", PRL Award acceptance talks, Physical Research Laboratory, Ahmedabad, 12 August, 2014.
33. "Oxygenation of Earth's atmosphere-ocean system", UK-India Frontiers of Science Meeting, Khandal, 9-13 October, 2014.
34. "Interior of Terrestrial Planets", Planex Workshop at Physical Research Laboratory, Ahmedabad, 05 January, 2015.

**M. M. Sarin**

35. "Atmospheric black carbon and organic aerosols from Northern India", International Geosphere Biosphere Programme Symposium, Indian Institute of Science, Bengaluru, 07 April, 2014.
36. "Atmospheric outflow of nutrients to the Bay of Bengal: Impact of continental sources", European Geosciences Union - 2014, Vienna, Austria, 26 April - 03 May, 2014.
37. "Acidification of coastal waters: Relative impacts of CO<sub>2</sub> versus other anthropogenic gases", Indian Institute of Technology, Dept. Geology & Geophysics, Kharagpur, 30 June, 2014.
38. "Atmospheric chemistry and climate change: Role of black carbon and organic aerosols", International Conference on Futuristic Materials, Chemistry Department, Nagpur University, 4 - 7 February, 2015.

**R. D. Deshpande**

39. "Water on Earth and challenging issues", Special Lecture in Refreshers Course on Environmental Studies, UGC Staff College, Gujarat University, Ahmedabad, 17 June, 2014.
40. "Career opportunities in basic research", Foundation Day Lecture, Zydus School for Excellence, Vejalpur, Ahmedabad, 28 August, 2014.

**R. Ramesh**

41. "Climate Change: Possible new areas of research", National Geophysical Research Institute, Hyderabad, 09 May, 2014.
42. "Climate Change: Indian records", INSA lecture at Indian Institute of Technology, Powai, Mumbai, 22 August, 2014.
43. "Observed changes in Indian monsoon from paleoclimate and proxy records", 6<sup>th</sup> Annual Workshop on Climate Change, INCOIS, Hyderabad, 01-02 September, 2014.
44. Key note address for the 7<sup>th</sup> International Conference on Geoscience Education, University of Hyderabad, 05 September, 2014.
45. Hindi lecture on "Oceanography", Hindi technical Seminar, Indian Institute of Tropical Meteorology, Pune, 06 September, 2014.
46. "Past records of aerosols in oceans", International workshop on Assessing the Impact of Aerosols & Changing Climate on Monsoon & Extreme Events, 12-15 January, 2015.
47. "Environmental controls on new and primary production in the northern Indian Ocean", Ocean Science Society Conference, National Institute of Oceanography, 23 March, 2015.

**S. K. Singh**

48. "Application of Mass spectrometry in studying Earth surface and oceanographic processes", ISMAS Conference, Jodhpur, Rajasthan, 2-6 February, 2015.

**Theoretical Physics****U. Sarkar**

49. "LHC and Baryon Number Violation", Neutron - Antineutron Meeting, Nevis Laboratory, Columbia University, 30-31 January, 2015.

**R. Rangarajan**

50. "Inflation after Planck and BICEP2" Invisible Matters: Neutrino and Dark Matter, IIT Hyderabad, 29-31 October, 2014.
51. "Inflation after Planck and BICEP2" Institute of Mathematical Sciences, Chennai, 01 December, 2014.
52. "Inflation after Planck and BICEP 2", XXI DAE-BRNS High Energy Physics Symposium, IIT Guwahati, 08-12 December, 2014.
53. "Resonant Gravitino Production in the Early Universe", XXI DAE-BRNS High Energy Physics Symposium, IIT Guwahati, 08-12 December, 2014.

**S. Goswami**

54. "Neutrino Phenomenology: Highlights of oscillation results and future prospects", Invited Plenary talk, ICHEP, Valencia, July, 2014.
55. "Neutrinos in the time of Higgs", Invited Plenary talk UNICOS, Punjab University, Chandigarh, May, 2014.

**P. Konar**

56. "SUSY and alike, mass measurements at the LHC" - Plenary talk, '4<sup>th</sup> KIAS Workshop on Particle Physics and Cosmology', Korea Institute for advanced Study (KIAS), 27-31 October, 2014.
57. "Micro to Macro" - Public lecture at 'Astro-fest AGAAM 2014', OVSRCSC, Rajkot, 31 May - 01 June, 2014.

**B. K. Sahoo**

58. "Atom: the building block of the matter is a mini universe", Invited talk at INSPIRE Science Camp for the school children held at the M S University, Vadodra, India, 25-29 July, 2014.
59. "Relativistic many-body methods for fundamental physics", Invited talk at the 11<sup>th</sup> Asian International Seminar on Atomic and Molecular Physics held at Sendai, Japan, 6-10 October, 2014.

**D. P. Dewangan**

60. "Rydberg atoms and some fundamental points of physics", XXIX<sup>th</sup> Gujarat Science Congress 2015 (Symposium on future trends in science and technology), Gujarat Science City, Ahmedabad, 01 March, 2015.

**V. K. B. Kota**

61. "Group Theory for Embedded Random Matrix Ensembles", 30<sup>th</sup> International Colloquium on Group Theoretical Methods in Physics, Ghent University, Ghent (Belgium), 14-18 July, 2014.
62. "Random Matrix Theory with U(N) Racah Algebra for Transition Strengths", in the XVI International Conference on "Symmetry Methods in Physics", JINR, Dubna (Moscow region, Russia), 13-18 October, 2014.
63. "Basics of Shell Model and Interactions" (four lectures), DST (Govt. of India) SERB school on "Nuclear structure, at high angular momentum and isospin", TIFR, Mumbai, 05-25 October, 2014.

64. "Shell Model and Pairing Symmetries" (5 lectures and 3 tutorials), DST (Govt of India) SERB special school on "Modern Theories of Nuclear Structure", IIT Roorkee, Roorkee, 23 February - 05 March, 2015.
65. "Classical to Embedded random matrix ensembles in Nuclear Structure", in the National Seminar on "Recent Advances in Physics", Berhampur University (Odisha), 05-06 May, 2014.

**N. Singh**

66. "Infrared conductivity of cuprates using Yang-Rice-Zhang ansatz: Review of our recent investigations", International Conference on Condensed Matter Physics (ICCMP-2014), HP University, Shimla, Himachal Pradesh, India, 04-06 November, 2014.
67. "Infrared/optical conductivity of Cuprates using Yang-Rice-Zhang ansatz", HP university, Himachal Pradesh, India, 06 May, 2014.
68. "How to choose your career in Physics", Kanya Maha Vidyalaya, Jalandhar, Punjab India, 13 May, 2014.

**Atomic, Molecular and Optical Physics****R. P. Singh**

69. "Optical vortex: Experimental aspects", Frontiers in Light-Matter Interactions, ICTS School, IACS Kolkata, 08-18 December, 2014.
70. "Vorticity of scattered optical vortices", IONS-Asia6 Kharagpur, IIT Kharagpur, 10-12 December 2014.
71. "Interferometry in classical and quantum optics", C. K. Majumdar Memorial Summer Workshop in Physics 2014, S. N. Bose National Center for Basic Sciences, Kolkata, 17-27 June, 2014.
72. "Optical vortices: entanglement, teleportation and quantum key distribution", Workshop on Quantum Paradigms and Security, IISER Kolkata, 27-28 September, 2014.

**B. Sivaraman**

73. "Synthesizing the basic unit of PAH", Invited review talk, International conference on interstellar dust, molecules and chemistry, Tezpur University, 15-18 December, 2014.
74. "Can we use the absorption at the Hartley band to confirm the presence of ozone on icy bodies in the solar system?", IRC conference on Research in Astronomy-opportunities and Challenges, Nirmala College, Muvattupuzha, 08-10 December, 2014.

# Lectures at Universities / Institutions

## Astronomy and Astrophysics

### A. Chakraborty

1. "PARAS & Exoplanets": Indian Institute of Science, Bangaluru, India, August, 2014.

### T. Chattopadhyay

2. "X-ray Polarimetry Programs at PRL (India)", Istituto di Astrofisica e Planetologia Spaziali (IAPS)-INAF, Rome, Italy, 29 April, 2015.
3. "Development of a Hard X-Ray focal Plane Compton Polarimeter", Centrum Badan Kosmicznych, Polskiej Akademii Nauk (CBK-PAN), Wroclaw, Poland, 27 April, 2015.

### A. K. Singal

4. "Our Motion in the Universe", Rajasthan School, Ahmedabad, 18 November, 2014.
5. "Large relative motion observed between three different cosmic reference frames: Is the cosmological principle in jeopardy?", NCRA, Pune, 29 September, 2014.
6. "Radio telescopes : Our big ears to the Universe", Lucknow Planetaria, 04 June, 2014.
7. "Absolute Motion of the Earth in the Universe", Lucknow University, 05 June, 2014.

## Solar Physics

### A. Ambastha

8. "Understanding our daytime star: The Sun", Rajasthan Vidyapeeth-Shramjeevi College, Udaipur, 20 February, 2015.

### U. Kushwaha

9. "Multi-wavelength investigations of solar eruptive phenomena: a few case studies", Astronomical Institute of Wroclaw, Wroclaw, Poland, 07 April, 2014.

### V. Panditi

10. "Formation and initiation of magnetic flux ropes", IIA, Bangalore, 17-21 August, 2014.

### N. Srivastava

11. "Evolution, interaction and impact of coronal mass ejections", colloquium at Center of Excellence in Space Sciences, India (CESSI), IISER Kolkata, 10 April, 2014.
12. "Solar optical instrumentation", Two lectures in space astronomy course, Center of Excellence in Space Sciences, India (CESSI), IISER Kolkata, 10-11 April, 2014.

**Planetary Sciences and PLANEX Program****J. P. Pabari**

13. "Space Research and Instrumentation", Parul Institute of Engineering and Technology, Waghodia, Gujarat, 04 February, 2015.
14. "Role of Electronics and Communication in Space Research", Venus International College of Technology, Kalol, Gujarat, 29 September, 2014.

**S. V. S. Murty**

15. Special lecture at Rajasthan High School, Ahmedabad, "Mars Orbiter Mission of ISRO", 28 November, 2014.

**Space and Atmospheric Sciences****D. Pallamraju**

16. "A brief introduction to Space Weather and its effect on space and ground-based systems", 9th UNCSSTEAP program, 25 November, 2014.

**H. Chandra**

17. "UN Course on Space Science": 52 lectures

**S. Lal**

18. Four Lectures on "Ozone and other trace gases and atmospheric Chemistry" during Satellite Meteorology and Global Climate (SATMET) course of Centre for Space Science and Technology Education in Asia and the Pacific (CSSTEAP), SAC, Bopal, Ahmedabad, 12-16 January, 2015.

**S. K. Sharma**

19. "Science and Importance of the Earth's Atmosphere", DST INSPIRE Program, Christ College, Saurashtra University, Rajkot, 25 April, 2014.
20. "Earths Middle and Upper Atmospheric Climate Change" Radio Astronomy Centre, (TIFR), Ooty, 05 May, 2014.
21. "Lidar and Radar Exploration of the Earths Atmosphere", Joint Session of CSSTE-AP, Space Science Course and Remote Sensing Course, Space Applications Center, Ahmedabad, 07 August, 2014.
22. "Study of the Earths Atmosphere using Ground based and Satellites based Instruments" Rashtriya Post Graduate College, Purvanchal University, Jaunpur, 20 October, 2014.
23. "Space and Atmospheric Research: Indian Perspective" M. B. Patel Education Trust and College of Engineers, Kadi, Gandhinagar, 01 December, 2014.

**S. P. Gupta**

24. "Introductory lecture on Space Physics" to the participants of 9th Space and Atmospheric Science course, CSSTEAP, PRL, September, 2014.

**S. Ramachandran**

25. "Global Warming, Ozone and Air Pollution" INSPIRE Internship Science Camp-2014, Saurashtra University, Rajkot, 02-06 July, 2014.

**T. A. Rajesh**

26. "Climate Dynamics and Earth System Interactions", 22 Lectures for M. Sc. (Earth Science), Sardar Patel University, Vallabh Vidyanagar, Anand, August-November, 2014.

**V. Sheel**

27. "Variability of trace gases over Asia", School of Geosciences, University of Edinburgh, UK, 23 May, 2014.

**Geosciences****M. G. Yadava**

28. "Application of statistical tools in polar and ocean studies", National Centre for Ocean and Antarctic Research, Goa, 8-12 December, 2014 (10 lectures).
29. "Radiocarbon dating method", Centre for Earth and Space Sciences, University of Hyderabad, Hyderabad, 28 February, 2015.
30. "Advanced Statistical Concepts in Atmospheric and Ocean Sciences", Indian National Centre for Ocean Information Systems, Hyderabad, 23-28 February, 2015 (10 lectures).

**R. Bhushan**

31. "Oceanography: An emerging Science", DST-Inspire lecture, Institute of Life Sciences, Ahmedabad University, Ahmedabad, 04 November, 2014.

**R. Ramesh**

32. "Paleoclimate methods and monsoons in the past", DST-SERB School on Science on Basics of Atmospheric Sciences, S.V. University, Tirupati, 27 May, 2014 (2 lectures).
33. "Oceanography and Atmospheric Sciences", International earth Science Olympiad Training Camp, Geological Society of India, Bengaluru, 27-29 May; 18-20 September, 2014 (19 lectures).
34. "DST-INSPIRE lecture", M.S. University, Vadodara, 27 July, 2014.
35. "DST-INSPIRE lectures", K. R. Rangasamy College, Thiruchengodu, 12 -13 & 28-29 July; 8, 16-17 August, 2014 (13 lectures).
36. "Application of statistical tools in polar and ocean studies" , National Centre for Ocean and Antarctic Research, Goa, 8-12 December, 2014 (12 lectures).
37. "Geological Oceanography", Centre for Earth and Space Sciences, University of Hyderabad, 2-3 April; 3-4 September, 2014 & 24-26 February, 2015 (9 lectures).
38. "Oceanography", Indian Institute of Science Education and Research, Pune, 28-29 January, 2015 (3 lectures).
39. "Advanced Statistical Concepts in Atmospheric and Ocean Sciences", Indian National Centre for Ocean Information Systems, Hyderabad, 23-28 February, 2015 (12 lectures).

**Theoretical Physics****U. Sarkar**

40. "Neutron - Antineutron Oscillation and Baryogenesis", Physics Department, Arizona State University, 05 February, 2015.

**H. Mishra**

41. "Lectures on Quantum Field Theory", (6 lectures), Berhampur University, Bhanjavihar, Odisha, 08-20 March, 2015.

**R. Rangarajan**

42. "Gravitinos, Reheating and the Matter-Antimatter Asymmetry of the Universe", Institute of Mathematical Sciences, Chennai, 27 November, 2014.
43. "Gravitinos, Reheating and the Matter-Antimatter Asymmetry of the Universe", Indian Institute of Science Education and Research, Pune, 3 December, 2014.

**A.C.Das**

44. "Physics of Magnetosphere" at Ninth post graduate course on Space and Atmospheric Sciences of CSSTEAP, SAC Ahmedabad during December, 2014 and January, 2015.( 23 Lectures ).

**P. Konar**

45. "Dark connection and progress in mass measurements at the LHC" - Theory talk at Harish-Chandra Research Institute (HRI), Allahabad, 21 July, 2014.
46. "T cup and beyond" - Theory talk at the Korea Institute for advanced Study (KIAS) on 06 November, 2014.

**B. K. Sahoo**

47. "Future direction of studying atomic properties of francium isotopes" at the Radiation Nuclear Physics Group, Department of Physics, Tohoku University, Sendai, Japan, 17 October, 2014.
48. "Possible temporal violation of fine structure constant", Department of Physics, MS University, Vadodara, India, 28 July, 2014.

**D. P. Dewangan**

49. "Understanding nature", DST INSPIRE Programme, Institute of Life Science, Ahmedabad University, Ahmedabad, 07 November, 2014.

**Atomic, Molecular and Optical Physics****A. K. Singhvi**

50. "South Asian Academies Congress, New Delhi- Evolution and Present status of International Geological Congress , 2020", Indian National Science Academy, 10 October, 2014.
51. IGBP Steering Committee Meeting; Symposium on "Geosphere Biosphere Interactions in a Future Earth" on Up-scaling point data to Regional and Global Scale, and their implication on Stratigraphic Correlations on Global Change time scale: How realistic are these? Bengaluru, 7 April, 2014.

**B. Sivaraman**

52. A series of 10 lectures on the "Atmospheres and interfaces of other Solar System bodies", at the UN Space Course.

**R. P. Singh**

53. "Optical vortices: some experiments in classical and quantum optics", IIT Madras, Chennai, 11 June, 2014.

# SCIENCE at PRL

## Astronomy and Astrophysics

### Unprecedented brightness levels in blazar S5 0716+71

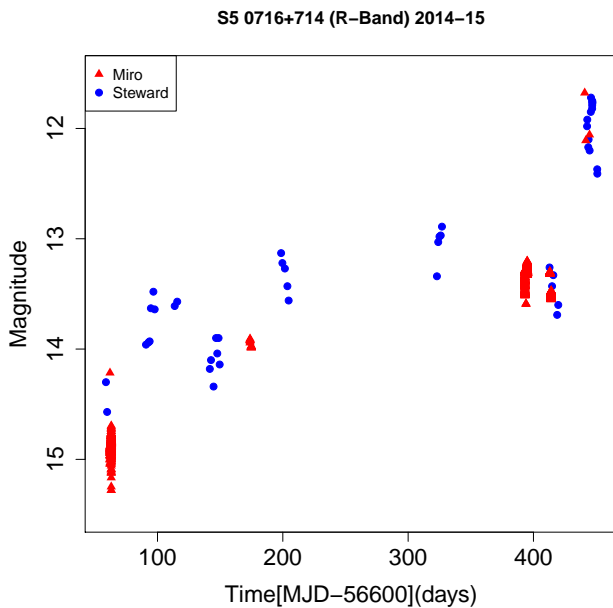


Figure 1: Variation in brightness (Mag) as a function of time (MJD), for S5 0716+71 during Jan 2014 to Feb 2015. Source shows lowest and highest brightness levels ever reported.

The intermediate energy peaked BL Lac object S5 0716+71, one of the most active blazars, is being monitored regularly from Mt. Abu Observatory. Based on the long-term trends in the light-curve, encompassing 1971 to 2013, we had predicted last year (Annual Report 2013-14, p26) that the source should start brightening towards the beginning of 2015. The inference was based on the possibility of the long-term changes in the brightness of the source to be caused by the precession of the relativistic jet on its axis. According to this, the source brightens as the viewing angle decreases due to precession of the jet and vice versa. The source started brightening towards the end of 2014 and reached unprecedented levels (11.6 mag in R band) in January 2015. S5 0716+71 was very active during February 2015 as well. It also showed very high and variable degree of optical polarization along with flaring in  $\gamma$ -ray and x-ray as reported by other groups. The variations appear to be quasi-simultaneous giving credence to their co-spatial origin. Figure 1 shows the variation in R-band (our data along with those of Steward Observatory) for S5 0716+71 during 2014-15, notice the faintest ( $R > 15$  mag) and brightest ( $R < 11.7$  mag) states.

(K. S. Baliyan, N. Kaur, Sameer, S. Chandra and S. Ganesh)

### Intra and inter night variable polarization in S5 0716+71

This source has extensively been observed in total flux at almost all the energies it has been detected in. However, polarization measurements on this source are

very scanty. Considering its very active nature at short and long timescales, we have conducted optical polarization observations of this source to see its behaviour in polarized light. Our observations during December 2009 show the source showing rapid intra-night variations during which degree of polarization (DP) changes from  $\sim 11.4\%$  to about  $6.5\%$  in just about hour and half. To study its inter-night behaviour, we used polarization data from Steward Observatory (Dec. 15-21, 2009) in addition to our data (Dec. 10-14, 2009). The polarization curve shows two humps with peak DP as 17 and  $28\%$ , respectively while position angle varies between  $140$  and  $80$  degrees. During this period, source is in pre-flare phase at high energies and optical, before the major flare. The changes in the DP and PA along with multi-frequency fluxes, could be indicative of the shock progressing down the jet, compressing the plasma and leading to alignment of tangled magnetic field. Figure 2 shows intra-night variation in the degree of polarization.

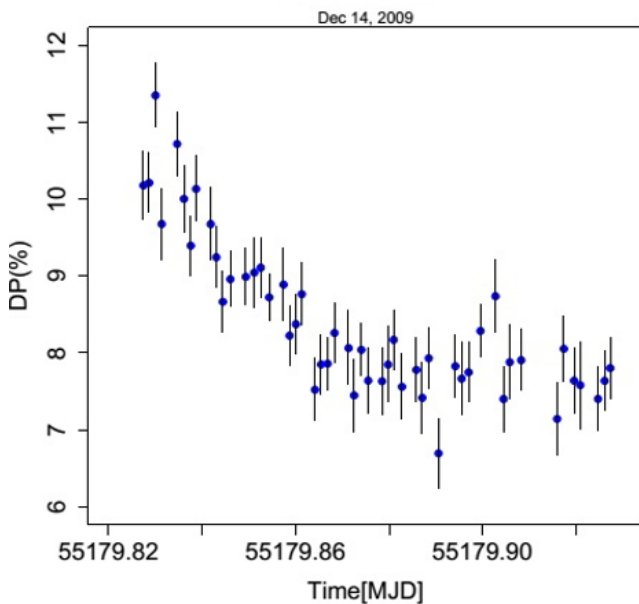


Figure 2: Intra-night variation in degree of polarization and position angle for the source S5 0716+71 during December 14, 2009.

(K. S. Baliyan, N. Kaur, Sameer, S. Chandra and S. Ganesh)

### Spectral energy distribution of CGRaBS J0211+1050

CGRaBS J0211+1051 was detected by Fermi space borne observatory in flaring state in high energy  $\gamma$ -rays. To understand the nature of the source, we had conducted optical polarization measurements on the source during 2011 and found the source to have high and variable optical polarization. A significant change in the position angle of polarization was also noted. Based on this study, we had proposed the source to be a low energy peaked blazar (LBL). However, the true classification is possible only with

the location of low energy synchrotron peak in its SED. Therefore, multi-wavelength data on the source was used to estimate various parameters and to verify its classification vis-a-vis blazar sequence. The light curves show variations in the high-energy  $\gamma$ -rays to be correlated with X-ray, UV, and optical variations, indicating to co-spatial origin of these emissions. Our optical data, quasi-simultaneous with UV (Swift-UVOT) and X-ray (Swift-XRT) data, enabled us to trace the low-energy (synchrotron) component of the spectral energy distribution (SED) for CGRaBS J0211+1051 for the first time. The SED shows the synchrotron peak to lie at  $\approx 1.35 \times 10^{14} \text{ Hz}$ , confirming CGRaBS J0211+1051 to be an LBL. Some other parameters, such as the local magnetic field  $\sim 5.93 \text{ G}$  and black hole mass ( $\approx 2.4 \times 10^8 M_{\odot}$ ), are also estimated which are in agreement with their typical values for the blazars.

(K. S. Baliyan, N. Kaur, S. Chandra and S. Ganesh)

### Dependence of Fanaroff-Riley break of radio galaxies on luminosity and redshift

The morphological differences in the two classes (FR 1 and 2 types) of sources were investigated to see if these are due to the differences in their luminosities, as usually assumed in the literature, or could these as well be primarily a redshift-dependent effect? By using a large enough sample, that allowed us to compare sources with similar luminosities but at different redshifts as well as examine sources at similar redshifts but with different luminosities, a successful separation of the otherwise two intricately entangled effects was achieved. It turned out that the morphology type is not directly related to redshift and that the break between the two types of morphologies seems to depend only upon the radio luminosity.

(A. K. Singal and K. Rajpurohit)

### Discordance of the unified scheme with observed properties of quasars and high-excitation galaxies in the 3CRR sample

We examine the consistency of the unified scheme of FR II-type radio galaxies and quasars with their observed number and size distributions in the 3CRR sample. We separate the low-excitation galaxies from the high-excitation ones, as the former might not harbor a quasar within and thus may not be partaking in the unified scheme models. A foreshortening in the observed sizes of quasars, a must in the orientation-based model, is not seen with respect to radio galaxies even when the low-excitation galaxies are excluded. This dashes the hope that the unified scheme might still work if one includes only the high-excitation galaxies.

(A. K. Singal)

## Supernova SN2014J in M82

Supernova 2014J was the brightest and closest supernova Type Ia in the last four decades. It was studied extensively from Mount Abu both spectroscopically and photometrically. Given its proximity, it offered the best opportunity to date to study a thermonuclear supernova (SN) over a wide range of the electromagnetic spectrum. Optical/IR observations on the rising light curve show that SN 2014J is a spectroscopically normal Type Ia supernova (SN Ia), albeit exhibiting high-velocity features in its spectrum and heavily reddened by dust in the host galaxy. A total-to-selective extinction,  $R_V$  greater than 3.1, is ruled out with high significance. The best fit at maximum using a Galactic type extinction law yields  $R_V = 1.4 \pm 0.1$ . The observed reddening of SN 2014J is also compatible with a power-law extinction as expected from multiple scattering of light. Seventeen optical and 23 NIR spectra were obtained from 10 days before (-10d) to 10 days after (+10d) the time of maximum B-band brightness. The relative strengths of absorption features and their patterns of development can be compared at one day intervals throughout most of this period. Carbon is not detected in the optical spectra, but we identify C I 1.0693 micron in the NIR spectra. Mg II lines with high oscillator strengths have higher initial velocities than other Mg II lines. We show that the velocity differences can be explained by differences in optical depths due to oscillator strengths. The spectra of SN 2014J show that it is a normal SN Ia, but many parameters are near the boundaries between normal and high-velocity subclasses. The velocities for O I, Mg II, Si II, S II, Ca II, and Fe II suggest that SN 2014J has a layered structure with little or no mixing. That result is consistent with the delayed detonation explosion models.

*This work is done in collaboration with Prof. A. Goobar and colleagues of the Oskar Klein Center, Stockholm and Dr. G.H. Marion of the University of Texas, USA.*

**(D.P.K. Banerjee, V. Venkataraman, V. Joshi and N. M. Ashok)**

## Detection of a powerful infrared blast wave in the recurrent nova V745 Scorpii

The recurrent nova V745 Scorpii underwent its third known outburst on 2014 February 6. Infrared monitoring of the eruption from Mt. Abu on an almost daily basis, starting from 1.3 days after discovery, shows the emergence of a powerful blast wave generated by the high velocity nova ejecta exceeding 4000 km/s plowing into its surrounding environment. The temperature of the shocked gas is raised to a high value exceeding 108 K immediately after outburst commencement. The energetics of the outburst clearly surpass those of similar symbiotic systems like RS Oph and V407 Cyg which have giant secondaries. The shock does not show a free-expansion stage but rather shows a decelerative Sedov-Taylor phase from the beginning. Such strong shock fronts are known to be sites for gamma ray generation. V745 Sco is the latest nova, apart from five other known novae, to

show gamma ray emission. It may be an important testbed to resolve the crucial question of whether or not all novae are generically gamma ray emitters by virtue of having a circumbinary reservoir of material that is shocked by the ejecta rather than gamma ray generation being restricted to only symbiotic systems with a shocked red giant (RG) wind. The lack of a free-expansion stage favors V745 Sco to have a density enhancement around the white dwarf (WD), above that contributed by a RG wind. Our analysis also suggests that the WD in V745 Sco is very massive and a potential progenitor for a future SN Ia explosion.

**(D. P. K. Banerjee, V. Joshi, V. Venkataraman and N. M. Ashok)**

## Twists and turns in the spectral evolution of recurrent nova T Pyx

Near-infrared observations were made from Mt Abu of the latest 2011 outburst of recurrent nova T Pyxidis. Spectra, commencing from one day after outburst, are reported for a total of 18 epochs spread over the first 50 d of the eruption. A major finding is the transition of the nova from the He/N to the Fe II class within a few days after the outburst. The transition is inferred from the appearance of prominent He I lines soon after the onset of the eruption which then fade rapidly in strength within the next few days. Certain lines of carbon which are near-IR hallmarks of the Fe II class of novae are also used to establish and trace the transition. This nova was found to revert later to the He/N class. The evolution in the strength and shape of the line profiles is presented and discussed. A Case B recombination analysis is done which shows that the Brackett lines are affected by optical depth effects from the start to the end of the observations. Based on the observation that the Br  $\gamma$  line is clearly optically thick, we are able to place lower limits on the emission measure and electron density in the ejecta.

**(V. Joshi, D. P. K. Banerjee and N. M. Ashok)**

## The expanding fireball of Nova Delphini 2013

Near-infrared interferometric measurements of the angular size of Nova Delphini 2013 were obtained, starting one day after the explosion and continuing with extensive time coverage during the first 43 days. Changes in the apparent expansion rate can be explained by an explosion model consisting of an optically thick core surrounded by a diffuse envelope. The optical depth of the ejected material changes as it expands. We detect an ellipticity in the light distribution, suggesting a prolate or bipolar structure that develops as early as the second day. Combining the angular expansion rate with radial velocity measurements, we derive a geometric distance to the nova of 4.54 kiloparsecs. Spectra, obtained from Mount Abu, were used in the data analysis and interpretation.

*This work was done in collaboration with by Dr. G.H. Schaefer of the Georgia State University, USA who led the study.*

**(D. P. K. Banerjee, N. M. Ashok and V. Joshi)**

### **Near Infrared studies during maximum and early decline of Nova Cephei 2014 and Nova Scorpii 2015**

Multi-epoch near-infrared photo-spectroscopic observations of Nova Cephei 2014 and Nova Scorpii 2015 were done from Mt. Abu Infrared Telescope with Near Infrared Camera Spectrometer (NICS). Nova Cep 2014 shows the conventional NIR characteristics of a Fe II class nova characterized by strong CI, HI and O I lines, whereas Nova Sco 2015 is shown to belong to the He/N class with strong He I, HI and OI emission lines. The highlight of the results consists in demonstrating that Nova Sco 2015 is a symbiotic system containing a giant secondary. The evidence for the symbiotic nature is three-fold; first is the presence of a strong decelerative shock accompanying the passage of the novae ejecta through the giant's wind, second is the H-alpha excess seen from the system and third is the spectral energy distribution of the secondary in quiescence typical of a cool late type giant. The evolution of the strength and shape of the emission line profiles shows that the ejecta velocity follows a power law decay in time. Using Case B recombination analysis of the HI Brackett lines we make estimates for both the novae of the emission measure, the electron density and the mass of the ejecta.

(M. K. Srivastava, N. M. Ashok and D. P. K. Banerjee)

### **Near-infrared studies of V5558 Sgr: an unusually slow nova with multiple outbursts**

NIR photospectroscopic results were obtained from Mt. Abu of the unusually slow nova V5558 Sgr (2007). V5558 Sgr showed a slow climb to maximum that lasted for about 60 d and then underwent at least five strong secondary outbursts. A novel approach is adopted to derive a distance estimate of  $1.55 \pm 0.25$  kpc as conventional maximum magnitude-rate of decline relation may not be applicable for a slow nova. In the pre-maxima stage, the spectra showed narrow and strong emission lines of Paschen and Brackett series with prominent P-Cygni components. In the later phase, the spectra show significant changes with the development of strong and broad emission lines of H I, He I, O I and N I and some uncommon Fe II emission lines. V5558 Sgr has been shown to be a rare hybrid nova showing a transition from He/N to Fe II type from optical spectra. However, the near-infrared data do not show such a transition. A recombination analysis of the Brackett lines allows us to estimate the electron density, emission measure and mass of the ejecta.

*This work was done in collaboration with Dr. R. K. Das and Dr. S. Mondal of the S. N. Bose National Centre for Basic Sciences, Kolkata.*

(D. P. K. Banerjee and N. M. Ashok)

### **The hybrid, coronal lines nova V5588 Sgr and its six repeating secondary maxima**

The outburst of Nova V5588 Sgr was followed with optical and near-IR photometric and spectroscopic observations for 3.5 yr, beginning shortly before the maximum reached on 2011 April 2.5. On top of an otherwise normal decline, six self-similar, fast evolving and bright secondary maxima (SdM) appeared in succession. Only very few other novae have presented such clear SdM. Both the primary maximum and all SdM occurred at later times with increasing wavelengths, by amounts in agreement with expectations from fireball expansions. The radiative energy released during SdM declined following an exponential pattern, while the breadth of individual SdM and the time interval between them widened. Emission lines remained sharp throughout the whole nova evolution, with the exception of a broad pedestal with a trapezoidal shape which was only seen during the advanced decline from SdM maxima and was absent in between SdM. V5588 Sgr at maximum light displayed a typical Fe II-class spectrum which did not evolve into a nebular stage. About 10 d into the decline from primary maximum, a typical high-ionization He/N-class spectrum appeared and remained visible simultaneously with the Fe II-class spectrum, qualifying V5588 Sgr as a rare hybrid nova. While the Fe II-class spectrum faded into oblivion, the He/N-class spectrum developed strong [Fe X] coronal lines.

*This work was done in collaboration with Prof. U. Munari of the Astronomical Observatory of Padova, Asiago, Italy.*

(D. P. K. Banerjee and N. M. Ashok)

### **V838 Monocerotis: the central star and its environment a decade after outburst.**

V838 Monocerotis erupted in 2002, brightened in a series of outbursts, and eventually developed a spectacular light echo. A very red star emerged a few months after the outburst. The whole event has been interpreted as the result of a merger. We obtained near- and mid-IR interferometric observations of V838 Mon at the Very Large Telescope Interferometer (VLTI) array. A significant new result is the detection of a compact dusty structure around V838 Mon. The extension of the structure increases from a FWHM of 25 mas at  $8 \mu\text{m}$  to 70 mas at  $13 \mu\text{m}$  or equivalently the dust is spread 150 to 400 AU around V838 Mon. The MIDI visibilities reveal a flattened structure whose aspect ratio increases with wavelength. The major axis is roughly oriented around a position angle of  $-10^\circ$ , which aligns with previous polarimetric studies reported in the literature. This flattening can be interpreted as a relic of the 2002 eruption or as caused by the influence of the currently embedded B3V stellar companion. The data provide a new diameter for the pseudo-photosphere, which shows that its diameter has decreased by about 40% in 10 yr, reaching a radius of  $750 \pm 200$  times the radius of the sun.

*This work was done in collaboration with colleagues at the Observatoire de la Côte d'Azur, Nice, France with Olivier Chesneau (now deceased) as lead author.*

(D. P. K. Banerjee and N. M. Ashok)

### Optical/IR studies of Be stars in NGC 6834

Optical and infrared photometric and spectroscopic studies were made of two Be stars in the 70-80-Myr-old open cluster NGC 6834. NGC 6834(1) has been reported as a binary from speckle interferometric studies whereas NGC 6834(2) may possibly be a  $\gamma$  Cas-like variable. Infrared photometry and spectroscopy from the United Kingdom Infrared Telescope (UKIRT), and optical data from various facilities are combined with archival data to understand the nature of these candidates. High signal-to-noise near-IR spectra obtained from UKIRT have enabled us to study the optical depth effects in the hydrogen emission lines of these stars. We have explored the spectral classification scheme based on the intensity of emission lines in the H and K bands and contrasted it with the conventional classification based on the intensity of hydrogen and helium absorption lines.

*This work was done in collaboration with Dr. Blesson Mathew, Swinburne University, Australia.*

(N. M. Ashok and D. P. K. Banerjee)

### Timing and spectral properties of Be/X-ray pulsar EXO 2030+375 during a Weak Type I outburst

Be/X-ray binaries represent the largest subclass of High-Mass X-ray Binary (HMXB) systems. The compact object in these systems is generally a neutron star (pulsar), whereas the companion is a B- or O-type star that shows Balmer emission lines in its spectrum. The objects in these binary systems are typically in a wide orbit with moderate eccentricity. Though evolutionary model calculations show that binary systems with a white dwarf and Be star or a black hole and Be star should also exist, clear evidence of the existence of such binary systems has not been found as yet. The neutron star in these Be/X-ray binary systems accretes matter while passing through the circumstellar disk of the companion Be star. The abrupt accretion of matter onto the neutron star while passing through the circumstellar disk of the Be companion or during the periastron passage results in strong X-ray outbursts. During such outbursts, the X-ray emission from the pulsar can be transiently enhanced by a factor of more than 10. Be/X-ray binary systems generally show periodic normal (type I) X-ray outbursts that coincide with the periastron passage of the neutron star and giant (type II) X-ray outbursts that do not show any clear orbital dependence apart from the persistent low-luminosity X-ray emission during quiescent. The neutron stars in the Be/X-ray binary systems are found to be accretion powered X-ray pulsars, except for a very few cases.

We present results from a study of broad-band timing and spectral properties of Be/X-ray binary pulsar EXO 2030+375 using a Suzaku observation on 2012 May 23, during a less intense Type I outburst. Pulsations were clearly detected

in the X-ray light curves at a barycentric period of 41.2852 s, which suggest that the pulsar is spinning-up. The pulse profiles were found to be peculiar, e.g. unlike those obtained from the 2007 May 14 Suzaku observation. A single-peaked narrow profile at soft X-rays (0.5–10 keV range) changed to a double-peaked broad profile in the 12–55 keV energy range and again reverted back to a smooth single-peaked profile at hard X-rays (55–70 keV range). The energy resolved pulse profiles of the pulsar are shown in Figure 3.

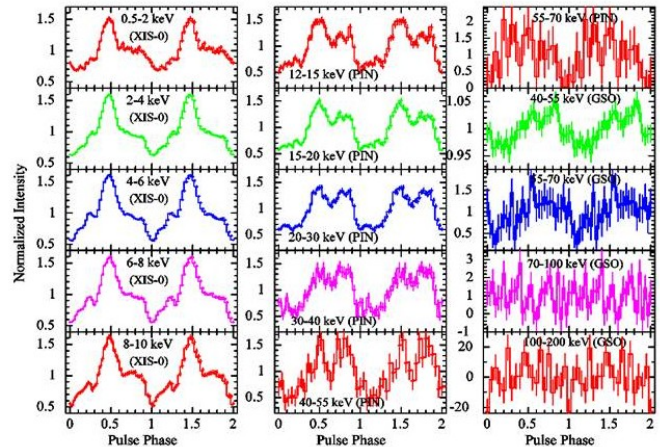


Figure 3: Energy-resolved pulse profiles of EXO 2030+375 obtained from XIS, HXD/PIN and HXD/GSO light curves at various energy ranges. The presence of absorption dips in profiles at higher energies can be seen in the 0.6-0.8 pulse phase range. The error bars represent  $1\sigma$  uncertainties. Two pulses in each panel are shown for clarity.

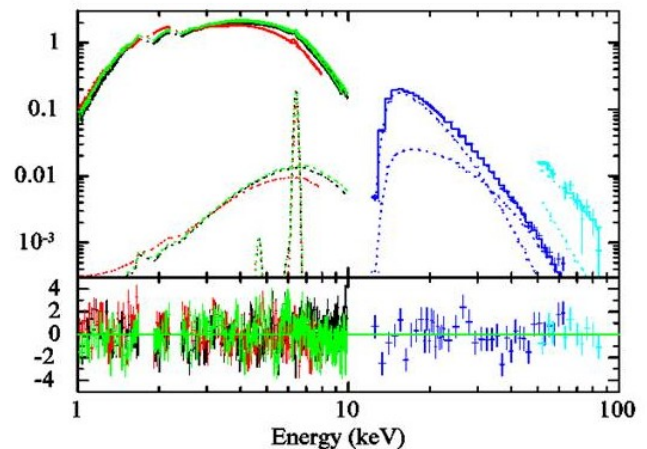


Figure 4: Energy spectra of EXO 2030+375 obtained with the XIS-0, XIS-1, XIS-3, PIN, and GSO detectors of the Suzaku observation during the 2012 May-June X-ray outburst. The data are plotted with the best-fit model comprised of a partially absorbed NPEX continuum model and a Gaussian function for the narrow iron emission line along with the interstellar absorption. The contributions of the residuals to the  $\chi^2$  for each energy bin for the best-fit model are shown in the bottom panel.

The 1.0–100.0 keV broadband spectrum of the pulsar was found to be well described by three continuum models

described as (i) a partial covering high energy cut-off power-law model, (ii) a partially absorbed power-law with high-energy exponential rolloff and (iii) a partial covering Negative and Positive power law with EXponential (NPEX) continuum model. Unlike the earlier Suzaku observation during which several low energy emission lines were detected, a weak and narrow Iron  $K\alpha$  emission line at 6.4 keV was only present in the pulsar spectrum during the 2012 May outburst (as shown in Figure 4). Non-detection of any absorption like feature in the 1–100 keV energy range supports the claim of the absence of the cyclotron resonance scattering feature in EXO 2030+375 from the earlier Suzaku observation. Pulse-phase resolved spectroscopy revealed the presence of additional dense matter causing the absence of a second peak from the soft X-ray pulse profiles. The details of the results are described in the paper.

(S. Naik and G. K. Jaisawal)

### Broad-band Spectroscopy of the Eclipsing High Mass X-ray Binary 4U 1700-37

The high mass X-ray Binary 4U 1700-37 was discovered with the Uhuru satellite in 1970. Extensive follow-up observations of the X-ray source with Uhuru revealed the system as an eclipsing binary with an orbital period of 3.412 d. One of the most luminous and hottest optical star (HD 153919) was identified as the optical companion of the X-ray source. The orbital parameters of the binary system were derived by using BATSE monitoring data.

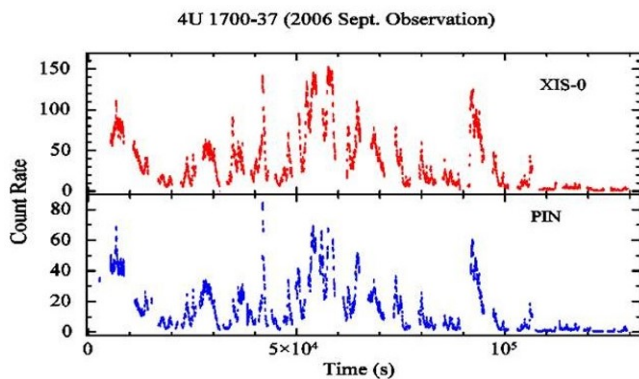


Figure 5: Light curves in 0.5–10 keV and 10–70 keV ranges, obtained from the Suzaku observation of the high-mass X-ray binary 4U 1700-37 are shown in top and bottom panels, respectively. Data from XIS-0 and HXD/PIN detectors are plotted here. Flux variability by an order of 10–15 can be seen in both the panels of the figure.

The distance of the binary system was estimated to be 1.9 kpc. Though the X-ray source has been observed with many X-ray observatories, the nature of the compact object in 4U 1700-37 binary system is quite unclear. A tentative detection of pulsation at  $\sim 67$  s was reported though it was not confirmed in later observations. However, the spectrum of 4U 1700-37 had been described with several continuum models generally used to describe neutron star spectrum. A soft X-ray excess component was also detected in the spectrum during eclipse and eclipse-ingress observations of the X-ray source. Observed hard X-ray spectrum and non-detection of

pulsation suggested the X-ray source as a low-mass black hole candidate. However, the 2–200 keV spectrum of 4U 1700-37 was found to be well fitted with a high energy cutoff power law model representing the classical spectrum of an accretion powered X-ray pulsar.

We tried to investigate the nature of the X-ray source in the binary system and present here the results obtained from broad-band spectroscopy of the high-mass X-ray binary 4U 1700-37 using data from a Suzaku observation in 2006 September 13–14 covering 0.29–0.72 orbital phase range. The light curves of the X-ray source showed significant and rapid variation in source flux during entire observation (as shown in Figure 5). We did not find any signature of pulsations in the light curves. However, a quasi-periodic oscillation at  $\sim 20$  mHz was detected in the power density spectrum of the source. The 1–70 keV spectrum was fitted with various continuum models. However, we found that the partially absorbed high-energy cut-off power law and Negative and Positive power law with Exponential cut-off (NPEX) models described the source spectrum well. Iron emission lines at 6.4 and 7.1 keV were detected in the source spectrum. An absorption-like feature at  $\sim 39$  keV was detected in the residuals while fitting the data with NPEX model. Considering the feature as cyclotron absorption line, the surface magnetic field of the neutron star was estimated to be  $\sim 3.4 \times 10^{12}$  G. To understand the cause of rapid variation in the source flux, time-resolved spectroscopy was carried out by dividing the observation into 20 narrow segments. The results obtained from the time-resolved spectroscopy are interpreted as the accretion of inhomogeneously distributed matter in the stellar wind of the supergiant companion star as the cause of observed flux variation in 4U 1700-37. A sharp increase in column density after  $\sim 0.63$  orbital phase indicates the presence of an accretion wake that blocks the continuum and produces the eclipse like low-flux segment.

(S. Naik and G. K. Jaisawal)

### Investigation of Iron emission lines in the eclipsing high mass X-ray binary pulsar OAO 1657-415

In HMXB systems, mass transfer occurs from the binary companion to the neutron star through the capture of stellar wind, accretion through the Be circumstellar disk or the Roche lobe overflow. Based on the mechanism of mass accretion, the supergiant X-ray binaries (SGXBs; a subclass of HMXBs) are classified into disk-fed and wind-fed SGXB. HMXBs exhibit a definite positions in the spin period versus orbital period diagram (Corbet diagram) depending on the type of mass accretion. The wind-fed SGXBs are distributed in the form of horizontal line in Corbet diagram with exceptions in OAO 1657-415 and 2S 0114+65. However, the three known disk-fed SGXBs such as Cen X-3, SMC X-1 and LMX X-4 show anti-correlation between spin and orbital period. The moderate values of spin and orbital period of OAO 1657-415 make the pulsar as an unique transitional source from wind-fed to disk-fed SGXB.

The pulsar OAO 1657-415 being at low galactic latitude, the

X-ray spectrum shows significant photoelectric absorption at soft X-rays with an equivalent hydrogen column density of  $\geq 10^{23}$  atom  $\text{cm}^{-2}$ . Broad-band spectrum of the pulsar in 1.0-100 keV energy range, obtained from BeppoS AX observation, was found to be well described by a cutoff power law or power-law modified by a high energy cutoff continuum model along with an iron fluorescence line at 6.5 keV. Also there was a hint of the presence of a cyclotron absorption feature at  $\sim 36$  keV as required by one of the above continuum model, the absence of such feature in the model independent Normalized Crab ratio - a technique used to identify cyclotron scattering resonance features in the spectra of X-ray pulsars made the detection inconclusive. We carried out a detailed spectral study to understand the characteristics properties of iron emission lines and broad-band spectral properties by using a Suzaku observation of OAO 1657-415. We investigated the properties of iron emission lines at different orbital phases of the pulsar and tried to interpret the results by applying clumpy wind model.

We summarise here the results obtained from the spectral studies of high mass X-ray binary pulsar OAO 1657-415 using a Suzaku observation in 2011 September. X-ray pulsations were detected in the light curves up to  $\sim 70$  keV. The continuum spectra during the high- and low-flux regions in light curves were well described by high energy cutoff power-law model along with a blackbody component and iron fluorescent lines at 6.4 keV and 7.06 keV. Time resolved spectroscopy was carried out by dividing the entire observations into 18 narrow segments. Presence of additional dense matter at various orbital phases was confirmed as the cause of low-flux regions in the observations. Presence of additional matter at several orbital phases of the pulsar was interpreted as due to the inhomogeneously distributed clumps of matter around the neutron star. Using clumpy wind hypothesis, the physical parameters of the clumps causing the high- and low-flux episodes in the pulsar light curve were estimated. The equivalent width of iron emission lines was found to be significantly large at certain orbital phases of low-flux segments. We investigated the iron line emitting regions and suggest the existence of neutral and ionized iron atoms in emission sites that are located within the accretion radius.

(S. Naik and G. K. Jaisawal)

### Near-Infrared monitoring of Be/X-ray binary pulsars

Be/X-ray binaries represent the largest subclass of HMXB systems. The compact object in these systems is generally a neutron star (pulsar) whereas the companion is a B- or O-type star that shows Balmer emission lines in its spectra. The objects in these binary systems are typically in a wide orbit with moderate eccentricity. The neutron star interacts with the Be optical companion star while passing through the periastron. At periastron passage, the neutron star accretes matter from the circumstellar disk of the companion Be star due to its strong gravity. The abrupt accretion of matter onto the neutron star while passing through the circumstellar disk of the Be companion or during the periastron passage results in strong X-ray outbursts. During such outbursts, the X-ray

emission from the pulsar can be transiently enhanced by a factor of more than 10. Be/X-ray binary systems generally show periodic normal X-ray outbursts that coincide with the periastron passage of the neutron star. The neutron stars in the Be/X-ray binary systems are found to be accretion powered X-ray pulsars. As the regular outbursts in Be/X-ray binary pulsars are associated with the periastron passage of the neutron star, it is interesting to study the pulsars in X-rays and the Be companion star in infrared/optical bands during outbursts. For the study of X-ray properties of the pulsar, we use data from several X-ray observatories whereas for near-infrared study of the Be companion star, we use monitoring data from Mt. Abu observatory. In this near-IR monitoring program, we observe a sample of Be/X-ray binary pulsars to investigate/understand the evolution of the circumstellar disk of the Be companion star.

(S. Naik, G. K. Jaisawal and P. R. Epili)

### Investigating the origin of Quasi Periodic Oscillations (QPO) in black hole binary systems

Black hole binaries are highly variable sources, both on longer ( years) and shorter ( ms) timescales. Power density spectra, widely used as a tool to explore their variability on shorter timescales, reveals the presence of quasi periodic oscillations (QPOs) superimposed on the band limited continuum during hard states. The QPOs observed in frequency range 0.1-30 Hz, known as intermediate frequency QPOs, are particularly puzzling. Several studies have convincingly shown the association of QPOs and the Comptonization component of the spectrum. However, the mechanism of their generation is far from being understood. In this study we attempted to investigate the link between QPOs and the spectral components by simulating the light curves in different energy ranges with the counts from the spectrum.

An observation of the enigmatic black hole GRS 1915+105 during its plateau state was studied with the NuSTAR data. The power density spectrum shows a strong QPO at 1.5 Hz and the spectrum is dominated by the Comptonization component with almost no contribution from the disk. The spectrum was fitted with a cut-off power law and its reflection from the disk and the model counts were given as input to the simulation which considers the oscillation of spectral parameter(s) at a frequency equal to that of the QPO. The entire parameter space from the best-fit spectral model was investigated and we found that the oscillation of power law index can produce the observed behaviour of QPOs. The shape of the spectrum of QPO power is reproduced for a range of amplitudes of oscillations, except a flattening observed at 10 keV. A model based on Lense-Thirring precession is considered as the most successful model to explain the observed QPO behaviour, however our results of oscillating power law index at QPO-frequency is not explained by the model. Our simulation results provides a crucial information on the oscillation of power law index which can be of great importance in the overall understanding of the mechanism of generation of QPOs.

(A. Rao, P. S. Mithun and S. V. Vadawale)

### A curious case of a Red Giant star hosting a Jupiter

We report here about the evidence of a transiting Jupiter planet around a metal-rich red Giant star found using precision radial-velocity (RV) measurements. PARAS (PRL Advanced Radial-velocity Abu-sky Search) is a high-resolution fiber-fed echelle spectrograph operating at the PRL 1.2m Mt. Abu telescope under the only dedicated exoplanet search program in India.

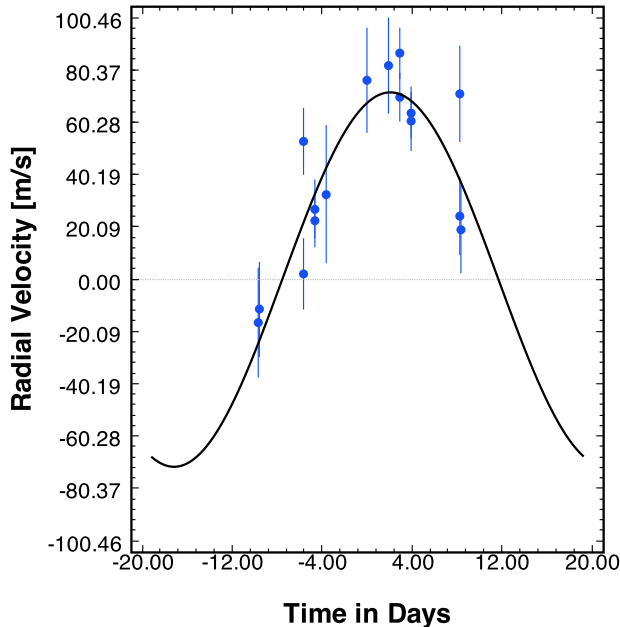


Figure 6: Phase plot of the RV curve showing the evidence of a Jupiter mass planet around the Giant star.

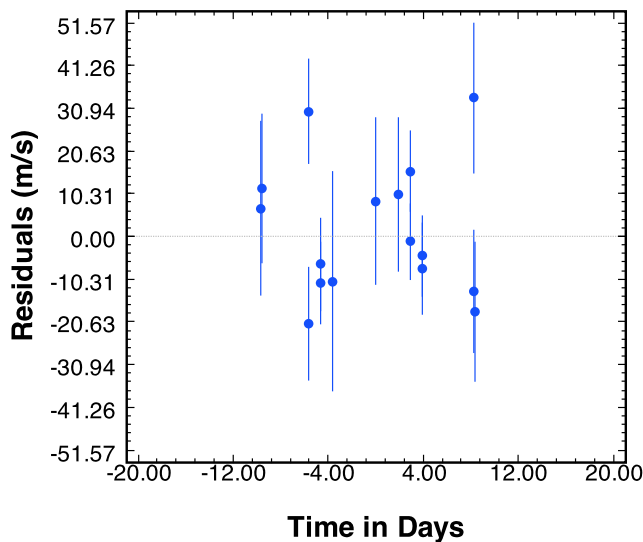


Figure 7: The residual of the model fitting, where the rms of the fit is 15m/s, with a minimum chisq of 1.7. X-axes for both the plots are in days (time) and the Y-axes are in m/s.

We have been following up many suspected transiting candidates that have come out from the SuWASP transit

survey program (prospective candidates list obtained through private communication under joint collaboration). Typically, such a list of prospective transiting exoplanet candidates has success rate of 15% to 25%. Rest are either eclipsing low mass binaries or false positives. There are about 560 known exoplanets, which are as massive as Jupiter or bigger, and this is about one-third of the known population of the exoplanets. Most of these exoplanets orbits around Sun-like dwarf stars. Despite large and diverse population of such Jupiters, only a handful of them are found around Giant stars (evolved stars that have finished Hydrogen burning in their core) with an orbit of less than 0.5AU semi-major axis. Such evolved stars have typical radii of 2 to 10 solar radii. Hence, exoplanets in the close proximity usually get destroyed due to very strong tidal interactions and heat and eventually get engulfed.

Our discovery shows existence of a transiting Jupiter of mass 1.4 Jupiter mass and approximate period of 39 days around an evolved star of 1.5 Solar Mass (upper limit) with stellar radius of 2 to 4 solar radii. The planet has an orbital eccentricity of 0.05 and semi-major axis of 0.255 AU and measured K-value (semi-amplitude) of 65m/s. Figures 6,7 show the RV curve (and residual) from PARAS observations. Clearly the planet has so far been able to survive the ordeal. The star is 9.2mag in the V band and 10mag in the B band and is close to the limit of the observations possible with the 1.2m telescope.

Further, from the detailed stellar spectra analysis we also found that the host star has a Fe/H (abundance) of +0.2, higher than the Sun (0.0); a log(g) value of 3.5 to 3.7 indicating the star is in a Giant phase of its evolutionary track; and a stellar surface temperature of 5300K. We have now successfully developed a code that determines the most important stellar parameters, surface temperature, surface gravity and abundances (index for the chemical composition of the star) from the observed spectra of PARAS. These stellar parameters are important to determine the mass of the host star and its evolutionary status and also to characterize the exoplanet. More RV observations will be required to complete the phase plot (see figure) and accurately determine the period to an accuracy of an hour. A few more transit observations are required to accurately determine the radius of the planet, which will give the density of the planet.

(A. Chakraborty, P. Chaturvedi, B. G. Anandarao, V. Shah, A. Patel and S. Doshi)

### ATVS High Time Resolution Observation of SZ Lyn in BVR Bands

SZ Lyncis is a  $\delta$  Scuti type binary with high amplitude variability and a short time period. Very high time resolution observations were carried out using the ATVS (50 cm CDK telescope with EMCCD camera at Mount Abu Observatory) over six nights during the first quarter of year 2014. In each night observations covering few cycles of main pulsation period of 2.89 hours were taken. Image exposures with cadences of 3 seconds were taken in the BVR bands. The higher frame rate per second and negligible read out noise ( $< 1$  electron with EM gain) of the imaging system are

ideal for the observations of short period variable stars with very high time resolution. The high time resolution, pseudo simultaneous, light curves (Figure 8) clearly revealed the main pulsation periods of BVR bands and the presence of their harmonics. The main pulsation period was determined as  $0.12 \pm 0.01$  days in all three bands. In addition to the radial oscillations there are evidences of non-radial oscillations characterized by three orthogonal directions,  $n$  - radial mode,  $l$  - degree of the mode and  $m$  - azimuthal order. The degree of the mode  $l$ , for SZ Lyn was determined as  $l = 1$ .

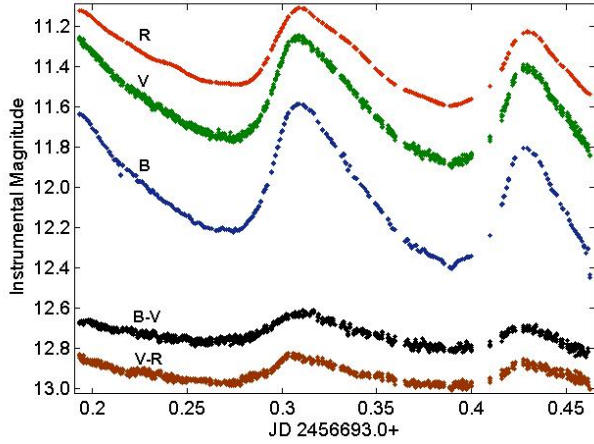


Figure 8: Light curve of SZ Lyn in B, V and R bands and colour curves (B - V) and (V - R) for 4th February 2014. Instrumental B magnitude was shifted by 0.8 and B-V and V-R were shifted by 11.5 and 12.7 magnitudes respectively in order to bring to the vicinity of V and R in the above plot. B and R magnitudes are interpolated values at the time points (Julian day) of V band.

(J. Adassuriya, S. Ganesh and S. Arora)

### Probing the Inner Scale of the Turbulent Spectrum in the Solar Wind using Interplanetary Scintillation Observations.

We have used IPS observations at 327 MHz to infer density fluctuations of spatial scales of 50 to 1000 km, a range of scale sizes that the IPS technique is sensitive to. It is worth examining how these scales relate to the dissipation scale of the turbulent cascade, often referred to as the inner scale of turbulent fluctuations. If the length scales probed by the IPS technique are in the inertial range, it is reasonable to presume that the magnetic field is frozen-in, and the density fluctuations can then be taken as a proxy for magnetic field fluctuations. In order to investigate this issue, we considered three popular inner scale prescriptions. One prescription for the inner scale assumes that the turbulent wave spectrum is dissipated due to ion cyclotron resonance, and the inner scale is the ion inertial scale. In this case, the inner scale ( $l_i$ ) is given as a function of heliocentric distance  $r$  by

$$l_i = 684 n_e(r)^{-1/2} \text{ km} \quad (1)$$

where  $n_e$  is the number density in  $\text{cm}^{-3}$ . A second prescription identifies the inner scale with the proton gyroradius. In this case the inner scale is given by

$$l_i(r) = 1.02 \times 10^2 \mu^{1/2} T_i^{1/2} B(r)^{-1} \text{ cm} \quad (2)$$

Where,  $\mu (\equiv m_p/m_e)$  is the proton to electron mass ratio,  $T_i$  is the proton temperature in eV and  $B$  is the Parker spiral magnetic field in the ecliptic plane. However, recent work seems to suggest that the dissipation could occur at scales as small as the electron gyroradius. The third prescription considered is therefore one where the inner scale is taken to be equal to the electron gyroradius and is given by

$$l_i(r) = 2.38 \times T_e^{1/2} B(r)^{-1} \text{ cm} \quad (3)$$

Where,  $T_e$  is the electron temperature in eV.

The inner scales using these three prescriptions (Eqs. (1), (2) and (3)) are shown in Figure 9 as a function of heliocentric distance. The grey band denotes the range of length scales ( $\approx 50 - 1000$  km) to which the IPS technique is sensitive. We have used electron and proton temperatures of  $10^5$  K in order to compute the proton and electron gyro radii respectively. The magnetic field is taken to be a standard Parker spiral. In order to compute the inner scale using Eqn. (1), we need a density model. We have used two representative density models – the Leblanc density model and the fourfold Newkirk density model. If the length scales probed by the IPS technique (denoted by the grey band in Figure 9) are larger than the inner scale, we can conclude that the density fluctuations discussed in this paper lie in the inertial range of the turbulent spectrum.

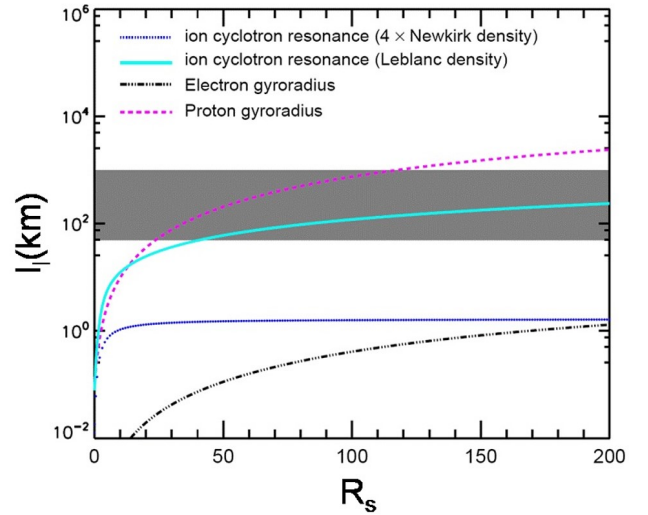


Figure 9: Shows the inner scale  $l_i$  in km as a function of heliocentric distance in units of solar radii ( $r_s$ ). The dashed lines show the proton gyroradius using a proton temperature of  $10^5$  K. The solid and dotted lines show the inner scale governed by ion cyclotron resonance using the Leblanc et al density model and the fourfold Newkirk density model respectively. The dot-dashed line shows the electron gyroradius using an electron temperature of  $10^5$  K. The light gray region denotes the range of spatial scales for which IPS observations are sensitive.

From Figure 9, it is evident that this is the case all the way from the Sun to the Earth only if the inner scale is the electron gyroradius, or if it is due to proton cyclotron resonance, and the density is given by the fourfold Newkirk model. On the other hand, if the inner scale is given by the proton gyroradius, or if the inner scale is due to proton cyclotron resonance and the density model is given by the prescription, the density fluctuations probed by the IPS technique are probably smaller than the dissipation scale for heliocentric distances beyond 30–40  $R_{\odot}$ .

*This work was carried out in Collaboration with Dr. Prasad Subramanian, IISER, Pune.*

**(S. K. Bisoi and P. Janardhan)**

### **Encounter of Comet C/2013 A1 (Siding Spring) with Mars**

Comet C/2013 A1 (Siding Spring), was discovered at Siding Spring during the first fortnight of January 2013 by Robert McNaught. The comet had a close encounter with Mars on 19th October 2014 just weeks after the arrival of ISRO's Mars Orbiter Mission(MOM) into orbit around Mars. Imaging observations with the Mt Abu telescopes (1.2m and 50cm) were made over several days during January - March 2014 and again during October (including around the dates of the encounter). These observations provided strategic inputs regarding the size of the coma to the ISRO MOM team. During the period of the encounter, the comet and Mars were close to the Galactic plane. With the 1.2m telescope we observed Mars with an optical spectrograph just hours before and after the encounter. At the time of closest approach, Mars and the comet had gone below the local horizon at Mt Abu. Within the limits of our ground based observations, we do not see any changes in the spectra of Mars before and after the encounter. Spectra of the comet showed it to be relatively poor in gas content.

**(S Ganesh, K. Venkataramani, S. Ghetiya, S. Arora and K. S. Baliyan)**

### **Asteroid 2004 BL86 - polarimetry during Earth flyby**

Asteroid 2004 BL86, is a small near Earth asteroid discovered in 2004. Estimated to be about 550m dia in size, it flew past the Earth on 26th/27th January 2015 at about 3 times the Earth-Moon distance. It was observed from Mt Abu for optical linear polarization as it flew past. On the night of the 26th January, the asteroid covered nearly 20 degrees in declination (from -11.5 to +8.5 degrees). The rapid movement of the asteroid(over 1arcsec/second northwards) necessitated using the non-sidereal tracking mode of the 1.2m telescope at Mount Abu. The phase angle (Sun-Asteroid-Observer angle) ranged from nearly 30deg down to 10deg. This covered the all important phase angle range where the orientation of the linearly polarized light changes by 90deg (i.e. from positive to negative polarization). The newly developed imaging polarimeter was employed for these observations

at the Cassegrain focus of the 1.2m Mt Abu telescope. In contrast to comets, this asteroid shows relatively low degree of polarization, indicating the rocky, rather than dusty, nature of the body.

**(S. Ganesh, I. Varatharajan, K. Venkataramani, A. Mishra and K. S. Baliyan)**

### **Indian multi-wavelength astronomy mission: ASTROSAT**

Astrosat is a first Indian satellite mission fully dedicated for multi-wavelength astronomical observations. It is planned to be launched during late 2015 and will have five instruments covering wavelength range from optical to hard X-rays as shown in Figure 11. CZTI (Cadmium Zinc Telluride Imager) is one of the five instruments with primary objective of hard X-ray imaging spectroscopy in the energy range of 20 - 100 keV. It consists of a coded aperture mask along with a large area 1024 cm<sup>2</sup> pixilated detector plane (pixel size of 2.5 mm × 2.5 mm resulting in total 16384 pixels).

We are involved in the calibration of the CZTI instrument including generation of the necessary calibration database, multi-pixel response matrix as well as designing of the in-flight performance verification program of CZTI. Apart from this, we have also investigated prospects of utilizing the large pixilated detector plane of CZTI as Compton polarimeter and have obtained very promising results as described below:

#### *Generation of calibration database and preliminary response matrix for CZTI*

Each pixel of CZTI is essentially an independent X-ray detector. Thus CZTI consists of total 16384 individual detectors each having slightly different characteristics. Reduction and analysis of CZTI data requires detailed calibration information for each pixel. To allow data reduction and analysis software to be independent of calibration information, it is stored in the form of calibration database known as CALDB, which is defined by HEASARC, NASA. CALDB convention was adopted for the structure of calibration files and for file indexing. The file formats were carefully designed to include all the calibration information required by the downstream pipeline. Careful measurement of the individual pixel properties was carried out in collaboration with TIFR, VSSC and IUCAA and this ground calibration data was used to generate first version of CZTI CALDB.

Spectrum from CZTI will be obtained by mask weighting technique, where the pixel wise spectra are added together with weight determined by the mask open fraction for that pixel, to obtain background subtracted spectrum. Analysis of this spectral data requires response matrix which accounts for the instrumental response to the incident photons. Ground calibration data consist of spectrum of different mono energetic lines from radioactive sources. This data is fitted with Gaussian line model to obtain the resolution at different energies. Pixels having similar response are grouped together and are assigned with common redistribution matrix. The overall response of the instrument is obtained by weighted addition of individual pixel responses. Anticipated variation

in detector temperature is also taken into account in the response calculation.

*Accurate response matrix for CZTI*

Accurate response matrix for pixelated CZT detectors requires precise modeling of the X-ray lines as a function of energy. It is generally known that the shape of mono-energetic line measured by CZT detectors is not a Gaussian, but have a strong tail towards low energies because of trapping of the charge carriers due to their low mobility ( $\mu$ ) and lifetime ( $\tau$ ). This effect is found to be more significant for high energy photons as the probability of charge loss increases with the depth of interaction. Therefore, precise line modeling in case of CZT detectors needs accurate measurement of  $\mu\tau$  values for electrons and holes. For pixelated detectors, other significant components in the line modelling come from the crosstalk between pixels due to charge sharing, fluorescence photons and Compton scattering. In PRL, we have experimentally measured mobility and lifetime for 4 cm  $\times$  4 cm and 5 mm thick CZT detectors with pixel dimension of 2.5 mm  $\times$  2.5 mm, procured from Orbotech Medical Solutions (similar to the modules used in CZTI, Astrosat). We also generated pixel-wise response matrix for the CZT modules and test in laboratory by fitting a known continuum spectra in 20 - 50 keV using a X-ray gun. The same methodology will be used for generating accurate CZTI response, which will be further refined during the initial six months of performance verification observations.

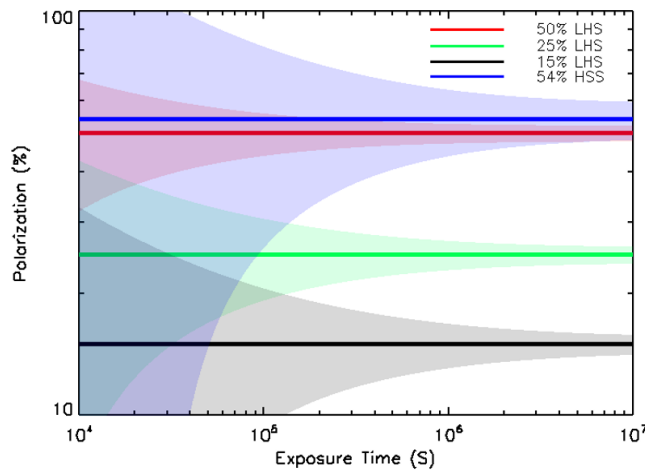


Figure 10: Expected polarimetric performance of CZTI - Possible constraints on the hard X-ray polarization fraction of Cygnus X-1 in terms of expected uncertainty (shaded regions) as a function of time for various model predictions in the literature.

*Hard X-ray Polarimetry with Astrosat-CZTI*

Because of its pixelated nature and significant Compton scattering probability at energies beyond 100 keV, CZTI offers feasibility of doing X-ray polarimetry in Compton mode, where X-ray photons are scattered by a pixel and absorbed by the neighboring pixels constituting the basic azimuthal angle distribution. We carried Geant4 simulation of the instrument to estimate the polarimetric sensitivity, which was reported earlier. Now we have experimentally

verified the polarization measurement capability of CZTI using partially polarized X-rays in the laboratory. Estimation of the expected sensitivity for polarization measurement also required accurate understanding of the polarimetric background. We have carried out detailed background modelling and found that that CZTI will certainly have significant polarimetric capability for bright X-ray sources. For example, in case of black hole binary sources such as Cygnus X-1, it will be able constrain (Figure 10) many theoretical models available for the hard X-ray polarization whereas in case of pulsar sources such as Crab, it will provide detailed phase resolved polarization measurements as shown in Figure 11. Thus CZTI will significantly enhance the field of X-ray polarimetry which has been totally unexplored so far.

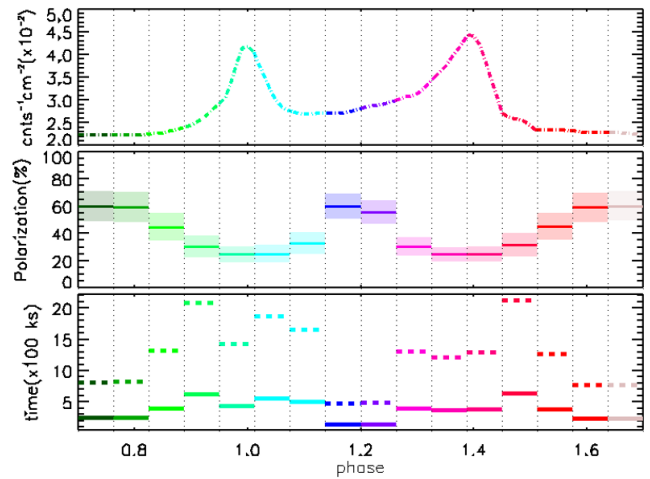


Figure 11: Expected polarimetric performance of CZTI - Feasibility of phase-resolved polarimetry with CZTI for Crab - the top panel shows Crab pulse profile in 100 - 300 keV. The middle panel shows polarization in 16 phases for a total exposure time of 1 Ms. The bottom panel shows the required exposure time to determine polarization for all phases with minimum 3  $\sigma$  (solid lines) and 5  $\sigma$  (dashed lines) confidence levels.

(T. Chattopadhyay, P. S. Mithun and S. V. Vadawale)

**Development of a Focal Plane Compton X-ray Polarimeter (CXPOL)**

We are developing a hard X-ray Compton polarimeter as a focal plane instrument for Hard X-ray telescope. The basic instrument design consists of a 10 cm long plastic scintillator surrounded by a cylindrical array of 15 cm long CsI(Tl) scintillators. The plastic scatterer is read out by a conventional PMT whereas the CsI(Tl) scintillators are readout by new generation Si-photomultipliers. The basic operating principle of such a polarimeter is that a polarized beam of radiation after being scattered by the plastic, shows asymmetry in the azimuthal angle of scattering when collected by the surrounding CsI(Tl) scintillators. The asymmetry being directly proportional to the polarization fraction of the beam, is used to retrieve the degree and angle of polarization of the photons. Results of the detailed Geant4 simulations as well as experimental characterization of the plastic scatterer were reported in previous years. This year we carried out

detailed characterization for each of the 16 CsI(Tl) scintillators and measured their low energy threshold, which is a critical parameter for achieving the required polarization sensitivity. Subsequently, we have successfully assembled the complete instrument and verified the operational stability. Performance of the polarimeter has been tested with both unpolarized and polarized beam of radiation at various energies. The results are quite encouraging and agree well with the simulation

results as shown in Figure 12. Based on the successful demonstration of the proof-of-concept experiment, we plan to propose an experiment for polarization measurements of hard X-rays from the Sun as an initial space experiment which can be conducted without the hard X-ray focusing optics.

**(T. Chattopadhyay, P. S. Mithun, S. K. Goyal, R. Shukla, A. Patel, M. Shanmugam and S. V. Vadawale)**

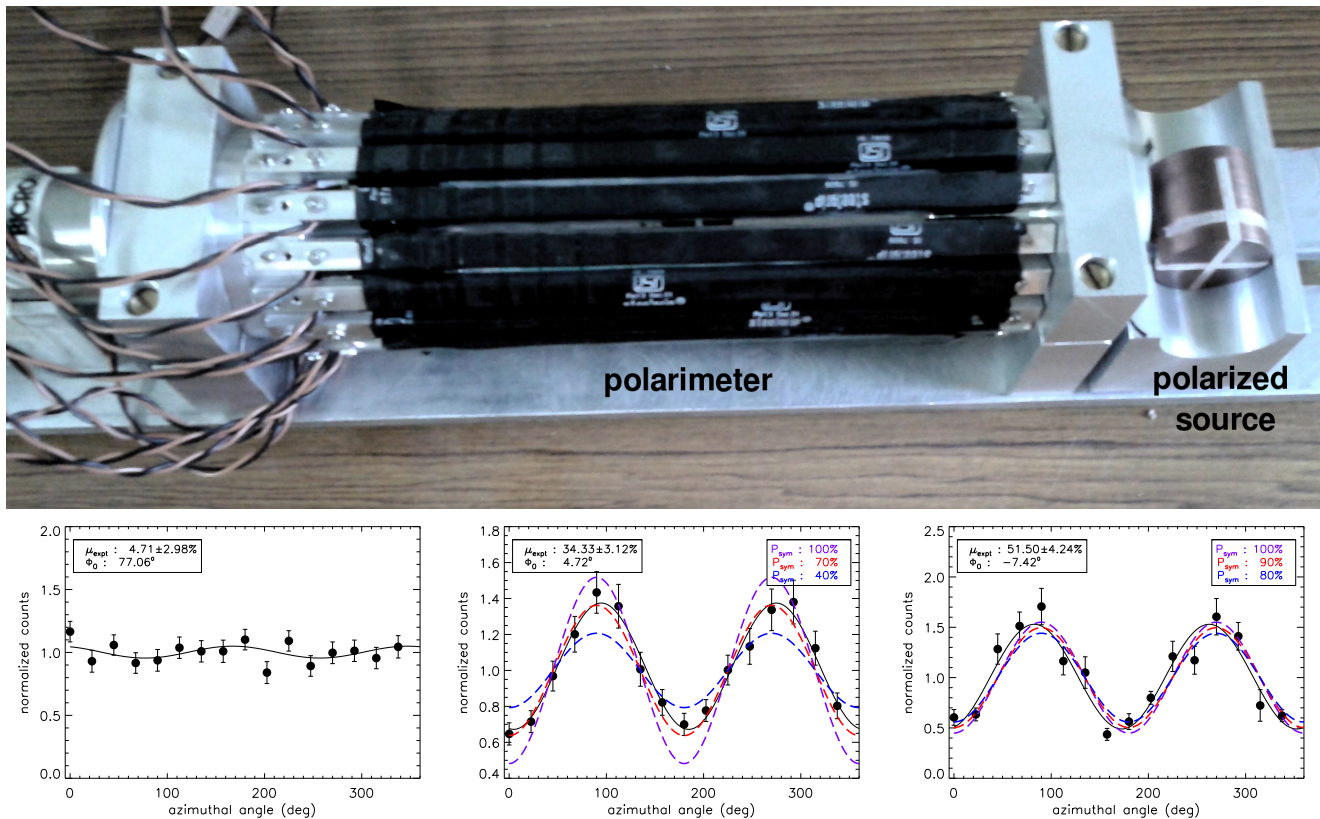


Figure 12: Fully assembled hard X-ray polarimeter (top) and measured modulation curves (bottom) for unpolarized X-rays, partially polarized mono-energetic X-rays and partially polarized continuum X-rays respectively.

# SCIENCE at PRL

## Solar Physics

### Evidence for flare-induced global oscillations in the Sun: GOLF and VIRGO observations

We have analyzed the disk-integrated velocity and intensity observations of the Sun obtained from the GOLF and VIRGO instruments, respectively, on board SOHO spacecraft covering several flare events, for the period from 11 February, 2011 to 17 February, 2011, of which 11 February, 2011 remained a completely quiet day and served as a control data for the investigation. Application of Fourier Transform to these disk-integrated velocity and intensity signals indicates that there is enhanced power of predominant p-modes as well as high-frequency modes in the Sun during the flare, as compared to the control data (Figure 1 and Figure 2).

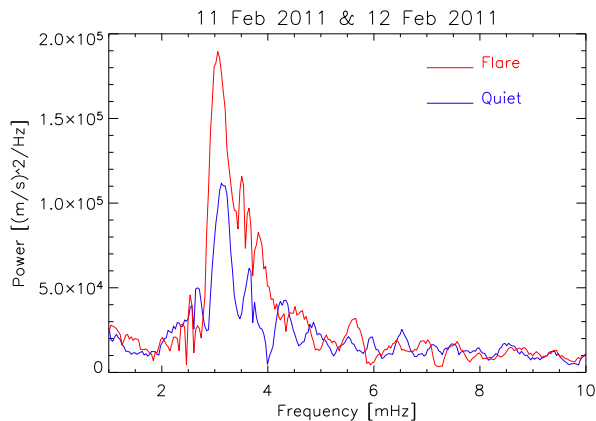


Figure 1 : The blue solid line shows the smoothed Fourier power spectrum as obtained from the sun-as-a-star velocity observations from GOLF instrument onboard SOHO spacecraft for the period from 08:00 UT to 16:00 UT on 11 February 2011 (quiet day). The red solid line shows the same for the period from 08:00 UT to 16:00 UT on 12 February 2011 (flare day). It is evident that the power of velocity oscillations is enhanced in the predominant p-mode band as well as high-frequency band on the flare day as compared to the quiet day. The GOLF observations are obtained using Na D1 and D2 lines which are formed in the upper solar photosphere.

The GOLF instrument obtains velocity observations using Na D1 and D2 lines which are formed in the upper solar photosphere, while the intensity data are obtained by VIRGO instrument using the 8620 Å line which is formed within the

solar photosphere.

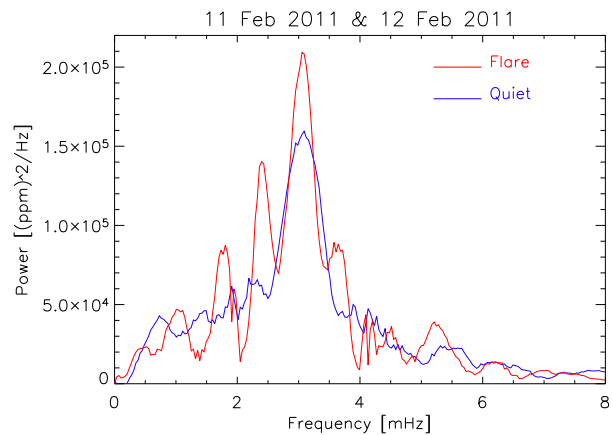


Figure 2 : The blue solid line shows the smoothed Fourier power spectrum as obtained from the sun-as-a-star intensity observations from VIRGO instrument onboard SOHO spacecraft for the period from 08:00 UT to 16:00 UT on 11 February 2011 (quiet day). The red solid line shows the same for the period from 08:00 UT to 16:00 UT on 12 February 2011 (flare day). As seen in the case of GOLF observations, here also we observe that the power of intensity oscillations is enhanced in the predominant p-mode band as well as high-frequency band on the flare day as compared to the quiet day. These VIRGO observations are obtained using 8620 Å line which is formed within the solar photosphere.

Despite the fact that the two instruments sample different layers of the solar atmosphere using two different parameters (velocity v/s intensity), we have found that both these observations show the signature of flare-induced global oscillations in the Sun.

These results can refine our knowledge about the seismic responses to transient events, such as flares, in the Sun. Hence, this study will be extended to similar such epochs which cover successive flare events with different strengths. The recent space missions dedicated to asteroseismology, such as *Kepler* and *CoRoT*, provided high-quality data to probe the magnetic activity cycles and starspots in other stars. Therefore, we can also hope to identify the asteroseismic signature of stellar flares using the knowledge gleaned from the solar results.

This work has been done in collaboration with Siddharth Sharma of MNIT, Jaipur (India), Savita Mathur of Space Science Institute, Boulder (USA), Rafael A. Garcia of IRFU/DSM/CEA, Saclay (France), and Antonio Jimenez of IAC, Tenerife (Spain).

(B. Kumar, H. K. Saini, and P. Venkatakrishnan)

### Study of magnetic-jerk driven photospheric oscillations during a large solar flare

A large two-ribbon M6.5 class flare occurred in the solar active region NOAA 11719 on 11 April 2013. We have analyzed the velocity and magnetic field changes in this active region using the high-resolution Fe I 6173 Å photospheric Dopplergrams and magnetograms obtained by the HMI instrument onboard SDO spacecraft. Accompanying these observations from space, we have also used the near-simultaneous full-disk H $\alpha$  6563 Å chromospheric observations obtained by the GONG instrument located at the Udaipur Solar Observatory to study the evolution of flare ribbons in the active region. The analysis of the line-of-sight magnetograms from HMI show magnetic jerks (very fast magnetic field changes) at different locations of the active region during the flare, both, on, as well as away from the flare ribbons in the active region (Figure 3).

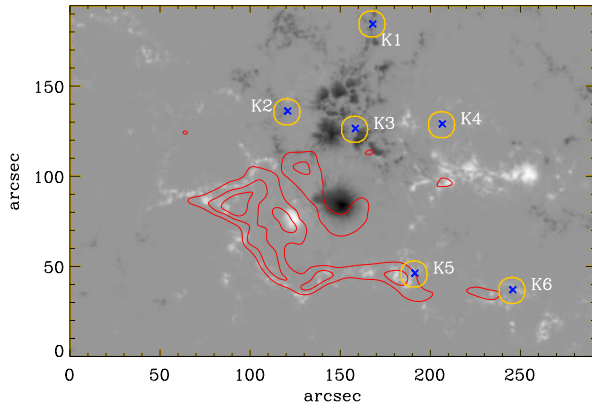


Figure 3 : The background shows the mean line-of-sight photospheric magnetic fields for the period from 07:01 UT to 08:51 UT on 11 April 2013 in the active region NOAA 11719, as measured by the HMI/SDO. The overlaid contours shown in red color are the locations of the chromospheric H $\alpha$  flare ribbons averaged over the period 07:01 UT to 08:51 UT in the aforementioned active region during an M6.5 class flare on 11 April 2013, as observed with the GONG instrument at USO. Here, the contours are drawn at the 70%, 80% and 90% of the maximum brightness in H $\alpha$ . The crosses shown in blue within the yellow circles are the locations where magnetic jerks are observed in the active region during the flare. It is evident that the magnetic jerks are localized on and away from the flare ribbons in the active region.

It is believed that the Lorentz force launched by the magnetic jerks can produce disturbances in the solar atmosphere. Hence, we have studied the velocity oscillations in the locations of the magnetic jerks for the epochs, before and spanning the flare. For this purpose, we have estimated Fourier power spectrum of the velocity oscillations in the aforementioned locations. It is observed that the power of velocity oscillations is enhanced in the locations of magnetic jerks spanning the flare as compared to the pre-flare condition

(Figure 4). This enhancement is found for all locations showing magnetic jerks, both, on the flare ribbons and away from the flare ribbons. This indicates that the magnetic jerks could also excite the photospheric oscillations, apart from the flare driven oscillations in the solar atmosphere, from events such as solar quakes. These magnetically driven velocity oscillations in the active regions are important for understanding the transport of acoustic energy to the higher solar atmospheric layers.

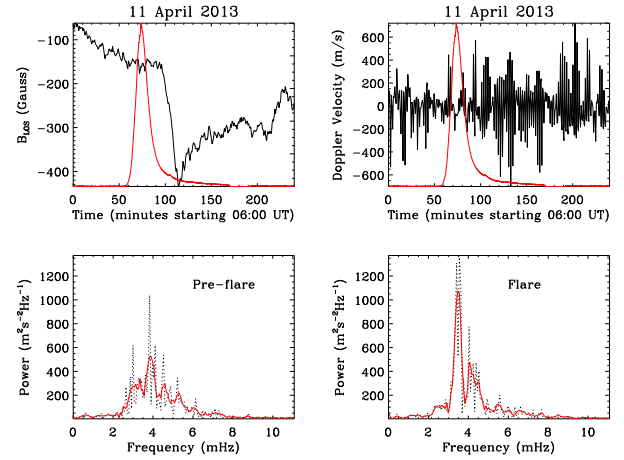


Figure 4 : The solid black lines in the upper panels show, respectively, the time evolution of the line-of-sight photospheric magnetic field and the Doppler velocity for the period from 06:00 UT to 10:00 UT on 11 April 2013 in AR 11719 during an M-class flare. These are averaged over nine pixels in one of the locations of the magnetic-jerk seen in the active region. The magnetic field and velocity measurements shown here are from the HMI/SDO. The red solid lines in these upper panels represent the evolution of GOES soft X-ray flux in 1-8 Å. The dotted black lines in the lower panels show, respectively, the average Fourier power spectrum of velocity oscillations estimated over the aforementioned locations for the period from 01:00 UT to 05:00 UT (pre-flare condition) and for the period from 06:00 UT to 10:00 UT (spanning the flare). Here, the red solid lines in both the panels represent a smoothing fit applied to the original power spectrum to estimate the power envelope. It is evident that the power of velocity oscillations is enhanced in the location of the magnetic-jerk during the flare.

(B. Kumar, A. R. Bayanna, P. Venkatakrishnan, and S. K. Mathew)

### Sunspot magnetic field structure as revealed by decomposition of vertical current density into shear and chiral components

We examined the Parker's prediction of zero net vertical current over a cross-section of a flux tube from a single polarity region at the photosphere, by decomposing vertical current into chiral and shear components. We used the photospheric vector magnetic field observations of active region (AR) NOAA 11158 supplied by Helioseismic Magnetic Imager. The net current in each polarity over the entire AR exhibits systematic evolution and is a combined result of different kinds of flux motions in the sub regions. In most (60-65%) of the pixels, the chiral current density has same sign as the vertical current density and the evolution of its net integrated value over a particular polarity flux resembles the trend of net vertical current. The sign of shear current

density distribution is opposite in most (60-65%) pixels to that of chiral current distribution, although smaller in magnitude, and its time profiles bear no systematic trend. These results are tested against two different sunspot models, viz. the fibril model and the monolithic model. Comparison of the mean ratio of shear to chiral current density for different values of pixel resolution is shown to favour the monolithic model, although a fibril structure at deeper layers cannot be ruled out. Observations of vector magnetic fields of sunspots using the infrared FeI line around 1560 nm could perhaps resolve this issue.

*This work is done in collaboration with B. Ravindra of the Indian Institute of Astrophysics.*

(P. Venkatakrishnan and P. Vemareddy)

**Initiation and eruption process of magnetic flux rope from solar active region NOAA 11719 as an Earth-directed CME**

Magnetic flux rope (FR) is a commonly observed physical structure in the solar corona during solar eruptions. It is modelled as a volumetric current channel with helical field lines wrapping around its central axis. Filaments/prominences seen in  $H\alpha$ , and coronal features of sigmoids are often considered as FRs in ARs.

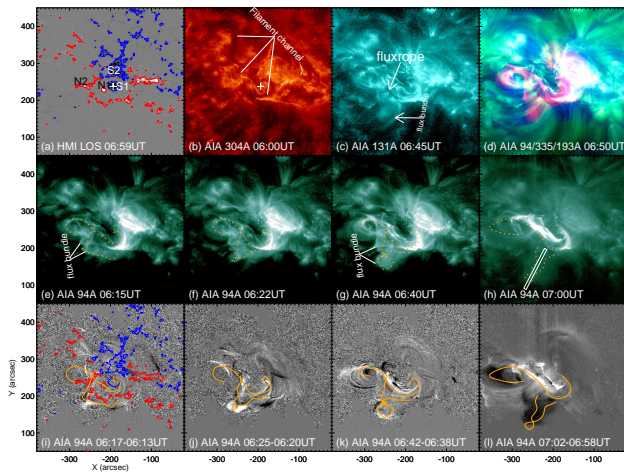


Figure 5 : The pre-eruption scenario of AR 11719. a) HMI line-of-sight magnetogram overplotted with contours at  $\pm 100$  G in red/blue. b) Filament channel in AIA 304 Å, showing its origination from sunspot N1. c) Inverse-S shaped sigmoidal flux rope channel from N1 flux to P1 flux region in its rising phase seen in AIA 131Å ( $\sim 10$  MK). d) Composite snapshot of hot flux rope channel showing core flux system as sigmoidal structure, (e)-(f) Morphological evolution of sigmoidal flux rope system in AIA 94 Å observations, depicting the initiation of rise motion. The traces of FR and overlying helical threads are highlighted with yellow dotted lines in each panel. Rectangular slit is shown for further kinematic evolution of this helical thread. (i-l) Difference images in 94 Å giving details about heated compression front above the rising part of both flux rope and helical thread indicated by yellow curves. Similarly, flare ribbons formed beneath the rising FR can also be noticed in the last panel.

The preexistence, formation and role of magnetic flux rope are not well understood. It has been traditionally believed that magnetic reconnection plays the main role and flux rope is treaded as secondary, but different views exist. Keeping these scientific interests in mind, photospheric magnetic

fields and multi-channel coronal EUV observations from Solar Dynamic Observatory, were used to analyze and interpret a case of Earth-directed Coronal Mass Ejection outlined with a conspicuous FR channel.

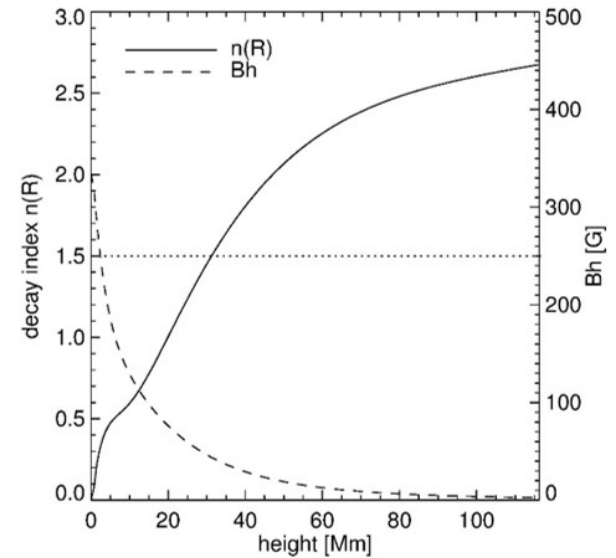
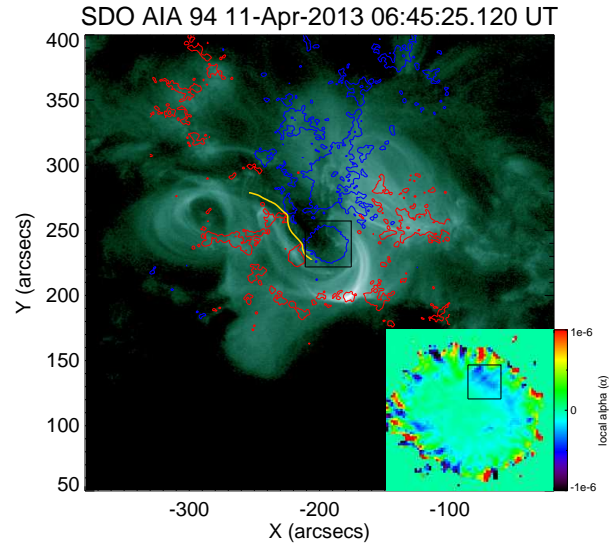


Figure 6 : Top panel: Snapshot of corona in AIA 94 Å passband showing FR structure with plasma loops. Contours of line-of-sight magnetic flux at  $\pm 150$  G are overlaid in red/blue color to indicate the link between photospheric magnetic flux and coronal FR structure. The distribution of the force-free parameter  $\alpha (= J_z / B_z)$  of the main sunspot region (marked by black square box) is depicted in the inset plot. The region outlined by the square box in the inset plot indicates negative signed alpha  $\alpha_{av}$ , having a critical average value for kink instability criteria. The gold color curve is PIL. Bottom panel: the decay index of Bh as a function of height. Also shown is  $B_h = \sqrt{B_x^2 + B_y^2}$  with the y-axis scale on the right. The dotted horizontal line refers to the critical decay index value.

The magnetic flux distribution of the AR 11719 from which this eruption launched, is plotted in Figure 5a. It shows a major sunspot of negative flux (S1) surrounded by parasitic diffused positive flux. The sunspot is flanked by small sunspot of positive polarity and a negative polarity patch.

This distribution of magnetic flux concentrations corresponds to a multi-polar  $\beta\gamma$ -configuration. The co-spatial image in the AIA He II 304 Å pass-band (that gives plasma information from chromosphere and transition region at  $\sim 10^4$  K), clearly shows existence of a dark filament channel approximately oriented in north-south direction (panel 1b). One of the legs of this filament is anchored in S1, and extends to the northern plage regions of dispersed positive flux. Filament channels containing cool plasma material compared to underlying plasma will appear as a dark trace, thus usually visible in 304 Å or  $H_\alpha$ . This filament channel swirls around the sunspot in a clockwise direction, which appears as an inverse-S structure. A composite image made from images at different coronal temperatures shows the stacked flux system of the filament, the sigmoid, and the overlying twisted flux bundle (panel 1d).

Observations in AIA 94 Å reveal overlying flux bundle and its peculiar geometrical evolution (Figure 5(e-f)). This kind of evolution transforming the flux bundle from V- through  $\gamma$ - to  $\gamma$ -shape is presumed to be a signature of writhing of the flux bundle. When the twist in the flux-rope increases, the axis of the rope loops around itself resulting in writhing and the flux rope experiences kinking. When observed in a particular orientation, this will appear as either a  $\gamma$ - or  $\gamma$ -shaped flux rope due to projection. These observational signatures of kink-writhe-rise evolution are usually seen in the  $H_\alpha$  observations of limb prominences. In our case, the flux bundle is oriented as if we see it on the limb, allowing us to visualize its kinked behavior. It evolved to a clear kinked structure with closed loop above the legs. The inferred evolution of the flux bundle is similar to writhing motion. The availability of magnetic twist required for such coronal observational signatures of FR structures can be checked using the magnetic field observations at the photosphere, which in turn confirms the observed evolution of this flux bundle as being a consequence of magnetic twist.

During the writhing phase of the flux bundle (06:06-6:30UT), the FR is observed with slow rise motion. It is then followed by further upward motion of both the FR and the flux bundle during the time 06:30-06:55 UT, culminating in their drastic rise phase and the eventual eruption. Therefore, the kink-writhe-rise evolution of the flux bundle could be an indication of the availability of critical twist. Its co-temporal rise with the FR would then imply that either the rising flux bundle allowed the underlying FR to rise or that the FR itself had super-critical twist so that it itself can rise. Both these assumptions need to be supported by the observations of the sufficient twist in the AR flux system by means of photospheric magnetic fields. Our results suggest that the FR initiated the slow upward motion by a kink-instability to reach to a height (31 Mm) above which, the steep gradients of horizontal fields (torus-instability criteria, Figure 6) drives its further expansion in outer corona. The eruption resulted in a halo CME that headed towards Earth at a linear speed of around 860 km/s.

*This work was done in collaboration with Jie Zhang, George Mason University, Fairfax, USA.*

(P. Vemareddy)

### Impulsive energy release and non-thermal emission in a confined M4.0 flare triggered by rapidly evolving magnetic structures

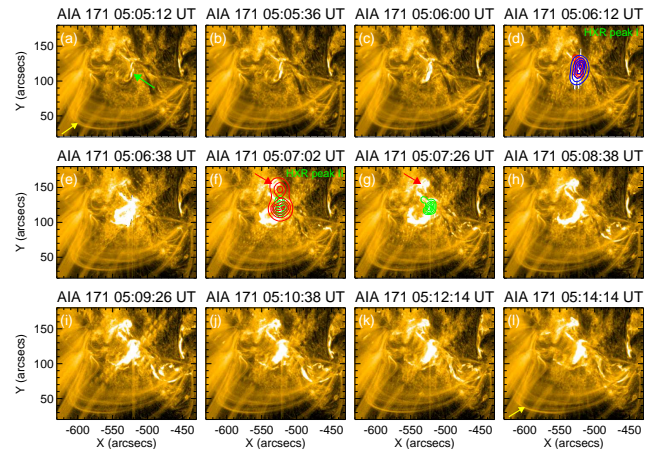


Figure 7 : Sequence of AIA 171 Å images presenting flare evolution as well as its magnetic loop environment of the flaring active region. A small J-shaped filament/flux rope is indicated by an arrow (green) in panel (a). Flaring site is fully enveloped by overlying loop systems, which are preserved throughout the event and marked by arrows (yellow) in panels (a) and (l). Red arrows in panels (f) and (g) indicate EUV brightening at a relatively distant location. The RHESSI PIXON images at different energy bands (i.e., 25-50 (green), 50-100 (red), and 100-200 keV (blue)) are overlotted on some of the co-temporal 171 Å images. The contour levels for X-ray images are set as 15%, 30%, 50%, 70%, and 90% of peak flux for each image.

We have performed an extensive multi-wavelength study of an M4.0 flare that occurred in AR NOAA 11302 on 2011 September 26. Although the flare displayed a very impulsive behavior and compact morphology, the set of high resolution observations at temporal, spatial, and spectral domains from SDO, RHESSI, and NoRH enabled us to explore the possible triggering mechanism and energy release processes in detail. The flare light curves exhibit an abrupt rise of non-thermal emission with co-temporal HXR and MW bursts that peaked instantly without any precursor emission. This stage was associated with HXR emission up to 200 keV that followed a power law with photon spectral index ( $\gamma$ )  $\sim 3$ . Another non-thermal peak was observed after 32 s from the first one which was more pronounced in MW light curves than HXR profiles. Dual peaked structure in the MW and HXR light curves was suggestive of a two-step magnetic reconnection process. During the impulsive phase, EUV images exhibit a sequential evolution of the inner and outer core regions of magnetic loop system while the overlying loop configuration remained unaltered (Figure 7). The combined multi-wavelength observations in HXR, (E)UV, and  $H_\alpha$  provided support for flare models involving the interaction of coronal loops. The magnetograms obtained by the HMI reveal emergence of magnetic flux that began  $\sim 5$  hours before the flare. However, the more crucial changes in the photospheric magnetic flux occurred about 1 minute prior to the flare onset in the form of opposite polarity magnetic transients appearing at the early flare location within the inner core region.

The spectral, temporal, and spatial properties of magnetic transients suggest that the sudden changes in the small-scale magnetic field have likely triggered the flare by destabilizing the highly sheared pre-flare magnetic configuration.

*This work has been done in collaboration with Astrid Veronig (University of Graz, Austria; K. S. Cho (Korea Astronomy and Space Science Institute (KASI), Daejeon, South Korea); Sanjiv Kumar Tiwari (NASA Marshall Space Flight Center, Huntsville, USA).*

(U. Kushwaha, B. Joshi and S. K. Mathew)

**Large-scale implosion in coronal loops during the pre-flare phase of an M6.2 flare associated with confined eruption of a flux rope**

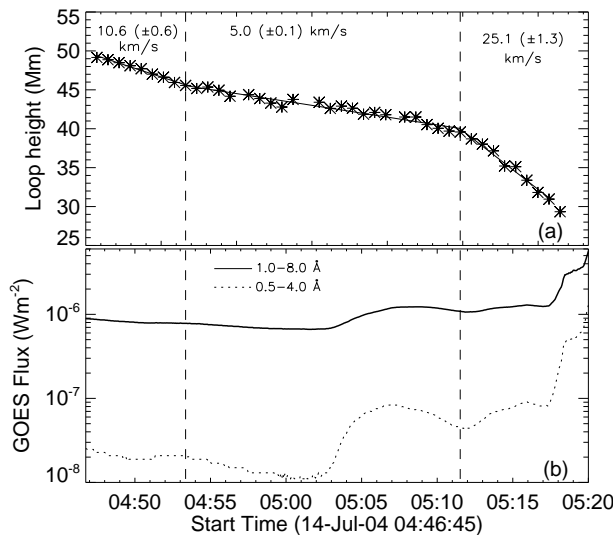


Figure 8 : Height-time plot of the coronal loop system showing implosion between 04:47 UT and 05:18 UT (panel (a)). The speed of downward motion of the contracting loops during different phases is also indicated with their respective uncertainty in the measurements. To compare the evolutionary phases of loop contraction with the flare evolution, we plotted the GOES flux profile for the same time interval in the panel (b).

We have made a comprehensive analysis of an M6.2 flare of 14 July 2004 which was associated with a confined eruption of a prominence using TRACE, RHESSI, and NoRH observations. The pre-flare phase of this event is characterized by spectacular large-scale implosion in the overlying EUV coronal loops during which the loop system was subjected to an altitude decrease of  $\sim 20$  Mm (40% of the initial height) for an extended span of  $\sim 30$  minute (Figure 8). This phase of coronal implosion is accompanied by sequential EUV brightenings associated with hard X-ray (HXR) (up to 25 keV) and microwave (MW) sources from low-lying loops in the core of the flaring region which together with X-ray spectra indicate strong localized heating in the source region before the filament activation and associated M-class flare. With the onset of the impulsive phase of the M6.2 flare, we detect HXR and MW sources that exhibit intricate temporal and spatial evolution in relation with the fast rise of the

prominence. Following the flare maximum, the filament eruption slowed down and subsequently confined within the large overlying active region loops; the event did not lead to a coronal mass ejection (CME). During the confinement process of the erupting prominence, we detect MW emission from the extended coronal region with multiple emission centroids which likely represent emission from hot blobs of plasma formed after the collapse of the expanding flux rope and entailing prominence material. RHESSI observations reveal high plasma temperature ( $\sim 30$  MK) and substantial non-thermal characteristics with electron spectral index ( $\delta$ ) $\sim 5$  during the impulsive phase of the flare. The time-evolution of thermal energy exhibits a good correspondence with the variations in cumulative non-thermal energy which suggest that the energy of accelerated particles efficiently converted to hot flare plasma implying an effective validation of the Neupert effect (Figure 9).

*This work has been done in the collaboration with Dr. Astrid Veronig (University of Graz, Austria; Y. J. Moon (School of Space Research, Kyung Hee University, Yongin, Gyeonggi-Do, Korea).*

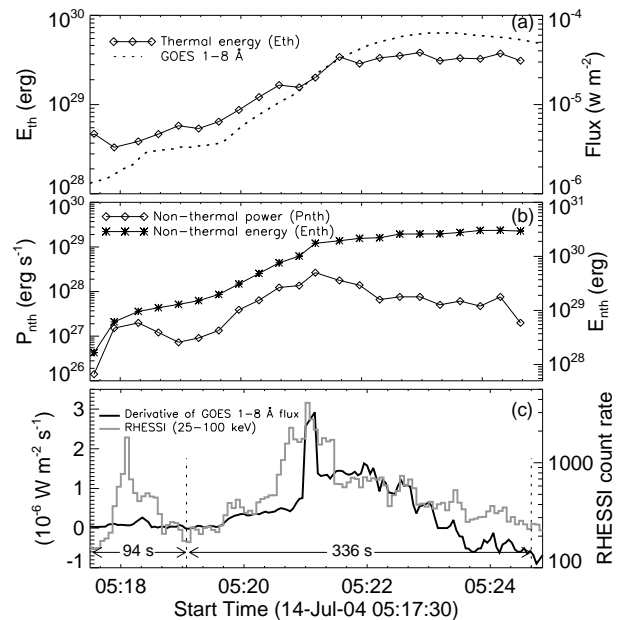


Figure 9 : Temporal evolution of (a) thermal energy ( $E_{th}$ ) along with GOES SXR flux at 1-8 Å, (b) non-thermal power ( $P_{nth}$ ) and cumulative non-thermal energy ( $E_{nth}$ ) during the M6.2 flare. We have also shown the comparison of RHESSI HXR flux profile at 25-100 keV with derivative of GOES 1-8 Å flux to check the Neupert effect in panel (c).

(U. Kushwaha and B. Joshi)

**Heliospheric tracking of CME features as enhanced density structures**

A Coronal Mass Ejection (CME) is an inhomogeneous structure consisting of different features which evolve

differently with the propagation of the CME. Simultaneous heliospheric tracking of different observed features of a CME can improve our understanding about relative forces acting on them.

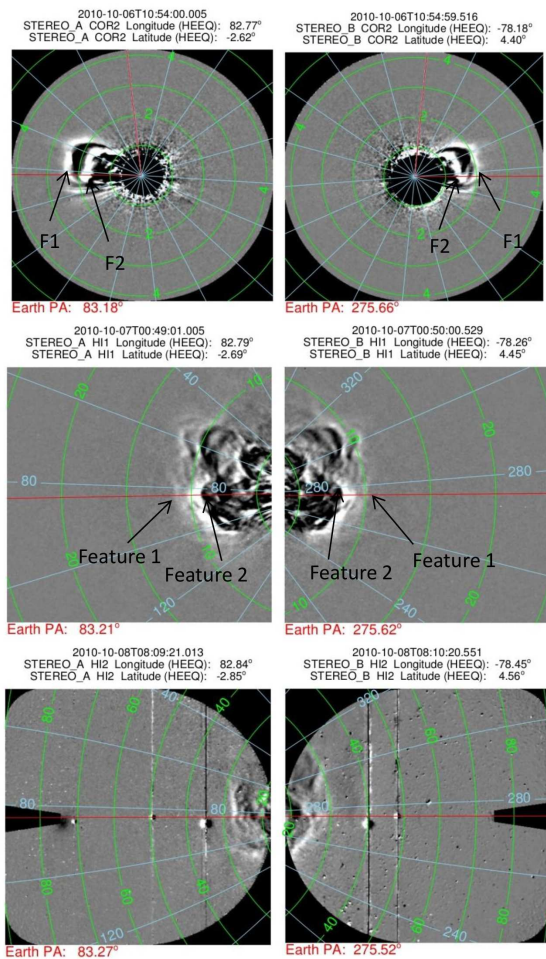


Figure 10 : Evolution of the 2010 October 6 CME observed in COR2, HI1 and HI2 images from *STEREO-A* (left column) and *STEREO-B* (right column). Contours of elongation angle (green) and position angle (blue) are overlotted. The vertical red line in the COR2 images marks the 0 degree position angle contour. The horizontal lines (red) on all panels indicate the position angle of Earth. The features (F1 and F2) tracked in coronagraph fields of view and the features (Feature 1 and Feature 2) tracked in the HI field of view are shown with arrows (black) in the top and middle panels, respectively.

Based on a single event study, we highlight the relevance and significance of Heliospheric Imager (HI) observations in identification of the three-part structure of the CME. Tracking of different features also helps to estimate accurately their arrival times at the Earth. This also enables to find association between remotely observed features and in-situ observations near the Earth. We attempted to continuously track two density enhanced features, one at the front and another at the rear edge of the 2010 October 6 CME by using time-elongation maps constructed from *STEREO/SECCHI* observations (Figure 10). We derived the kinematics of the tracked features using various reconstruction methods. The estimated kinematics were used as inputs in the Drag Based Model (DBM) to estimate the arrival time of the

tracked features of the CME at L1. On comparing the estimated kinematics as well as the arrival times of the remotely observed features with in-situ observations by *ACE* and *Wind*, we found that the tracked bright feature in the *J*-map at the rear edge of 2010 October 6 CME corresponds most probably to the enhanced density structure after the magnetic cloud detected by *ACE* and *Wind*. In-situ plasma and compositional parameters provide evidence that the rear edge density structure correspond to a filament associated with the CME while the density enhancement at the front corresponds to the leading edge of the CME (Figure 11).

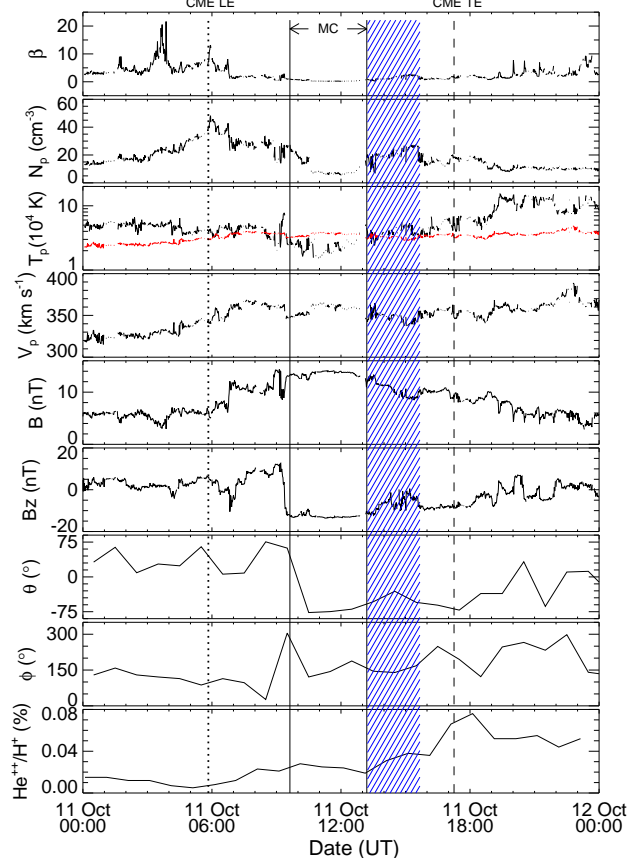


Figure 11 : From top to bottom, panels show plasma beta, proton density, proton temperature, flow speed, magnitude of magnetic field, z-component of magnetic field, latitude, longitude of magnetic field vector, and alpha to proton ratio. The red curve in the third panel shows the expected proton temperature. From the left, the first (LE), second, third and fourth (TE) vertical lines mark the arrival of CME leading edge, start of magnetic cloud, end of magnetic cloud, and trailing edge of CME respectively. The blue hatched regions mark the region associated with tracked Feature 2.

(W. Mishra and N. Srivastava)

### Evolution and consequences of interacting CMEs of 2012 November 9-10 using *STEREO/SECCHI* and in Situ Observations -

Understanding of the kinematic evolution of Coronal Mass Ejections (CMEs) in the heliosphere is important to estimate their arrival time at the Earth. It is found that kinematics

of CMEs can change when they interact or collide with each other as they propagate in the heliosphere. We studied the kinematics and interaction of two Earth-directed CMEs, launched successively on 2012 November 9 and 10. A combination of heliospheric imaging and in situ observations were used to estimate the CME kinematics, post-collision characteristics and nature of collision using white light imaging observations from STEREO/SECCHI and in situ observations taken from *Wind* spacecraft. We tracked two density enhanced features associated with leading and trailing edge of November 9 CME and one density enhanced feature associated with leading edge of November 10 CME by constructing *J*-maps. We found that the leading edge of November 10 CME interacted with the trailing edge of November 9 CME (Figure 12).

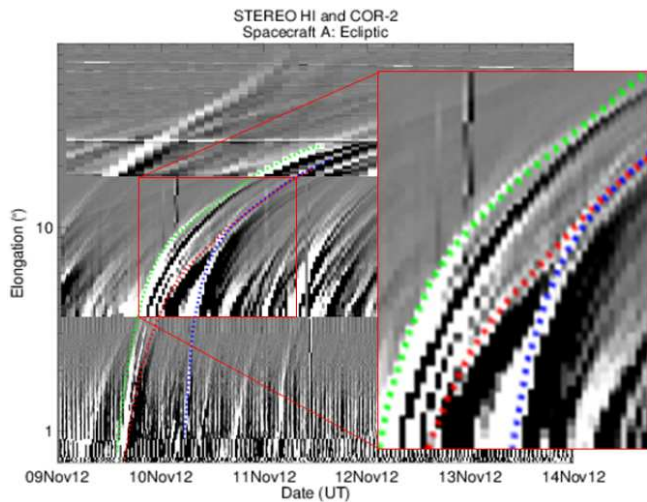


Figure 12 : Time-elongation map (*J*-map) using the COR2 and HI observations of STEREO/SECCHI spacecraft during the interval of 9-14 November 2012. The features corresponding to the November 9 CME leading edge (LE), its trailing edge (TE), and November 10 CME leading edge are (LE) tracked and overplotted on the *J*-map with green, red, and blue, respectively. The red rectangle (rightmost) is an enlarged plot of the red rectangle (on the left), which clearly shows that the red and blue tracks meet in the HI1 FOV.

We also noticed a significant change in their dynamics after interaction. Our analysis shows an improvement in arrival time prediction of CMEs using their post-collision dynamics than using pre-collision dynamics. Estimating the true masses and speeds of these colliding CMEs, we found that the collision is close to perfectly inelastic. In in situ observations, we identified heating and compression as signatures of CME-CME interaction. The investigation also places in perspective, the geomagnetic consequences of these two CMEs and their interaction in terms of occurrence of geomagnetic storm and triggering of magnetospheric substorms.

(W. Mishra, N. Srivastava and D. Chakrabarty)

**Repetitive formation and decay of current sheets in magnetic loops: an origin of diverse magnetic structures**

This work explores asymptotic topologies of magnetic field

lines shaped up by repeated events of magnetic reconnection using computations relying on the Implicit Large Eddy Simulation (ILES) property of non-oscillatory numerics. For the purpose, the initial magnetic field is constructed by superposing two linear force-free fields, solved appropriately in the  $z > 0$  positive half-space of a partially periodic Cartesian coordinate system. This use of the positive half-space being traditional in describing the solar atmosphere, the computations presented here are of direct relevance to observations. Also the corresponding initial magnetic field lines are of the form of loops, similar in geometry to the observed coronal loops.

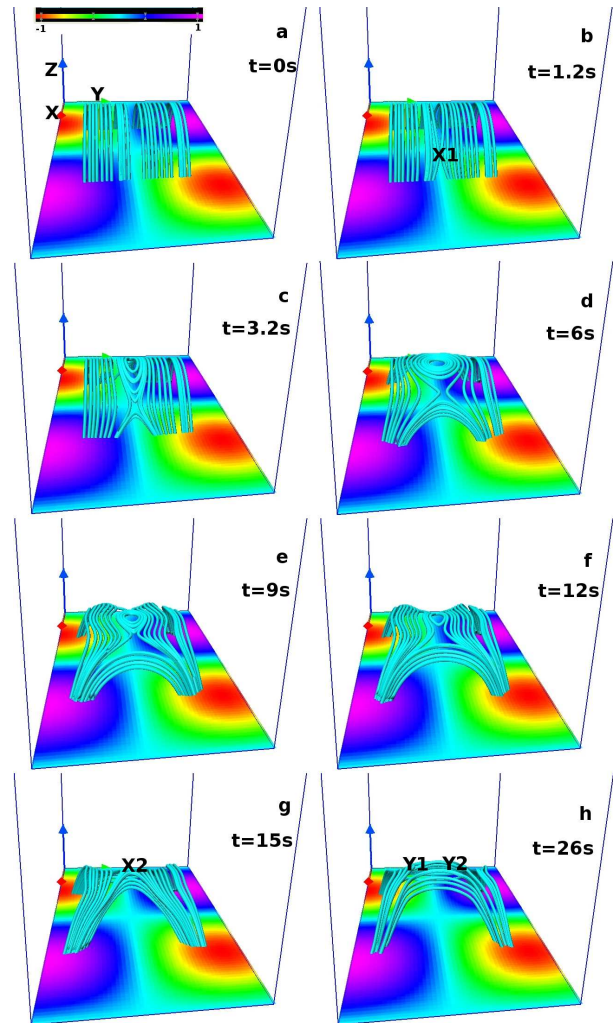


Figure 13 : Snapshots of magnetic field lines in their evolution when the initial footpoint geometry is mirror symmetric. Noteworthy are the developments of magnetic island (marked with closed field lines) and two Y-type nulls.

The dynamics of these initial field lines are investigated in terms of their footpoint evolution with an objective to explore the development of physically realizable magnetic structures through the process of successive magnetic reconnections (MRs). To be in conformity with the analytical requirements of current sheet (CS) formation, the magnetofluid is evolved from an unbalanced state of rest via viscous relaxation under the condition of flux freezing. In the process, magnetic

field gradients sharpen unboundedly, ultimately generating under-resolved scales. These scales are then filtered out from the system through numerically assisted MRs. After MRs, the computations are again well-resolved and satisfy the condition of flux-freezing. The field lines frozen to the reconnection outflow then press onto other flux systems and repeat the above process. In particular, the work explores this repetitive process for field lines characterized with three distinct cases of footpoint geometry with increasing complexity.

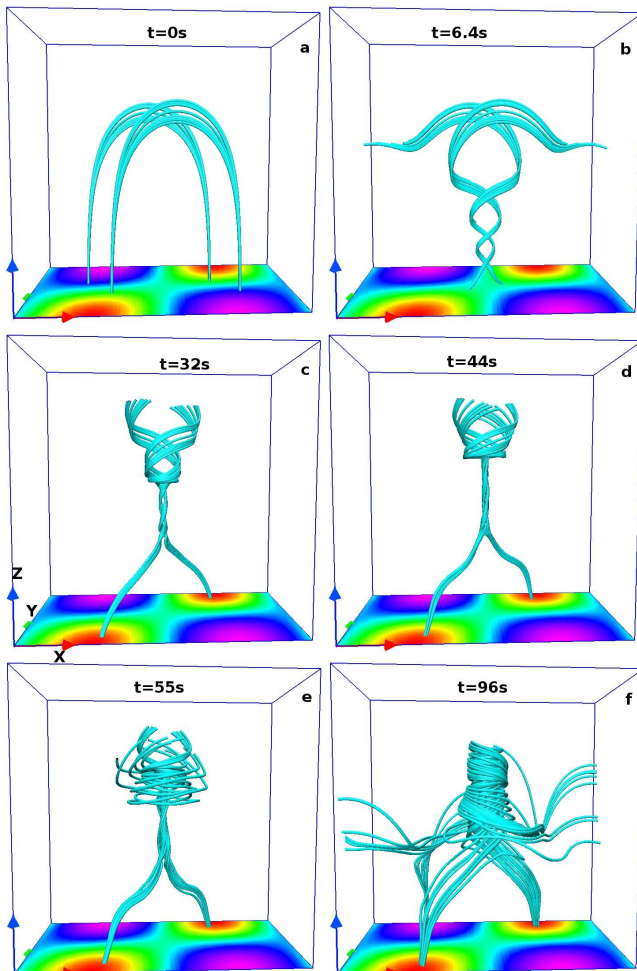


Figure 14 : Snapshots of magnetic field lines in their evolution when the initial footpoint geometry is glide symmetric. Notably, the footpoint reconnections lead to helical field lines resembling a solar tornado.

In Case i, we choose the initial magnetic field to be untwisted with footpoints of opposite polarities satisfying a mirror symmetry and having straight polarity inversion lines (PILs). The magnetofluid evolves with footpoint reconnections and leads to the formation of magnetic islands along with two X-type neutral points. Further, these X-type neutral points vertically ascend along with a simultaneous increase in separation between the footpoints of the underlying reconnected field lines, a phenomenon observed in solar flares. More importantly, continual pressing of these islands develop a new pair of X-type neutral points which when further squashed, generate two Y-type neutral points and an extended CS in accordance to the Parker's optical analogy.

The initial field lines in Case ii are also untwisted but characterized with curved PILs. The corresponding footpoints of opposite polarities satisfy a glide symmetry and hence are topologically more complex in comparison to the footpoints of Case i. The dynamics of the system is predominantly determined by the pressing of glide-symmetric footpoints toward each other. The resulting MRs impart a swirling motion of the magnetofluid along with the generation of helical magnetic field lines which are geometrically similar to the observed solar tornadoes. Additionally, the computations also confirm a later "untwisting" motion of these helical field lines as a consequence of repeated MRs. Such untwisting motions are also observational features of a solar tornado.

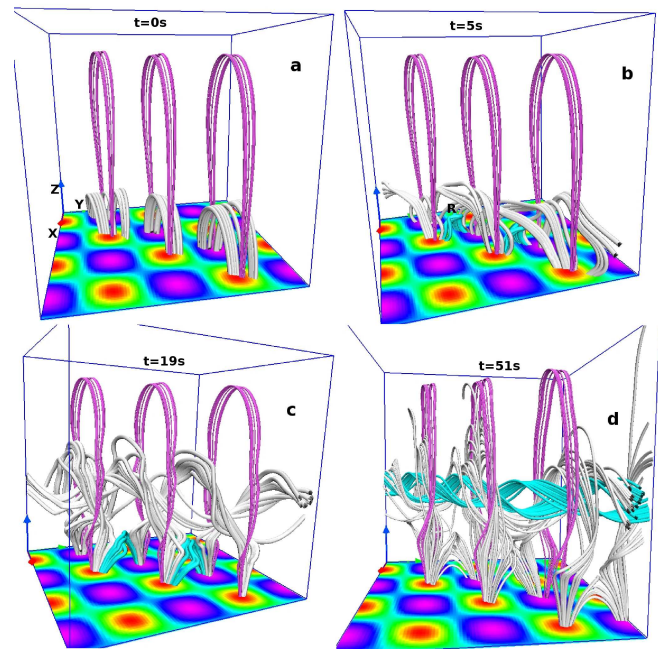


Figure 15 : Instances of field lines corresponding to case iii where the initial field is glide symmetric and twisted. Important are the formations of helical field lines resembling a twisted flux rope, depicted in color cyan at panel (d).

The Case iii investigates the evolution where the initial Lorentz force pushes two neighbouring sets of twisted, glide-symmetric field lines. The repeated MRs in this case, generate magnetic structure similar in appearance to a detached, twisted flux rope. The computations also suggest a sustained ascent of this flux rope driven by a difference in magnetic pressure, above and below the rope. Noteworthy is the development of an extended CS below the flux rope.

The importance of this work lies in its demonstration that different magnetic structures observed in the solar atmosphere can have a common origin in repeated MRs - sustained by an interplay of forcing and magnetic diffusion in a system of loops. Such repeated MRs (along with the prerequisite development of CSs), being fundamental to astrophysical plasmas; the resulting magnetic structures are expected to develop in other stellar coronae also. Moreover, we find that implicit large eddy simulations are capable to imitate MRs in a high magnetic Reynolds number magnetofluids in terms of their localized occurrences.

This work was done in collaboration with P. K. Smolarkiewicz of ECMF, Reading, UK.

(D. Kumar and R. Bhattacharyya)

**On the role of topological complexity in spontaneous development of current sheets**

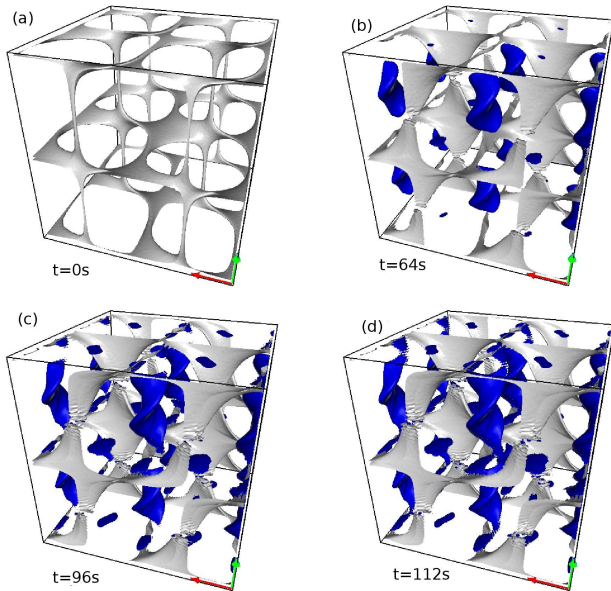


Figure 16 : Instances of CS (color blue) development overlaid with magnetic nulls (color grey). The initial field lines are strongly interlaced (not shown). Notably, the CSs are distributed throughout the computational domain.

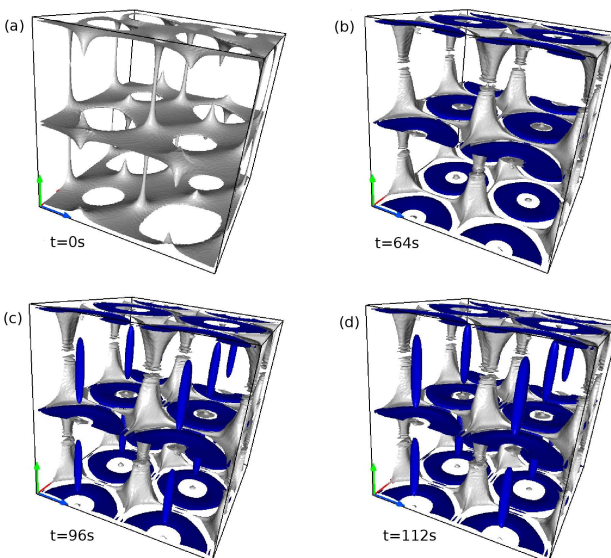


Figure 17 : Instances of CS (color blue) development overlaid with magnetic nulls (color grey). The initial field lines are less intensely interlaced (not shown). The corresponding CSs are localized in space.

Numerical computations presented in this work aim to quantify the intensity of field line interlacing in development of current sheets (CSs) by tracking viscous relaxation of an incompressible, thermally homogeneous magnetofluid having infinite electrical conductivity. A relevant initial value problem is constructed by superposing two untwisted component fields - each being represented by a pair of global magnetic flux surface. The relative amplitude of the two superposed fields determines the strength of interlacing. Numerical experiments are performed by varying this relative amplitude to achieve the aim. Also for a direct visualization of CS formation, we follow the evolution of flux surfaces instead of the vector magnetic field. An important finding of this work is in the demonstration that initial field lines with stronger interlacing tend to develop CSs which are distributed throughout the computational domain and are located away from sites like - magnetic nulls or field reversal layers with favorable magnetic topology. The onset of these CSs are attributed to favorable contortions of magnetic flux surfaces where two oppositely directed parts of the same field line or different field lines come to close proximity. While for less intensely interlaced field lines, the simulations confirm development of CSs at sites where the magnetic topology is favorable. Furthermore, these CSs are not distributed homogeneously over the computational domain, and originate as two sets of anti-parallel complimentary field lines press onto each other.

This work was done in collaboration with P. K. Smolarkiewicz of ECMF, Reading, UK.

(S. Kumar and R. Bhattacharyya)

**Polarimeter for Multi-Application Solar Telescope: Characterization of liquid crystal variable retarders (LCVRs)**

The Multi-application Solar Telescope (MAST) is a 50 cm off-axis Gregorian telescope installed at the lake site of Udaipur Solar Observatory. One of the scientific objectives of MAST is to study the evolution of vector magnetic field in the solar atmosphere and its connection to various solar activities. In order to measure the vector magnetic field in the solar atmosphere, we are developing a Polarimeter for the MAST, which will be used for precise measurements of the Stokes vector at two different wavelengths i.e. at 617.3 nm and 854.2 nm, corresponding to photospheric and chromospheric heights, respectively.

Table 1: Modulation scheme for Vector Observing mode of MAST polarimeter.

$\delta 1$ (in degree)	$\delta 2$ (in degree)	Measured Intensity
315.0	305.264	$I_1 = I + Q/\sqrt{3} + U/\sqrt{3} + V/\sqrt{3}$
315.0	54.736	$I_2 = I + Q/\sqrt{3} - U/\sqrt{3} - V/\sqrt{3}$
225.0	125.264	$I_3 = I - Q/\sqrt{3} - U/\sqrt{3} + V/\sqrt{3}$
225.0	234.736	$I_4 = I - Q/\sqrt{3} + U/\sqrt{3} - V/\sqrt{3}$

MAST Polarimeter will modulate the polarization signal using two liquid crystal variable retarders (LCVR) along with a linear polarizer (one set each for the above wavelengths). Figure 18 shows the configuration of the fast axis orientation of the LCVRs with respect to the linear polarizer.

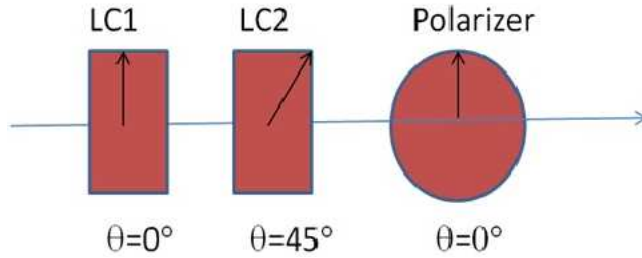


Figure 18 : Configuration of the MAST Polarimeter. Where, LC1: LCVR 1, LC2: LCVR2.

Modulation scheme for measuring the Stokes parameters  $I$ ,  $Q$ ,  $U$  and  $V$  are listed in Table 1. This modulation scheme requires only four measurements to retrieve all the Stokes parameters and also provide maximum modulation efficiency.  $\delta_1$  and  $\delta_2$  are the retardances of the LCVRs for different measurements. Measurements of all the Stokes parameters are required to obtain the vector magnetic field, whereas some of the studies require only longitudinal magnetic measurements (and thus only Stokes  $V$  measurements). This could be done using the modulation scheme listed in Table 2 with only two measurements.

Table 2: Modulation scheme for Longitudinal Observing mode of MAST polarimeter.

$\delta_1$ (in degree)	$\delta_2$ (in degree)	Measured Intensity
360.0	90.0	$I_1 = I - V$
360.0	270.0	$I_2 = I + V$

LCVRs are electrically tunable retarders; the retardance also varies with wavelength and temperature. In order to use the LCVRs for the Stokes vector measurement, the voltages required for the retardance listed in Tables 1 and 2 need to be measured for specific wavelengths. We have characterised two sets of LCVRs (two each for 617.3 nm and 854.2 nm) for their retardance dependence on voltage. A lab set-up including a white light source and band-pass filters are used for the characterisation. The LCVR is placed between two linear polarizers, such that the fast axis of the LCVRs is fixed at  $45^\circ$  to the first linear polarizer. Two sets of intensity measurements are carried out by changing the orientation of the second linear polarizer parallel ( $I_{\parallel}$ ) and perpendicular ( $I_{\perp}$ ) to the first linear polarizer axis. The retardance is calculated from those measurements as;

$$\delta = \cos^{-1} \left( \frac{I_{\parallel} - I_{\perp}}{I_{\parallel} + I_{\perp}} \right)$$

Figure 19 & 20 show the measured voltages and corresponding retardance for each sets of LCVR at 617.3 nm and 854.2nm, respectively. The solid and dashed lines indicate the voltages required for the retardances  $\delta_1$  and  $\delta_2$

listed in the modulation schemes (table 1 & 2). Later on these measured voltages will be used for the measurement of Stokes parameters in real time solar observations. Figure 21 shows the changes in the retardances with voltages at different temperatures.

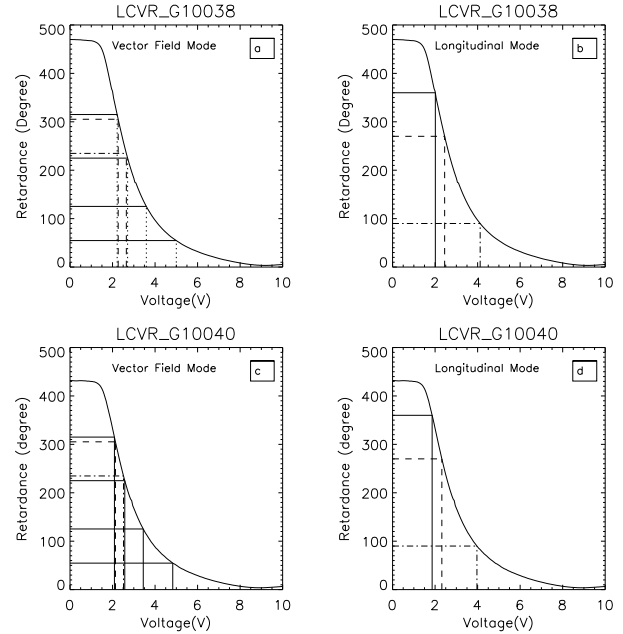


Figure 19 : Calibration curves of both the LCVRs at 617.3 nm showing the voltages and retardances for the vector and longitudinal modes respectively.

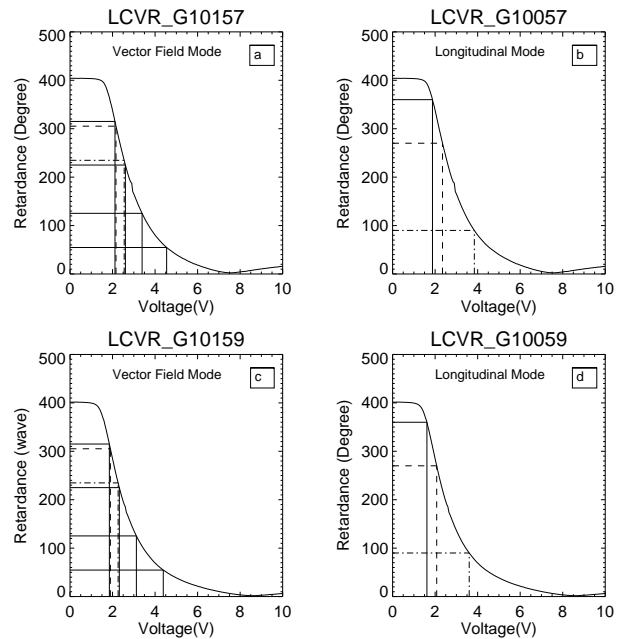


Figure 20 : Calibration curves of both the LCVRs at 854.2 nm showing the voltages and retardances values for the vector and longitudinal modes respectively.

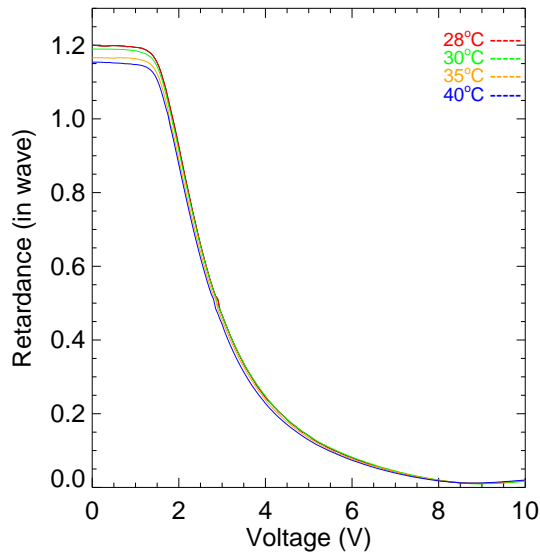


Figure 21 : Calibration of one of the LCVRs showing the voltages and retardance values for different temperatures. The effect on retardance due to temperature is  $\sim 0.04\%$  per degree retardance.

(A. R. Tiwary and S. K. Mathew)

### Milne-Eddington inversion for MAST polarimetry

The information about the physical properties of solar atmosphere is solely given by the observed characteristics of the electromagnetic waves. Unfortunately, there is no direct way to measure the temperatures, densities, velocities, magnetic field and other physical quantities to probe the solar atmosphere. Hence, the role of inversion techniques or inversion of Stokes profiles becomes important. Inversion techniques are the most powerful and sophisticated tool to infer information about the solar magnetic field and the thermodynamic properties from the Stokes profiles of a particular spectral line. The basic idea of inversion technique is to fit the synthetic Stokes profiles with the observed ones to retrieve the magnetic and thermodynamic properties of the solar atmosphere.

Polarimeter is one of the back-end instruments of MAST which will provide us polarimetric images in future. This instrument can be used to measure the polarization state of light or full Stokes vectors  $[I, Q, U, V]$  across the neutral iron line at 617.33 nm. These Stokes vectors contain the information about the physical properties of the solar atmosphere. We are developing an inversion code, for the Fe I 617.33 nm photospheric spectral line, to retrieve the magnetic field information from the polarimetric images. The code is based on the solution of radiative transfer equations (RTE; Unno-Rachkovsky equations) in the presence of magnetic field after taking in account the Zeeman effect and quantum mechanical corrections. A typical RTE can be expressed as,  $d\mathbf{I}/d\tau = \mathbf{K}[\mathbf{I}-\mathbf{S}]$ , here  $\mathbf{I}$  is a set of four Stokes vectors,  $\mathbf{K}$  is the propagation matrix ( $4 \times 4$ ) whose elements are function of absorption, dispersion profiles, and geometrical coordinates,  $\tau$  is optical depth, and the source function is given by  $\mathbf{S}$  which is equal to Planck's function  $[\mathbf{B}(T), 0, 0, 0]$  under

local thermodynamic equilibrium. It is observed that all the thermodynamic, magnetic, dynamic, atomic, and geometric medium properties are included in  $\mathbf{K}$  and  $\mathbf{S}$ .

To simulate the Stokes profile we assume that the solar atmosphere is described by a Milne-Eddington (ME) atmosphere in which the solar atmosphere can be described by a set of physical parameters. The set of physical parameters contains information of magnetic field strength, field inclination, field azimuth, line-of-sight velocity ( $V_{LOS}$ ), source function ( $S_1$ ), source function gradient ( $S_0$ ), continuum to line absorption ratio ( $\eta_0$ ) and damping constant ( $a$ ). Under the ME atmosphere the physical parameters are constant with the depth in the photosphere and source function varies linearly with the depth. This set of physical parameters is used to solve the RTE. We are writing the code in C programming language in order to generate and fit the synthetic Stokes profiles with the observed ones. The absorption and dispersion profiles have been computed using Voigt and Faraday-Voigt functions, respectively. To compute the non-linear equation we have employed standard programming packages such as LAPACK, BLAS, SVD (modified) etc. The module to synthesise the Stokes profiles has been developed and compared with the existing inversion codes. Using synthetic module the Stokes profiles have been generated and tested for longitudinal, transverse and weak magnetic fields. One example of synthetic profile is shown in Figure 22, where the synthesised Stokes profiles for Fe I 617.33 nm generated for different magnetic field strengths in a ME atmosphere with parameters  $a=0.05$ ,  $\theta=\pi/4$ ,  $\phi=\pi/6$ ,  $\eta_0=10$ , and  $S_0/S_1=4$ . After the synthesis of Stokes profile next step of inversion scheme is to fit it with the observed ones. The fitting is initiated by a set of guess parameters, during each iterative process the free parameters are modified to minimize the difference between the observed and the synthetic Stokes profiles. Now we are developing a fitting module, which is based on the Levenberg-Marquardt non-linear fitting algorithm. The sensitivities of the spectral lines for different atmospheric parameters (response function) can be calculated analytically, which is one of the main advantages of using ME atmosphere to solve the RTE.

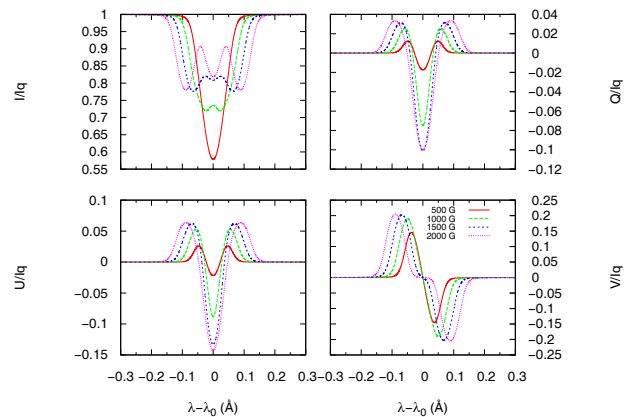


Figure 22 : The synthesised Stokes profile (normalised with continuum intensity,  $I_q$ ) for Zeeman triplet ( $\lambda_0 = 617.33 \text{ \AA}$ ) in M-E atmosphere with parameters  $a=0.05$ ,  $\theta=\pi/4$ ,  $\phi=\pi/6$ ,  $\eta_0=10$ , and  $S_0/S_1=4$ .

(R. Yadav and S. K. Mathew)

# SCIENCE at PRL

## Planetary Sciences and PLANEX Program

### Meteorite Studies

#### Presolar silicates from $^{15}\text{N}$ -rich clasts in Isheyevu CH/CB chondrite

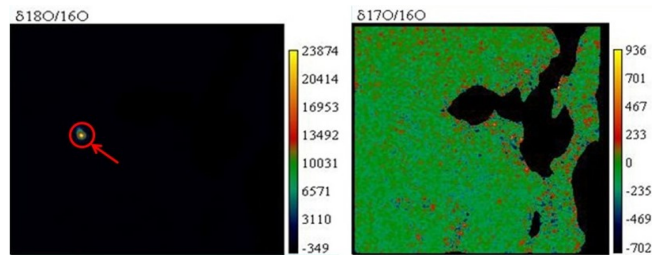


Figure 1 :Ratio images of the three O isotopes given in terms of delta values (variation with respect to terrestrial value) for a  $10\ \mu\text{m} \times 10\ \mu\text{m}$  region from the Isheyevu lithic clast. Images are scaled to the brightest pixel, and the color bars provide ion counts per second. Ratio image reveals an isotopically anomalous grain that is highly enriched in  $^{18}\text{O}$ . Si/O ratio and anomalous  $^{18}\text{O}/^{16}\text{O}$  in this grain indicates it to be a presolar silicate of the supernova origin.

The Isheyevu CH/CB carbonaceous chondrite contains hydrated lithic clasts up to a millimeter in size that contain matrix-like material with aqueous alteration products such as serpentine phyllosilicates, sulfides, magnetite, carbonates etc.. Carbon-rich organic matter is also embedded in the phyllosilicate matrix, which is enriched in  $^{15}\text{N}$  relative to other solar system materials. Bulk clasts can have  $\delta^{15}\text{N}$  values up to 1000 ‰ (while hotspots can reach values up to 5000 ‰). Such high  $^{15}\text{N}$  enrichment in these clasts suggests their primitive nature and possibility of preserving primordial

molecular cloud material. Abundance of presolar grains in these clasts should be significant and provide indication of the stellar source contributing to the initial molecular cloud composition from which our solar system formed.

We searched in situ for presolar silicate and oxide grains in a section of Isheyevu in lithic clasts with  $\delta^{15}\text{N}$  as high as 3000 ‰ using high spatial resolution (150 nm) with nanoSIMS (nano Secondary Ion Mass Spectrometer). Around 35300 sq. micron area was searched with  $\text{Cs}^+$  beam for anomalous oxygen isotope composition. Six grains (250-700 nm in size) have been identified as presolar silicates/oxides (Figure 1). The total abundance estimated for the presolar silicate/oxide in three clasts is  $\sim 22$  ppm. Three oxygen isotope plot (Figure 2) of presolar silicates/oxides obtained till date have been shown in red symbols. Four of the presolar grains belong to the group 1 region. These grains are believed to have formed in envelopes of red giant branch (RGB) or asymptotic giant branch (AGB) stars whose oxygen isotopic compositions are determined by partial H-burning during main-sequence evolution followed by the first (and second) dredge-up. Hydrogen-burning by the CNO cycle results in zones within the star with enhanced  $^{17}\text{O}$  and depleted  $^{18}\text{O}$ , relative to the initial composition. The grain with large  $^{18}\text{O}$  depletion (group 2) indicates that the envelope material of its parent star experienced partial H burning during the RGB and/or AGB phases. This could have occurred either by cool bottom processing (CBP), extra mixing that occurs when material from the envelope is cycled to regions hot enough for H burning. Grain highly enriched in the heavy O isotopes (group 4) probably formed in stars with higher-than-solar metallicity, or given the high anomaly (large  $^{18}\text{O}$  excesses)

could have originated in a supernovae (SNe). Both equilibrium and non-equilibrium condensation models in supernova ejecta predict the condensation of silica/oxide grains in O-rich layers, and the astronomical observations also support these models. Analysis of SNe tracers like  $^{44}\text{Ca}$ ,  $^{26}\text{Al}$  on the grain might further confirm the supernova origin. A FIB (focused ion beam) along with TEM (Transmission electron Microscopy) analyses is planned on these grains to obtain their mineralogy.

*This work was done in collaboration with Dr. M. Bizarro from University of Copenhagen, Denmark.*

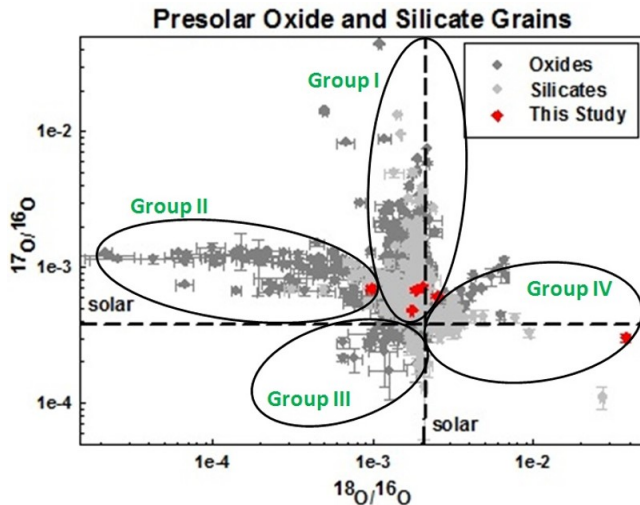


Figure 2 : Oxygen isotopic compositions of the presolar silicates, oxides identified in this study along with the literature data. Four out of six grains have enrichments in  $^{17}\text{O}$  (group 1) and one with large depletion in  $^{18}\text{O}$  (group 2). Grain with high enrichment in heavy isotope ( $^{18}\text{O}$ ) indicates its Supernova origin (group 4). The dotted lines shows the isotopic ratios of solar system materials ( $^{17}\text{O}/^{16}\text{O} = 3.83 \times 10^{-4}$ ;  $^{18}\text{O}/^{16}\text{O} = 2.01 \times 10^{-3}$ ).

(K. K. Marhas, M. Sanghani and L. Shukla)

### Simultaneous extraction of Si and Mg for their isotopic analysis using MC-ICPMS

Si and Mg are some of the most abundant elements of the solar system and are found to be coexisting in a number of naturally occurring minerals such as forsterite ( $\text{Mg}_2\text{SiO}_4$ ) and enstatite ( $\text{MgSiO}_3$ ) because of their similar condensation temperature. Thus, the study of stable isotope variations of Mg and Si are important to understand the behavior of magnesian silicates during their evaporation, condensation and evolution in early solar nebula, as well as planet formation processes and time scales.

With the advent of Multi-Collector Inductively Coupled Plasma Mass Spectrometry (MC-ICPMS), isotopic studies of Si, Mg and other non traditional isotopes have propelled in the last decade. But for high precision stable isotopic analyses, it is essential to have very pure solutions of Si and Mg. A new technique has been established based on alkaline fusion followed by ion-exchange chromatography for the separation and purification of Si and Mg from a single aliquot of natural

sample. This procedure is given more emphasis in the context of studying meteorites which are rare and precious and hence care is required to extract as much information as possible from a single chip of meteorite.

The separation and purification of Si is achieved using BioRad cation exchange resin 50W-X12 (200-400 mesh) in  $\text{H}^+$  form, filled to 1.8 ml resin bed in BioRad columns. Si concentrations in each cut were measured using ICP-AES and recovery was found to be  $\sim 98\%$ . ICPMS was used to find the concentrations of all major cations (Na, Ca, K, Mg, Al) and trace metals (Fe, Ni, Mo) in these Si cuts and were found to be negligible (Figure 3). After separation of Si, all the ambient cationic species are effectively retained in the cation exchange resin. Quantitative purification of Mg from these cations has been established and the recovery of Mg in processed sample solutions was found to be 95%. Si and Mg purification has been carried out in terrestrial rock standards obtained from USGS. The same protocol will be applied to meteorites for determination of their isotopic compositions using High-Resolution Neptune MC-ICPMS at Physical Research Laboratory, Ahmedabad.

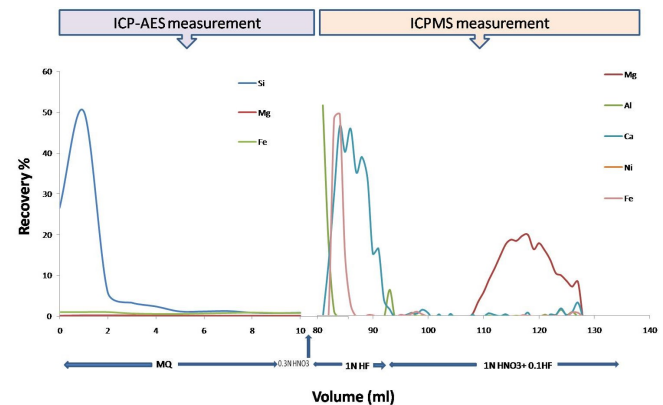


Figure 3 : Simultaneous purification of Si and Mg from terrestrial rock sample.

(J. Sikdar and V. K. Rai)

### Mineral Characterization of L3 chondrite QUE 97008 using EPMA

The study of stable isotope variation of Mg and Si in inter mineral phases of meteorites are important to understand the behavior of magnesian silicates during their evaporation, condensation and subsequent evolution in space. Although there is accumulating evidence that magmatic differentiation and planetary accretion alters bulk Si isotope ratio but not Mg-isotope ratios, the study of inter-mineral Si and Mg isotope fractionation among terrestrial and extra terrestrial objects have remained neglected. In order to understand the fractionation of Si and Mg isotopes among different phases of meteorite, clean extraction of pure minerals from different phases of chondrites will be carried out using New Wave Micromill. But prior to microsampling, electron probe analyses of the sample must be done since the micromilling technique

is destructive. Such preparation is important for making decisions on sample localities so that inclusions or cracks can be avoided, and zones of mineral phases of particular interest can be sampled.

In the present study, characterization of minerals in L3 chondrite QUE 97008 was carried out using EPMA. The Acceleration voltage and sample current used were 15 kV and 15 nA respectively. And the beam diameter was 1  $\mu\text{m}$ . The studied meteorite is characterized by low siderophile content and a large volume percentage of chondrules, with only 10-15 vol % of fine-grained matrix. The presence of unequilibrated mineral assemblages in this meteorite suggests that it has undergone least terrestrial alteration. But numerous shock veins were seen. Most of the glasses and chondrules are surrounded by a rim of sulphides. A number of Si and Mg bearing phases have been identified which are listed below: Enstatite ( $\text{Mg}_2\text{Si}_2\text{O}_6$ ), Forsterite ( $\text{Mg, Fe})_2\text{SiO}_4$ , Hornblende ( $\text{Ca, Na})_3(\text{Mg, Fe, Al})_5(\text{Si, Al})_8\text{O}_{22}(\text{OH, F})_2$ . Apart from these silicates, metals and sulfides were also identified. Analyses of Si and Mg isotopic composition among these phases will be carried out using MC-ICPMS.

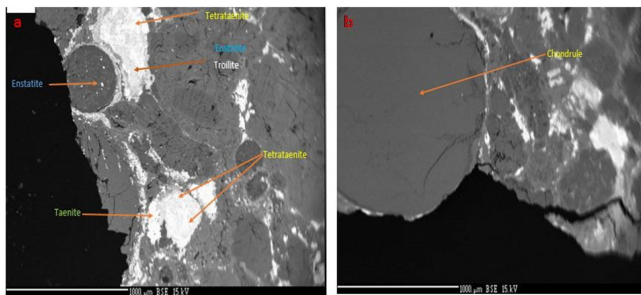


Figure 4 : (a) BSE image of QUE 97008 showing its different phases and (b) BSE image of 1mm chondrule consisting entirely of Olivine crystals (light) set in dark matrix

(J. Sikdar and V. K. Rai)

### Troilite-metal nodule in Katol chondrite - role of impact and noble gas evidences

Katol, a troilite-metal nodule bearing strongly equilibrated L6-7 chondrite, is a recent fall in India (May, 2012). Origin of the troilite-metal nodules, largely in L chondrites remain least understood although role of shock melting, impact-induced vaporisation or sub-solidus diffusion are proposed. Present study focuses on formation mechanism of troilite-rich, Fe, Ni-metal nodule ( $\sim 2$  cm across) that includes a large variety of shock-induced melt-dominated micro-textures. We have also studied noble gases in the nodule to discern preferential gas loss due to shock, if any, compared to the bulk.

Katol nodule is essentially an immiscible submicron scale intergrowth of Ni- rich troilite [mean (in wt %) Ni:1.81, S: 32.63], S-bearing kamacite (S:0.55, Ni: 6.18) and taenite (S:0.64, Ni:8.65). Metal-troilites are juxtaposed with intensely fractured silicate minerals, mainly olivine, low-Ca pyroxene

and large volume of maskelynite (Figure 5). Moderate shock evidences are clearly imprinted in chondritic silicates (PDF in olivine, diaplectic plagioclase crystal and glass), while compression shock wave and subsequent shear-stress resulted in several ductile-brittle micro-textures (swiss cheese, fizz troilite, sheared troilite, metal-droplets and globules, shear melt veins, melt pockets including high pressure phases, maskelynite-I that quenched under high pressure [Raman bands, 510 and 580  $\text{cm}^{-1}$ ], wadsleyite [Raman bands, 716, 918  $\text{cm}^{-1}$ ] and ringwoodite [Raman bands, 799, 841  $\text{cm}^{-1}$ ]) within the nodule.

Noble gas isotopes indicate that Ne is purely cosmogenic while all other noble gases are a mixture of cosmogenic, radiogenic and trapped components. Cosmogenic ( $^3\text{He}$ ,  $^{21}\text{Ne}$ ) and radiogenic ( $^4\text{He}$ ,  $^{40}\text{Ar}$  and  $^{129}\text{Xe}$ ) amounts are comparable in this nodule with the bulk sample, though  $(^{22}\text{Ne}/^{21}\text{Ne})_c$  are different, indicating different depths of sample location.

Based on the complexly intergrown troilite-metal texture, the nodule formation is likely a localised event by a high energy impact which facilitates spatially focused frictional heating at the structural and compositional discontinuities. Our results correspond to calibrated peak shock pressure of  $\sim 45$  GPa with peak shock temperature between 900°C to 1500°C.

*This work was carried out in collaboration with Dr. K. Chakraborti of GSI, Kolkata.*

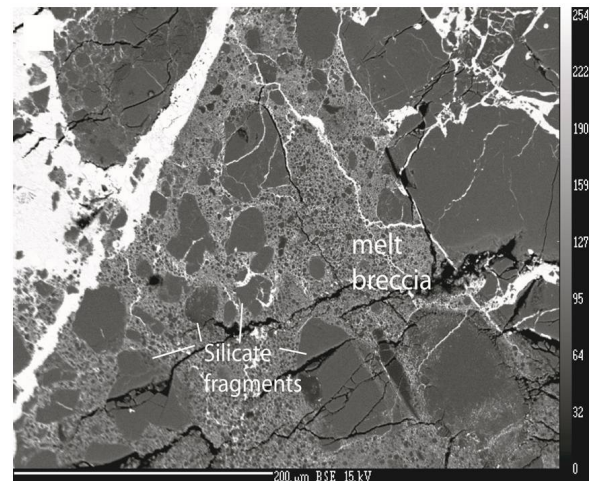


Figure 5 : BSE images of Katol melt breccias that show randomly distributed assorted silicate fragments in Fe-Nitroilite melt.

(D. Ray, R. R. Mahajan, S. Ghosh and S. V. S. Murty)

### Cosmogenic nuclides in Katol ordinary chondrite

Within a few days of this meteorite fall we have collected several individual pieces. Cosmogenic radionuclides are measured in some of these fragments, using the ultra low background HPGe detector and noble gases in one of

the pieces by standard procedures. Most notable is the occurrence of the neutron produced  $^{60}\text{Co}$  in all fragments measured, in variable amounts (13 to  $> 200$  dpm/kg), indicating that these fragments came from different depths of a large pre-atmospheric meteoroid. Isotopic composition of noble gases indicate that  $^3\text{He}$  and  $^{21}\text{Ne}$  are purely cosmogenic, while Ar, Kr and Xe are a mixture of trapped, radiogenic and cosmogenic components. We use the maximum observed  $^{60}\text{Co}$  to derive the radius of Katol meteoroid as 85 to 120 cm. Within this size range and the measured  $(^{22}\text{Ne}/^{21}\text{Ne})_c$  ratio, we use production rates for depths and arrive at exposure ages (Ma) of 17-19( $T_3$ ), 40-43( $T_{21}$ ) and 44-50( $T_{38}$ ). After correcting for  $^{36}\text{Ar}_n$ , due to  $^{35}\text{Cl}(n,\gamma)$  contribution,  $T_{38}$  goes up to 47-54 Ma. Low  $T_3$  could be due to partial  $^3\text{He}$  loss.  $T_{21}$  and  $T_{38}$  are consistent within experimental errors. We consider the exposure age of  $50 \pm 5$  Ma as representative for Katol.

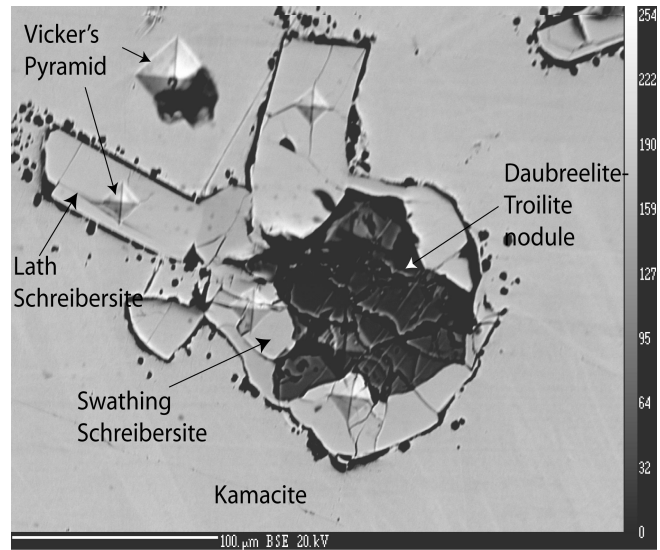
Excesses over spallation production are clearly seen at  $^{80,82}\text{Kr}$  and  $^{128}\text{Xe}$ , due to  $(n,\gamma)$  reactions on  $^{79,80}\text{Br}$  and  $^{127}\text{I}$  respectively. We calculate  $(^{80}\text{Kr}/^{82}\text{Kr})_n = 2.5$  which agrees with the value expected for epithermal neutrons. Based on  $^{82}\text{Kr}_n$  and a value of  $(^{36}\text{Ar}/^{82}\text{Kr})_n \sim 3000$  for Cl, Br contents of L chondrites, we calculate  $^{36}\text{Ar}_n = 0.64 \times 10^{-8}$  ccSTP/g, which translates in to  $^{36}\text{Cl}$  production rate of  $\sim 83$  dpm/gCl, taking 50 Ma as exposure age and Cl content of 80 ppm for L chondrites. We estimate a radius of 85-170 cm based on  $^{36}\text{Cl}$ , consistent with the estimate based on  $^{60}\text{Co}$ .

(S. V. S. Murty, R. R. Mahajan, A. D. Shukla and P. M. Ranjith Kumar)

### Shock-thermal history, metallographic cooling rate and cosmic ray exposure history of recent Iron Meteorite falls

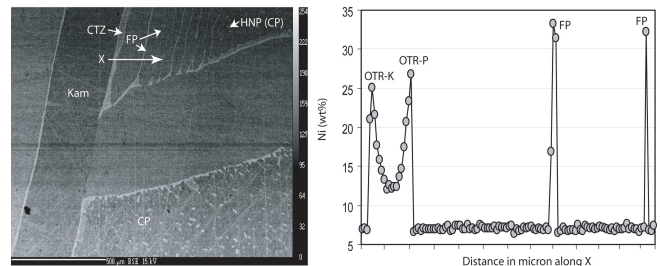
We have studied two irons, Raghunathpura (IIAB) a fall from Rajasthan, India and Nyaung (IIIAB) iron, a fall from Myanmar. Shock-thermal history has been assessed by studying chemistry of different mineral phases, their morphology and micro textures. Metallographic cooling rate is estimated through Ni profiling across the Fe-Ni phases. Finally, cosmic ray exposure history of irons is determined using noble gas isotopes.

A two-core model is envisaged for the formation of sulphide nodule bearing Raghunathpura iron (Figure 6). The cooling of metallic magma was initiated in the P- rich lower core where most of the phosphides were exsolved out as different modes of inclusions in the kamacite matrix. The residual metallic melt was enriched with trapped (S+P) melt in the S-rich upper core after about 8.5 % of crystallisation. Extremely slow cooling rate ( $4^\circ\text{C}/\text{Ma}$ ) of Raghunathpura also appears conducive to maintain the equilibrium between the two cores throughout as indicated from absence of marked discontinuity in metal composition between initial and residual phase. Finally, a strong, late-stage metal fractionation carries higher Ga, Ge and Ir concentration enabling higher degree of trapped melt fractionation (up to three order of magnitude), as validated by late P/S ratio of 0.69 compared to the estimated initial value of 0.25.



Troilite micronodule in Raghunathpura iron

Figure 6: Raghunathpura nodule

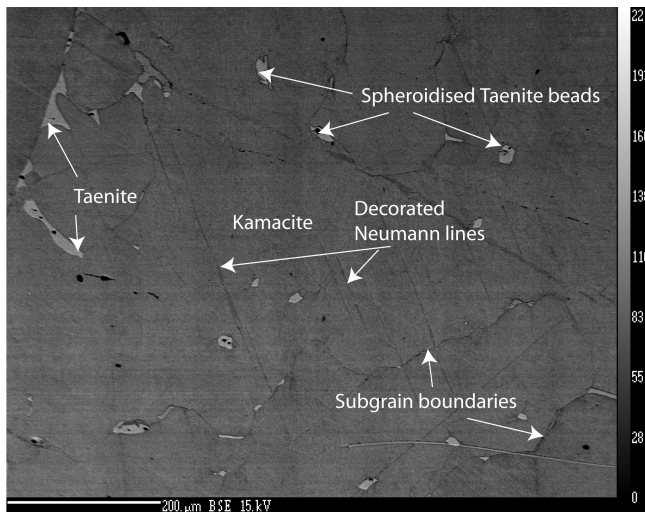


Ni Profiling in different Plessite regions of Kavarpura iron

Figure 7 : Kavarpura Ni profiling

Rapid rate of cooling of Nyaung molten core may be explained in terms of fractional crystallisation of small body of molten core insulated with a very thin silicate mantle. It may be postulated that a high degree of shock equivalent to  $\sim 600$  kb caused by impact, either during closing phase or, subsequent to cooling has damaged the thick silicate mantle to the extent of a thin layer, and caused annealing in the parent body of Nyaung IIIAB iron. He, Ne and Ar are mostly cosmogenic. Cosmogenic  $^{21}\text{Ne}$  is profusely produced from P and S, which are heterogeneously distributed in the sample, while no such composition specific production occurs for  $^3\text{He}$  and  $^{38}\text{Ar}$ . Using the  $(^{22}\text{Ne}/^{21}\text{Ne})_c$  of the sample, it is possible to estimate the contribution of S+P in the sample to the total  $^{21}\text{Ne}_c$  and calculate the exposure age using the amount and production rates from Fe+Ni only. The depth of the analysed sample in the pre-atmospheric size of the body is needed for using the correct production rate to obtain the cosmic ray exposure age. Isotopic ratio  $(^3\text{He}/^4\text{He})_c$  as well as the elemental ratios  $(^3\text{He}/^{21}\text{Ne})_c$  and  $(^{38}\text{Ar}/^{21}\text{Ne})_c$  are good size and depth indicators. However, due to possible partial loss of  $^3\text{He}$  and  $^{21}\text{Ne}$  by thermal/shock effects, resulting in the change of elemental ratios, we choose to use  $(^3\text{He}/^4\text{He})_c$  as

depth indicator. For Raghunathpura, sample at a depth of 12-14 cm, in a 25 cm radius iron meteorite matches the He isotopic ratio and using corresponding production rates we obtain the exposure ages (in Ma) of 165, 200 and 276 based on  $^3\text{He}_c$ ,  $^{21}\text{Ne}_c$  (from Fe+Ni only) and  $^{38}\text{Ar}_c$ . We take  $276 \pm 41$  Ma as the exposure age, attributing lower ages due to  $^3\text{He}$  and  $^{21}\text{Ne}$  due to partial gas loss, possibly during the shock event of magnitude  $\sim 100$  kb derived from micro hardness measurements. CRE age of Nyaung is similarly determined to be 670 Ma.



Shock and Post shock annealing microtextures of Nyaung iron

Figure 8 : Nyaung microtextures

(D. Ray, S. Ghosh and S. V. S. Murty)

### Geochemistry of texturally different fractions of Piplia Kalan Euclite

Howardite, euclite and diogenite (HED) meteorites represent the largest clan of achondrites and are presumably derived from the differentiated asteroid 4-Vesta. Piplia Kalan euclite contains texturally and compositionally different components in its main mass. A detailed chemical study of texturally distinct fractions to understand their petrogenesis, using trace elements, especially the REE systematics has been performed. Piplia Kalan euclite is an equilibrated, monomict, non-cumulate basalt. Two main lithologies are observed, coarse-grained (ophitic) and fine-grained. The lithic clasts (60-80 vol %) are embedded in a brecciated matrix. Pyroxene and plagioclase are the dominant mineral phases; while the accessory phases are Cr-spinel, ilmenite, sulfide (troilite) and Fe-metal. Pyroxene and plagioclase composition ranges between  $\text{Wo}_{0-48}\text{En}_{27-38}$  and  $\text{An}_{85-91}$ , respectively.

Piplia Kalan is characterized by a relatively flat-REE pattern,  $\sim 10\times\text{CI}$ -chondrite with slightly descending trend towards the HREE  $\sim 6\times\text{CI}$ -chondrite (Figure 9). Interestingly, the coarser fraction of this euclite demonstrates a positive Eu-anomaly, while the finer fraction shows a negative

Eu-anomaly. From LREE to MREE (La to Dy) the coarser and finer fractions are the mirror images of each other. The HREE trends, however, in the bulk, the coarse and the fine fractions are sub-parallel. The variation in REE compositions together with textural diversity in the Piplia Kalan euclite indicates possible chemical heterogeneity through different petrogenetic processes. Earlier study, based on similar major and few minor element data among texturally different fractions stated that they formed co-genetically in a shallow intrusive body. It is to be noted that the differences in the trace-elements are good indicators of the heterogeneity in the source region, while the major-elements generally signify the fractionation effects during the course of melt crystallization as magma leaves the source region. The Sc and La content of Piplia Kalan is in the range of the Main group - N Laredo euclites, while both the coarse and fine fractions are within or near the range of the cumulate euclites. Interestingly earlier result reported Piplia Kalan as a non-cumulate euclite. The strong positive Eu-anomaly of the coarser fraction probably indicates contribution from plagioclase. The mirror image symmetric trend of the LREEs and MREEs of the coarse and fine fractions must be mutually related during their process of crystallization.

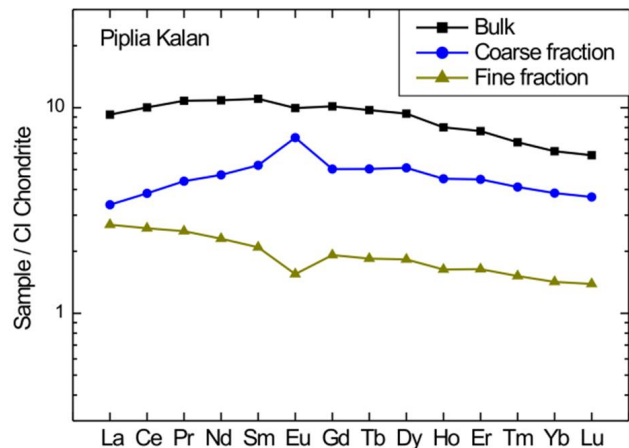


Figure 9 : REE abundances of bulk sample, and coarse and fine fractions of the euclite Piplia Kalan

(A. B. Sarbadhikari and M. S. Sisodia)

### Remote Sensing Data Analysis

#### Lobate flow features on pole-facing slope of craters in Alba Patera, Mars: Characterization of an ice-driven, moderate glacial process

A major outstanding question that remains to be understood is the nature of glacial environment existing between the moderate and minor glacial periods that led to formation of concentric crater flows (CCF) and gullies, i.e. between  $\sim 100-10$  Ma. We have therefore carried out morphological and topographical analysis of lobate flow features (LFFs)

emerging from the pole-facing walls of craters distributed within Alba Patera (between  $30^{\circ}$ - $60^{\circ}$  N and  $80^{\circ}$ - $140^{\circ}$  W) to report additional evidence for young, less moderate glaciation, a process not well documented on Mars. Our detailed investigation of LFFs revealed presence of polygonal cracks, moraine-like ridges, brain-terrain like texture, and ring mold crater that together confirmed its glacial origin. From the estimates of area occupied by LFFs spread over the crater floor, we could decipher that the depositional process has involved relatively excess amount of ice/snow in comparison to what was required for forming gullies (Figure 10).

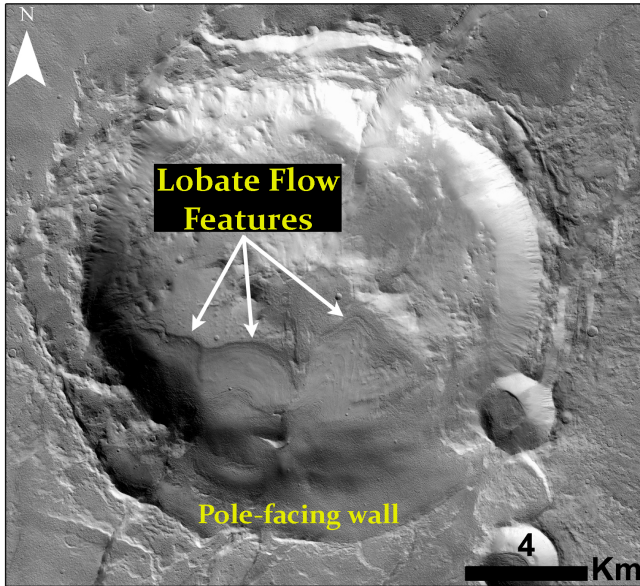


Figure 10 : Example of lobate flow features extending from the pole-facing wall of crater to its floor

Accordingly, its radial/unidirectional flow indicated that the required amount of ice/snow should have been relatively less than that involved in emplacement of CCF-like flows that completely filled the craters floor from all the sides. We support our interpretation over difference in amounts of ice from our crater size frequency distribution results, wherein it was found that LFFs typically formed in an intermediate period, i.e. between CCF and gullies (within  $\sim 100$ - $10$  Ma). Such a time gap on Mars possibly faced a significant change in accumulation extent and flow of glacial ice in its Late Amazonian history. In addition, LFFs presence has been abundant over the pole-facing wall of craters, which helped us to introduce the idea that the periods prior to gully formation accumulated excess ice/snow over the same pole-facing walls over which gullies preferred to form later in the recent glacial epochs with relatively less accumulation extents.

In the climatic perception, addition of LFFs into the Late Amazonian glacial history of Mars, i.e. between CCF and gully formation periods ( $\sim 100$ - $10$  Ma), envisages a scenario where prior to the period of melting of the minor amount of ice/snow trapped within alcoves, the moderately accumulated ice/snow mass has undergone sublimation from the pole-facing walls of craters. The climate during this  $\sim 90$  Ma which supported LFF formation recently changed to a phase in which the

accumulation extents of ice/snow significantly reduced and is confined to the small alcoves at certain locations during the last  $\sim 10$  Ma.

(R. K. Sinha, S. Vijayan and S. V. S. Murty)

### Association between Desiccation Polygons and Smectites on Mars: An Assessment through Morphological and Spectral Studies

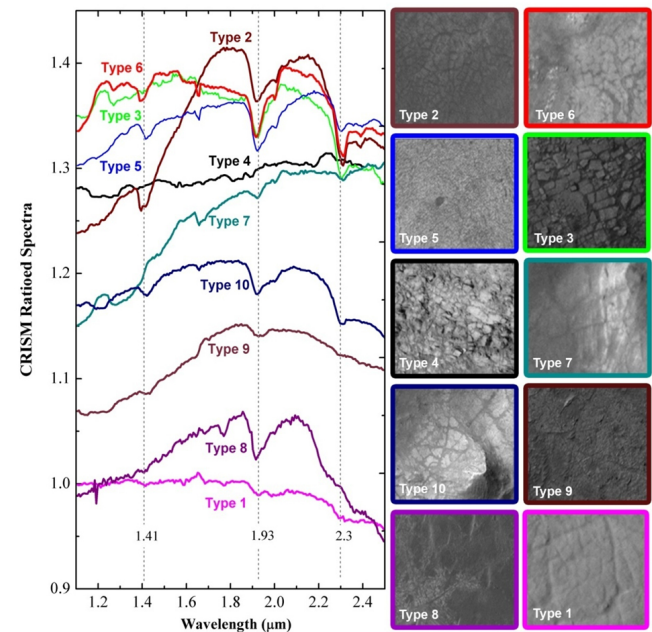


Figure 11 : Ten types of smectite exposures that display distinct polygonal morphology and spectral behavior.

We examined morphologic and spectral variations of desiccation polygons exposed or buried under the partial-to-thick dust cover using HiRISE and CRISM datasets. The prime focus of this study was to decipher and understand the correlation between smectite and polygons and to explore the extent to which the morphology of polygons buried under dust could indicate the presence of smectite. Twenty-four locations with definite presence of smectite were examined to segregate different types of polygons based on their size, texture, pattern, topographic-relief, and compaction. Spectroscopic analysis leads to map the variations in absorption strength and band center of smectites associated with different polygon types including partial-thick dust-covered polygons. Accordingly, we have categorized smectite-bearing polygons into ten types based on morphological analyses. Our results reveal that polygons laid after the periods of aqueous alteration were larger ( $\sim 50$ - $200$  m) than previously suggested (within  $\sim 30$  m). These large polygons were mostly dust-covered and spectrally bland in CRISM observations, but show signs of bulk silica in THEMIS DCS images (bands 6,4,2 and 9,6,4). It was found that the presence of desiccation polygons might not lead to a

one-to-one correlation with smectites, though in the absence of spectral information they may provide mineralogical insights to a certain extent. Nevertheless, there are certain differences between the textures of polygons associated with smectite and with other hydrous minerals in the vicinity. Moreover, the results tend to support that there are many more unexplored outcrops of smectite buried under the thick layers of dust as anticipated in the previous studies.

(I. Varatharajan, R. K. Sinha, S. Vijayan and S. V. S. Murty)

### Relationship between Morphometric parameters of LDA and Subsurface Ice

In the northern mid-latitudes of Mars, Lobate Debris Aprons (LDA) exist around elevated mesa/plateaus. The geomorphic and topographic relationships of these LDAs suggests that they formed by flow of ice and debris mixture away from the plateau during the past  $\sim 1$  Ga-100 Ma. Their geomorphic expression and restricted occurrence give evidence of accumulation of kilometer thick ice at certain depths in northern and southern mid-latitudes of Mars. Subsurface radar sounding of the apron extent has indicated that these deposits are composed mainly of water ice, which is preserved at shallow depths beneath the LDAs. The current presence of subsurface ice beneath LDAs and their surface geomorphic and topographic expressions have important implications for understanding the past climatic evolution, and for exploring the relationships in terms of overall morphological diversity and extents to which ice is detected beneath these diversified geomorphic units. In order to explain the consequences that led to compaction of ice into subsurface at different depths, we have investigated the surface and subsurface features by optical and microwave data sets respectively.

We have focused our study in Deuteronilus Mensae region of Mars ( $22.6^{\circ}\text{E}$ ,  $43.9^{\circ}\text{N}$ ). At first, we have tested the origin of LDAs and our detailed investigations substantiate the hypothesis that these LDAs are an outcome of down slope flow of debris-covered glaciers. Further, we have analyzed the role played by mesa orientation, surface morphometry, LDA extent and influence from proximal landforms in distributing ice at different extents in the subsurface. Over the LDA surface, we have noticed that areas having sublimation tills/pits, rugged/irregular morphology, etched surface etc. display weak radar subsurface reflections that correspond to comparatively lesser extent of ice with respect to areas having prominent LDA surface. Additionally, LDA surfaces with steep topography and thick deposits display presence of ice at deeper extents duly estimated from radar subsurface reflections, which we attribute to be related to the extents to which the LDA has developed. For all the mesa-LDA systems investigated in our study, we have noticed a positive correlation among the extents to which ice is detected in the subsurface and the pole-facing orientation of LDA surfaces. Our analysis has also attempted to resolve the extents of LDAs and presence of subsurface ice in those cases where a LDA from adjacent mesa has flown/overlapped with the pre-existing LDA in the direction of its flow. We estimate a

constant layer of subsurface ice at depth varying between -3500 to -3700 m to be existing in the Deuteronilus Mensae region of Mars.

(S. Chaudhary, R. R. Bharti, S. Mohan, S. Vijayan, R. K. Sinha and S. V. S. Murty)

### Multi layered ejecta craters on Mars: Role of volatile, crater-clusters and age

Images from Mars Global Surveyor (MGS) and Viking suggest that fresh impact craters on Mars are commonly surrounded by a layered or lobate ejecta morphology, in contrast to radial patterns seen around fresh craters on Mercury or Moon. The origin of these lobate morphologies can be explained as a result of impact and vaporization of subsurface volatiles or ejecta thrown into the thin Martian atmosphere. The observed diameter and latitudinal variations (Figure 12) of the ejecta morphologies is consistent with the subsurface volatile hypothesis.

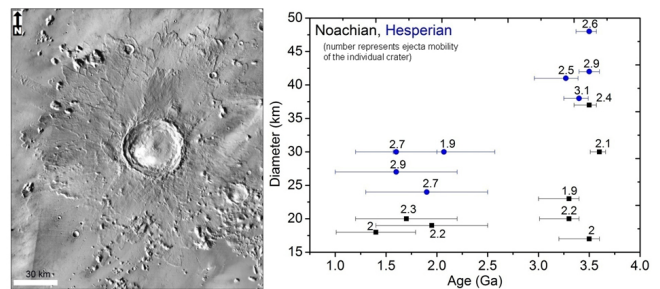


Figure 12 : MLE craters and the formation age of the craters on the Noachian and Hesperian surface.

Understanding of layered ejecta craters over different regions on Mars, in order to determine what differences in crater morphology may indicate about surface and subsurface composition, specifically in areas which may have contained volatiles (either as ice or liquid water) is most essential. The formation of layered ejecta craters in the equatorial regions suggests the role of volatile activity during the early period of Mars. In our study, we identified 366 multi layered ejecta (MLE) craters within  $\pm 30^{\circ}$  latitudes of northern (180 craters) and southern (186 craters) hemispheres. We find diverse trends between depth and diameter of these crater populations with respect to variations in the estimated values of ejecta mobility (EM) (range:  $\sim 1$ -3.5). The average EM value for all these craters corresponds to 2.3 with minor difference in the range of EM for craters distributed in similar latitudinal range within both the hemispheres, except for craters lying within  $\pm 5^{\circ}$ . We have noted large number of MLE craters with relatively higher EM over the host surfaces lying at elevation ranging from  $\sim -4$  to  $-1$  km (N-hemisphere) and  $\sim 0.5$ -3 km (S-hemisphere). We could identify four clusters (densely cratered regions, rugged and smooth plains, volcanic plains, and high and smooth lava plains) over which MLE craters having  $\text{EM} > 2.3$  are abundant, which could possibly decipher the role of subsurface volatiles distributed over those

regions. The best-fit ages for some of the potential MLE craters emplaced over diverse geologic settings of Noachian and Hesperian units reveal that the dominant period for emplacement of higher EM (>2.0) of MLE craters was early Hesperian (~ 3.5 Ga). In summary, the MLE craters formed predominantly from early Hesperian period, which marks the end of major volatile activity on Mars.

(S. Vijayan, R. K. Sinha and S. V. S Murty)

Recent volcanism on the Moon

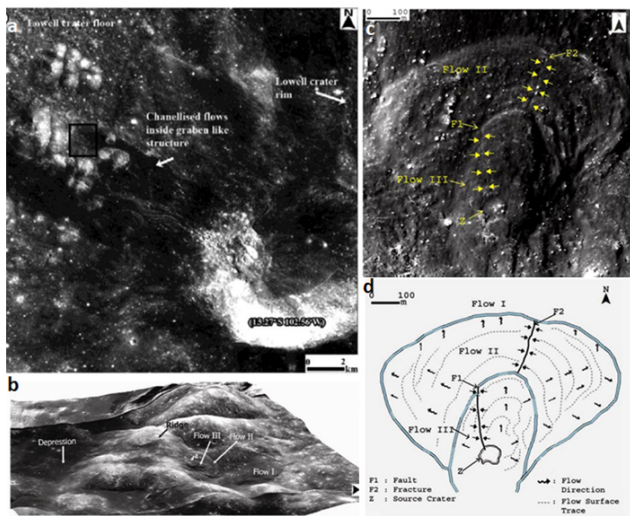


Figure 13 : a. A view of the Crater S and adjacent areas after Srivastava et al., 2013. Location of the small flows specifically studied here is indicated by dark rectangle; b. A perspective view generated from LROCNAC image data draped over Kaguya TC DTM; note that to the south of the three small flows under study, there occurs a ridge followed by a topographic depression; c. Enlarged view of the area from LROCNAC image M184196652L showing source crater Z and presence of a fault (F1) in flow-III and fracture (F2) in flow-II, both oriented such that they can be traced to crater Z. Interpretation map of the image shown in sub-section c.

It is generally believed that the Moon became internally dead ~ 1 Ga ago, and only  $\geq 1$  Ga volcanic flows occur on its surface forming the secondary crust. However, latest findings have indicated recent activity on the Moon represented by global presence of young thrust faults, exhalation of gases from the interior and also prediction of the presence of partially molten lower lunar mantle and core. We have used high-resolution datasets from NASA’s LRO, Kaguya of JAXA and ISRO’s Chandrayan-1 missions to examine the characteristics and origin of multiple relatively fresh, coaxial, superposed viscous flows spotted inside the Lowell crater on the far side of the Moon (Figure 13a). The topographic considerations apparently rule out the possibility of these melts being derived from nearby areas (Figure 13b). An associated likely source crater and tectonic structures (a fault and a fracture) of two different ages but emanating from the same crater and affecting different flows have also been located and exhibit a tectono-volcanic relationship (Figure 13c, 13d). These features provide evidences of likely volcanic activity in the region not too far in the past, are consistent with

recent results that the Moon may not be internally dead, and thus have implications to the thermal history and present-day geologic nature of the Moon.

*This work was carried out in collaboration with Dr. R.P. Gupta and Mr. R.K. Tiwari of IIT Roorkee.*

(N. Srivastava)

Geological evolution of Lowell crater region on the Moon

Remote sensing investigations of the Lowell crater region (a ~ 198 × 198 km<sup>2</sup> area in the north western quadrant of Orientale basin) using high resolution datasets from NASA’s LRO, Kaguya of JAXA and ISRO’s Chandrayan-1 missions have revealed topographical, morphological and spectral diversity of the region and age of selected units in the area. The observations and analyses have been used to assess a) pre - Lowell impact conditions such as target characteristics; b) the nature and time of Lowell impact event; and, c) the geological modifications of the region, thereafter. These inferences have been synthesized with general geology of Orientale basin and the Moon to derive evolutionary stages of the Lowell crater region. The rim-wall morphology and topography (Figure 14a), pronounced asymmetry in the ejecta distribution (Figure 14b) and crater density (Figure 14c) in selected parts of the proximal ejecta blanket suggests that the Lowell crater formed due to an oblique impact (~ 30° -45°) in the Montes Rook from the S-SW direction ~ 370 Ma ago. The lithological assemblages of the various components of the Lowell crater indicate that it would have excavated a deep-seated pre-existing (pre/ post Orientale) mafic pluton. It is possible that the sampled pluton was emplaced in the megareolith layer beneath thick layer of Orientale ejecta in the Montes Rook region. The region had witnessed volcanic eruptions as recently as ~ 2-10 Ma ago.

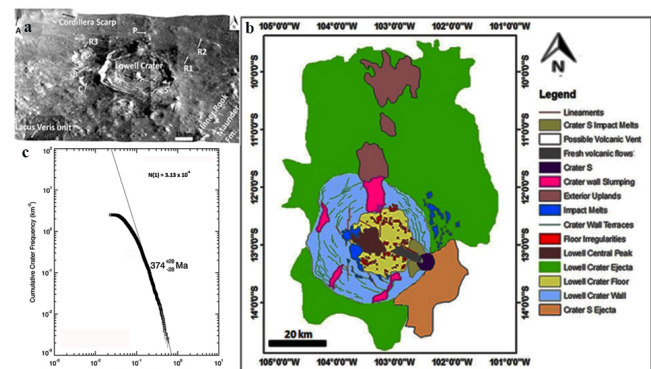


Figure 14 : a. A 3D view of the Lowell crater region from Kaguya DTM showing uneven topography and various geological units; b. Geomorphological map of the Lowell crater showing pronounced asymmetry in the exterior ejecta distribution; c. CSFD plot with fitted production function for craters counted in the proximal ejecta blanket of Lowell crater. Here, the production function and chronology function of Neukum et al. (2001) has been used to derive age of Lowell crater. 164 craters have been used in curve fitting and the estimated age is 374±28 Ma.

(N. Srivastava)

### Cabeus Crater Water Ice Content Retrieval Using Change-1 MRM Data

Study of a planetary surface can be carried out using remote sensing techniques from an orbiter. The microwave emission from an object is primarily dependent upon the temperature and dielectric properties of the object. Wherever water ice is present on the moon, its effective permittivity may be derived using mixture of water ice as well as the regolith, using standard models available in literature. We have simulated the microwave brightness temperature after considering the effective permittivity of the study region, based on the measured data of lunar soil stimulant JSC-1A and the pure ice in our laboratory. Microwave brightness temperature from Chang'e-1 has been used at the study point and water ice content has been retrieved in Cabeus crater of the moon. The results indicate that there is a possibility of water ice mixed with the regolith in the upper most layer whose depth is about 9 cm. The volume of water ice at the study point has been estimated as 2.9 %.

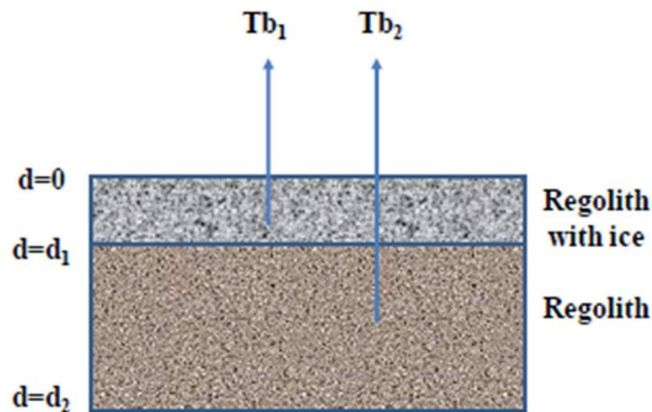


Figure 15 : Two layer lunar regolith model used in study

(J. P. Pabari and V. Patel)

### Clutter analysis tool for SHARAD radargram

There is always a surface and subsurface range ambiguity in Shallow Radar (SHARAD) onboard Mars Reconnaissance Orbiter (MRO) due to surface topography, material composition and the effect of ionosphere. So interpretation of radargram is not straight forward. To resolve this issue related to radargram analysis; we developed clutter analysis tool for SHARAD radargram for a given observation. It requires MOLA topography, SHARAD observation and hypothetical subsurface structure as inputs to generate a SHARAD expected response. An example is given (Biblis Tholus region) for illustration. Figure 16a shows the generated SHARAD radargram (clutter radargram). It gives an impression of subsurface reflection as in the original SHARAD radargram as shown in Figure 16b, but in reality it is a reflection of the crater walls. We can see the ground track of SHARAD on MOLA. T-T' is the SHARAD track and it is passing through lateral walls of crater. After analysis of clutter radargram it

becomes clear that these are the reflections of lateral walls of crater. So with the help of clutter radargram, we can interpret the SHARAD data to detect the genuine reflection from the subsurface.

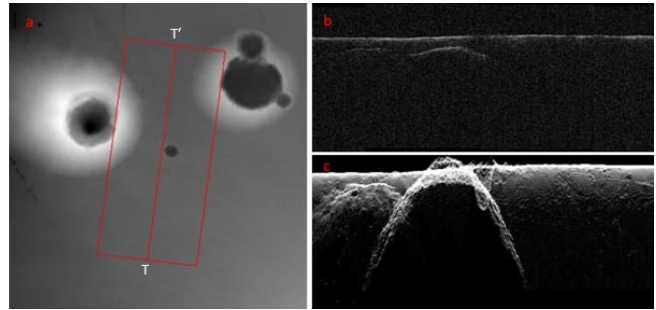


Figure 16 : (a) SHARAD ground track on MOLA, (b) Original SHARAD radargram (0193902) and (c) clutter radargram.

(R. R. Bharti)

### Payload Development

#### Alpha Particle X-ray Spectrometer on-board Chandrayaan-2 Rover

Alpha Particle X-ray Spectrometer (APXS) is one of two instruments onboard Chandrayaan-2 rover. The objective of the APXS instrument is to analyze several soil/rock samples along the rover traverse for the major elements with characteristic X-rays in 1 to 25 keV range. The working principle of APXS involves measuring the intensity of characteristic X-rays emitted from the sample due to Alpha Particle Induced X-ray Emission (PIXE) and X-ray fluorescence (XRF) processes using  $^{241}\text{Am}$  alpha source which allows us to determine elements from Na to Br, spanning the energy range of 0.9 to 16 keV.

Earlier, we planned to use  $^{244}\text{Cm}$  alpha source, but due to procurement problems, we plan to use  $^{241}\text{Am}$  source which has similar alpha and X-ray energies (Alpha particles at 5.4 MeV, X-rays at 14.3 keV, 17.9 keV). BARC will be preparing the source as per the activity requirements. The use of  $^{241}\text{Am}$  requires larger active area to achieve the desired source activity and also requires shielding around the source in three directions for safe handling due to the presence of 59.5 keV gamma ray line. Multi-layered shielding consisting of 2 mm thick gold (or depleted uranium), 1 mm thick silver and 0.1 mm thick copper is necessary to contain the radiation, and the XRF produced by the shielding material, thereby increasing the mass of the payload from the earlier estimate of 700 gm to 1 kg.

Based on our request, BARC has initiated two processes for making the sources: Electro deposition and Thermal diffusion. Using electro deposition technique, fabrication of source with high activity is not feasible as it requires larger area to achieve the desired source activity. Thermal diffusion technique is

shown to provide the required activity with the given area. Few samples were made using thermal diffusion technique and tested for the activity and spectral response by covering the front face of the source with Nickel coating to prevent leakage of radioactivity. It was shown that, when the Ni coating in-front of the source is  $\sim 5$  micron thick, containment of activity is achieved, but alpha spectrum is very poor. When the Ni layer thickness is reduced to  $\sim 2$  micron (desired), alpha spectrum is good but loose contamination is present. BARC has indicated that they are also attempting to fabricate the sources using deposition over Zirconium oxide to solve the issue of contamination. We also subsequently discussed to use Titanium foil of 3 micron thick in front of the source instead of direct Nickel coating to contain the contamination. To qualify the  $^{241}\text{Am}$  source made with thermal diffusion technique for APXS, we have received equivalent non-radioactive sources made using a similar technique. These dummy sources have been tested for Chandrayaan-2 vibration levels, and the thermo-vacuum test is under progress. The APXS package is modified to accommodate the new source configuration as shown in Fig 17. The Qualification Model PCBs were fabricated and tested individually for the performance.

*SAC, Ahmedabad is also involved for certain aspects of the payload developments.*

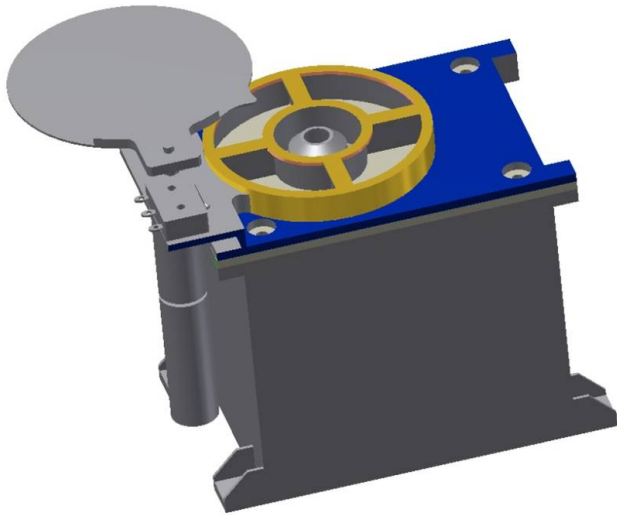


Figure 17 : Mechanical model of APXS accommodating new source configuration

**(M. Shanmugam, S. K. Goyal, A. Patel, T. Ladia, Y. B. Acharya, S. V. S. Murty and S. Vadawale)**

### Solar X-ray Monitor for Chandrayaan-2 Orbiter

As the flux of fluorescent X-ray lines from lunar surface is dependent on the flux and spectrum of the incident solar X-rays, it is essential to have simultaneous and accurate measurement of X-ray from both Moon and Sun. Thus a typical remote X-ray fluorescence experiment consists of two components, a Moon viewing X-ray detector (CLASS) to measure the fluorescent spectra and a Sun viewing X-ray detector (XSM) to measure direct solar X-ray spectra.

At PRL, we are involved in developing XSM payload for Chandrayaan-2 Orbiter.

XSM sensor package consists of SDD module coupled with Charge Sensitive Pre-Amplifier (CSPA), Shaping amplifier, HV supply for SDD module, controller for the peltier cooler and the moving mechanism. The XSM analog front end electronics include two independent channels of shaping amplifiers with two peaking times of 0.8 and 0.2 respectively. The slow channel is optimized for high energy resolution up to incident count rate of  $\sim 100$  k counts/s, where as the fast channel is used to independently count the total number of X-ray interactions on the detector so as to have proper dead time correction of the recorded X-ray spectrum. XSM processing electronics package consists of stack of two PCBs. The top PCB contains FPGA based digital control & data readout system and the bottom PCB contains DC-DC converter based payload powering, power On/Off circuits and driver circuits for linear motor based mechanism. It is also responsible for controlling the telemetry/tele-command and data handling interfaces with the spacecraft. The overall size of the XSM sensor package is about  $70 \times 140 \times 60$  mm<sup>3</sup> with mass of 600 gm and the size of processing electronics is  $130 \times 130 \times 45$  mm<sup>3</sup> with mass of  $\sim 900$  gm.

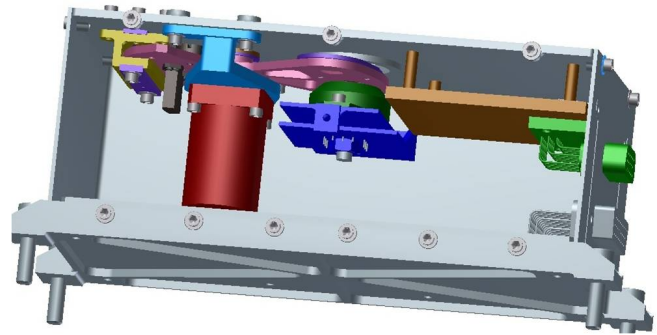


Figure 18 : XSM sensor package with stepper motor based mechanism

The lab model of the XSM instrument without motor based mechanism has been completed and tested for the performance requirements. The second preliminary design review of the XSM design has been completed and the mounting location of the XSM packages on Chandrayaan-2 spacecraft is finalized with clear FOV of  $\pm 45^\circ$  compared to the earlier requirement of  $\pm 55^\circ$ . The stepper motor based mechanism is finalized very recently and the XSM sensor package is modified accommodating the new mechanism and other thermal requirements as shown in Fig 18. The new PCB layout for both the packages has been designed and the fabrication of the same is in progress. A complete XSM model will be made by Aug. 2015 and subsequently, we will make qualification model of the payload.

*SAC, Ahmedabad is also involved in certain aspects of the payload developments.*

**(M. Shanmugam, A. Patel, S. K. Goyal, T. Ladia, Y. B. Acharya and S. Vadawale)**

### Aditya Solar wind Particle Experiment (ASPEX)

The uniqueness of solar studies from the Sun-Earth L1 Lagrangian point lies in the fact that it is outside the influence of the earth's magnetosphere and allows for unperturbed measurement of solar wind particles. The sun-earth line passes through the L1 point and L1 is therefore ideally located to study earth-bound solar wind particles and finally the L1 point offers an unhindered and continuous view of the sun. The ASPEX experiment onboard the Aditya mission consists of two particle analysers to take advantage of the unique location of the spacecraft at the L1 to carry out systematic and continuous observations of particle fluxes over an energy range spanning 100 eV to 5 MeV. The payload consists of two components to cover the entire energy range — the Solar Wind Ion Spectrometer (SWIS) covering the low energy range (100 eV to 20 keV) using an electrostatic analyser and the Supra Thermal Energetic Particle Spectrometer (STEPS) covering the high energy range (20 keV to 5 MeV) using solid state and scintillation detectors.

Though other experiments at the L1 Lagrangian point have measured particle fluxes and energies over the range covered by ASPEX, the uniqueness of our experiment lies in the fact that the SWIS package will have the ability to measure both the angular and energy distributions concurrently in addition to being able to separate protons,  $\alpha$ -particles and heavy ions. The STEPS package on the other hand will sample the solar wind along four different directions viz. along and opposite to the average Parker spiral direction at L1 and towards the ecliptic north and south poles. Time resolved energy spectral measurements of both protons and alpha particles from the four directions will provide one the ability to address the anisotropy in the energy distribution of particles in the direction of the Parker spiral vis-a-vis other directions. This, in turn, will help to trace the origin of supra-thermal particles which could not be explained by only solar wind propagation. It is to be noted that in addition to primary solar wind, planetary bow shocks, heliospheric current sheet, co-rotating interaction regions etc. are being conjectured to be potential processes that contribute to supra-thermal particles in the interplanetary medium.

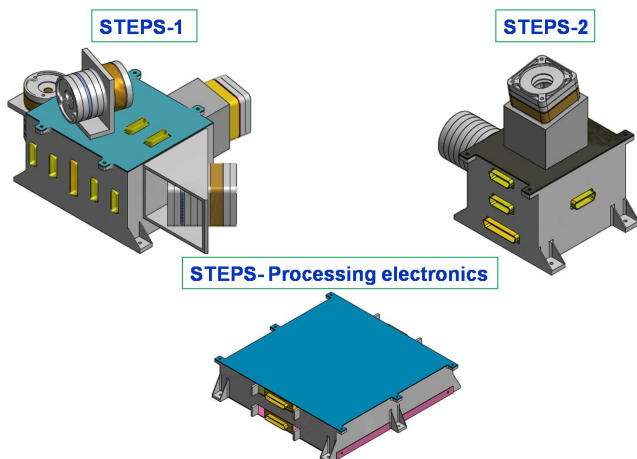


Figure 19 : Preliminary mechanical model of STEPS packages.

PLANEX is involved in developing full STEPS package and also the processing electronics of SWIS package with software. The STEPS part of the ASPEX is configured with three packages namely STEPS-1, STEPS-2 and processing electronics. The preliminary mechanical designs of these packages are shown in Fig 19. The preliminary design and testing of the electronics subsystems are in progress using the off-the-shelf SiPIN detector and scintillator with SiPM as shown in Fig 20. It is shown that the developed front-end electronics of SiPIN diode provides the desired low energy threshold of  $< 20$  keV. The actual detectors are ordered and expected to be available in few months time.

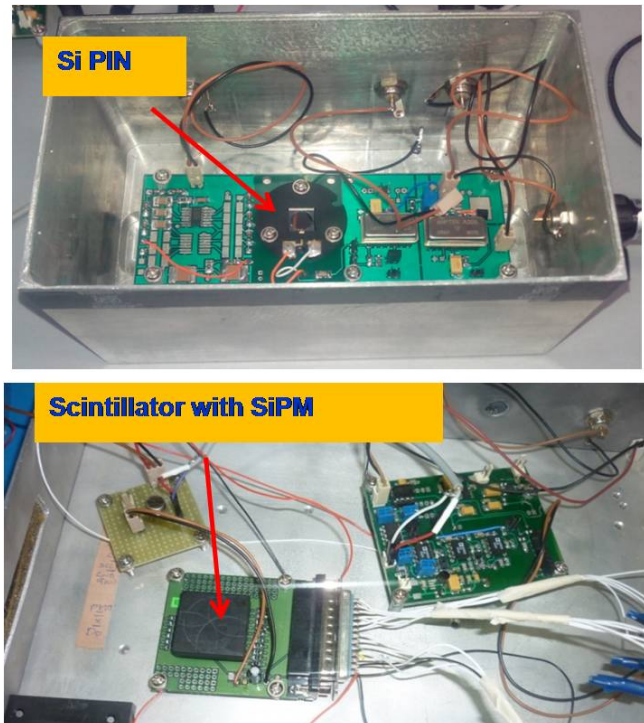


Figure 20 : Breadboard version of SiPIN and Scintillator with SiPM front-end readout electronics.

SAC, Ahmedabad is also involved in certain aspects of the payload developments.

(M. Shanmugam, S. K. Goyal, A. Patel, T. Ladia, D. Patel, A. K. Khan and S. Vadawale)

### Development of a $\text{LaBr}_3:\text{Ce}$ Gamma Ray Spectrometer

High energy ( $>100$  keV) gamma ray spectroscopy is an important technique for remote sensing studies of chemical composition of planetary surfaces, and has been used to study surface composition of the Moon, Mars and Asteroids at various spatial resolutions. We have developed a  $\text{LaBr}_3:\text{Ce}$  based gamma ray spectrometer in Thaltej Campus, PRL. A 3 inch  $\text{LaBr}_3:\text{Ce}$  crystal was procured along with a 3.5 inch PMT and a preamplifier to check its suitability. After testing of performance of the detector, different individual subsystems

including shaping amplifier, peak detection, analog to digital conversion and high voltage unit were developed. Once these modules were tested individually, we developed the bread board model for shaping-peak detector-ADC. The  $\text{LaBr}_3:\text{Ce}$  detector requires high voltage of 720 V DC, which is being presently provided using an Aplab High Voltage unit. The bread board model of high voltage module is under progress. The shaping amplifier and peak detector were designed with hybrid components. Tests were performed using a shaping time of  $3 \mu\text{s}$ . This unit has been set to the gain of  $\sim 3.5$ , and is used to change and amplify the pre-amplifier output to Gaussian shaped output. We have used a parallel ADC of 12-bit resolution. The control signal for peak detector and ADC are being generated through FPGA program. The realization of the newer version of bread board model for processing electronics has been done by using Actel A3PE250 FPGA. Along with the FPGA, the processing electronics sub-system consists of a discriminator unit for synchronization of shaping pulses with digital acquisition, a reference generator unit for ADC, line drivers for the signal compatibility of FPGA and 12-bits parallel ADC. The ADC digitized data is given to Data Acquisition Software developed in Labview. With the data acquisition software, we are able to get the counts from the bread-board model.

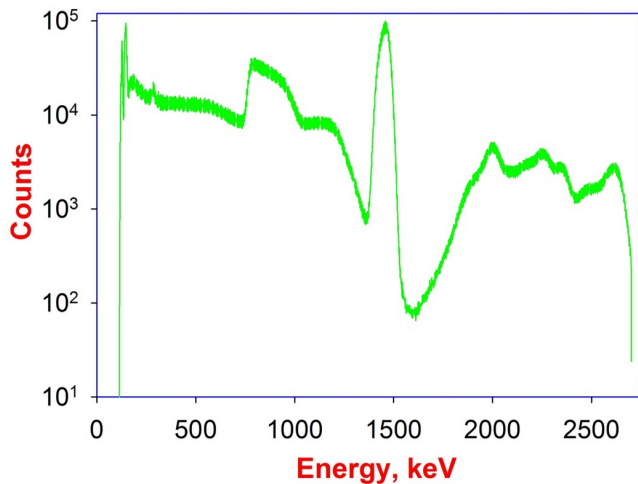


Figure 21 : Gamma ray background spectra obtained using  $\text{LaBr}_3:\text{Ce}$  gamma ray spectrometer

The energy resolution of the  $\text{LaBr}_3:\text{Ce}$  gamma ray spectrometer using front-end and processing electronics developed in-house has been measured at 511 and 1274 keV to be 4.1 % and 2.5 % respectively. The intrinsic activity count-rate for our  $3'' \times 3''$   $\text{LaBr}_3:\text{Ce}$  gamma ray spectrometer is  $\sim 61 \text{ counts s}^{-1}$  (i.e.  $\sim 0.18 \text{ counts s}^{-1} \text{ cm}^{-3}$ ) for the 40 K energy window (1400-1520 keV) and  $\sim 3.4 \text{ counts s}^{-1}$  for the  $^{232}\text{Th}$  (2550-2700 keV) energy window. Although this large intrinsic activity of the  $\text{LaBr}_3:\text{Ce}$  crystal inhibits estimation of the concentrations of Th and K, our attempts using a NaI (TI) gamma ray spectrometer (with electronics developed inhouse) were more successful. The Thorium concentration of US-110 was estimated to be  $\sim 11.4 \text{ ppm}$  and is within 14 % of the 13.2 ppm value determined using a HPGe gamma ray spectrometer. The K concentration of US-110 was estimated to be 0.87 %, and is within  $\sim 10 \%$

of the 0.78 % value determined independently using a HPGe gamma ray spectrometer.

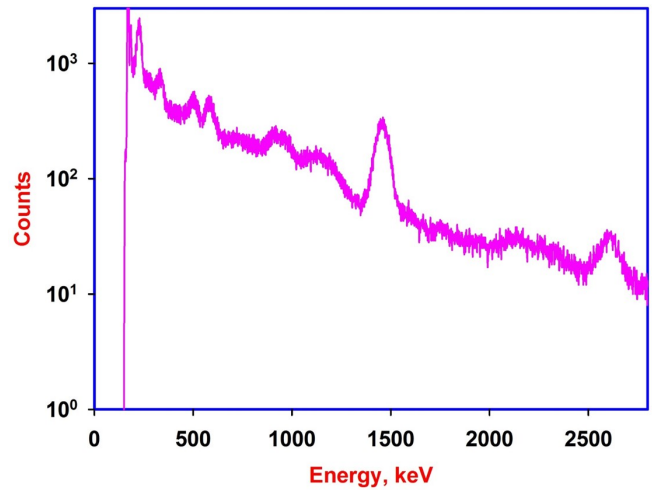


Figure 22 : Gamma ray spectra obtained using NaI (TI) gamma ray spectrometer from the sample STD-110

(D. K. Panda, D. Banerjee, S. K. Goyal, A. Patel and A. D. Shukla)

**Moon Electrostatic Potential and Dust Analyser (MESDA) for Future Lunar Lander**

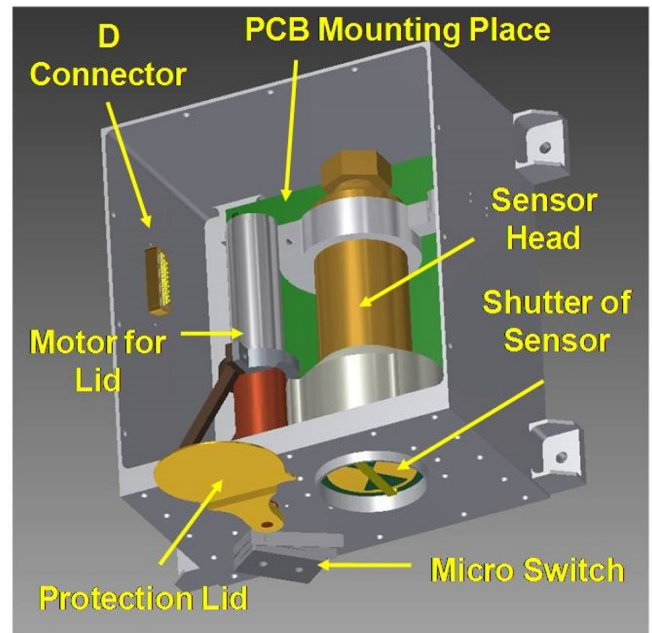


Figure 23 : Mechanical package of LSPD.

To study the lunar electrostatic and dust environment, a Moon Electrostatic Potential and Dust Analyser (MESDA) payload has been proposed for future lunar lander. There are two

independent instruments in the MESDA payload viz., Lunar Surface Potential Detector (LSPD) and Lunar Dust Detector (LDD). The LSPD will measure lunar electrostatic surface potential at  $\sim 50$  mm from the lunar surface, whereas the LDD will detect the presence of charged dust particles at a similar altitude using an IDT (Inter Digitated Transducer) dust sensor. Design and development of sensors and front end electronics for both the instruments have been initiated. A prototype of the LSPD has been developed and initial measurements have been carried out in the laboratory. Mechanical package of LSPD is shown in Figure 23. For the LDD, an IDT dust sensor with one micron inter-electrode spacing has been fabricated. A snapshot of one micron IDT is shown in Figure 24.

*The IDT was fabricated in collaboration with Micro-Electronics Group (MEG) at SAC, Ahmedabad.*

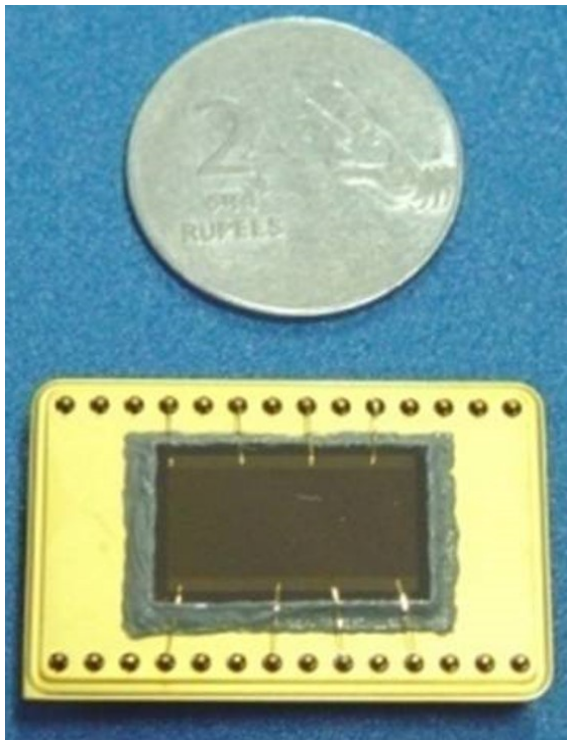


Figure 24 : Photograph of one micron IDT

(J. P. Pabari, S. K. Goyal, D. Banerjee and Y. B. Acharya)

### Modelling of Electrostatic Potential and Dust Levitation on Moon

The surfaces of airless, non-magnetized bodies in our solar system are directly exposed to the solar wind plasma and UV radiation, causing dust grains on their surface to be electrically charged. These electric fields can exceed surface forces (cohesion) and gravity for small dust particles, causing electrostatic dust levitation. Dust levitation almost certainly occurs within a few meters of the lunar surface, creating "lunar horizon glow" as captured by Surveyor lander camera during

early lunar missions. To study the lunar electrostatic and dust environment, a Moon Electrostatic Potential and Dust Analyzer (MESDA) payload has been proposed for future lunar lander. Model calculations have been carried out to understand the nature of the dust environment on the moon. Figure 25a shows the possible lunar surface potential as a function of plasma electron density and plasma electron temperature, while Figure 25b depicts the maximum radius of charged dust particle as a function of plasma electron density and plasma electron temperature.

The daytime results show that the lunar surface potential during high solar activity is  $\sim 20$  V, with the maximum radius of levitated dust particles being around 1 micron.

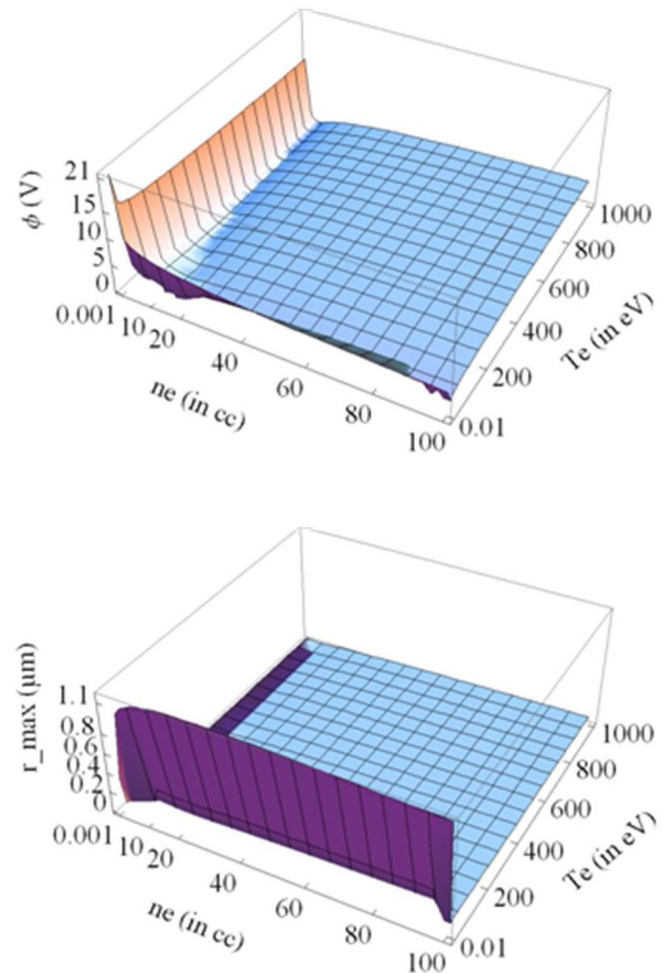


Figure 25 : Dependence of daytime (a) lunar surface potential and (b) maximum radius of lifted particles on plasma parameters.

(J. P. Pabari and D. Banerjee)

### "ChaSTE" Payload for Chandrayaan-2 Lander - Prototype development

Heat exchange within the uppermost surface regolith of the Moon is necessary for obtaining an equilibrium balance

between external (solar) and internal (due to radioactive decay and accretion) heat fluxes and helps in estimating the thermal state of the Moon. To derive more accurate lunar thermal models, it is very important to know the extent and the spatial variability of the insulating fluffy layer and thermal properties of the upper 100-200 mm of the lunar regolith. "Chandra's Surface Thermophysical Experiment (CHaSTE)" on-board Chandrayaan-2 lander proposes an in situ measurement of temperature profile on the lunar surface to derive the vertical temperature gradient up to a depth of 100 mm near the polar region, and In-situ measurements of thermal conductivity of lunar regolith. Chaste is being developed jointly by the Physical Research Laboratory (PRL), and the Space Physics Laboratory (SPL), VSSC, Trivandrum. Sensor Evaluation, Front-end electronics development and Probe integration and testing are being carried out by PRL while the probe material, back-end electronics and deployment mechanism development are done at SPL-VSSC.

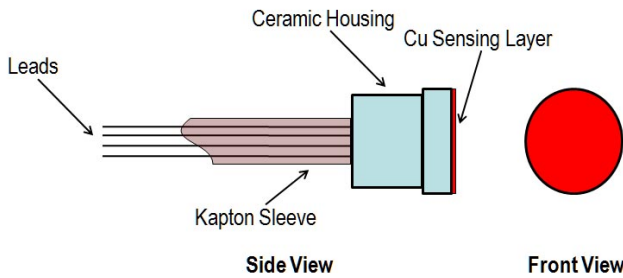
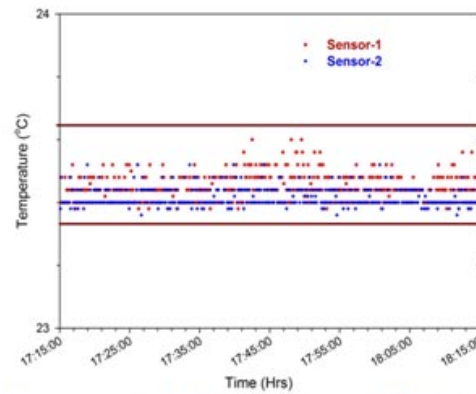


Figure 26 : Schematic view of the custom designed PRT proposed to be used for ChaSTE payload

The proof of concept of the proposed experiment was designed and demonstrated earlier. A laboratory prototype of the payload has been designed and tested recently. A series of designs/schemes for the front-end electronics were considered and evaluated for their functionality. A number of Platinum Resistance Thermocouple (PRT) sensors have been evaluated for their performance and it was finally found that a custom-made PRT is required to meet the scientific requirements of the payload. Accordingly a design for a custom-developed 4-wire PRT sensor has been made and sample sensors are under procurement. A schematic view of the custom-designed PRT proposed to be used for ChaSTE payload is shown in Figure 26. More than half a dozen configurations and four ADCs have been evaluated in detail for developing the ChaSTE front-end electronics in order to select the most optimized one. Optimization studies were carried out to reduce the harness length and overall number of components. After a series of experiments, a final configuration for front-end electronics for 8-channel temperature measurement has been finally arrived at. In order to optimize it further and reduction of harness, the front-end electronics of ChaSTE has been re-designed using an analog multiplexing scheme using a serial ADC. Bread board model

of the same is designed and its performance was evaluated. Bread board models of command/control electronics was also designed for testing the integrated system using a 4-wire PRT. Experiments under various conditions (Ambient and Vacuum) were conducted to characterise the performance of the designed prototype of CHaSTE. Results of these experiments are shown in Figure 27. The top panel shows the achieved stability of measurement (within 0.3°C) using the designed prototype. The bottom panel shows the result of the experiment carried out in active mode with the bare probe (placed inside a vacuum chamber), which clearly depicts the role of ambient environment in inhibiting the heat flow along the length of the probe. All the components to be used were identified and the respective circuits are being designed and evaluated to move on to the Engineering Model development of the payload. Material development and deployment mechanism are being developed at SPL.



Measurement of soil temperature - Stability test

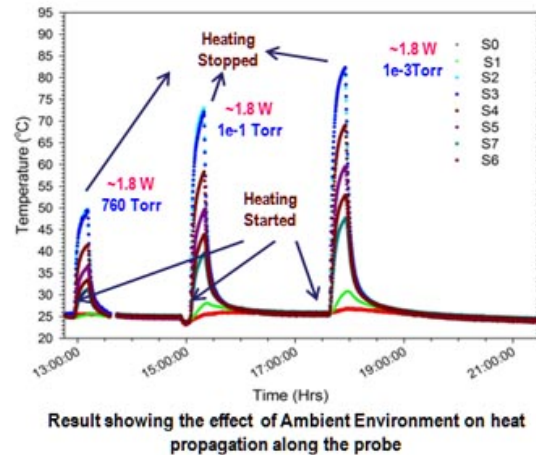


Figure 27 : Measurement of soil temperature stability test, plot showing effect of ambient environment on heat propagation along the probe

(K. Durga Prasad, V. Mani Teja, V. K. Rai and S. V. S. Murty)

# SCIENCE at PRL

## Space and Atmospheric Sciences

### **Spatiotemporal characteristics of aerosols in India: Observations and model simulations**

An evaluation of ground-based and satellite measurements combined with chemical transport models is necessary to obtain and understand a complete picture of optical, physical and chemical characteristics of aerosols. With this objective, an analysis of aerosol characteristics measured using sun photometers, satellites (Moderate Resolution Imaging Spectroradiometer (MODIS) and Multiangle Imaging SpectroRadiometer (MISR), and simulated using global aerosol models (Global Ozone Chemistry Aerosol Radiation and Transport (GOCART) and Model for Ozone and Related Tracers (MOZART)) over six distinctly different environments in India (Ahmedabad, Jaipur, Delhi, Nainital, Kanpur and Gandhi College), a regional aerosol hot spot was performed. Model AODs are lower than measured AODs, and exhibit a winter low and summer high, while features in measured AODs differ. Differences between measured and model AODs arise due to absence of seasonal cycle in model AODs which occurs mainly due to lack of proper representation of aerosol emissions and not due to meteorology. In model

simulations dust (>40% during premonsoon) and sulfate (40% during monsoon) contribute the maximum to total AOD. Model derived single scattering albedo (SSA) is higher than measured SSA over the study locations because simulated BC is low (Figure 1). The inter-annual variability in model derived SSA is lower than model-observation differences in SSA. The intra-regional variation in model AODs is lower than that of MODIS AODs. Sea salt contributes ~10% to total AOD during monsoon only over Peninsular and west Central India. The underestimation of AODs by GOCART and MOZART and space-time differences with observations strongly favors improving the emission inventories of aerosol sources and removal mechanisms of aerosols in the models. Results from present study can serve as inputs to tune models because not only total AODs but also species AODs, and their amount need to be properly simulated in order to reduce the uncertainty in radiative and climate impact of aerosols.

*This work was done in collaboration with Dr. S. Kedia, Centre for Development of Advanced Computing, Pune.*

**(S. Ramachandran and V. Sheel)**

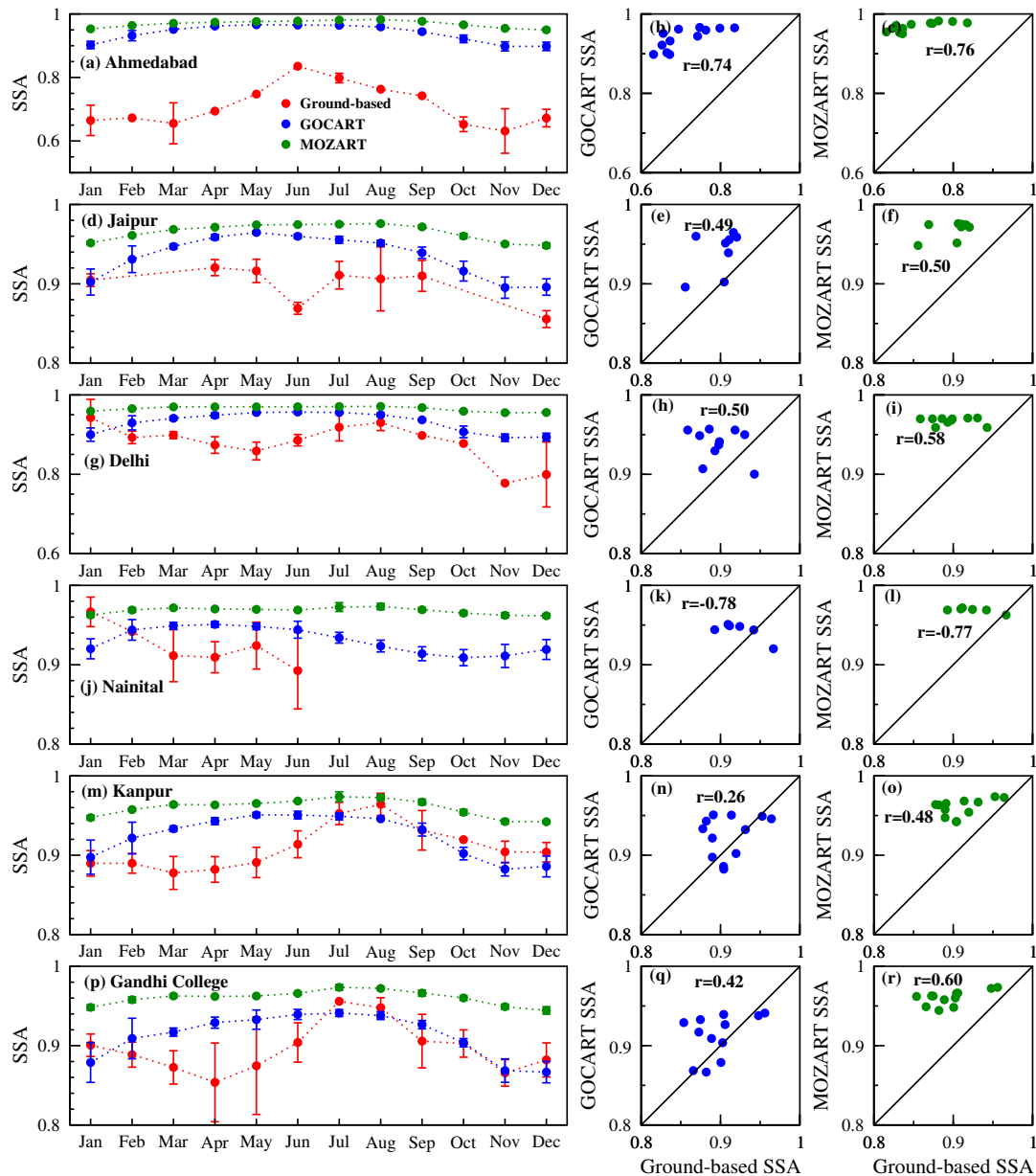


Figure 1 : Monthly mean 550 nm SSA from ground-based observations in comparison with GOCART and MOZART model derived AODs over (a) Ahmedabad, (d) Jaipur, (g) Delhi, (j) Nainital, (m) Kanpur and (p) Gandhi College. Scatterplots of ground-based vs. GOCART SSA, and ground-based vs. MOZART SSA over Ahmedabad (b, c), Jaipur (e, f), Delhi (h, i), Nainital (k, l), Kanpur (n, o) and Gandhi College (q, r) respectively. Solid line represents the 1:1 ratio.

**Aerosol mixing state: Radiative implications**

Anthropogenic aerosols can significantly influence the energy balance of the Earth-atmosphere system on regional scales. In this context, it is important to assess the extent to which aerosols of different types mix and can modify the aerosol composition which in turn can influence the radiative effects over different environments. Aerosol mixing states are determined over four environmentally distinct locations (Karachi, Gwangju, Osaka and Singapore) in Asia using measured spectral aerosol optical properties and optical properties model. Aerosol optical depth (AOD), single

scattering albedo (SSA) and asymmetry parameter (g) exhibit spectral, spatial and temporal variations. Aerosol mixing states exhibit large spatial and temporal variations consistent with aerosol characteristics and aerosol type over each location. External mixing of aerosol species is unable to reproduce the observed SSA over Asia, thus, providing a strong evidence that aerosols exist in a mixed state. Mineral dust (MD) (core)-Black carbon (BC) (shell) is one of the most preferred aerosol mixing states. Over locations influenced by biomass burning aerosols BC (core)-water soluble (WS, shell) is a preferred mixing state, while dust gets coated by anthropogenic aerosols (BC, WS) over urban regions influenced by dust. MD (core)-sea salt (shell) mixing is

found over Gwangju corroborating the observations. Aerosol radiative forcing exhibits large seasonal and spatial variations consistent with features seen in aerosol optical properties and mixing states. TOA forcing is less negative/positive for external mixing scenario because of lower SSA. Aerosol radiative forcing in Karachi is a factor of 2 higher when compared to Gwangju, Osaka and Singapore. Results from the study emphasize the need to include regionally and temporally varying mixing states in global climate models to ascertain more accurately the radiative effects of aerosols in contrast to prescribing a mixing state across the globe.

*This work was done in collaboration with Dr. R. Srivastava, Indian Centre for Climate and Societal Impacts Research, Mandvi.*

(S. Ramachandran)

### Simultaneous measurements of columnar aerosol characteristics and size distribution over urban region

Aerosols in urban region regions exhibit unique characteristics because of the dominant influence of manmade emissions, and their significant variations in terms of number density, season and location when compared to aerosols in the remote continental and maritime regions. Measurements of aerosol characteristics over urban regions, where absorbing aerosols are dominant are very crucial in order to reduce the uncertainty in aerosol radiative effects. Simultaneous measurements of columnar aerosol characteristics and size distribution have been conducted over Ahmedabad, an urban region in western India in 2014 using skyradiometer that measures direct solar irradiance and radiances. Aerosol optical depth (AOD) exhibits less diurnal and stronger monthly variations in Ahmedabad. 500 nm AOD is in the range of 0.2 to 0.6. Annual mean AOD in Ahmedabad is 0.46, which is lower than 0.62 (Kanpur) and 0.66 (Gandhi College) in Indo-Gangetic Plain. Single scattering albedo (SSA) at 500 nm is lowest in December ( $<0.85$ ) and highest in June (0.92) consistent with features seen in refractive index and type of aerosols that dominate the atmosphere in these months. Seasonal variations in SSA are similar to those reported over Kanpur, Gandhi College, Pune and Beijing. Asymmetry parameter at 500 nm is 0.696 and shows less variation (0.018).

Ångström wavelength exponent ( $\alpha$ ) is  $>1$  during winter and  $<1$  in premonsoon and monsoon. Near similar values of  $\alpha$  and  $\alpha_2 - \alpha_1$  suggest that curvatures in AOD spectra are not significant during 2014. Aerosol volume size distribution is bimodal peaking below and above  $0.6 \mu\text{m}$ . The coarse mode volume contributes more than 60% to the total aerosol volume and peaks in June ( $>85\%$ ) (Figure 2). The coarse mode dominance is supported by the lower  $\alpha$  value in Ahmedabad (0.75) when compared to Kanpur (0.96). These results can serve as regional representative for an urban regime in south Asia providing a better knowledge in understanding dissimilarities between observations and model climatology of aerosol characteristics.

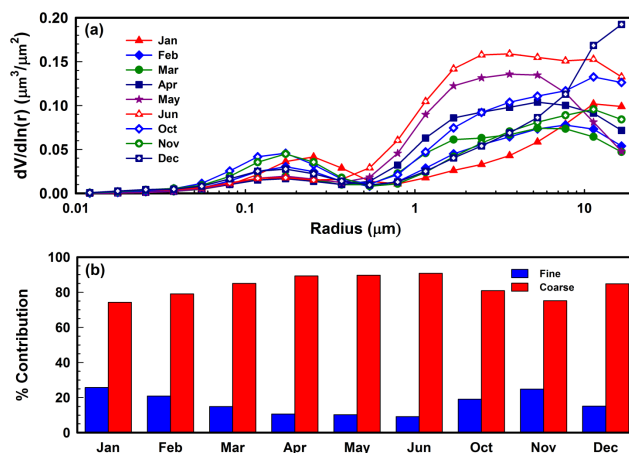


Figure 2 : Monthly mean aerosol volume size distribution during 2014 over Ahmedabad. (b) Monthly mean percentage contribution of fine and coarse mode aerosols to the total aerosol volume.

(S. Ramachandran and T. A. Rajesh)

### Aerosol optical properties over different environments in western India

Seasonal variability in aerosol optical depth (AOD) at 555 nm and aerosol Ångström exponent ( $\alpha$ ) at 443-860 nm are investigated over an urban location (Ahmedabad,  $23.03^{\circ}\text{N}$ ,  $72.55^{\circ}\text{E}$ , 55 m AMSL), a high altitude remote site (Gurushikhar,  $24.65^{\circ}\text{N}$ ,  $72.78^{\circ}\text{E}$ , 1680 m AMSL) and a desert location (Rann of Kutch,  $24.09^{\circ}\text{N}$ ,  $70.64^{\circ}\text{E}$ , 0 m AMSL) in western India from Multi-angle Imaging Spectroradiometer (MISR) data during January 2000 to December 2013. AOD and  $\alpha$  are found to exhibit large seasonal and spatial variations indicating varying aerosol size over the western India region (Figure 3).

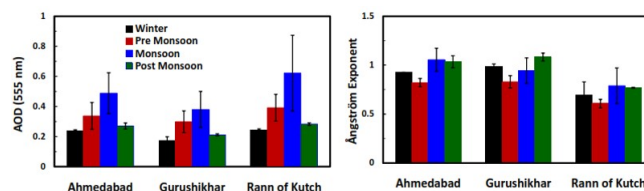


Figure 3 : Seasonal mean variation in (a) 555 nm aerosol optical depth and (b) Ångström exponent (443-860 nm) over Ahmedabad, Gurushikhar and Rann of Kutch calculated from MISR during 2000-2013. Vertical bars represent  $\pm 1\sigma$  deviation from the mean.

Annual mean AOD over Rann of Kutch is highest  $0.39 (\pm 0.17)$  due to the dominance of dust in the fine and coarse mode. The seasonal mean  $\alpha$  is lowest  $0.7 (\pm 0.1)$  over Rann of Kutch while  $\alpha$  is relatively higher  $1.0 (\pm 0.1)$  and over Ahmedabad  $\alpha$  lies between 0.7 and 1.0. The AOD spectra were analyzed by a second order polynomial fit to quantify the dominant mode of aerosols.

The percentage of AOD spectra having  $\alpha_2 - \alpha_1 < 1$  and  $1 < \alpha_2 - \alpha_1 < 2$  over Ahmedabad, Gurushikhar and Rann of Kutch are 75%, 60% & 100% and 25%, 40% & 0% respectively, which reveals the dominance of coarse mode aerosols over the entire western Indian region and exclusively so over Rann of Kutch. AOD species contribution over western India from GOCART model also supports the dominance of dust aerosols which are in coarse mode. These results on the seasonal variability in aerosol properties over distinctly different environments will be useful in modeling the radiative effects of aerosols.

(T. A. Rajesh and S. Ramachandran)

### High time and mass resolved PTR-TOF-MS measurements of VOCs at an urban site of India during winter season

High time and mass-resolved measurements of volatile organic compounds (VOCs) using the Proton Transfer Reaction Time Of Flight Mass Spectrometer (PTR-TOF-MS) were made at an urban site of Ahmedabad, India during winter 2013. The daily levels of oxygenated-VOCs (OVOCs) and aromatics were in the ranges of 3.5-37 ppbv and 0.85-23 ppbv, respectively with OVOCs accounted for up to 80% of total measured VOCs (Figure 4).

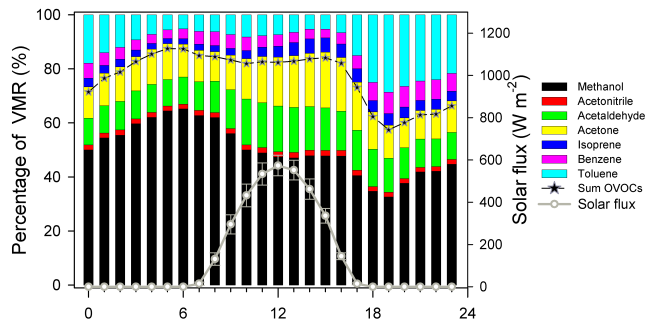


Figure 4 : Average diurnal variation of relative contribution (%) of each VOCs and sum of OVOCs to the total measured VOCs using PTR-TOF-MS in ambient air at Ahmedabad during winter season.

Impact of long-range transport from the polluted Indo-Gangetic Plain and clean Thar desert was observed during the episodes of high and low VOCs, respectively. VOCs exhibited strong diurnal variations with peaks during morning and evening hours and lowest in afternoon. Relatively elevated aromatics during evening hours coincided with the lowest-OVOCs indicating influence of fresh vehicular emissions. Emission ratios of isoprene and OVOCs with respect to benzene followed the diurnal cycles of temperature and solar flux indicating role of biogenic and photochemical processes, respectively. Correlation study of VOCs with benzene suggests major contribution from anthropogenic and also from biogenic and secondary sources to some extent. The higher emissions ratios of  $\Delta$ methanol/ $\Delta$ acetonitrile correspond to the episodes of long-range transport from biomass burning sources located in the Indo-Gangetic Plain

(IGP). In addition to the pattern of emission, the diurnal and day-to-day variations of VOCs were influenced by the local meteorological conditions and depth of planetary boundary layer (PBL).

(L. K. Sahu and P. Saxena)

### Ambient concentrations of benzene and toluene at different sites of Ahmedabad city: Analysis using TD-GC-FID instrument

Ambient mass concentrations of benzene and toluene were measured at different road junctions of Ahmedabad city, India during the months of March and April 2015. A Thermal Desorption-Gas Chromatography-Flame Ionization Detector (TD-GC-FID) technique was used for the analysis of two aromatic volatile organic compounds (VOCs) in air samples. In each of both 132 feet ring road (inner) and S P ring road (outer) six sites were selected to investigate the spatial variation of benzene and toluene. The mass concentrations of benzene and toluene show strong site-to-site and day-to-day variation. The average mass concentration of benzene varied in the ranges of 11-32  $\mu\text{gm}^{-3}$  and 3.6-12  $\mu\text{gm}^{-3}$  along the 132 feet road and S P ring road, respectively. The mass concentration of toluene varied in the ranges of 32-102  $\mu\text{gm}^{-3}$  and 5.2-22  $\mu\text{gm}^{-3}$  along the 132 feet road and S P ring road, respectively. The mass concentrations of benzene and toluene show good correlation suggesting their common emission sources (mostly vehicular). However, the  $\Delta$ Toluene/ $\Delta$ Benzene slopes of  $\sim 4.0$  along both roads are slightly higher than the typical values (1.5-3.5) reported from vehicular sources. The higher slopes of  $\Delta$ Toluene/ $\Delta$ Benzene are due to the emissions of VOCs also from industrial and other non-traffic sources. The daytime data shows significantly lower mass concentrations of both the compounds and lower  $\Delta$ Toluene/ $\Delta$ Benzene slope of  $\sim 2$  indicating the role of photochemical aging. The mass concentrations of aromatic VOCs show significant reduction during the weekend (Sunday) at most of the sites along both the roads. This study highlights the large spatio-temporal variability of aromatic VOCs within an urban domain and also the limitations of relying on a single unless air masses from different sources are well mixed.

(D. Pal, R. Yadav, J. Munkhtur, L. K. Sahu)

### Variability of surface $\text{O}_3$ , CO and $\text{NO}_x$ at an urban site of western India: Role of long-range transport and local meteorology

The data from the continuous in-situ measurements of surface ozone ( $\text{O}_3$ ), carbon monoxide (CO) and oxides of nitrogen ( $\text{NO}_x$ ) at an urban site, Udaipur in India during years 2011-2012 have been analyzed. Diurnal variation of  $\text{O}_3$  exhibited highest values in the afternoon hours and lower values from evening till early morning. The mixing ratios of CO and  $\text{NO}_x$  show peaks during morning and evening rush hours and lowest in the afternoon hours.

The magnitude of diurnal concentrations varied from season-to-season showing strong variability during winter and pre-monsoon seasons while weak during monsoon season. The daily means of  $O_3$ , CO and  $NO_x$  varied in the ranges of 5-53 ppbv, 121-842 ppbv and 3-29 ppbv, respectively. The mixing ratios of  $O_3$  were highest and lowest during the pre-monsoon and monsoon seasons, respectively. While both CO and  $NO_x$  showed highest and lowest values during the winter and monsoon seasons, respectively. The mixing ratios of CO and  $NO_x$  show good correlations during winter and pre-monsoon seasons, while poor correlation in the monsoon season. The emission ratio of  $\Delta CO/\Delta NO_x$  showed large seasonal variability indicating the influence of distinct air masses. The levels of CO and  $NO_x$  decreased with the increasing wind speed, while  $O_3$  tended to increase with the wind speed. Overall, the diurnal pattern of trace gases is controlled by the local emission, photochemistry and planetary boundary layer (PBL) depth, while seasonality of trace gases were governed by the long-range transport. The back-trajectory calculation suggests the transport of continental pollutants during winter and pre-monsoon seasons while cleaner marine air during monsoon.

*This work is done in collaboration with G. Beig, IITM, Pune and S. N. A. Jaaffrey, MLSU, Udaipur.*

(R. Yadav and L. K. Sahu)

### Transport effects on the vertical distribution of carbon monoxide in the troposphere over selected Indian regions

Variability in the vertical distribution of carbon monoxide in the troposphere over five selected urban regions (Delhi, Dibrugarh, Ahmedabad, Hyderabad and Trivandrum) representing different ecosystems in India has been studied using the available satellite (MOPITT) data for the period of 13 years (2001-2014). The average monthly results show highest CO mixing ratios at 900 hPa in the winter and lowest levels in monsoon season over all the regions. These results also show an enhancement in CO mixing ratios over all the study regions around 300 hPa mostly during the Indian summer monsoon, due to the convective lifting of the local air from surface to this height. However, significant increase in the levels of CO around 300 hPa over Ahmedabad and over Hyderabad and Trivandrum lying in the southern part of India has been found, for the first time, even in other seasons. The variability in the mixing ratios of CO indicate the dominance of seasonal variation compared to the inter-annual variability at 900 hPa over all the study regions, whereas the inter-annual variation dominates around 300 hPa mostly over Ahmedabad, Hyderabad and Trivandrum. Results from two chemistry-transport models have been compared with the observations. These models capture significantly the basic features like seasonal variations of CO, regional events (biomass burning effects) and increase in CO around 300 hPa due to the deep convection during monsoon. However, the observed elevated CO levels during other seasons are only partially captured.

*This work is in collaboration with A. Pozzer, Max Planck*

*Institute for Chemistry, Mainz, Germany.*

(N. Chandra, S. Venkataramani, V. Sheel and S. Lal)

### Emission characteristics of $CO_2$ and CO using simultaneous in situ measurements at Ahmedabad

In situ measurements of carbon dioxide ( $CO_2$ ), carbon monoxide (CO) and methane ( $CH_4$ ) are being made at PRL, Ahmedabad using a laser based cavity ring down spectrometer since November, 2013. These simultaneous measurements not only provide useful information about their variability but correlations among them and their slopes provide important information on the characteristics of emission sources. Atmospheric  $CO_2$  is emitted from different types of combustion sources along with number of trace gases in particular CO. The emissions of  $CO_2$  and CO depend strongly on the combustion efficiency of fuels. CO is the main product of incomplete combustion. Consequently, the slope ( $\Delta CO/\Delta CO_2$ ) will be high ( $>30$  ppbv/ppmv) in incomplete combustion sources and low in complete combustion sources ( $<20$  ppbv/ppmv). Further,  $CO_2$  levels are also affected by biospheric activities (photosynthesis and respiration). Hence, the correlations and slopes among them will vary with the time of the day also.

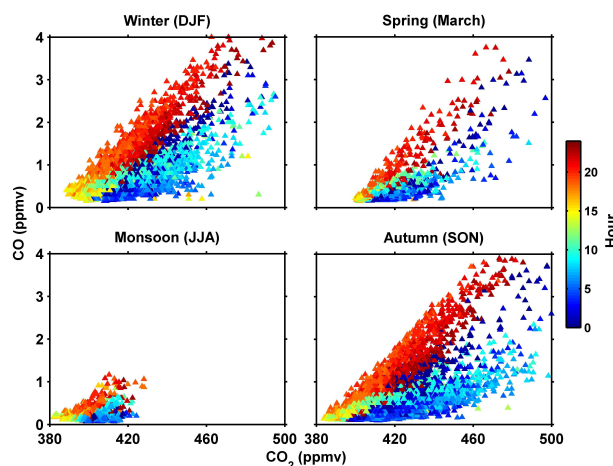


Figure 5 : Correlations of CO- $CO_2$  in different seasons from the simultaneous observations of these species at Ahmedabad during November, 2013- February, 2014 and July, 2014 - March, 2015. Colours show different hours.

Figure 5 shows correlations of CO with  $CO_2$  for the four different seasons using hourly average data. The data for spring season corresponds to March month only. In general, we get higher slopes (40 - 45 ppbv/ppmv) and very good correlations ( $> 0.80$ ) during the evening rush hours, which remains high till mid night in all the four seasons mainly due to the influence of common emission sources i.e. vehicular emissions. Lowest slopes ( $\Delta CO/\Delta CO_2$ ) have been observed during afternoon hours due to photosynthesis process effectively controlling  $CO_2$  levels. Consequently, we get poor CO- $CO_2$  correlation in afternoon hours.

(N. Chandra, S. Venkataramani and S. Lal)

### **Evaluation of a global model simulated AODs with AERONET and MODIS observations**

Aerosol optical properties vary widely globally due to their short residence times and the large variability in their composition and size resulting from varying sources. Nevertheless, there are not too many studies on climate model simulations with aerosols coupled as part of chemistry. In this study, we used the three-dimensional global atmospheric chemistry transport model MOZART (Model for Ozone And Related chemical Tracers) to simulate Aerosol Optical Depths (AOD) and compare with observations from MODIS (Moderate Resolution Imaging Spectroradiometer, Level 3) and AERONET (AEROSOL ROBOTIC NETWORK, Level-2) at regional and global scales for the period 2000-2007. Model and observations show intense aerosol burden over the parts of the world where developing countries are located. On a regional scale, varying features are noted for different regions depending upon geographic topography, regional emissions and weather conditions. MOZART captures the general features observed in AERONET and MODIS fairly well, however in biomass burning dominated regions (Central South America, South Africa and North Australia) it underestimates the observed AOD. In industrial regions (North Europe and Mediterranean) MOZART overestimates and over dust dominant regions (Saharan Africa, Middle East and East Asia) the model AODs are comparable to AERONET and MODIS observations. Over eastern North America there is weak agreement between model and observations (nearly anti-phase relation), the discrepancies likely resulting from uncertainties in emission inventories. Therefore, there is a need to update emission inventories and parameterization of physical processes in model simulation.

*This work is done in collaboration with R. P. Guleria, G. B. Pant Institute of Himalayan Environment and Development, Kullu.*

**(V. Sheel and S. Ramachandran)**

### **Variability of tropospheric carbon monoxide over Hyderabad based on aircraft observations and models**

The spatio-temporal variations of carbon monoxide (CO) were analysed over a tropical urban site, Hyderabad, with the help of vertical profiles from the MOZAIC aircraft observations, MACC reanalysis and two chemical transport model simulations (MOZART and MRI-CCM2) for the years 2006-2008. In the lower troposphere, the CO mixing ratio showed strong seasonality, with higher levels ( $> 300$  ppbv) during the winter and pre-monsoon seasons associated with a stable anti-cyclonic circulation, while lower CO values (up to 100 ppbv) were observed in the monsoon season. In the planetary boundary layer (PBL), the seasonal distribution of CO shows the impact of both local meteorology and emissions. While the PBL CO is predominantly influenced by strong winds, bringing regional background air from marine and biomass burning regions, under calm conditions CO levels are elevated by local emissions. On the other hand, in the free troposphere, seasonal variation reflects

the impact of long-range transport associated with the ITCZ and biomass burning. The inter-annual variations were mainly due to transition from El Nio to La Niña conditions. The overall modified normalized mean biases (normalization based on the observed and model mean values) with respect to the observed CO profiles, were lower for the MACC reanalysis than the MOZART and MRI-CCM2 models. The CO in the PBL region was consistently underestimated by MACC reanalysis during all the seasons, while MOZART and MRI-CCM2 show both positive and negative biases depending on the season.

**(V. Sheel and L. K. Sahu)**

### **Mesospheric turbulence studies from rocket-radar at Indian low latitudes**

A comprehensive study is made on radar scattering cross section of mesospheric echoes and mesospheric turbulence parameters based on several days of observations made during the two coordinated rocket-radar campaigns, one in July 2004 and another in April 2005, meant for studying mesospheric turbulence. Radar scattering cross section showed large local time and day-to-day variability with values as low as  $3.1 \times 10^{-18} \text{ m}^{-1}$  and as high as  $1 \times 10^{-14} \text{ m}^{-1}$  and the median values were in the range of  $4.4 \times 10^{-18} - 4.7 \times 10^{-16} \text{ m}^{-1}$ . Echoes connected with the low value of scattering cross section could be detected only when a long radar pulse width was used. Turbulence parameters were found to vary remarkably with time of the day and also from one day to another. In July, the turbulent kinetic energy (TKE) dissipation rate, outer scale and inner scale of turbulence were in the range of 0.08-150 mW/kg, 33-1500 m, and 1.9-50 m, respectively, with median values in the range of 5-52 mW/kg, 293-977 m, and 2-31 m, respectively. In April, these estimates were in the range of 0.9-69 mW/kg, 38-1081 m, and 4-21 m, respectively, with median values in the range of 1-12 mW/kg, 140-378 m, and 8-13 m, respectively. These parameters are found to agree quite well with those estimated from rocket-borne observations, which were in the range of 4-117 mW/kg, 220-1475 m, and 15-31 m, respectively, in July and 2-36 mW/kg, 170-680 m, and 17-37 m, respectively, in April. Interestingly, the inner and outer scales estimated using both radar and rocket observations agree exceedingly well with model values. These results are compared in detail with those reported from low, middle and high latitudes including model.

*This work was done in collaboration with D. Selvaraj and A. K. Patra, NARL, Gadanki and U. Das, National Central University, Taiwan.*

**(H. Chandra and H. S. S. Sinha)**

### **Equatorial electrojet**

Forty years of geomagnetic data from two stations in the Indian region, Trivandrum (TRD), located near the magnetic

equator and Alibag (ABG), located away from the magnetic equator for the period 1958-1998 were examined to study the daily ranges in H at TRD and ABG and in the strength of the equatorial electrojet (EEJ), obtained from the differences in the ranges at the two stations. Diurnal and month to month variations in H were studied over the 40 years for the two stations and also for EEJ. The annual mean ranges in H show linear increases with sunspot number ( $R_z$ ) and vary from 65 nT to 140 nT at TRD, 30 nT to 70 nT at ABG and from 40 nT to 72 nT for the EEJ. The rate of increase in H is faster at TRD than at ABG. Seasonal variations show equinoctial maxima for the range in H at TRD and in EEJ during the months of April and October. The range of H at ABG shows, in addition to maxima during April and October, a weak secondary maximum during June-July. During the months of June-July the range of H at ABG is stronger than that of EEJ. The occurrence of the afternoon counter electrojet is highest during low sunspot years and seasonally, during the June-solstices.

(R. G. Rastogi, H. Chandra, P. Janardhan and R. Shah)

#### Effect of cyclone Nilofar on upper atmospheric wave dynamics inferred from optical observations from Gurushikhar, Mt. Abu

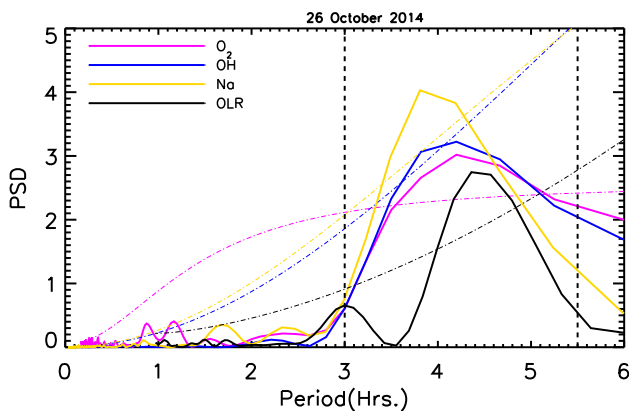


Figure 6 : Periodicity of  $O_2$ , OH, & Na airglow intensities and OLR for 26 October 2014. Notably, coherency in wave period of around 4-hours in all these emission intensities can be seen during cyclonic activity of Nilofar.

It is expected that strong cyclonic convections in the lower atmosphere have far reaching consequences on the upper atmospheric neutral dynamics through wave propagation. However, there have not been many instances to obtain unambiguous experimental evidence for the same. The cyclone Nilofar that occurred in the Arabian Sea during October 25-31, in 2014 provided such an opportunity as its effect extended to the proximity of Gurushikhar, where continuous optical observations are going on at the PRL's optical aeronomy observatory.  $O_2$  (0-1), OH (6-2), and Na nightglow emissions that emanate from mesospheric altitudes (87-94 km) were measured using NIRIS (Near infrared imaging spectrograph) and CMAP (CCD-based multiwavelength airglow photometer). Wave characteristics

have been obtained for all the nights of observation during October and November 2014. Interestingly, only on 26 October 2014 a coherency in wave periods of all these emission intensities has been noted, which was around 4-hours suggesting a strong common source of excitation that had potentially affected all these optical emissions. In order to explore the possibility of lower atmosphere in providing such a source of excitation during Nilofar, Outgoing Longwave Radiation (OLR) flux obtained from Kalpana-1 satellite (for one degree south of Gurushikhar) has been used as a tracer. Similar wave analysis as employed for optical emissions has been performed on OLR flux as well. Strikingly, it is noted that OLR flux too shows a strong periodicity at 4.3 hours, which is nearly coherent with those of mesospheric emissions, (Figure 6) which adds credence to the possibility of the convective activity due to cyclone Nilofar as the source. To resolve time period localization of this period, wavelet analyses have been performed which show the OLR 4.3-hour period to be localized a few hours prior to those observed in the optical emissions, and this time difference has been attributed to the propagation time of the waves from the ground to  $\sim 90$  km altitude. This result provides a clear signature of the effect of tropical cyclone Nilofar on upper atmospheric dynamics and presents an unambiguous evidence for the effect of cyclones in the troposphere to affect the upper atmospheric behaviour.

(R. P. Singh and D. Pallamraju)

#### Investigations on mesospheric dynamics using $O_2$ and OH airglow emission intensity and temperature variability

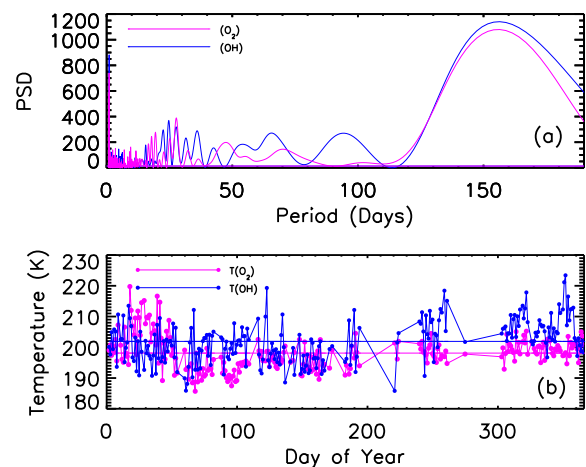


Figure 7 : (a) Power spectral density of OH and  $O_2$  emission intensities for the year 2013 showing common periodicities. (b) Nightly mean temperature at OH and  $O_2$  emission altitudes in mesosphere.

It is well known that planetary waves, gravity waves and tides play a crucial role in the behaviour of mesosphere lower thermosphere (MLT) structure and dynamics. In order to understand and quantify the primary cause of the variability of MLT region, long-term observations are extremely important. Analyses of an years (2013) data of  $O_2$  (0-1) and OH (6-2) mesospheric emission intensities (originating from  $\sim 94$  and 87 km) as obtained from Near infrared imaging spectrograph (NIRIS) from Gurushikhar, Mount Abu, ( $24.6^\circ N$ ,  $72.8^\circ E$ )

and the temperatures at these respective altitudes have resulted in some new findings on the mesospheric behavior. Lomb-Scargle periodograms of emission intensities for this year are shown in Figure 7.

It can be noted that semi-annual oscillation is the most dominant in both the emissions. In addition to several other periodicities in these emission intensities, it is striking to note that there are periods of planetary wave scales such as quasi-16 day, 27, and 30 days which are common to both the emissions. Some of them, such as 27-day are also present in solar flux variation. The daily mean mesospheric temperatures ( $T(O_2)$  and  $T(OH)$ ) are shown in Figure 7. It can be seen that the  $T(O_2)$  is, in general, lower than the  $T(OH)$  indicating that the mesopause layer is above the height of  $O_2$  emission layer (94 km). However, there are occasions during which  $O_2$  temperatures are greater than that of OH, which is possible if (i) the mesopause height reduces below the 94 km (the typical height of the  $O_2$  emissions), or (ii) there are mesospheric temperature inversions. It is to be also noted that in this year this feature has been observed for nearly 20 continuous nights. It needs to be investigated if any of the features mentioned above can be operative for such long duration.

(R. P. Singh and D. Pallamraju)

**Symmetric and asymmetric behavior in dayglow emission intensities**

Systematic investigations of daytime optical airglow emissions over a low-latitude location, Hyderabad (Geographic: 17.5° N, 78.5° E; Geomagnetic: 8.6° N, 151.8° E) that originate from multiple altitudes over a long period of time revealed symmetric and asymmetric variations (with respect to local noon) in their intensities. The emissions are OI 557.7 nm (originates at ~ 130 km above the surface of the earth), OI 630.0 (~230 km) and OI 777.4 nm (peak of F-layer). Such a behavior in the emission intensity variations can be brought out by changes in either the equatorial electrodynamics or neutral winds (or both), that alter the atmospheric processes that produce these emissions. Our investigations revealed several cases of all these factors contributing to the observed variability. Spectral and zonal scale sizes were analyzed on all these days separately. Statistically, it is seen that the number of smaller period gravity waves (periodicities less than 20 minutes) is larger on days with asymmetric behavior. Further, the zonal scale sizes tend to be longer on the days with asymmetric behavior.

*This work is done in collaboration with T. Vijayalakshmi and M. Anjireddi, JNTUH.*

(D. K. Karan, D. Pallamraju, and K. A. Phadke)

**Two-dimensional wave structure in the daytime upper atmosphere at different altitudes obtained for the first time**

The importance of neutral wave dynamics of the daytime upper atmosphere in modulating the atmospheric processes is well recognized. However, the ability to obtain such information at high cadence requires large field-of-view measurements from ground-based instrumentation. Multiwavelength Imaging Echelle Spectrograph (MISE) provides such possibility wherein systematic measurements of dayglow emission intensities at three different wavelengths are being obtained from the optical observatory at JNTU, Hyderabad. Being a slit spectrograph, it is possible to obtain the scale sizes of waves along the orientation of the slit. In a special campaign mode operation, MISE was operated in orthogonal directions sequentially to obtain the zonal and meridional components of the wave structure. From this information, resultant horizontal scale sizes and orientation of these waves at the three (emission) altitudes were obtained as a function of time and are shown in Figure 8.

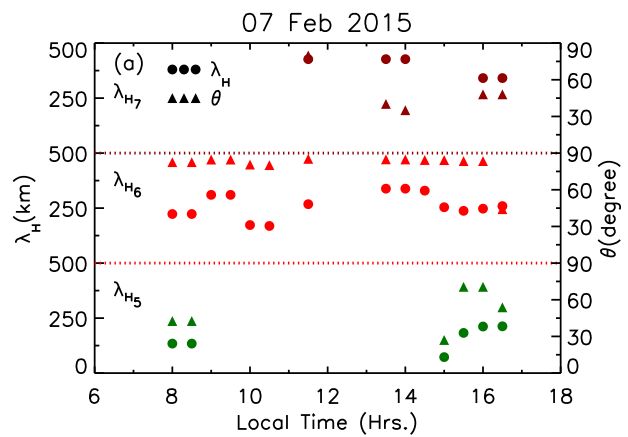


Figure 8 : Horizontal scale sizes  $\lambda_H$  at three different emission altitudes and their orientations ( $\theta$ ) on one day derived from zonal and meridional observations from MISE.

Thus, a synoptic picture of two-dimensional wave structure at three different altitudes has been generated as shown in Figure 9.

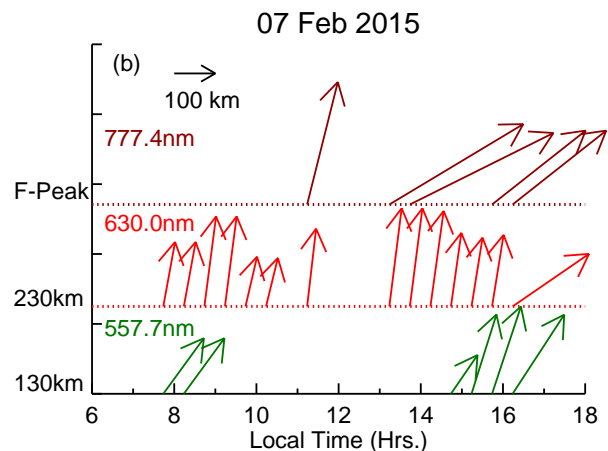


Figure 9 : A synoptic picture of horizontal scale sizes along with their orientations.

This feature has opened up a new dimension in the investigation of daytime upper atmospheric dynamics and has the potential of providing answers to several intriguing aspects of atmospheric coupling processes, may it be from lower below or due to geomagnetic disturbances.

(D. Pallamraju, D. K. Karan, K. A. Phadke)

### Gravity waves in the thermosphere: Solar activity dependence

A statistical study of the thermospheric gravity waves has been carried out using multiwavelength daytime oxygen airglow emission intensity and equatorial electrojet (EEJ) strength data, which originate from four different altitude regions of the thermosphere. The thermospheric daytime oxygen airglow emission intensities at wavelengths 557.7, 630.0, and 777.4 nm, obtained during January to March period in the three years 2011-2013, have been used. The percentage number of days in which waves with spectral periods in the gravity wave range have occurred are found to be greater for the relatively higher solar activity duration (in 2013) compared to that of low solar activity (in 2011). This observation is explained to be due to the altering background atmospheric density and temperature (that vary with solar activity), which, in turn, influences the propagation and dissipation of waves. Moreover, the higher frequency gravity waves (of periods between Brunt-Vaisala to 30 min) have been found to be present in greater numbers in the thermosphere compared to that of low-and-moderate frequency gravity waves (of periods 30-60 min). This behavior in the frequency selection by ambient conditions at thermospheric altitude is in accordance with earlier theoretical and simulation works. The ratios of high- to low-frequency occurrences have also been found to be greater in higher solar activity period of 2013 compared to that of the relatively low solar activity period of 2011. These results thus provide experimental evidence to the earlier simulation works suggesting similar behavior, as found here, for thermospheric gravity waves.

*This work is done in collaboration with B. Veenadhari, IIG, Mumbai, T. Vijaya Lakshmi and M. Anji Reddy, Jawaharlal Nehru Technological University, Hyderabad, and S. Chakrabarti, U. Massachusetts Lowell, USA.*

(F. I. Laskar and D. Pallamraju)

### Evidence for sudden stratospheric warming induced meridional circulation in the mesosphere thermosphere system

Oxygen dayglow emissions at multiple wavelengths that emanate from different heights (from around 130 km to peak altitude of the ionospheric F region) over a low-latitude location showed systematic enhancements in intensities throughout the daytime hours during four sudden stratospheric warming (SSW) events that occurred in the years 2010-2013. The lower thermospheric temperatures at

120 km obtained from the Sounding of the Atmosphere using Broadband Emission Radiometry instrument are found to be enhanced during SSW events at arctic latitudes and show a gradient with a decrease toward low-latitudes.

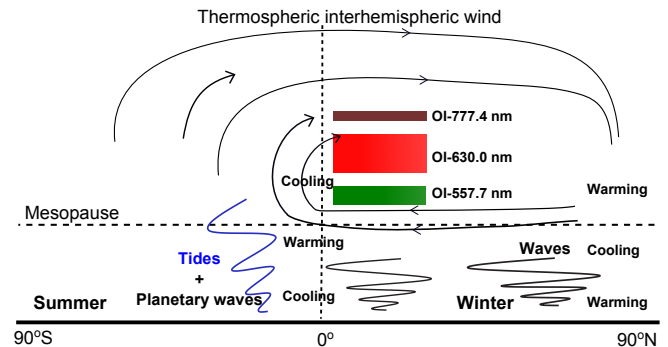


Figure 10 : A simplistic schematic depicting the SSW-time additional meridional circulation cell that is proposed in the mesosphere thermosphere system. The lines with arrowheads represent the direction and path of the winds. The dominant species in the lower thermosphere are transported with the wind through wind-induced diffusion. Due to this oxygen-rich air from high-to-low-latitude thermosphere all the low-latitude thermospheric oxygen emission intensities show simultaneous enhancement. The horizontal color bars show the representative altitudes from where the oxygen emissions originate.

During these events, the Thermosphere - Ionosphere - Mesosphere Energetics and Dynamics Doppler Interferometer measurements showed equatorward winds in the mesosphere lower thermosphere (MLT) altitudes over high-latitudes. Both the high-latitude lower thermospheric temperature enhancements and the MLT region equatorward winds occur nearly simultaneously with the observed enhancements in the atomic oxygen dayglow emission intensities at all the wavelengths over low-latitudes. Based on these measurements and other supporting information, it is proposed that a new cell of meridional circulation in the MLT winds is set up during SSW events, which enables transport of atomic oxygen from high-to-low latitudes. Such an additional contribution of oxygen density over low-latitudes interacts with lower thermospheric daytime dynamics in that region and is attributed to be the cause for the observed enhancement in the oxygen daytime optical emission intensities over low-latitudes. This circulation is summarized by a schematic in Figure 10.

(F. I. Laskar and D. Pallamraju)

### Solar-Terrestrial interactions in the high-latitude ionosphere

The solar wind and associated interplanetary magnetic field impinging on the Earth's magnetosphere can lead to a variety of processes in the magnetosphere-ionosphere (M-I) system which include geomagnetic storms and substorms. There have been earlier works towards understanding the relationship between source (solar wind) and response function (magnetospheric activity). However, one of the primary challenges for space weather research community is to quantitatively predict the state of the M-I system due to varying solar conditions. In order to achieve that, in the

present analysis the epsilon parameter ( $\epsilon$ ) and the auroral electrojet index (AE) have been considered as tracers of solar wind energy and magnetospheric activity. From analyses of four years of data (2010-13) it has been shown that for all geomagnetic disturbances, there is a consistent behavior in the temporal variation of both the  $\epsilon$  and AE, albeit with some time difference, which is due to propagation of solar wind from the ACE satellite location at L1 point to the auroral electrojet altitudes in the Earth's upper atmosphere. This time difference consists of two parts, (i) a laminar frictionless flow from LI to the Earth's magnetopause, and (ii) the from magnetopause to the auroral electrojet heights, wherein several acceleration/deceleration processes take place. Empirical relationships have been obtained for these time durations with respect to the solar wind speeds. These results not only advance the understanding of the state of magnetosphere associated with direct solar wind energy input but also are required for space weather applications.

(S. Yadav and D. Pallamraju)

#### **Evidence for tropospheric wind shear excitation of high-phase-speed gravity waves reaching the mesosphere using ray-tracing technique**

Sources and propagation characteristics of high frequency gravity waves observed in the mesosphere using OH airglow emissions from Gadanki (13.5° N, 79.2° E) and balloon-borne OI 297.2 nm emissions from Hyderabad (17.5° N, 78.5° E) are investigated using reverse ray tracing method. Wave amplitudes are also traced back, including both radiative and diffusive damping. The ray tracing is performed using background temperature and wind data obtained from the MSISE-90 and HWM-07 models, respectively. ERA-Interim products are utilized for constructing background parameters corresponding to the meteorological conditions of the observations. With the reverse ray-tracing method, the source locations for nine wave events could be identified to be in the upper troposphere, whereas for five other events the waves were found to be terminated in the mesosphere. Uncertainty in locating the terminal points of wave events in the horizontal direction is estimated to be within 50-100 km and 150-300 km for Gadanki and Hyderabad wave events, respectively. This uncertainty arises mainly due to non-consideration of the day-to-day variability in the tidal amplitudes. Prevailing conditions at the terminal points for each of the 14 events are provided. As no convection in-and-around the terminal points is noticed it is unlikely that it is the source. Interestingly, large vertical shears ( $\sim 9 \text{ ms}^{-1} \text{ km}^{-1}$ ) in the horizontal wind are noticed near the ray terminal points (at 10-12 km altitude) and are thus considered to be the source for generating the observed high phase-speed, high-frequency gravity waves observed in the mesosphere by balloon-borne measurements.

*This work is done in collaboration with M. Pramitha, M. Venkat Ratnam, A. Taori, NARL, Gadanki, S. Vijaya Bhaskar Rao, SVU, Tirupati and B. V. Krishna Murthy.*

(D. Pallamraju)

#### **Study of thermal structure differences from coordinated Lidar observations over Mt. Abu (24.5°N, 72.7°E) and Gadanki (13.5°N, 79.2°E)**

Rayleigh Lidars at Gadanki (13.5°N, 79.2°E), a tropical site, and at Mt. Abu (24.5°N, 72.7°E), a sub-tropical site, in India were operated simultaneously during the months of March, April and May 2004. Significant differences are found in the temperatures over both the locations. Higher temperature,  $\sim 10$ -20 K, in the altitude region of 40-65 km is found during March 2004 over Mt. Abu. The mean stratopause temperature during March 2004 is found  $\sim 284$  K at an altitude of 48 km over Mt. Abu, which is 18 K higher than the observed stratopause temperature of  $\sim 266$  K over Gadanki. During April and May 2004, the temperatures over Mt. Abu are higher in the entire altitude range of 30-70 km than over Gadanki. Lidar observed temperatures, over both the locations, are compared with the temperatures observed by SABER (onboard TIMED) and HALOE (onboard UARS). It is found that the Lidar observed temperatures are in qualitative agreement with the temperature observed by satellites; though quantitatively there are significant differences. A planetary wave type structure with a period of  $\sim 3$  days in the upper stratosphere ( $\sim 35$ -40 km) and in the lower thermosphere ( $\sim 50$ -60 km) have been found over both the locations.

*This work is done in collaboration with NARL, Gadanki.*

(S. K. Sharma, H. Chandra, S. Lal and Y. B. Acharya)

#### **Statistical study of Cloud Base Heights (CBH) over Ahmedabad using Ceilometer Lidar**

Ceilometer Lidar is in regular operation since November 2013 at PRL, Ahmedabad for the study of clouds and their characteristics. A statistical study of the Cloud Base Height (CBH) has been done using Ceilometer Lidar observations from January 2014-December 2014 over Ahmedabad. A comprehensive statistical analysis has been done to study the different cloud layers (upto three layers, low, medium and high levels) and their occurrence height. We found that the occurrence frequency of low clouds is  $\sim 67.7\%$  with the height range from 500 to 1000 meters. The highest cloud occurrence frequency has been found in the month of September with the data availability of  $\sim 96.7\%$  and annual cloud occurrence frequency is  $\sim 82\%$  with  $\sim 72\%$  data availability. The highest occurrence frequency of Cloud Base Heights, CBH1, and CBH2 is in the range of 500 to 999 meters where CBH1 is  $\sim 67\%$  and CBH2 is  $\sim 65\%$ . This indicates that the occurrence of low level cloud is very high and the dominant cloud base height is from 500 to 1000 meters. The highest occurrence frequency for third level of cloud CBH3 is only  $\sim 6.8\%$  and its height level is found between 2500-3000 meters over Ahmedabad.

(S. K. Sharma, R. Vaishnav, S. Lal and Y. B. Acharya)

#### **On the longitudinal differences of gradient drift waves over dip equator**

Investigations of equatorial electrojet irregularities have been carried out for several years over India using radars and

rocket borne experiments. Based on these measurements, gradient drift and streaming plasma waves were identified and characterized. In recent times, rocket flight experiments were conducted in 2010. These observations are compared with those obtained over the dip equatorial regions from different longitude sectors. This comparison revealed that the altitude of initiation of the gradient drift waves is invariably at lower heights over India in contrast to those observations over the American zone. In view of this, the growth rate expression of the gradient drift waves is examined.

This revealed that the growth rate of the gradient drift waves in the lower altitude region is proportional to the square of the strength of the geomagnetic field. The increase in the growth rate over Indian longitudes due to geomagnetic field strength in conjunction with the lower decay rate due to less electron densities at lower altitudes explains the initiation of these waves at a lower altitude compared to their counterpart over Jicamarca.

**(R. Sekar, S. P. Gupta and D. Chakrabarty)**

#### **Prompt electric field disturbance over low latitude associated with enhanced solar wind dynamic pressure**

During space weather events, several types of prompt penetration electric field disturbances affect equatorial ionosphere in daytime. These include electric fields due to the prompt penetration and overshielding effects associated with Z-component of the interplanetary magnetic field (IMF Bz), prompt penetration electric field associated with Y-component of interplanetary magnetic field (IMF By), substorm-induced electric field and electric field effect due to storm sudden commencements. Based on a case study, it is shown that solar wind dynamic pressure not only alters the global current systems and but can also impose transient prompt penetration electric field disturbances over equatorial ionosphere even before the onset of storm and in the absence of substorm.

*This work is done in collaboration with the scientists from Los Alamos National Laboratory, USA, Indian Institute of Geomagnetism and STEL, Nagoya University, Japan.*

**(D. Rout, D. Chakrabarty and R. Sekar)**

#### **On the unusual structure in the sodium layer over Gadanki**

An unusual structure (resembling a mirror image of ) in Na atom concentration based on the height-time-concentration (HTC) map obtained from sodium Lidar observations from Gadanki (a low latitude station in India) was obtained during an experimental campaign conducted by PRL with simultaneous airglow photometer and Lidar measurements. This kind of structure was not reported previously. Combining these observations with the meteor wind data from Thiruvananthapuram along with the temperature and winds profiles at different vantage points obtained from SABER on

board TIMED satellite, a possible explanation is provided for the origin of this structure. It is shown that the Kelvin-Helmholtz billow structure is formed by the observed shears in the background neutral wind. It is hypothesized that the KH billow remained in "frozen-in" condition for a few hours before getting deformed by the observed background wind structure to form the unusual structure observed by the Gadanki Lidar. This investigation indicates that KH billow structures can survive much longer than the expected lifetimes under favorable background conditions.

*This work is done in collaboration with scientists from multiple institutions/universities from USA along with INPE, Brazil and SPL, NARL, IITR India.*

**(R. Sekar and D. Chakrabarty)**

#### **Comparison of empirical models of plasma drifts over Indian sector and with the inferred drifts using multiple techniques**

The direct plasma drifts by ground based incoherent radar are not available over Indian longitudes. Therefore, the empirical model of vertical drifts needs to be validated. These empirical models are based on ion drift meter measurements on board satellites, Jicamarca incoherent measurements and the ionospheric irrotational electric field approximation. The model drifts values over Indian longitudes are compared with the inferred values of vertical drifts during nighttime by HF radars along with sparse barium cloud measurements during twilight. Further, the polarity and threshold values for the generation of plasma waves in the E-region are obtained from several rocket flights and VHF radar measurements conducted from Thumba. This comparison reveals that inferred drifts are consistent with the model drifts on almost all local times except during morning hours and post sunset hours particularly during solar minimum period.

**(K. Pandey, R. Sekar, S. P. Gupta, and D. Chakrabarty)**

#### **Satellite based Augmentation systems: A novel and cost effective tool for ionospheric and space weather studies**

Satellite-Based Augmentation Systems (SBASes) are designed to provide additional accuracy and robustness to existing satellite-based radio navigation systems for all phases of the flight of an aircraft. However, similar to navigation systems such as GPS which has proven its worth for the investigation of the ionosphere, the SBASes do have certain advantages. During the course of a recent study it has been proposed and demonstrated that the SBAS enabled systems have a potential applicability to ionospheric and space weather research in a novel and cost-effective way. The recent commissioning of the Indian SBAS, named GPS Aided Geo Augmented Navigation (GAGAN), covering the equatorial and low-latitude regions, centered around the Indian longitudes, provided the motivation for this approach. Two case studies involving different ionospheric behaviour

over low-latitude regions vindicate the potential of SBAS over extended areas. It has been shown that a single SBAS enabled receiver located anywhere could have access to all the network data with all the bias corrections duly applied and one which would be updated every five minutes and hence has the potential to emerge as a low cost ionosphere-space weather research tool.

*This work is done in collaboration with S. Sunda, SAC, B. M. Vyas, MLSU, P. V. Khekale, SAC, K. S. Parikh, SAC, A. S. Ganeshan, ISAC, C. R. Sudhir, AAI, S. V. Satish, AAI, and M. Bagiya, IIG.*

(R. Sridharan)

### **The spatial distribution of molecular hydrogen in the lunar atmosphere and its association with the surface topography-new results**

The measurements carried out by the Chandras Altitudinal Composition Explorer (CHACE) onboard the Moon Impact Probe (MIP) of Chandrayaan I mission is used to obtain information on the 2-D distribution of the lunar atmospheric  $H_2$  by a novel approach that makes use of the basic fact that the Moon has a Surface Boundary Exosphere (SBE). These are the first daytime in situ measurements of lunar  $H_2$  covering the  $20^\circ S$  to  $88^\circ S$  latitude region centered  $\sim 14^\circ E$  longitude. A critical examination of the observed spatial features of the surface concentration of  $H_2$  vis-a-vis the surface topography delineated from the Lunar Laser Ranging Instrument (LLRI) in the main orbiter Chandrayaan I, reveals significant similarity between them. Another constituent which exhibited spatial variation in the observed partial pressure is  $^{40}Ar$  and it was hypothesized that it is indicative of the spatial heterogeneity in the radiogenic activity of the Lunar interior. The absolute number density at the surface and also the latitudinal variation of the columnar densities, that are reported for the first time and their possible association with the lunar topography highlight the complexities of the sunlit lunar atmosphere.

*This work is done in collaboration with S. Thampi, SPL, T. P. Das, SPL, S. M. Ahmed, Hyderabad Central University, and J. A. Kamalakar, LEOS, ISRO.*

(R. Sridharan)

### **Meteor showers at Mars during the encounter of comet C/2013 A1: Predictions for the arrival of MAVEN/Mangalyaan**

We have estimated production rates, ion and electron densities of meteor ablation and ionization for different masses and velocities of meteoroids when comet C/2013 A1 crossed the orbit of Mars on 19 October, 2014 at 18:27 UT. Meteor ablations of small masses  $< 10^{-4}$  g have created a broad layer between altitude  $\sim 90$  km and 110 km. The

meteoroids of large masses  $\geq 10^{-4}$  g are burnt at around 60-90 km well below the main ionization peak at altitude  $\sim 160$  km produced in the nighttime by solar wind particle impact. The production rates and densities of 15 metallic ions ( $Mg^+$ ,  $Fe^+$ ,  $Si^+$ ,  $MgO^+$ ,  $FeO^+$ ,  $SiO^+$ ,  $MgCO_2^+$ ,  $MgO_2^+$ ,  $FeCO_2^+$ ,  $FeO_2^+$ ,  $SiCO_2^+$ ,  $SiO_2^+$ ,  $MgN_2^+$ ,  $FeN_2^+$ , and  $SiN_2^+$ ) have been computed self-consistently between altitudes 50 km and 150 km. The twelve major peaks in the Ion Mass Spectra (IMS) are predicted by our model calculations. Our predicted ion and electron density profiles of metals provide benchmark values that can be observed by plasma probes onboard Mars Express (MEX), Mars Atmosphere and Volatile Evolution (MAVEN) and Mangalyaan.

*This work is done in collaboration with Mr. B. Pandya, C. U. Shah College, Ahmedabad.*

(S. A. Haider)

### **Analysis of dust optical depths of Mars during MY24-MY32**

We have analyzed dust optical depth of nine Martian Years (MY24-MY32) observed by thermal infrared experiment onboard Mars Global Surveyor (MGS) and Mars Odyssey in the lower ionosphere. These measurements have suggested that a major dust storm occurs after  $\sim 3$  MY between solar longitude ( $L_s$ ) =  $180^\circ$ - $300^\circ$  for about a couple of weeks. In this region, MGS and Mars Odyssey have observed two major dust storms in MY25 and MY28 respectively, while local dust storms were observed every year during the summer. During the most intense period of the storms, the dust optical depths were increased by a factor  $\sim 10$  from its normal condition. We have estimated ion densities in the lower ionosphere of Mars during these two storm period. We have also studied the characteristics of dust aerosol particles of different size between 0.2 to 3  $\mu m$ . It is found that sub-micron sized dust particles are more dominant during the storm at the lower altitude.

(V. Sheel and S. A. Haider)

### **Seasonal variability of water vapour on Mars**

It has been suggested previously that heterogeneous chemistry on  $H_2O$  plays an important role in controlling the stability and composition of the Martian atmosphere. The water column abundance has been measured from Thermal Emission Spectrometer (TES) onboard Mars Global Surveyor (MGS) over the surface of Mars. We have developed earlier an energy loss method, which has been extended to estimate the global distribution of ion production rates of  $H_2O^+$  in the lower atmosphere of Mars. This model is zonal averaged over planetary longitudes. It varies with solar longitudes and latitudes between  $0$  to  $360^\circ$  and  $-90^\circ N$  to  $+90^\circ S$  respectively at five degree intervals. The altitudes

are varying from 0 to 50 km. The production rates of  $\text{H}_2\text{O}^+$  are decreasing and increasing due to condensation and sublimation processes respectively. It is found that the production rates of  $\text{H}_2\text{O}^+$  are maximum at latitude  $75^\circ\text{-}80^\circ\text{N}$  during northern summer ( $L_s=100^\circ\text{-}180^\circ$ ). It decreases in southern summer ( $L_s=270^\circ\text{-}360^\circ$ ) by about four orders of magnitude. This result is in consistent with the observations made by TES/MGS. In this model the density of  $\text{H}_2\text{O}$  is taken from Mars Climate database (MCD), which is freely available for global modeling of Mars climate.

(S. A. Haider and Y. S. Siddhi)

### Modeling of Planetary Fourier Spectrometer observations on Mars

The Planetary Fourier Spectrometer (PFS) onboard Mars Express observed emission intensity reflected from the surface of Mars in the short wavelength ( $1.2\text{-}5.5\ \mu\text{m}$ ) and long wavelength ( $5.5\text{-}4.5\ \mu\text{m}$ ) channels. We have analyzed PFS data of long wavelength channel for Martian Year 28, when a major dust storm occurred in the afternoon at low- to mid-latitudes in southern hemisphere between solar longitude ( $L_s$ )  $260^\circ$  and  $300^\circ$  for about a couple of weeks. Figure 11 represents observed and calculated radiance in southern hemisphere at wave numbers 0 to  $1500\ \text{cm}^{-1}$  for  $L_s=280^\circ$ . The latitudes are not changing much in the orbit # 4214, therefore we have averaged observed radiance over latitudes from  $0$  to  $90^\circ\text{S}$ . These measurements cover longitudes  $320\text{-}350\ \text{W}$  at local time 15 hrs. The radiative transfer model is developed to reproduce these measurements. In

this model the measured optical depths are used to estimate dust concentration. Later dust concentration, atmospheric density and temperature were used in the model to estimate the atmospheric radiance on Mars. In Figure 11 major drop designate the wave number  $667\text{-}668\ \text{cm}^{-1}$  corresponding to  $15\ \mu\text{m}$   $\text{CO}_2$  absorption bands. The maximum radiation from Mars occurs at  $15\ \mu\text{m}$   $\text{CO}_2$  band.

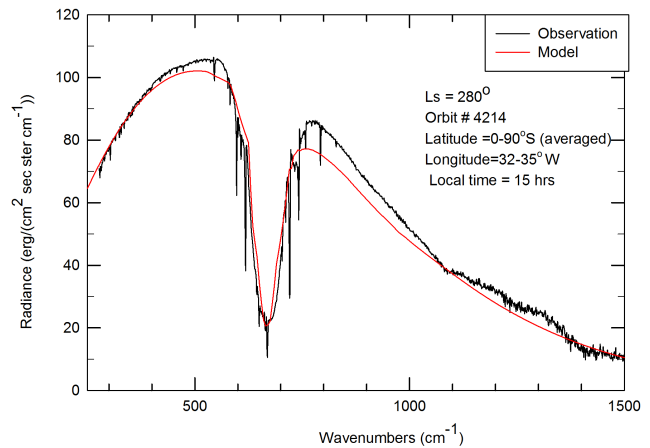


Figure 11 : Calculated and observed radiances in the southern hemisphere of Mars at wave numbers 0 to  $1500\ \text{cm}^{-1}$  for  $L_s=280^\circ$ . The dip in the radiances in the  $667\text{-}668\ \text{cm}^{-1}$  wave number range corresponds to  $15\ \mu\text{m}$   $\text{CO}_2$  absorption bands.

(S. A. Haider and M. P. Jethwa)

# SCIENCE at PRL

## Geosciences

### **Stable isotopic differences between summer and winter monsoon rains over southern India**

Rain drop size and isotopic composition of rain, important parameters that shed light on rain formation processes, are highly sensitive to the ambient weather. We reported earlier a significant correlation between them in individual rain events (with limited sampling), but this is yet to be tested with better, longer term sampling. We attempted to do so over a tropical region (i.e. Tirupati, India), in collaboration with NARL, Gadanki. Rain samples were collected at short time intervals ( $\leq 1$  h) to capture even small variations in their stable oxygen ( $\delta^{18}\text{O}$ ) and hydrogen ( $\delta\text{D}$ ) isotopic compositions. Isotopic analyses were made using an isotope ratio mass spectrometer, and a disdrometer measured the drop size distribution. Summer rains show a progressive  $^{18}\text{O}$  & D depletion with time, while the winter rains fluctuate about a mean value. We find no definite correlation between the drop size and stable isotope ratios as was reported earlier, based on a smaller number of samples: the complexity of rain formation process and varying ambient weather conditions for individual rain events could be the reason. Further, there is no significant difference between the local meteoric water lines ( $\delta^{18}\text{O}$ – $\delta\text{D}$  line) of summer and winter monsoon rains, though the intercepts in both the cases were significantly smaller than global meteoric waterline, suggesting significant strong influence of secondary evaporation. However, the winter rains are more depleted in D &  $^{18}\text{O}$ . Paleoclimate proxies such as  $\delta^{18}\text{O}$  of cave calcite or teak cellulose from this region need to be interpreted in terms of the relative seasonality of the rainfall rather than the total annual rain.

(R. Ramesh and R. Srivastava)

### **Nitrogen uptake rates and $f$ -ratios in the Equatorial and Southern Indian Ocean**

Nitrate, ammonium and urea uptake rates were measured in the Equatorial and Southern Indian Oceans, in collaboration with NCAOR, Goa and University of Agricultural Sciences, Bengaluru. Productivity ( $0.81$ - $2.23$   $\text{mmol Nm}^{-2}\text{d}^{-1}$ ) over the Equatorial Indian Ocean was low, but the  $f$ -ratio ( $0.13$ - $0.45$ ) was relatively high. In the Southern Indian Ocean total N-uptake rate varied from  $1.7$  to  $12.3$   $\text{mmol Nm}^{-2}\text{d}^{-1}$ ; it was higher in the Antarctic coast ( $69^\circ\text{S}$ ) and lower over most of the Southern Ocean, the lowest being at  $58^\circ\text{S}$ . The  $f$ -ratio also showed significant spatial variation, but was higher compared to values at the Equatorial Indian Ocean. The mean  $f$ -ratio in the Southern Indian Ocean was  $0.50$ . The nitrate-specific uptake rates and  $f$ -ratios appear to have increased significantly in the recent past relative to earlier estimates. While productivity in the Southern Ocean is comparable to that in the Equatorial Indian Ocean, higher  $f$ -ratios in the former underscore its importance in the uptake of  $\text{CO}_2$ . Data on the N-uptake rates and  $f$ -ratio characteristics of EIO and SIO confirm that the productivity is low in this part of the world ocean. Capability of the equatorial ocean for export production is lower relative to that of the Northern Indian Ocean and SO. Owing to significantly higher  $f$ -ratios compared to its equatorial counterpart, SIO has a greater potential in removing  $\text{CO}_2$  on longer timescales. A mean  $f$ -ratio of  $0.50$  in SIO indicates that the autotrophic community uses nitrate as well as regenerated nutrients equally. Further studies are needed to explain the seasonal and/or geographical variabilities in the production and  $f$ -ratio in these two basins.

(S. Prakash and R. Ramesh)

### Effects of dead carbon fraction and the mineralogy of speleothems on their stable carbon and oxygen isotopic variations

Four speleothem samples formed in different caves were investigated for dead carbon content and mineralogy (calcite/aragonite). These were dated by liquid scintillation spectrometry which indicates that they span from the present to ~3400 yr BP. Two of these show the presence of bomb carbon at their tips, one forming in a chamber where overlying soil and bedrocks are merely ~3m thick and the other, forming below ~30 m thick layers. The rest two were actively forming at the time of collection and had overlying layers between 8–10 m thick, show apparent ages of 880 yr BP and 1320 yr BP. These results clearly indicate the insignificant role of soil and bedrock thickness in controlling the dead carbon content in speleothems. Internal conditions of the seepage pathways seem to be responsible for such differences. To explore if precipitation has any control on the mineral structure of speleothems, mineralogical studies were done. In addition we investigate the behavior of  $^{87}\text{Sr}/^{86}\text{Sr}$  ratios in the speleothems as well. As changes in the stable oxygen isotope ratio ( $\delta^{18}\text{O}$ ) in these speleothems are found to respond to the amount of precipitation, investigation was carried out for those spots where  $\delta^{18}\text{O}$  had extreme values. Only one speleothem sample showed an association between  $\delta^{18}\text{O}$  and the mineral type. Spots having depleted  $\delta^{18}\text{O}$  levels had a higher calcite content (60 to 90 %), the remaining being aragonite. In contrast, the spots showing enriched values in  $\delta^{18}\text{O}$  had more of aragonite (80 to 95%) than calcite.

(R. Ramesh and M.G. Yadava)

### Role of cyclonic eddy in enhancing primary and new production in the Bay of Bengal

Eddies can be important in sustaining primary production in the tropical oceans, but their role for nutrient cycling is poorly understood in the undersampled northern Indian Ocean. To assess the role of cyclonic eddies in enhancing primary production, measurements of primary production were carried out at four stations in the northern Bay of Bengal during the early winter CE 2007, around a cyclonic eddy close to 17.8°N, 87.5°E. Shoaling of the thermocline and halocline by 10 m was observed within the eddy compared to the surroundings; mixed layer depth was also reduced within the eddy. The highest surface productivity ( $2.71 \mu\text{M Cd}^{-1}$ ) and chlorophyll *a* ( $0.18 \mu\text{g L}^{-1}$ ) were found within the eddy, and the lowest, at its outer edge. Further, the eddy supplied nutrients to the surface layers, shoaling the subsurface chlorophyll maximum as well. Integrated production in the euphotic top layers was more than twice within the eddy compared to its outer edge, confirming the role of cyclonic eddies in enhancing the primary production in the otherwise less productive Bay of Bengal. Given new nitrogen input via vertical mixing, river discharge or aerosol deposition, the additional primary production due to this new nutrient input and its contribution to the total production (*f*-ratio, fraction of exportable organic matter) increased significantly from 0.4 to 0.7, and thus the

Bay of Bengal can potentially transfer a high fraction of its total production to the deep, assisted by eddies. We suggest possible improvements in experiments for future studies, and the potential for assessing the role of eddies in biogeochemistry.

(N. Gandhi, S. Prakash, R. Ramesh and A. Singh)

### Environmental controls on new and primary production in the northern Indian Ocean

Oceans are a significant part of the atmospheric carbon dioxide ( $\text{CO}_2$ ) sink, but their efficiency to sequester  $\text{CO}_2$  is constrained by the availability of reactive nitrogen, a major limiting nutrient in most of the surface ocean. Because the export flux is difficult to measure directly, new production estimates are useful as a measure of annual carbon export from the sunlit ocean layer. We have analyzed data on new, regenerated and primary production based on the  $^{15}\text{N}$  tracer incubation experiments from a series of research cruises that were conducted during 1994–2007 in the northern Indian Ocean with an aim to identify environmental variables which control ocean productivity. There are a number of hypotheses concerning the environmental controls on productivity, most of which have not been assessed against direct measurements. Using step-wise multi linear regression (*MLR*) analysis, we found significant correlation between primary production and sea surface temperature (*SST*), phosphate ( $\text{PO}_4^{3-}$ ) and silicate (*Si*). Sea surface salinity (*SSS*), nitrate ( $\text{NO}_3^-$ ), *N:Si* and solar radiation are identified as the predictors explaining the most variance in the observed *f*-ratio (ratio of new production to total production). The observed spatial variations in new production could neither be significantly explained by linear regression nor *MLR*, however, using primary production and *f* ratio, we have significantly modelled new production on a basin scale. Our findings suggest that the Bay of Bengal could be as important as the Arabian Sea in its efficiency to export carbon to the deep ocean.

(R. Ramesh and A. Singh)

### Estimating the loss of Himalayan glaciers under global warming using the $\delta^{18}\text{O}$ –salinity relation in the Bay of Bengal

Quantifying the water loss of Himalayan glaciers due to global warming from direct measurement is difficult, as some glaciers are advancing or stable in spite of an overall retreat. We use a novel approach to provide an alternative estimate of the amount of Himalayan ice melt. Because a major part of this melted ice debouches into the Bay of Bengal through the Ganga–Brahmaputra basin, it causes significant variations in the oxygen isotopic composition ( $\delta^{18}\text{O}$ ) and salinity (*S*) of the sea surface water and their mutual linear relationship. In collaboration with *GSI*, we documented the temporal change in the  $\delta^{18}\text{O}$ –*S* relation for the bay at three different times during the period from *CE* 1994 to 2006, and using a model, we infer that  $2.4 \times 10^{11} \text{m}^3$  water was lost

by melting from the Ganga–Brahmaputra basin during this period. A significant change in the  $\delta^{18}\text{O}$ –S relationship of the surface waters of the Bay of Bengal has been observed during CE 1994–2006. This change is mainly caused by river discharge containing glacier melt with highly depleted  $^{18}\text{O}$  that mixes with the surface water of the Bay of Bengal. We estimate that  $2.43 \times 10^{11} \text{m}^3$  of Himalayan ice is likely to have melted during CE 1994–2006. This is a conservative estimate because it is based on an increase in the fresh water contribution from Himalayan glaciers only to the Bay of Bengal. If Himalayan glaciers continue to melt at this rate, then their ice will disappear in 200–400 years.

(R. Ramesh and A. Singh)

### Stalagmite $\delta^{18}\text{O}$ variations in southern India reveal divergent trends of Indian Summer Monsoon and East Asian Summer Monsoon during the last interglacial

Indian monsoon variations for the period around  $\sim 100$  ka have not been documented from terrestrial archives, while limited data do exist from the Indian Ocean. Some paleoceanographic studies have reported abrupt and stepwise changes in the monsoon intensity during the last deglaciation, but similar observations have not been possible for earlier periods such as the interglacial to glacial transition, mainly because of the coarse resolution ( $\sim 500$  to  $1000$  years) provided by marine archives of that age. A new  $\delta^{18}\text{O}$  data set from a stalagmite (3-ACN) that grew in the Belum caves, Andhra Pradesh, a semi-arid region in southern India, with a resolution of  $\sim 85$  years was generated in collaboration with scientists at NCAOR, Goa, University of Hyderabad, and the National Taiwan University. Age assignment to different growth layers consistent with associated analytical errors indicates that the record could span  $\sim 9$  ky during part of Marine Isotope Stage (MIS) 5d–c, from  $\sim 108$  to  $\sim 99$  ka.  $\delta^{18}\text{O}$  variations in this stalagmite, if interpreted using the 'amount effect', i.e.,  $^{18}\text{O}$  depletion of  $\sim 1.5$  ‰ per 100 mm increase in monsoon rainfall, indicate a step-like increase during the transition from the cooler stadial MIS 5d to warmer interstadial MIS 5c, signifying an abrupt reduction in monsoon rain. The new data presented highlight divergent trends between the Indian and the East Asian Summer Monsoons for a time period for which not many high-resolution comparisons are available. We present here a high-resolution record of Indian Summer Monsoon (ISM) precipitation during onset of the last glaciation based on a speleothem from the Belum caves, Andhra Pradesh. Such high-resolution records for a climatically important period that far back in time were hitherto not available; the limited available marine records suffer from coarser resolution. We find a step-wise decline in ISM precipitation at around 105 ka, which was previously reported only for the last deglaciation. We also note an opposite relation with the East Asian Summer Monsoon (EASM): the interrelationship between the two sub-systems of the Asian monsoon is still open to debate and this study makes an important contribution for a time period for which not many studies exist.

(A.H. Laskar, R. Ramesh and M.G. Yadava)

### $^{18}\text{O}$ depletion in monsoon rain relates to large scale organized convection rather than the amount of rainfall

Oxygen isotopic variations in rainfall proxies such as tree rings and cave calcites from South and East Asia have been used to reconstruct past monsoon variability, mainly through the amount effect: the observed  $^{18}\text{O}$  depletion of rain with increasing amount, manifested as a negative correlation of the monthly amount of tropical rain with its  $\delta^{18}\text{O}$ , both measured at the same station. This relation exhibits a significant spatial variability, and at some sites (especially North-East and peninsular India), the rainfall proxies are not interpretable by this effect. We show here that relatively higher  $^{18}\text{O}$ -depletion in monsoon rain is not related necessarily to its amount, but rather, to large scale organized convection. Presenting  $\delta^{18}\text{O}$  analyses of 654 samples of daily rain collected during summer 2012 across 9 stations in Kerala, southern India, we demonstrated that although the cross correlations between the amounts of rainfall in different stations is insignificant, the  $\delta^{18}\text{O}$  values of rain exhibit highly coherent variations (significant at  $P \approx 0.05$ ). Significantly more  $^{18}\text{O}$ -depletion in the rain is caused by clouds only during events with a large spatial extent of clouds observable over in the south eastern Arabian Sea. To summarize, the presence of large scale cloud bands during ISM leads to a marked  $^{18}\text{O}$ -depletion in the monsoon rain. This signature of convective activity is well captured in rain  $\delta^{18}\text{O}$  rather than in the local rainfall amount. This is confirmed by an analysis of the spatial pattern of clouds using OLR and the TRMM derived rainfall. Intense cloud activity with large spatial extent is associated with a strong cross equatorial flow and high moist air convergence over Kerala during all the high  $^{18}\text{O}$ -depletion rain events. Analyses of proxies of convection such as OLR, vertical wind velocity and the air mass back trajectory show high moisture convergence and heavy convection in the southern Peninsular India. This can effectively take the recycled high  $^{18}\text{O}$  depletion moisture from the sub cloud layer. Thus paleomonsoon proxies such as teak tree cellulose from Kerala may be interpretable in terms of the degree of large scale convective activity during the summer monsoon rather than the amount of monsoon rainfall.

(R.A. Jani, P.R. Lekshmy, M. Midhun and R. Ramesh)

### Stable isotope variations in Indian carbonatites

Stable oxygen and carbon isotope measurements were carried out on samples collected systematically by S.G. Viladkar of Bombay University, from several Indian carbonatite alkalic complexes. The implications of these data were inferred using some models that have been proposed for the evolution of stable isotope ratios in primary and secondary carbonatites. The evolution of carbonatite from the early to the later phase is reflected in the two isotope plots in Amba Dongar and Newania carbonatites. Primary carbonatites of Amba Dongar are interpreted to have evolved from a carbonatite parent magma of  $\delta^{18}\text{O} \sim 8.5$  ‰ and  $\delta^{13}\text{C} \sim -5.5$  ‰. The initial molar ratio of  $\text{H}_2\text{O}$  to  $\text{CO}_2$

that best explains the trend is  $\sim 0.9$ , with a crystallization temperature of  $\sim 800^\circ\text{C}$ . The later generation carbonatites (mainly ankeritic) in Amba Dongar appear to be altered mainly by a hydrothermal fluid with  $\text{H}_2\text{O}/\text{CO}_2$  ratio between 0.001 and 0.1 at temperatures between 100 and  $200^\circ\text{C}$ . This model also applies to the late phase carbonatite dikes from Amba Dongar. Compared to Amba Dongar, stable isotope results from Newania show depletion in the  $\text{H}_2\text{O}$  to  $\text{CO}_2$  ratio of the parent magma (between 0.3 and 0.4, i.e., the magma had much more carbon dioxide, relatively) and also relatively cooler temperatures of crystallization ( $\sim 600^\circ\text{C}$ ). The later generation carbonatites appear to have been altered mainly by meteoric water interaction.

(R. Ramesh)

### Estimation of past atmospheric carbon dioxide levels using tree-ring cellulose $\delta^{13}\text{C}$

The recent progressive increase of the atmospheric carbon dioxide concentration ( $C_a$ ) has earned considerable attention due to its role in global climate change. This has necessitated the identification of sources and sinks of this atmospheric gas. Although a few sources and sinks have been identified from the instrumental data, such studies are limited due to short-time range of the dataset. The only long-term (1800-1978 CE) annual  $C_a$  data that can be validated against instrumental observations are available from ice cores of Law Dome, Antarctica. The preceding ice core data with resolution of 2–10 years stop at 1939. There are some tree ring data that could be used to obtain high resolution records of past  $C_a$ . In a collaborative study with scientists at IITM, Pune, we studied the applicability of the Farquhar model for carbon isotopic discrimination (change in carbon isotopic composition from air  $\text{CO}_2$  to tree-ring cellulose) in  $\text{C}_3$  plants to trees growing in the field. Two new carbon isotope datasets from Himalayan conifers with published data from another eight sites across the world show disparate trends in the plot of carbon isotope discrimination versus atmospheric carbon dioxide concentration, in contrast to the model prediction of absence of any trend. This is because the model assumes that the tree adjusts its stomatal conductance for water-use efficiency to maintain a constant ratio of carbon dioxide concentrations inside and outside the leaf and treats the diffusive and biochemical fractionation factors as constants. By introducing a simple linear dependence of these fractionation factors on ambient temperature and humidity, we have enhanced the applicability of the model to naturally growing trees. Further, despite the disparate trends exhibited by the 10 trees, we show using the inverse modeling that it is possible to derive a unique record of past atmospheric  $\text{CO}_2$  concentrations using tree cellulose  $\delta^{13}\text{C}$  data. The reconstructions also replicate the summer  $\text{pCO}_2$  gradient from tropics to mid-latitudes. We also discuss the merits and demerits of the model, and compare the model-derived  $\text{pCO}_2$  with that of the ice core-based records from Law Dome.

(T. Bose and R. Ramesh)

### Provenance of the Late Quaternary sediments in the Andaman Sea

Geochemical and Sr–Nd isotopic study was carried out on a sediment core collected from the Andaman Sea in an attempt to reconstruct the Late Quaternary weathering and erosion patterns in the watersheds of the river systems of Myanmar and understand their controlling factors. Age control was established based on nine radiocarbon dates and  $\delta^{18}\text{O}$  stratigraphy. The rate of sedimentation was strongly controlled by fluctuations of the monsoon.

We identify three major sediment provenances: (1) the Irrawaddy catchment, (2) the western slopes of the Indo-Burman-Arakan mountain ranges and the Andaman Islands, and (3) the catchments of Salween and Sittang and the Bengal shelf, with the first two contributing 30–60% of the material. Enhanced contributions from juvenile sources and corresponding positive shifts of  $\delta^{18}\text{O}$  are observed at seven time periods (11–14, 20–23, 36, 45, 53, 57, and 62 ka) of which five are synchronous with cooling of the northern hemisphere, suggesting a link between the changes in sediment provenances and the shifting of the locus of the summer monsoon, southward from the Himalayas, without substantial reduction in intensity.

Our data, and that from other cores in the region suggest that an eastward moving surface current disperses sediments, derived from the Bengal shelf and western margin of Myanmar, from the eastern Bay of Bengal into the western Andaman Sea and that its strength has increased since the LGM. The existence of this current during the LGM implies that the Andaman Sea and the Bay of Bengal were well connected during the last glacial period.

(N. Awasthi, J.S. Ray, S.T. Band and V.K. Rai)

### Age of subaerial lava flows of Barren Island volcano

Little was known about the nature and origin of the deep crust beneath the Andaman Island Arc in spite of the fact that it formed part of the highly active Indonesian volcanic arc system, one of the important continental crust forming regions in Southeast Asia. This arc, formed as a result of subduction of the Indian Plate beneath the Burma Microplate (a sliver of the Eurasian Plate), contains only one active subaerial magmatic center, Barren Island volcano, whose evolutionary timeline had remained uncertain. In this work, we present results of the first successful attempt to date crustal xenoliths and their host lava flows from the island, by incremental heating  $^{40}\text{Ar}/^{39}\text{Ar}$  method, in an attempt to understand the evolutionary histories of the volcano and its basement. Based on concordant plateau and isochron ages, we establish that the oldest subaerial lava flows of the volcano are  $1.58 \pm 0.04$  ( $2\sigma$ ) Ma, and some of the plagioclase xenocrysts have been derived from crustal rocks of  $106 \pm 3$  ( $2\sigma$ ) Ma. Mineralogy (anorthite + Cr-rich diopside + minor olivine) and isotopic compositions ( $^{87}\text{Sr}/^{86}\text{Sr} < 0.7040$ ;  $\varepsilon_{\text{Nd}} > 7.0$ ) of xenoliths not

only indicate their derivation from a lower (oceanic) crustal olivine gabbro but also suggest a genetic relationship between the arc crust and the ophiolitic basement of the Andaman accretionary prism. We speculate that the basements of the forearc and volcanic arc of the Andaman subduction zone belong to a single continuous unit that was once attached to the western margin of the Eurasian Plate.

*This work was done in collaboration with K. Pande, Indian Institute of Technology, Bombay.*

(J. S. Ray)

**A sensitive flow injection system for determination of dissolved iron (DFe) in seawater by chemiluminescence method**

An automated flow injection system has been developed to measure the dissolved concentrations of iron in sea water. The method detects Fe (III). The Fe(III) in the acidified sample is selectively preconcentrated on iminodiacetate chelating resin and then eluted with dilute hydrochloric acid. The resulting eluent is mixed with luminol, aqueous ammonia and hydrogen peroxide solution successively, and then mixture is introduced in to the chemiluminescence cell. The chemical reaction between luminol and hydrogen peroxide which is catalyzed by iron results in the emission of light. The chemiluminescence intensity is obtained by using Hamamatsu photon counting head (PCH) (H8259-01).

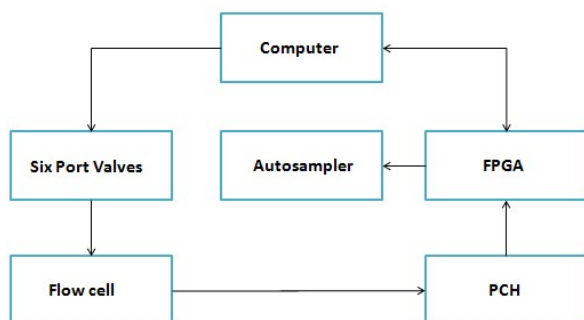


Figure 1 : Fe-FIS system (top) and block diagram of system operation (bottom).

The samples are aspirated to the system using in-house developed auto sampler which can intake 18 samples continuously without user intervention. The software and user

interface are developed in Labview. The chemiluminescence signal read by PCH is sent to Computer via FPGA. After the end of each run, the software calculates peak height and peak area for respective sample. The system is calibrated using known standards which are used to calculate the unknown concentration of the samples.

**Method Assessment**



Figure 2 : Typical chromatogram of Fe (top) and calibration graphs for both peak height and peak area (bottom).

The accuracy and precision of the system and method was ascertained by analyzing standard reference seawater samples from *GEOTRACES* Intercalibration Programme provided by Prof. Kenneth Bruland, California University, USA. The results are shown in a table.

Sr. No.	Standard	Reference Value (nM)	Our Value (nM)
1	GS	0.546 ± 0.046	53 ± 0.03 (n=11)
2	GD	1 ± 0.1	0.961 ± 0.07 (n=7)

**Seawater Analysis**

This method was applied to the analysis of sea water samples collected during the cruise SK-304, SK-311 and SK-312 on ORV Sagar kanya in Indian Ocean waters. A typical profile measured in the Indian Ocean is shown in Figure 3.

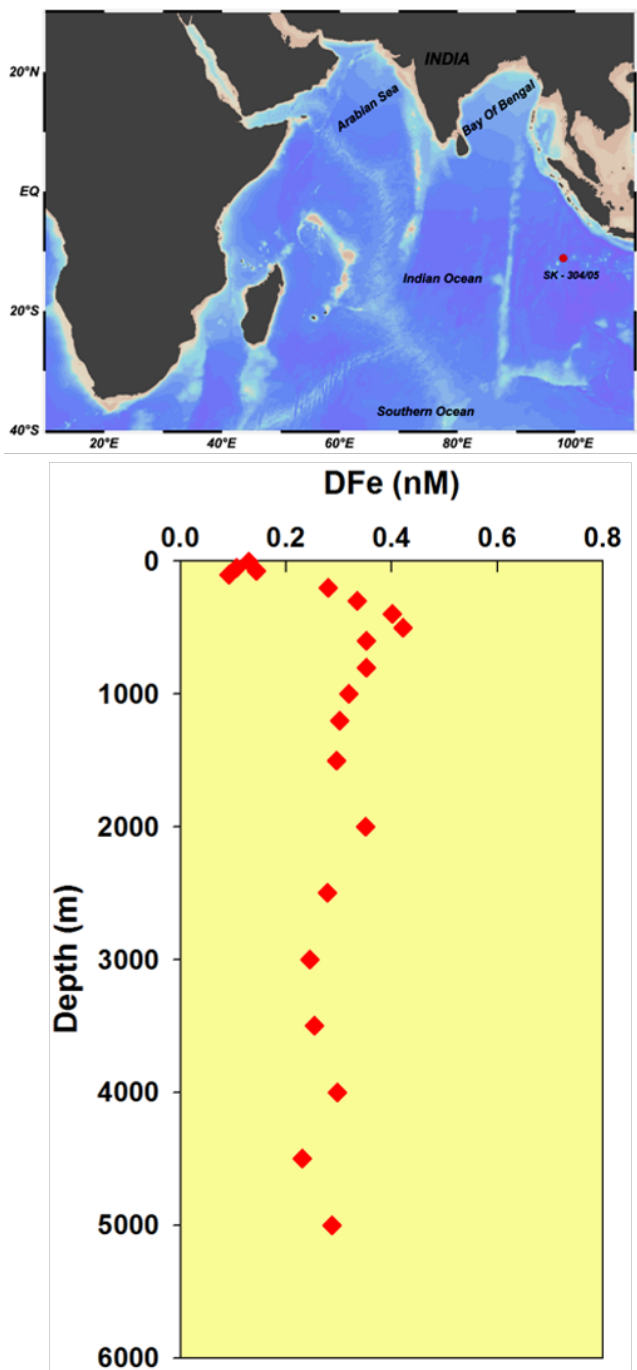


Figure 3 : Vertical profile of iron at 10°S - 97°E.

(V. Chinni, M. Shah and Sunil K. Singh)

**Distributions of dissolved iron (DFe) in the Indian Ocean**

Iron (Fe) undoubtedly is an important micronutrient for micro organisms present in the oceans to sustain their life's. Even though it is a fourth most abundant element in earth's crust the dissolved iron in water columns of ocean are very low, vary

from 0.02nM to 2.8 nM in open oceans due to the hydrolysis of thermodynamically stable Fe(III).

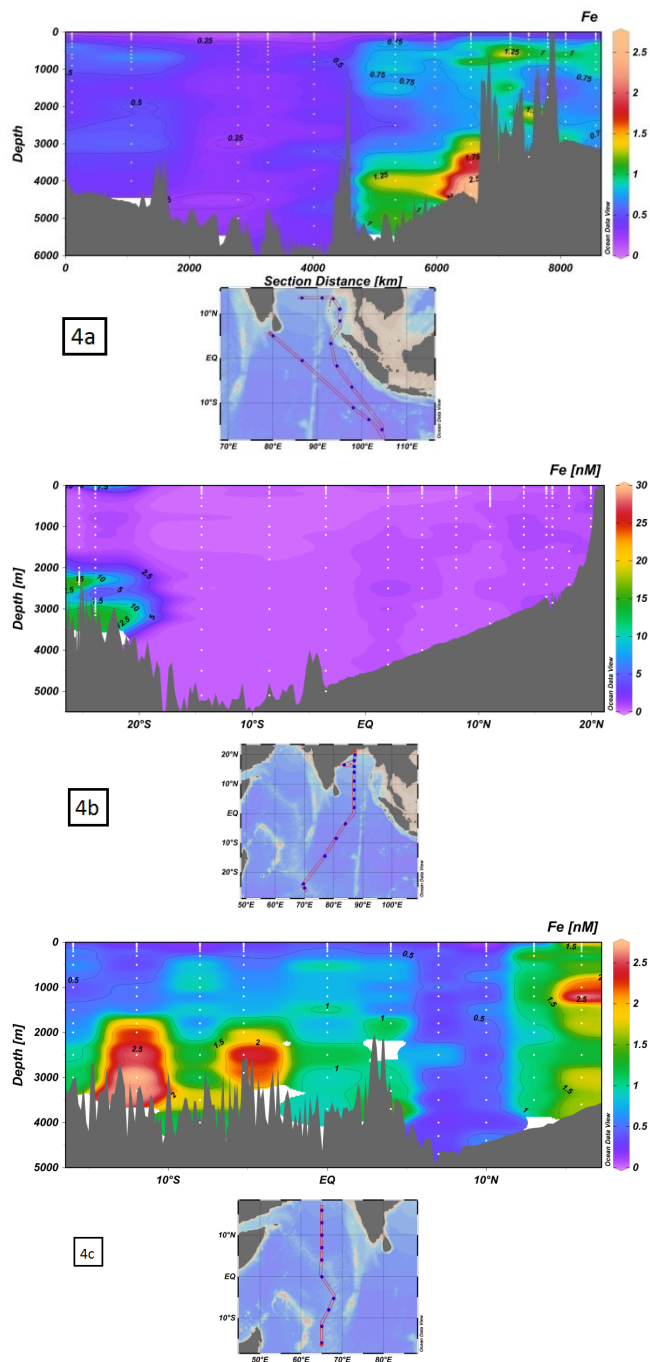


Figure 4 : DFe concentrations in Indian Ocean along different meridional sections. (4a). SK-304, (4b). SK-311, (4c). SK-312. Note the change in scale of DFe concentrations.

Here, we present the data of dissolved iron (DFe) concentrations from different meridional sections in Indian Ocean collected during *GEOTRACES-INDIA* cruises SK-304, 311 and 312 between 18°N to 28°S. The clean sampling and measurement techniques are validated using measurement of DFe at cross over stations in the Indian Ocean and by analyzing GEOTRACES and SAFe reference

samples. The DFe in Surface waters of the Indian Ocean ranges from 0.06 nM to 1.8 nM. The higher surface concentrations are observed in Arabian Sea which shows the high amount of dust deposition from nearby desert sources. The concentrations of DFe in sub-surface waters got elevated and reach a maximum of 1.5 nM.

Remineralization of sinking organic matter may be the cause for the elevated concentrations of DFe in the sub-surface waters and remains constant throughout the water column. Water sampled around some of the hydrothermal sections along the central Indian ridge display high DFe concentrations, reaching a maximum of 27 nM.

(V. Chinni, Sunil K. Singh, R. Rengarajan and R. Bhushan)

### Weathering in the Mahanadi River system

The Mahanadi River is one of the major peninsular rivers of India with annual average water and sediment discharges of 66 km<sup>3</sup> and 15.74×10<sup>6</sup>t respectively to the Bay of Bengal. Geologically, the basin is characterized by Precambrian rocks of the Eastern Ghats, rocks associated with the Gondwana supercontinent and recent littoral deposits.

Water and sediment samples have been collected from the Mahanadi river system (Figure 5) to study weathering processes and the factors influencing them. Major ion composition, Sr concentrations and its isotopic compositions are measured in the solute phase in the Mahanadi River. The total dissolved solids (TDS) vary from 55–180 mg/L throughout the Mahanadi river system. The dissolved Sr and <sup>87</sup>Sr/<sup>86</sup>Sr in this system display variation from 28 to 290 μg/g and 0.71268 to 0.72854 respectively. The 1/Sr vs. <sup>87</sup>Sr/<sup>86</sup>Sr plot (Figure 6) shows in general two end-members mixing between carbonate and silicates.

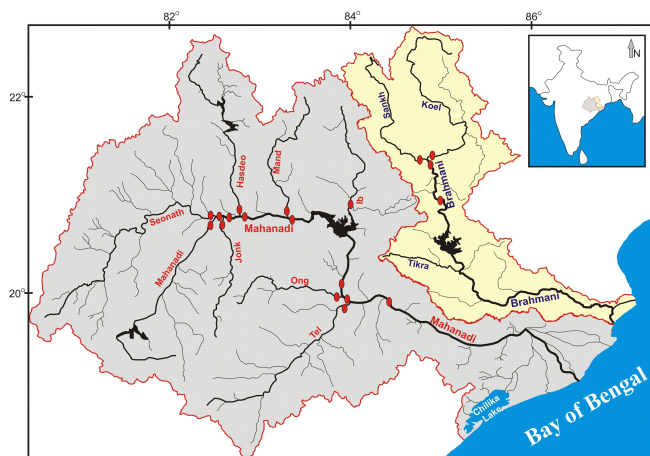


Figure 5 : The sampling locations in the Mahanadi and the Brahmani Rivers.

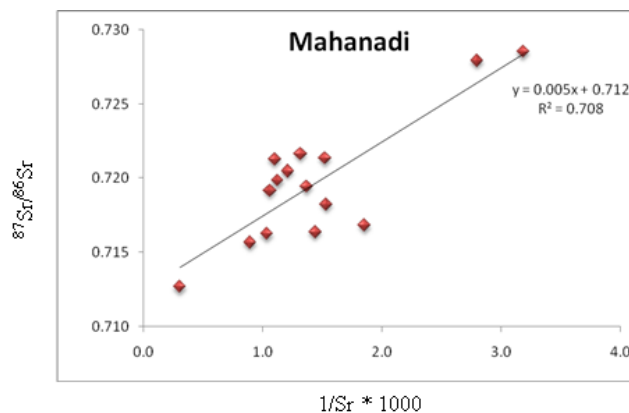


Figure 6 : 1/Sr vs. <sup>87</sup>Sr/<sup>86</sup>Sr plot showing the mixing pattern in dissolved phase of the Mahanadi River system.

This work is carried out in collaboration with Dr. Gyana Ranjan Tripathy, IISER, Pune.

(K. Damodara Rao and Sunil K. Singh)

### Tracing the evolution of seawater anoxia during Proterozoic-Early Cambrian using $\delta^{98}/_{95}$ Mo of Black Shales

Molybdenum (Mo) isotopes are promising tracers for reconstructing ocean paleoredox conditions. It gets fraction during adsorption with Fe-Mn hydroxide in oxic condition where as its removal in anoxic/euxinic condition leads to preservation of seawater signature in sediments. In this study an attempt being made to reconstruct the redox conditions during proterozoic-Early Cambrian period using  $\delta^{98}/_{95}$  in black shales from Aravalli, Vindhyan and outer Lesser Himalaya. This time span has witnessed the extreme events in the early earth such as rise in atmospheric oxygen and changes in the biosphere. Samples processed for this study were collected from Jhamarkotra Formation of Lower Aravalli, Bijaigarh Shales of Kaimur formation of the Vindhyan and Lower Tal formation of the Lesser Himalaya. The depositional ages of these formations were estimated to be ~2000 Ma, ~1200 Ma and ~540 Ma for Jhamarkotra, Bijaigarh and Tal formations respectively.

Mo isotopic composition of black shales were determined by using <sup>97</sup>Mo – <sup>100</sup>Mo double spike followed by acid digestion and Mo purification by column chromatography. Later these purified samples were analysed using Neptune MC-ICP-MS.

$\delta^{98}/_{95}$  Mo measured in Jhamarkotra formation shows variation from -0.17 to 0.3‰ with concentration from 5–35 ppm, Bijaigarh Shales indicate variation from 0.4 to 1.35‰ with concentration ranging from 1.6–34 ppm whereas the Tal black shales display variability of 0.3-1.5‰ with concentration 16–80 ppm.

The near zero  $\delta^{98}/_{95} \text{Mo}$  in Jhamarkotra shales of Aravalli imply anoxic basin during Paleoproterozoic. Increasing Mo isotope composition (Figure 7) from the Proterozoic to the Early Cambrian indicates gradual increase in proportion of oxic vs anoxic condition in the global Figure 7.

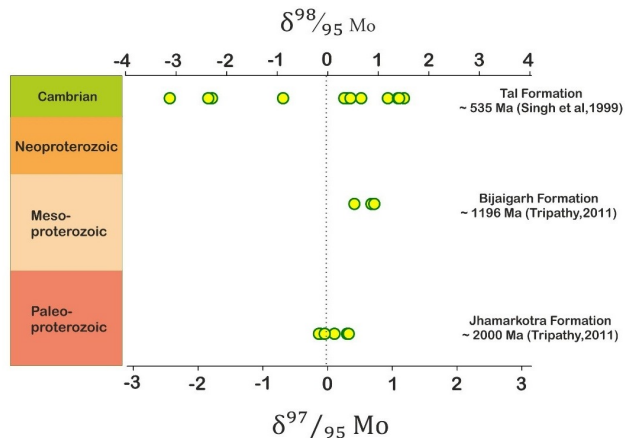


Figure 7 : Increasing trend of  $\delta^{98}/_{95} \text{Mo}$  in Black Shale of Proterozoic to Early Cambrian ocean during this time period. Based on these data it can be inferred that proterozoic ocean was more anoxic compared to that of Early Cambrian and the contemporary ocean.

(S. Sawant, Sunil K. Singh and V.K. Rai)

### $\delta^{98} \text{Mo}$ in the Indian rivers and estuaries

Application on Molybdenum (Mo) isotopes as a proxy of paleo-redox condition of oceans depends on the quantification of continental input of Mo and its isotopes and their behaviour in estuaries. It is important to investigate their behaviour in rivers and estuaries with different geological and environmental characteristics to obtain a more representative data on the riverine flux of Mo and the isotope composition of dissolved Mo supplied to the oceans. Mo concentration and its isotope composition have been measured in dissolved and particulate phases of the Ganga, Mahanadi, Godavari and Krishna rivers and their estuaries (Figure 8) (i) assess the impact of physical/chemical weathering in the basin on the isotope fractionation of Mo and (ii) constrain its flux and  $\delta^{98} \text{Mo}$  of the Ganga to the Bay of Bengal. The water and suspended load from the mainstems and tributaries were sampled along the course of rivers during monsoon seasons.

Their Mo concentration and  $\delta^{98} \text{Mo}$  were determined using double spike on Neptune MC-ICP-MS at PRL. Mo concentration and its isotope composition in the Ganga mainstream and tributaries range from 9–22 nmol/kg and -0.3–0.2‰ respectively.  $\delta^{98} \text{Mo}$  of the Ganga mainstream remains close to 0‰ and displays little variation along the course. Lower  $\delta^{98} \text{Mo}$  of the Ganga could be due to higher physical weathering compared to chemical weathering. In Hooghly estuary dissolved  $\delta^{98} \text{Mo}$  varies from -0.16 to 2.10‰ between salinity 0 to 32.4 with concentration 16 to 86

nmol/kg. Mo concentration shows conservative behavior with salinity in the Hooghly and Godavari estuaries, however,  $\delta^{98} \text{Mo}$  displays non-conservative behaviour in these estuaries. Non-conservative behaviour of  $\delta^{98} \text{Mo}$  in these estuaries could be due to exchange of Mo between dissolved and particulate phase or could be due to its supply from submarine groundwater discharge.

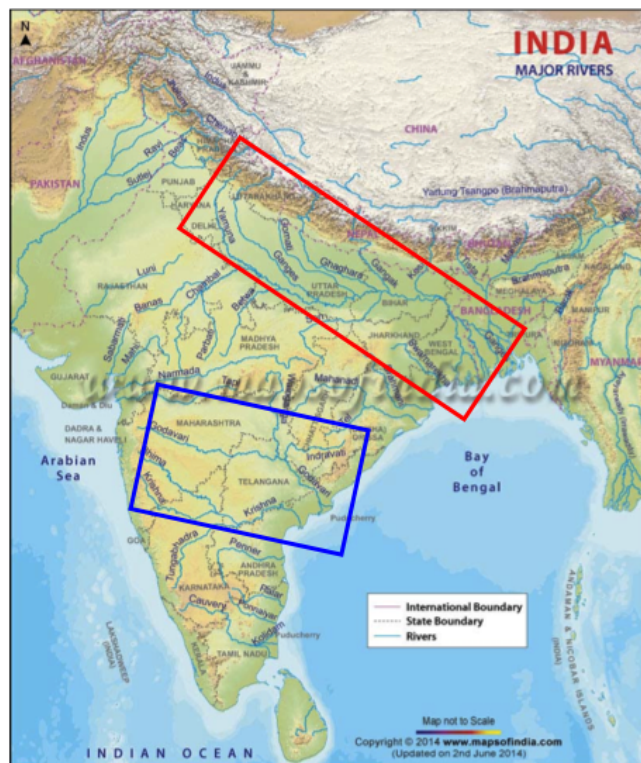


Figure 8 : Sampling locations for  $\delta^{98} \text{Mo}$  in the Indian Rivers and estuaries.

(V. Goswami, Sunil K. Singh and V.K. Rai)

### $\epsilon_{Nd}$ in the Arabian Sea: Water Mass mixing vs particle-water interaction

Arabian Sea is characterized by intermediate water column oxygen minimum zone resulting from high productivity sustained by upwelling during SW monsoon. It receives significant amount of particulates from the rivers such as the Indus, the Narmada etc and atmospheric dust from adjoining arid landmasses. An extensive study of Nd isotope composition has been carried out in the Arabian Sea to characterize the various water masses present and quantify the Nd sourced from the fluvial and Aeolian particles by their interaction with the seawater. Several water profiles were collected onboard Sagar Sampada during April 2012 in the Arabian Sea along 68°E meridional section between equator and 21°N (Figure 9). Nd isotope composition were determined using MC-ICPMS after pre-concentrating and purifying it from ~20 liters of seawater.  $\epsilon_{Nd}$  in the Arabian Sea vary significantly from -14.37 to -5.57 with less radiogenic

values in the northern Arabian Sea and more radiogenic Nd in the surface waters between 4°N and 16°N (Figure 9). The  $\epsilon_{Nd}$  results demonstrate the significant presence of Antarctic Bottom Water (AABW) and North Atlantic Deep Water (NADW) in the bottom and deep Arabian Sea respectively. Persian Gulf water (PGW) and Red Sea Water (RSW) are present at water depth 400 to 1000 m between 4°N to 16°N. Important features of this study are the non-radiogenic Nd in the northern Arabian Sea and the radiogenic Nd in the surface water of the Central Arabian Sea, between 4°N to 16°N. Northern Arabian Sea is dominated by less radiogenic Nd resulting from its release from the lithogenic particles with  $\epsilon_{Nd} \sim -14$  brought by the river Indus. Radiogenic Nd of the surface water of the Central Arabian Sea is contributed by dissolution of Aeolian dust having  $\epsilon_{Nd} \sim -6$ . Particle-water interaction seems to have a dominant control on the Nd budget of the Arabian Sea with Nd contribution from fluvial particles increases towards northern Arabian Sea whereas Aeolian contribution decreases towards northern and eastern Arabian Sea.

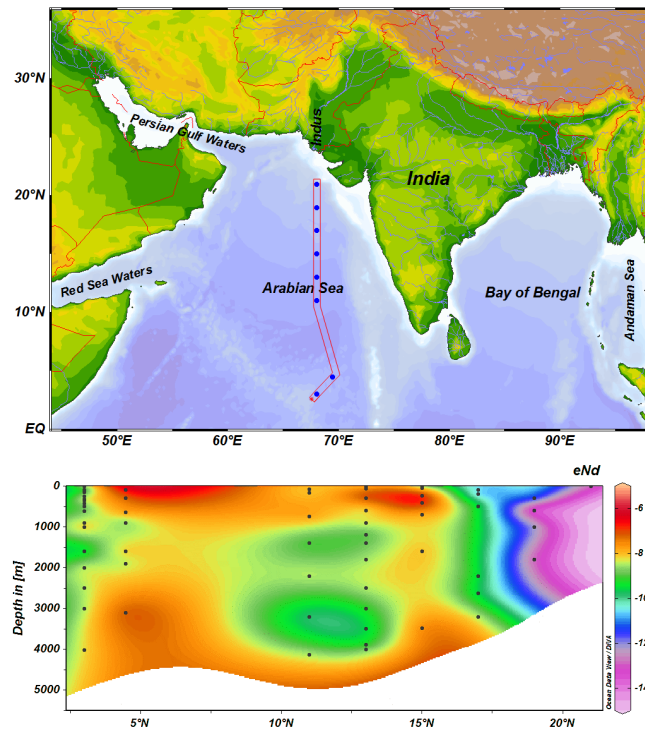


Figure 9 : Meridional section of Nd sampling and distribution  $\epsilon_{Nd}$  in the Arabian Sea.

(K. Damodara Rao, Sunil K. Singh, R. Bhushan and V.K. Rai)

**Pan-India seasonal and annual isotopic maps for precipitation across the country reveals hydro-meteorological processes**

As part of the IWIN national programme daily and fortnightly accumulated precipitation samples were collected from more than 40 stations across the country. These samples have been analysed for their oxygen and hydrogen isotopic composition ( $\delta^{18}O$  and  $\delta D$ ) using Isotope Ratio Mass Spectrometer (IRMS) with a view to discern various

hydrometeorological processes which govern spatio-temporal variation in the isotopic characteristics of precipitation. With the help of this data it has now been possible to prepare pan-India annual, seasonal and monthly isotopic maps showing geographical distribution of  $\delta^{18}O$  and d-excess in precipitation, and corresponding diagnostic plots ( $\delta^{18}O$  vs.  $\delta D$  regression and  $\delta^{18}O$  vs. d-excess).

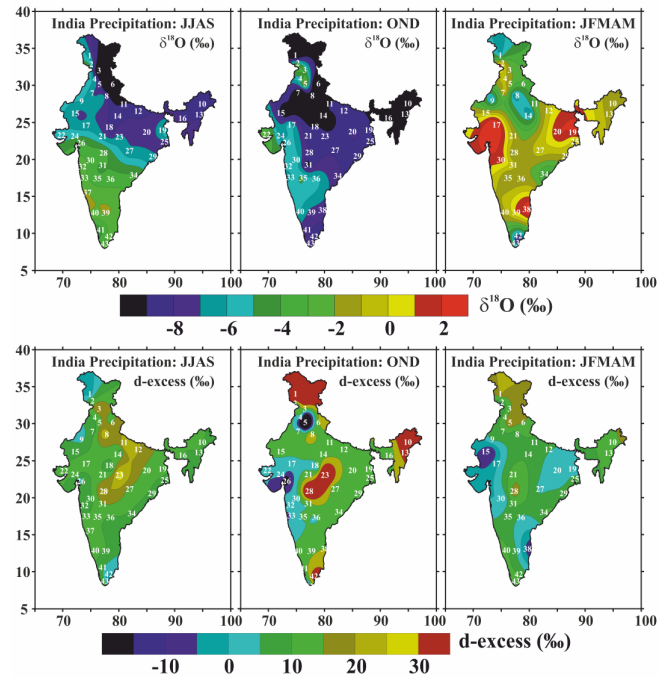


Figure 10 : Seasonal isotopic maps showing geographical distribution of  $\delta^{18}O$  and d-excess in precipitation across the country. Digits on the contour maps indicate the location of 43 sampling stations.

This study has revealed some of the important hydro-meteorological processes concerning hydrological cycle over India.

These are: (1) Isotopic composition of precipitation across the country becomes isotopically depleted in the later part (Aug-Sept) of the southwest monsoon season; (2) Precipitation in the winter months (ONDJ) is isotopically depleted across the country. (3) The so called amount effect, i.e. isotopic depletion with increasing amount of rainfall, is not clearly observed at all stations; (4) There are large regions in central India and northern India where high (>10‰) d-excess in precipitation is observed, particularly during later part of the southwest monsoon; (5) Precipitation in the northeastern Himalayas (Assam) is characterized by high d-excess and higher intercept of the  $\delta^{18}O$ - $\delta D$  regression line indicating significant recycling of moisture in this part of Himalaya; (6) Precipitation in southern Indian peninsula, during northeast monsoon season is isotopically depleted compared to that during southwest monsoon. In addition to above there are several other useful observations regarding isotopic features which indicates underlying subtle processes.

(R.D. Deshpande, V. Padhya, S.K. Gupta and Harsh Oza)

### Water Vapor source identification for daily rain events at Ahmedabad in semi-arid western India: wind trajectory analyses

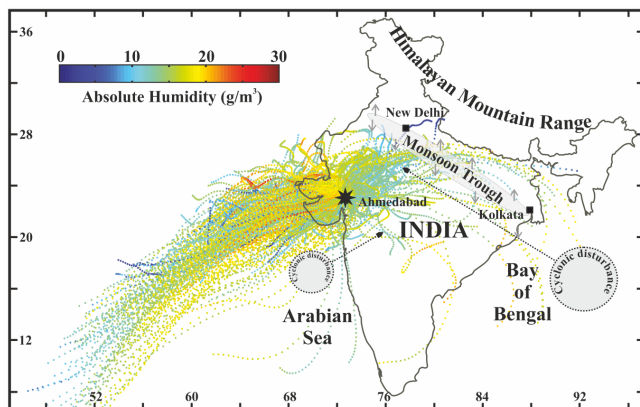


Figure 11 : (a) Diagram showing broad meteorological features affecting rainfall over India during SW monsoon. Ensemble of the 48 hr backward wind trajectories converging at Ahmedabad for 120 daily rainfall events during June-July-August-September of 2005-2008 investigated in this study are also superposed. Back trajectories to Ahmedabad have been drawn using the HYSPLIT Single Particle Lagrangian Integrated Trajectory Model (HYSPLIT) from <http://ready.arl.noaa.gov/HYSPLIT.php>.

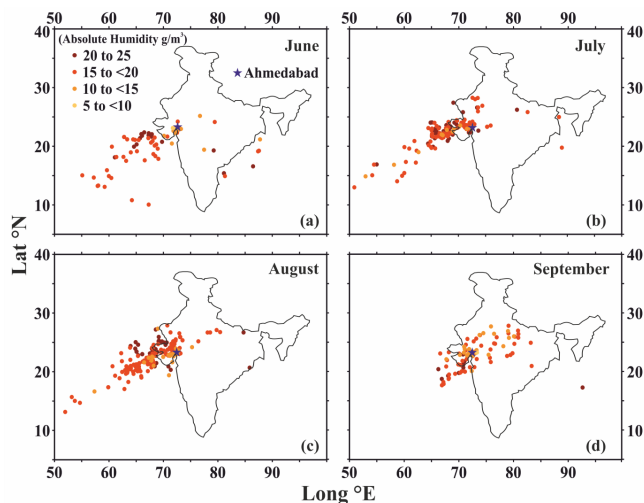


Figure 11 : (b) Distribution of the 600 points of the highest absolute humidity, obtained for the 120 rainfall events and grouped according to the month during which they occur in the rainy season of 2005-2008.

The Arabian Sea (AS), the Bay of Bengal (BOB) and the continental recycling are three principal vapor sources identified for the rain events at Ahmedabad located in the semi-arid western India. In this study, the 48 hours backward wind trajectory, at 6 hourly intervals, converging at an altitude of 1.5 km above the ground level, for 120 daily rain events during the monsoon seasons of 2005-2008 have been examined using HYSPLIT model. Temperature, relative humidity, altitude and rainfall along each trajectory were studied at hourly intervals. The temperature and relative humidity data were used to compute the absolute humidity ( $\text{g m}^{-3}$ )

of the air parcel at its location at hourly intervals. The relationship between the height of the air parcel, its relative humidity and rainfall along each trajectory was used to identify the vapor pick-up region.

The region around the maximum value of absolute humidity for each trajectory was designated as the dominant vapor pick-up region for each rain event at Ahmedabad. In this manner, principal vapor source identification was unambiguously possible for 93.3% of all the 120 rain events. The fraction of total events and the fractions of total rainfall attributable to the three principal vapor sources respectively are: AS –68.3% and 62.1%; BOB –2.5% and 1.5%; Recycled –22.5% and 24.5%; Mixed –6.7% and 11.8 %. Most of the rain events with recycled vapor contribution occur during the latter part of the monsoon season, namely during September.

*This work is being carried out in collaboration with Mr. Hrishikesh Kumar from Space Applications Centre, Ahmedabad.*

(R.D. Deshpande, M. Dave, V. Padhya and S.K. Gupta)

### Aeolian Flux and Productivity Variation in the Northwestern Arabian Sea during Late Quaternary

The northwestern Arabian Sea is known for enhanced productivity with increased supply of nutrients by upwelling and essential trace elements via terrestrial and/or aeolian dust. The monsoonal winds are only responsible for upwelling but also assist transport of dust from the northeast Africa to this region. During Boreal winter, westerlies are responsible for transport of dust from Arabian and Saharan desert to this oceanic region. The present study is based on a sediment core located in the northwestern Arabian Sea and aims to record variation in productivity and aeolian supply since Last Glacial Maximum (LGM). Two major shift in sediment composition are observed are at 15 ka BP and 6 ka BP. The first shift shows relative increase in biogenic matter concentration and decrease in aeolian component at 15 ka BP synchronous with the onset of African Humid Period (AHP), wet period in North Africa. A short period of increased aeolian and decreased biogenic sediment concentration is observed at 12 ka BP, roughly contemporaneous with the younger dry as period and can be attributed to higher dust deposition transported from dry subtropical Africa (Sahara desert). The Aeolian sediment component gradually increases from 6 ka indicates gradual increase in aridity and dust production in subtropical Africa and also marks the termination of AHP. Relatively low and gradual decrease of biogenic sediment concentration observed at 12 & 6 ka BP respectively were due to the changes in aeolian supply and also supported by constant increase in siliceous productivity (biogenic silica:  $\text{B-SiO}_2$ ) since 15 ka BP (Figure 12). Gradual increase in siliceous productivity from 15 ka shows increase in nutrient availability through upwelling (southwest monsoon) and thereby effect of nutrient utilization and dominance of siliceous productivity.

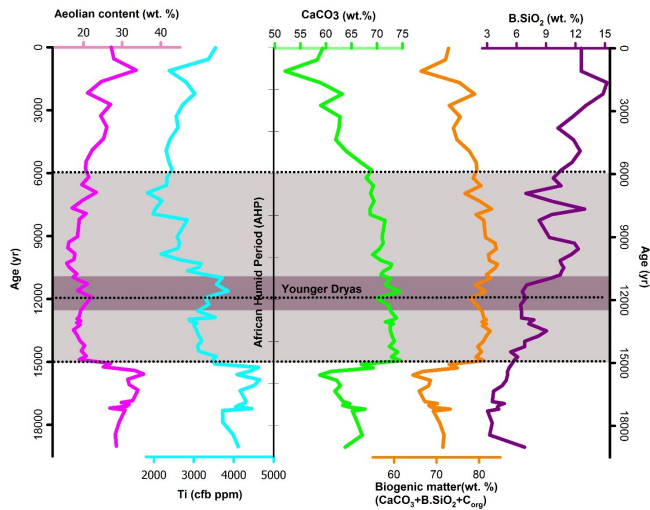


Figure 12 : Downcore variation in core SS-164/4018 for Aeolian content, Titanium cfb (carbonate free basis), Biogenic matter and productivity proxies (CaCO<sub>3</sub> & Biogenic silica). Dotted lines marks the periods of major changes in sediment composition.

This work is being carried out in collaboration with Mr. D. Balaji, M.S. Univeristy of Baroda, Vadodara.

(R. Bhushan)

**Distribution of Dissolved Organic Carbon in the Northern Indian Ocean and its implications to regional carbon budget.**

The Bay of Bengal in the northern Indian Ocean experiences significant influence of discharge of fresh water and sediment from various rivers and productivity associated with seasonally reversing southwest and the northwest monsoon. The *DOC* concentrations determined in the vertical profiles of seawater from the Bay of Bengal and the Indian Ocean show highest *DOC* concentration were in the northern Bay of Bengal in the surface waters due to the influence of fresh water with higher *DOC*. The surface *DOC* concentration in the Bay of Bengal varies from 75-100µM, whereas in the Indian Ocean it varies from 70-90µM (Figure 13). In the northern Bay of Bengal, the sub-surface *DOC* concentrations show enhanced *DOC* concentrations upto ~700m when compared to the other southern stations. The subsurface *DOC* concentration is more than 85 µmol/L, which is very high compare to all other oceans and can be attributed to the release of *DOC* from the enormous flux of (0.5×10<sup>12</sup> mol·C·yr<sup>-1</sup>) particulate organic carbon (*POC*) from the Ganga-Brahmaputra river system. Lower concentration of dissolved oxygen in similar depths indicates oxygen consumption due to degradation of the enhanced flux of *POC*. Thus, in addition to productivity, the distribution of *DOC* in the Bay of Bengal appears to be significantly controlled by fresh water and sediment discharge and has strong implications to the regional carbon budget.

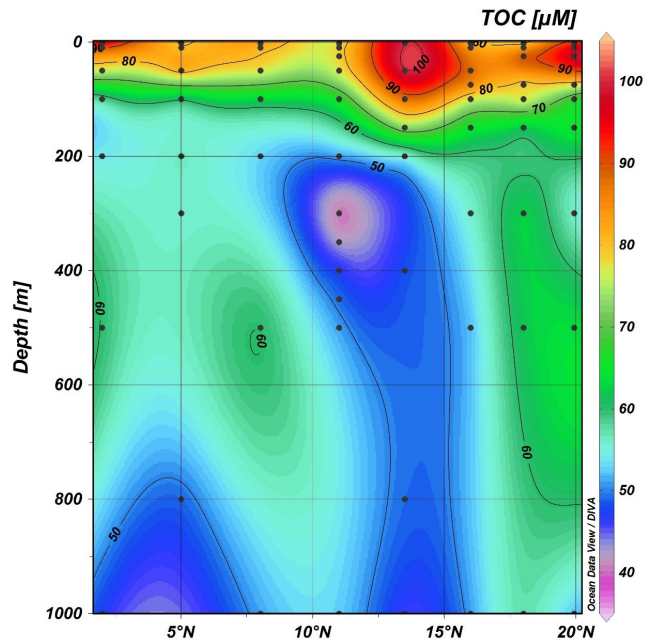


Figure 13 : DOC depth profile of Bay of Bengal along 87°E in North-South section.

(C.S Shah, A.K. Sudheer and R. Bhushan)

**Signatures of Global climatic event of last two millennia from the active mudflat of Rohisa, Southern Saurashtra coast, Gujarat**

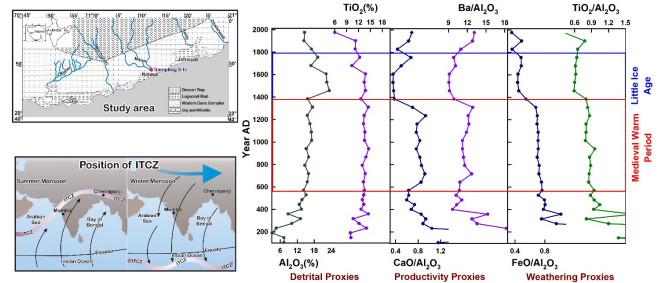


Figure 14 : Response of active mudflat of the southern Saurashtra towards Global climatic events of last two millennia as indicated by various climatic proxies.

Climatically, the last two millennia is divided in to four major climatic events viz, Roman Warm Period (*RWP*: ~200 BC–AD 450), Dark Ages Cold Period (*DACP*: 450–950 AD) Medieval Warm Period (*MWP*: 950–1300 AD), Little Ice Age (LIA: 1350–1850 AD), and Modern warming (MW: 1850 AD– Present). To reconstruct the climatic history of last two millennia of Saurashtra peninsula, Gujarat, a sediment core from the active mudflat of Rohisa, southern Saurashtra coast has been investigated. The detrital, productivity and weathering proxies between 40–400 AD indicates warm and humid period which corresponds to *RWP*, followed by short

period of reduced value of proxies between 400–500 AD indicating dry climate corresponding to *DACP*. The region regained the warm and humid conditions between 500–1300 AD corresponding to MWP (Figure 14). Between 1300|1600 AD, for the period represented as *LIA*, existence of warm and humid climate is observed but less warmer than the previous two warm climatic events (*MWP* and *RWP*). The present day climatic conditions were attained since 1800 AD. The present study indicates that the mudflat of Saurashtra responded in accordance with the global climatic events of last two millennia.

*The chronology of the section was established by radiocarbon dates in collaboration with Prof. A.J.T. Jull, NSF-AMS Facility, University of Arizona, Tucson, USA.*

**(U.S. Banerji, N. Juyal and R. Bhushan)**

### Isotopic records from the Great Rann of Kachchh basin sediments, Western India for the last 13ka: Implications to land-marine interaction changes.

The Great Rann of Kachchh (GRK) accumulated huge amount of sediments throughout the post glacial times. The gulf like conditions existed with navigable water column at least from ~2ka to as recent as ~500 yr BP at places. The present day vast and flat monotonous Rann surface is elevated to ~2–6m amsl and undergoes an annual inundation cycle during the monsoonal season. These marginal marine basins sensitive to changes in the land-marine interaction are key to the evolution of the GRK. In the present study, isotopic systematics were employed to reconstruct the land-marine interaction records for past ~17ka using two sediment cores from central and south marginal parts of GRK. The  $\delta^{13}\text{C}$  values for the GRK basin sediments range from -26.9 to -21.0‰ indicating that central GRK basin remained under marine environments throughout during the last ~17ka, however, the southern GRK was flooded by marine waters only after ~9.5 ka BP.

Both the cores show significant temporal  $\delta^{13}\text{C}$  variation indicating increased/decreased terrestrial/marine derived organic matter influx into the basin. The marine  $\delta^{13}\text{C}$  signatures (-21 to -22‰) during late Pleistocene (~17ka BP) to mid Holocene (~7ka BP) in the central GRK indicates predominantly marine environment during this period. Rapid shift at ~7ka BP to -25‰ suggests sudden high influx of terrestrial components. The transition from terrestrial to marine environment was restored again post ~7ka towards the late Holocene. The increasing  $\delta^{13}\text{C}$  values indicate relative increase in marine influence in sediments which punctuated at ~7ka BP showing abrupt decrease indicates enhanced terrestrial influx event. This phenomenon is coeval with the central GRK indicating basin wide changes in the paleoenvironmental conditions ~7ka before present.

*This work is done in collaboration with Prof. D.M. Maurya of M.S. University of Baroda, Vadodara and Dr. R. Agnihotri from NPL, Delhi.*

**(N. Khonde and R. Bhushan)**

### Equatorial Upwelling and nutrient utilization in the northern Indian Ocean during the past 25ka

The northern Indian Ocean experiences seasonally reversing monsoon associated with high winds thereby causing changes in circulation pattern of surface waters in the northern Indian Ocean. To reconstruct the past climate variability for the last 25 ka, a sediment core from located south of Sri Lanka near Equator in the equatorial Indian Ocean was investigated. In addition to the equatorial processes, this region not only records both SW and NE monsoon but also has the reversal patterns of the Arabian Sea and the Bay of Bengal surface waters. The equatorial oceanic regions are known for increased siliceous productivity during enhanced upwelling as a resultant of nutrient utilisation process. The Holocene period is known for intensification of monsoon and thus the productivity. Intensification of the SWM during Holocene has been noticed with the increase in biogenic silica content from 3 to 10%. Decreased C<sub>org</sub> and CaCO<sub>3</sub> flux during LGM indicates weakening of *SWM*. After 14 ka during early deglacial period there was increase in burial flux of CaCO<sub>3</sub> indicating strengthening of the SW monsoon upto 11 ka. The Younger Dryas period (~11ka) shows a rapid decrease in C<sub>org</sub> and CaCO<sub>3</sub> flux with increased biogenic silica concentration.

*The AMS radiocarbon dates were carried out in collaboration with Prof. A.J.T. Jull from NSF-AMS Facility, University of Arizona, Tucson, USA.*

**(K. R. Chandana and R. Bhushan)**

### High-Resolution Paleoclimatic Records from Corals

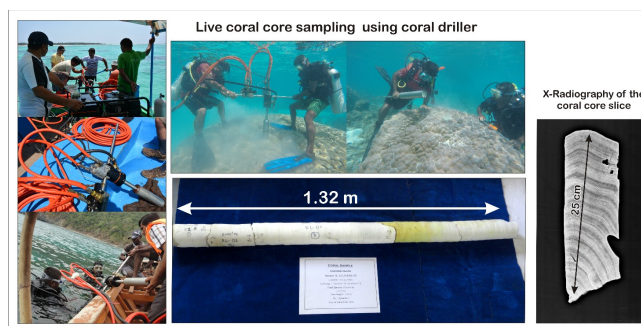


Figure 15 : Demonstration of the underwater coral driller in operation. Coral core section recovered from the Lakshadweep Islands and X-Ray section of the sample showing annual bands.

Corals offers a rich archive of high-resolution past climate variability by recording the changes in ambient surface sea water properties which provides paleoclimatic and paleoceanographic conditions on intra-annual-to-centennial timescales. As part of *GEOTRACES*, scientific programme on corals has been initiated to reconstruct high-resolution paleoclimatic record from the Indian sub-continent based on

coral samples collected from the Gulf of Kachchh, Andaman and Lakshadweep Islands. Towards this, an underwater coral driller has been procured and we have been able to demonstrate the successful operation of underwater coral drilling for the first time with selective coral species identified with massive growth. Several samples of live Coral colonies (Porites) were selected from Gulf of Kachchh, Andaman and Lakshadweep Islands and various cores ranging from 50–200 cm were raised using underwater coral driller (Figure 15).

Presently, these samples are being sub-sampled and being X–radiographed for deciphering the growth rate and calcification rates during last centuries (Figure 15). Geochemistry of corals would provide high-resolution records of upwelling, anthropogenic impacts, salinity, pH and other aspects of the ocean system that occurred during last century and will help in understanding the past changes in ocean chemistry and predicting the future trends in the climate perturbation.

(U.S. Banerji, C.S. Shah and R. Bhushan)

**High-resolution proxy record of precipitation variation during ~5 kyr in Chhattisgarh**

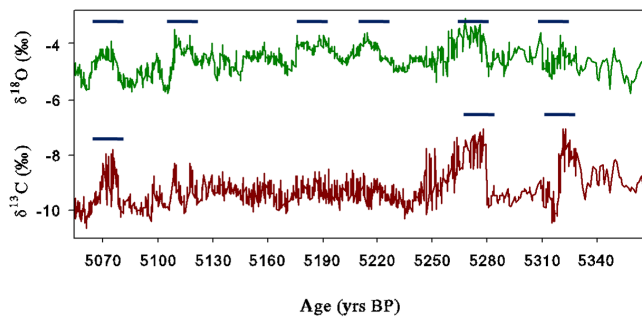


Figure 16 : Stable isotopes of oxygen and carbon show enriched levels (marked by blue lines) indicating low rainfall periods in the record.

Column shaped carbonate deposits, often found in limestone caves can be used to reconstruct past monsoon, sometimes with yearly resolution when they have distinct calcite layers. A stalagmite sample (*KOT-1*) collected from Kotumsar cave, Chhattisgarh, is used to reconstruct high-resolution precipitation record (annual to sub-annual scale) for the time interval 5500–5000 yr BP using stable isotopes of oxygen and carbon ( $\delta^{18}\text{O}$  and  $\delta^{13}\text{C}$ ). Six major drought events are recorded as positive excursion in  $\delta^{18}\text{O}$  values signifying weaker phase of monsoon. These events are contemporaneous to human settlements in the cave based on the radiocarbon dates of burnt earth and charcoal patches suggesting that the caves were shelter to the people during extreme drought conditions. Wavelet analysis on the  $\delta^{18}\text{O}$  time series shows appearance of dominant power for the ~20 year solar cycle clustered at ~5100 yr BP when  $\delta^{18}\text{O}$  had very high depletion in the reconstruction. Solar cycle seems to affect monsoon system which generates regional precipitation heterogeneity.

(S. Band, R. Ramesh and M.G. Yadava)

**Upper Ocean carbon export using  $^{210}\text{Po}/^{210}\text{Pb}$  disequilibrium**

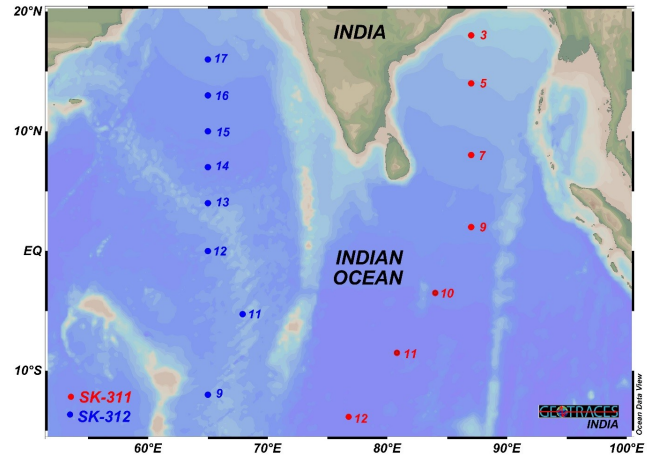


Figure 17 : Station locations where  $^{210}\text{Po}/^{210}\text{Pb}$  profiles were collected during March–May, 2014.

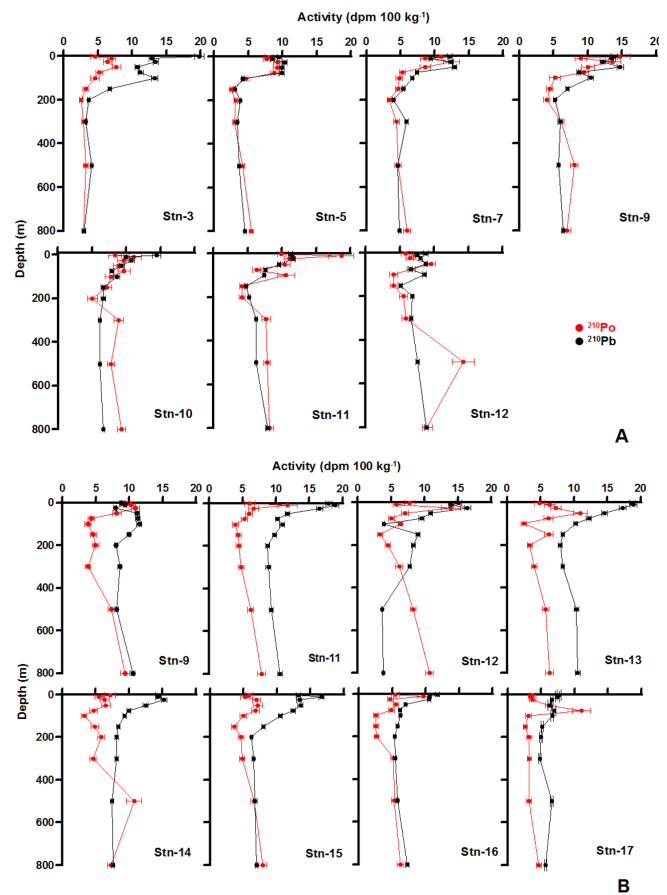


Figure 18 : Vertical distribution of total (dissolved + particulate)  $^{210}\text{Po}$  and  $^{210}\text{Pb}$  along the two transects from the Arabian Sea, Bay of Bengal and the Indian Ocean during (A) SK-311 and (B) SK-312 cruises. Error bars represent uncertainty based on propagated counting errors ( $\pm 1\sigma$ ).

As an interface for exchange of  $\text{CO}_2$  between the surface ocean and interior ocean, the euphotic zone plays a key role

in the production, removal and cycling of biomass. Fluxes within the euphotic zone of carbon, nutrients and other associated elements involved in biogeochemical cycles are very important in the study of global CO<sub>2</sub>. Naturally-occurring particle-reactive radionuclides (<sup>234</sup>Th, <sup>210</sup>Po) provide possible means for quantifying export flux of particulate organic carbon (POC) from the surface ocean at various time scales, because of their specific half-lives. The naturally occurring radionuclide <sup>210</sup>Po is typically deficient relative to its parent <sup>210</sup>Pb in the surface ocean due to preferential removal by biota, while it is in near equilibrium or excess below the surface mixed layer due to rapid regeneration from sinking organic matter.

Seawater profiles for <sup>210</sup>Po and <sup>210</sup>Pb from surface to 800 m water depth were collected at several locations from the Arabian Sea, Bay of Bengal and the Indian Ocean during March–May, 2014 under *GEOTRACES* programme (Figure 17). The Arabian sea, being more productive zone, shows more deficit of <sup>210</sup>Po relative to <sup>210</sup>Pb indicating intense biological removal of <sup>210</sup>Po. Generally surface waters of the Indian Ocean have excess <sup>210</sup>Pb, which increases sharply north of the equator (Figure 18) due to atmospheric input of <sup>210</sup>Pb from continental aerosol. Removal flux of <sup>210</sup>Po relative to <sup>210</sup>Pb from 0–300 m depth from two transects along 87°E and 65°E between 18°N to 14°S ranged widely from 0.03 to 84.4 dpm m<sup>-2</sup>d<sup>-1</sup>. The C/<sup>210</sup>Po ratio in particulates ranged between 239 and 717 μM dpm<sup>-1</sup>. The derived export flux of POC using <sup>210</sup>Po varied from 0.01 to 33.2 mmol m<sup>-2</sup>d<sup>-1</sup> due to the variable source of biogenic particles and spatial changes in the surface biogeochemical and physical conditions.

(R. Rengarajan and S. Anand)

### Understanding secondary organic aerosols formation using online measurements of WSOC at the source region of biomass burning

Carbonaceous aerosols are often the major fraction of fine particles. Among them, secondary organic aerosols (SOA) are documented to be the major component; however, understanding on their formation processes is meager. Emissions from biomass burning have been widely recognized as significant source of primary carbonaceous aerosols as well as precursors of SOA in the atmosphere. Present study was carried out before, during and after large scale paddy-residue burning over Patiala, Punjab, located in the Indo-Gangetic Plain (IGP) during October–November, 2014. The aim of this study was to understand SOA formation processes during biomass burning. Water soluble organic carbon (WSOC), measured online using Particle into Liquid Sampler (PILS) coupled to Total Organic Carbon (TOC) analyzer, exhibited large variability (range: 0.4 to 189 μg m<sup>-3</sup>) during the study period. In parallel, carbon monoxide (CO), nitrogen oxides (NO<sub>2</sub>, NO), and black carbon (BC) were also measured online, and filter-based chemical composition of PM<sub>2.5</sub> was measured offline. The diurnal trends of online WSOC, CO, RH, and NO<sub>x</sub> were somewhat similar Figure 19). Photochemical SOA formation was evident during morning hours (07: 00 to 09: 00 hrs) whereas late evening/night hours

(18: 00 to 22: 00 hrs) WSOC can be attributed to both due to primary emission and/or secondary formation of WSOC. Daytime decrease in the abundance of WSOC, CO and NO<sub>x</sub> is attributed to expansion of boundary layer. During burning period, BC concentrations at 370nm (representing absorption by organic compounds) was ~2 times higher than that at 880 nm (representing absorption by black carbon). This observation suggests that emissions from biomass burning also contain considerable absorbing organic aerosols.

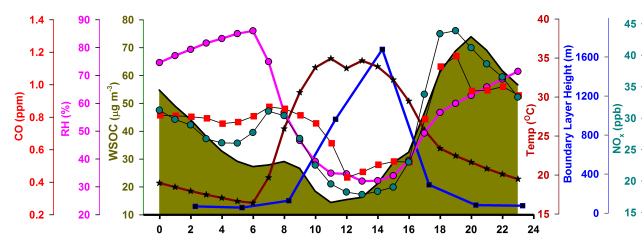


Figure 19 : Diurnal trends of WSOC, RH, CO, Temperature, Boundary layer height and NO<sub>x</sub> during the study period.

*Logistic support for the sample collection was provided by Mr. Atinderpal Singh and Prof. Darshan Singh (Punjabi University, Patiala).*

(R.V. Satish and N. Rastogi)

### First real-time measurement of light absorbing water soluble organic carbon (or Brown Carbon) over India

Until recent years, black carbon (BC) was known as the major light absorbing component in the atmospheric carbonaceous aerosols and their organic portion was completely considered as scattering species. Recent studies have shown that certain type of water soluble organic carbon (WSOC), termed as 'Brown Carbon (BrC)', absorb light from near UV to visible region. Major sources of BrC in the atmosphere can be emissions from biomass burning, fossil fuel burning, or both. However, studies on the sources and characteristics of BrC are very limited.

To study the characteristics of BrC along with WSOC, particle-into-liquid sampler (PILS) was connected to total organic carbon analyzer (TOC) through liquid waveguide capillary cell (LWCC, Figure 20). The LWCC continuously measures the absorbance of water-soluble aerosols coming from PILS, and TOC analyzer measures WSOC at every 4 minutes. This is the first PILS-LWCC-TOC measurement in India and limited in the world. Preliminary results from the measurements carried out over Ahmedabad during March–April, 2015 reveal the higher abundance of BrC during early morning which vanishes during noon and afternoon and appears again during evening rush hours. Such an observation suggests there could be primary and/or secondary sources of BrC during morning and evening hours and likely there is a sink (photo-bleaching of BrC) during noon/afternoon.

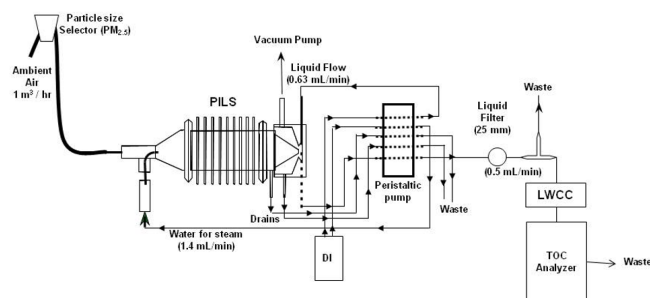


Figure 20 : Schematic diagram of PILS-LWCC-TOC system for real-time measurements of water-soluble organic carbon (and brown carbon). The figure is not to scale.

(R.V. Satish and N. Rastogi)

### Long term study of carbonaceous aerosols over a high altitude site (Mt. Abu) in western India

Carbonaceous aerosols are important fraction of ambient fine particles and their effects range from human health to climate change. The major sources of primary carbonaceous particles are emissions from biomass and fossil fuel burning whereas secondary sources of organic carbon also include biogenic emissions in addition to biomass and fossil fuel burning. Large variability on temporal and spatial scale causes large uncertainty in assessing effects of aerosols. In this regard, remote high altitude sites like Mt Abu are ideal to understand regional aerosol composition and its variability with time. The sampling of particulate matter smaller than 10  $\mu\text{m}$  diameter ( $\text{PM}_{10}$ ) was started at Guru Shikhar, Mt Abu in January 2013 and still continuing. Low-volume ( $\text{PM}_{10}$ ) samples were collected on 47 mm diameter tissue quartz filters and analyzed for aerosol mass and carbonaceous aerosol concentrations. ( $\text{PM}_{10}$ ) mass concentration varied from 36 to 134  $\mu\text{g m}^{-3}$  during the study period with highest concentrations during May (summer) and lowest during January (winter). Organic carbon (OC) and elemental carbon (EC) concentrations varied from 4.6 to 34  $\mu\text{g m}^{-3}$  and 1.0 to 8.4  $\mu\text{g m}^{-3}$ , respectively. Characteristic OC/EC ratio, which indicates the relative dominance of biomass vis-à-vis fossil fuel burning emissions, varied from 2.7 to 14.8. Usually, the OC/EC ratio centers around 4 but goes as high as  $\sim 15$  during summer months. Such studies are very important in assessing the aerosols effects on regional climate.

(A. Patel and N. Rastogi)

### Chemical and isotopic composition of ambient aerosols over the Bay of Bengal: Impact of continental outflow

Biogeochemistry of surface ocean over the northern Indian Ocean can be strongly affected by the transport of pollutants through South and Southeast Asian continental outflow. To understand these effects, long-term monitoring of pollutants

over oceans is necessary; however, it is very difficult due to logistics issues. Islands can be useful sites for such monitoring. This study presents the chemical and isotopic composition of  $\text{PM}_{10}$  collected at Port Blair (PB) island located in the Bay of Bengal (BoB) during the late NE-monsoon (February-April), when the BoB receives considerable continental outflow. These samples ( $n=50$ ) were analyzed for major ions, carbonaceous species and trace metals. Isotopic composition of total C, N and S present in  $\text{PM}_{10}$  were also measured. The mass concentration of  $\text{PM}_{10}$  ranged from 24 to 65  $\mu\text{g m}^{-3}$  during the study period.  $\text{PM}_{10}$  composition was dominated by anthropogenic and organic species ( $\sim 60\%$ ) whereas, EC contributed  $\sim 5\%$ , and sea-salt was only 3% even though the PB is located in the middle of the ocean. Near quantitative chloride depletion from sea-salts (range: 57 to 100%, avg: 98%, sd: 7%) was observed, and attributed to high abundance of non-sea-salt- $\text{SO}_4^{2-}$ . Such an observation indicates the effect of continental pollutants on the marine atmospheric boundary layer. Further, average ( $\pm$  standard deviation) isotopic composition of  $\delta^{13}\text{C}$  ( $-25.61 \pm 0.53$ ),  $\delta^{15}\text{N}$  ( $13.73 \pm 5.06$ ) and  $\delta^{34}\text{S}$  ( $1.06 \pm 0.11$ ) in  $\text{PM}_{10}$  reveals that  $\delta^{15}\text{N}$  exhibits maximum variability. The  $\delta^{13}\text{C}$  showed a positive correlation with WSOC/OC ratio, suggesting the aging of aerosols may affect  $\delta^{13}\text{C}$ .

*Logistic support for the sample collection at Port Blair was provided by Mr. Santosh Kumar Pandey and Dr. S. Suresh Babu (Space Physics Laboratory, Thiruvananthapuram). Isotopic composition of C, N and S was measured by Dr. Rajesh Agnihotri (National Physical Laboratory, New Delhi).*

(N. Rastogi)

### Nitrogen and carbon cycling in a tropical estuary and adjacent coastal region

Estuaries and adjacent coastal regions are vulnerable ecosystems due to increased nutrient loading from anthropogenic activities. Excess nutrients enter the system as organic and inorganic nitrogen (N) and phosphorus (P) compounds through rivers and the atmosphere, and threaten coastal ecosystems. Anthropogenic inputs cause many estuarine-coastal systems to shift drastically from N limitation to an N surplus leading to eutrophication, a major threat to most of the estuaries and coastal waters around the world. At present, our knowledge of N and C cycling, particularly N uptake dynamics and its dependence on N and P distribution in tropical estuaries and the adjacent coastal waters remains rudimentary. Information about the rates of transformation of N and C in such systems is needed to develop mitigation strategies to restore and save the estuarine-coastal coupled systems from eutrophication.

Experiments were conducted to quantify rates of  $\text{NO}_3^-$ ,  $\text{NH}_4^+$ , and C uptake along with  $\text{N}_2$  fixation rates in the Cochin Estuary and coastal Arabian Sea along two transects, viz. off Cochin and Mangalore using stable isotopes tracer techniques. Significantly higher DIN uptake rates in the Cochin estuary and at a near shore location in the adjacent Arabian Sea compared to other coastal locations provided a

clear evidence of anthropogenic effects on N uptake dynamics in the region. Results obtained suggested that nutrients delivered via rivers from anthropogenic activities upstream have the potential ability to modulate the estuarine-coastal biogeochemistry. Measurable  $N_2$  fixation rates despite very high DIN concentrations were observed in the estuary. Significant negative correlations of  $NH_4^+$  uptake and  $N_2$  fixation rates with TN: TP suggested that the N assimilation in the estuary depended more on the relative balance of N and P than on just N or P alone (Figure 21).

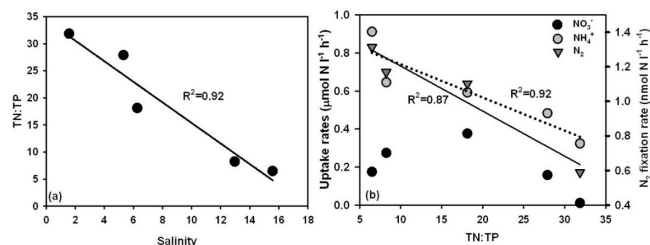


Figure 21 : Relationship between DIN uptake and  $N_2$  fixation rates with TN: TP in the Cochin estuary.

*This work is being done in collaboration with Dr. G.V.M. Gupta of Centre for Marine Living Resources and Ecology, Cochin, India.*

(S. Kumar and P.S. Bhavya)

### Biogeochemistry of freshwater ecosystems

Anthropogenic activities have caused strong alterations in the structure and function of our ecosystems by altering the biogeochemical cycles of major life sustaining elements like nitrogen (N). Humans have approximately doubled the rate of N input into the terrestrial N cycle, and these rates are still increasing. Eutrophication due to N and/or phosphorus (P) loading in a region produces excessive organic matter leading to degradation of water quality. In the future, nutrient loading is likely to increase further as population growth and resource intensification rises, especially due to the use of fertilizer, fossil fuel burning and urbanization. These may cause huge water crisis for country like India with more than a billion people. Our understanding of the biogeochemistry of freshwater systems in India is poor, which is highly required to develop a mitigation strategy to save these systems from the adverse effects of eutrophication.

Aim of this project is to extensively study the biogeochemistry of freshwater ecosystems in India. The major focus has been on freshwater lakes and reservoirs. We intend to sample lakes like Nal Sarovar to study the effect of avian migration on the biogeochemistry of the lake. At present, monthly sampling of an urban lake (Kankaria) situated in Ahmedabad has been started. Preliminary results indicate very high rates of nutrient uptake in the lake with little evidence of  $N_2$  fixation.

(S. Kumar and R. Mukherjee)

### Red boles from Deccan Trap flood basalt province, India: Implications for aqueous alteration and paleoweathering on Mars

Aqueous process and chemical weathering are two major processes that might have played important role in the formation of clay minerals on early Earth and on ancient Mars ( $\sim 4.5$ -3.7 Ga). Weathering profiles of basaltic substrate describe the formation history of clay horizon over geologic time period and refer to the past climatic conditions in which these clay horizons had formed through the aqueous alteration processes of mafic-ultramafic Martian crust. Deccan Continental tholeiitic flood basalts (DFCB) in India, being chemically similar to Martian basalt, are considered potential candidate for Martian crust analogue. Paleosols or Red-boles occurring between the two basalt flows in DCFB are the ideal horizons to infer ancient clay formation process (s).

Mineralogy (using XRD technique) of Deccan red-bole reveals smectite with characteristic peak at  $d=15$  Å. FTIR (doublet at  $457$ - $465$  $cm^{-1}$  and  $523$ - $527$  $cm^{-1}$ ) further confirms they are mostly ferruginous smectite and or near montmorillonite in composition. Altered basalt clasts often found within red-bole show secondary Fe-Ti rinds, usually expected in weathered terrestrial basalts. Compositionally, smectite group of minerals of Deccan Red bole are Al and Fe-rich with  $Al_2O_3$  and  $FeO_t$  up to 21 wt% and 17 wt% respectively and closely correspond to its parent whole-rock composition which shows  $Al_2O_3$  13-14 wt% and  $FeO_t$  20 wt% respectively. These geochemical signatures further reveal that extensive leaching of DCFB mainly accounts for removal of Na, K, Ca and Mg. Similarity in bulk composition of the Deccan red bole and its underlying basalt flow suggests the formation of red bole from underlying basalt through chemical leaching and formation of secondary clay minerals from alteration of primary minerals. By contrast, the overlying basalt flow exhibits the highest Fe and Al content as a result of residual enrichment. Lowest MgO content ( $\sim 1.35$  wt%) of the overlying basalt flow possibly suggest intense leaching of Mg by downward percolation leaving Fe residue. Apart from low temperature hydrothermal alteration, chemical weathering under more specifically acidic conditions often favoured the formation of kaolinite. Therefore, the redbole weathering profile reveals a clear evolution of the chemistry and mineralogy of the altered basalt including the fall out pyroclastics and ashes.

Red bole shows well developed smectite compared to kaolinitic clay of altered basalts and the degree of residual weathering is responsible for such mineralogical contrast.

The Chemical index of alteration or, CIA [mole  $Al_2O_3$ /mole ( $Al_2O_3$ )+ $CaO^*$ + $Na_2O$ + $K_2O$ )], is generally used to assess the degree of chemical rock weathering. In general, CIA of fresh basalts lies between 30 and 45. In contrast, CIA of Deccan red bole reaches up to 80 while its underlying and overlying basalt horizons exhibit the CIA values varying between 62 to 91. Highest CIA value of the overlying altered basalt suggests the removal of mobile elements (Ca,Na, K) as weathering progresses. Our studied red bole samples mostly follow the

terrestrial weathering trend and plot within the smectite field while the overlying basalt falls close to the  $\text{Al}_2\text{O}_3$  apex. Similar trend of terrestrial weathering is also reflected in A–CNK–FM diagram (Figure 22).

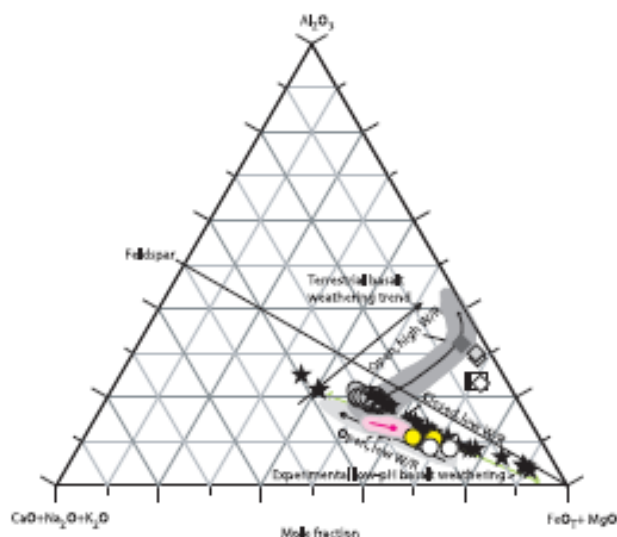


Figure 22 : Recently obtained data on mineralogy, phase composition and bulk chemical composition from Mudstone at Yellowknife Bay of Gale crater (~155 km diameter), Mars is significant from the viewpoint of Noachian age and its location at the dichotomy boundary between northern lowland and heavily cratered southern highland. Since open system, long-term chemical weathering might not prevail on Mars, a closed system, subsurface water-induced chemical weathering on Mars is more important for formation of smectite phyllosilicates (Figure 22).

In summary, the present work suggests that red-bole in DCFB formed due to aqueous alteration of underlying basalt unit and it was further aggravated due to top-down (pedogenesis) leaching process. It is also inferred that the weathering-induced clay formation processes on Earth and Mars were contrasting in nature. The high water-rock ratio (W/R), open system and substantial leaching of soluble elements were predominant on Earth, while on Mars, low W/R, preferably in closed subsurface system and isochemical changes played the major role in the clay formation. It is envisaged that the complex diagenetic processes might have involved in the formation of Martian clays and the currently available in situ analyses of phyllosilicates from sedimentary clays could be one of the possible reason for this contrasting weathering style between the Mars and the Earth.

(A.D. Shukla and D. Ray)

### Geochemical study of Mafic Rocks of the Precambrian terrains of Assam and Western Meghalaya, northeastern India

A geochemical analysis of selected metamorphosed/un-metamorphosed rocks from the Precambrian Terrain had been studied in detail for their geochemical evolution and

possible linkages with their counterpart in the Gondwanaland rocks in the Indian Peninsula. Their importance and significance can be understood in the Alpine Himalayan Orogeny. The rocks in the area are similar to the Precambrian Shield of Peninsular India and are exposed in the Karbi Anglong and Goalpara districts of Assam; East and West Khasi Hills and Garo Hills districts of Meghalaya. Here the Precambrian gneissic complex intruded by several suites of younger granites and enclosing enclaves of metabasic rocks are the lithounits. The Precambrian assemblage are intruded by numerous small, discontinues, intrusive bodies, predominantly dykes of basic igneous and metamorphic rocks. The Significance of the mafic rocks of this region is not well constrained because of lack of systematic study of these rocks. Whole rock geochemical data show trace compatible element contents and high  $\text{Mg}\ddagger$  representatives of primitive magmas.  $\text{Mg}\ddagger$  vs.  $\text{SiO}_2$ ,  $\text{CaO}$  and  $\text{SiO}_2/\text{Al}_2\text{O}_3$ , variation diagrams, trace elements and REE patterns of the rocks are consistent with fractional crystallization. Primitive mantle normalized incompatible trace element concentrations show enriched to mildly enriched LILE (Sr, K, Rb, Ba etc.), LREE (La, Ce, Sm etc.), depleted HFSE (e.g., Ti, Y) and HREE. The bulk rock chemistry of mafic rocks is consistent with an alkaline to tholeiitic magmatism and show basic to intermediate composition. Studied samples are  $\text{SiO}_2$  saturated to under saturated with olivine in the norm, while some are olivine and nepheline normative alkaline olivine basalts.

*This work was carried in collaboration with Dr. M. Bidyananda, Manipur Central University, Imphal.*

(A. D. Shukla)

### Aerosol chemical composition and associated precursor gases over an urban environment in western India: Gas-aerosol equilibrium Characteristics

Atmospheric particulate matter with aerodynamic diameter less than  $2.5 \mu\text{m}$  ( $\text{PM}_{2.5}$ ) has the potential to alter the radiative balance of the Earth by scattering or absorbing radiation and influence cloud microphysics. The bulk of dry, fine-particle mass is inorganic (typically 25-75%), with  $\text{NH}_4^+$ ,  $\text{SO}_4^{2-}$  and  $\text{NO}_3^-$  as main components. In addition,  $\text{Na}^+$ ,  $\text{Cl}^-$ ,  $\text{Ca}^{2+}$ ,  $\text{Mg}^{2+}$  and  $\text{K}^+$  may also be present, associated with crustal and sea-salt sources depending on the location. These species exist in aqueous phase or solid form depending on ambient temperature and relative humidity, and some can get partially volatilized as  $\text{NH}_3$ ,  $\text{HNO}_3$  and  $\text{HCl}$  vapours. Hence, the gas and the particle phases of these semi-volatile constituents are generally assumed to be related through thermodynamic equilibrium partitioning. Inorganic ionic constituents ( $\text{Na}^+$ ,  $\text{NH}_4^+$ ,  $\text{K}^+$ ,  $\text{Mg}^{2+}$ ,  $\text{Ca}^{2+}$ ,  $\text{Cl}^-$ ,  $\text{NO}_3^-$  and  $\text{SO}_4^{2-}$ ) of  $\text{PM}_{2.5}$  and associated trace gases ( $\text{NH}_3$ ,  $\text{HNO}_3$  and  $\text{HCl}$ ) were measured simultaneously by Ambient Ion Monitor - Ion Chromatograph (AIM-IC) system with a time resolution of one hour at Ahmedabad during summer and winter. The average  $\text{NH}_3$ ,  $\text{HNO}_3$  and  $\text{HCl}$  concentrations were  $11.6 \pm 5.0$ ,  $2.9 \pm 0.8$  and  $0.15 \mu\text{g m}^{-3}$ , respectively,

during winter. During summer,  $\text{NH}_3$  and  $\text{HNO}_3$  concentrations were of similar magnitude, whereas  $\text{HCl}$  concentration was less than  $\sim 0.03 \mu\text{g m}^{-3}$ .  $\text{NH}_3$  concentration exhibited a distinct diurnal variation during both seasons. However,  $\text{HNO}_3$  did not show a specific diurnal trend during the observation period in both seasons. The data obtained were used to study gas-aerosol equilibrium characteristics using a thermodynamic equilibrium model, ISORROPIA II. The results suggest that  $\text{NH}_3$  exists in equilibrium between  $\text{PM}_{2.5}$  and gas phase with a systematic bias of  $\sim 14\%$  in model output, whereas  $\text{HCl}$  and  $\text{HNO}_3$  deviate significantly from the modelled data. These observations have implications on thermodynamic equilibrium assumptions used for estimating various aerosol parameters such as liquid water content, pH, etc., thus causing significant bias in chemical transport model results over the study region.

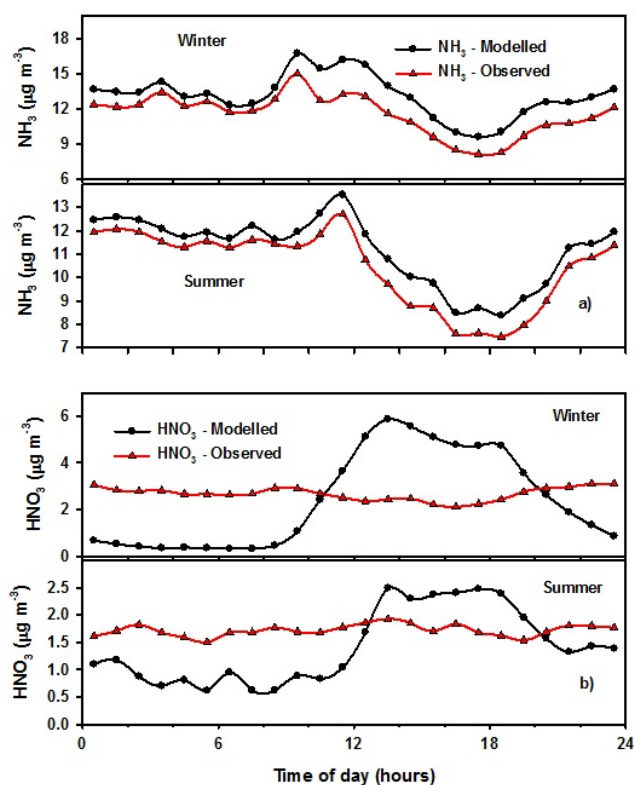


Figure 23 : a) Diurnal variation of observed and modelled  $\text{NH}_3$  concentrations depicting good agreement during both winter and summer. Concentration is overestimated by  $\sim 14\%$  by ISORROPIA II model. b) Diurnal variation of observed and modelled  $\text{HNO}_3$  concentrations during winter and summer depicting a discrepancy in both diurnal trend as well as concentration.

(A. K. Sudheer and R. Rengarajan)

### In-house Development of Low cost Autosampler based on a Robotic Arm

Analysis of liquid samples, especially water samples is an essential process in most chemistry laboratories. During such analyses, manual handling of each sample can become

time-consuming, especially when there are large numbers of samples to be worked upon and likely to add contamination. The varieties of autosamplers are commercially available in the market but they are very costly.



Figure 24 : (a) Autosampler Structure (3D), (b) Autosampler with Robotic Arm and (c) Software User Interface for control.

Here we present an innovative and low cost approach, using a robotic arm, to perform contamination free handling of liquid samples. It consists of a robotic arm with control electronics and has provision of handling 42 samples in a single run. In this approach, a robotic arm reaches to sample

bottles as per the user determined sequence and a sampling tube attached to its arm gripper is inserted into the sample bottles for suction. The arm movement calculations are based on inverse kinematics approach. The autosampler can be integrated with any analytical instrument making it useful for various liquid sampling applications such as measuring concentration of different ions in water or any liquid samples. The setup has demonstrated reliable results and is currently attached to Flow-Injection System for measuring dissolved iron in seawater samples.

**(M. Shah, H. Vaghela and L. Vora)**

### **Evidence for acid processing of mineral dust during atmospheric transport from the Indo-Gangetic Plain**

Atmospheric transport of chemical constituents from the Indo-Gangetic Plain (IGP) to the Bay of Bengal is a conspicuous seasonal feature occurring during the late NE-monsoon (January-March). With this perspective, aerosol composition and abundance of mineral dust have been studied from a sampling site (Kharagpur: 22.3°N, 87.3°E), representing the atmospheric outflow to the Bay of Bengal. The chemical composition of PM<sub>2.5</sub> suggests dominance of nss-SO<sub>4</sub><sup>2-</sup> (6.9–24.3 μg m<sup>-3</sup>); whereas the abundance of mineral dust varied from 3 to 18 μg m<sup>-3</sup>. The concentration of aerosol iron (Fe<sub>Tot</sub>) and its fractional solubility (Fe<sub>ws</sub>% = Fe<sub>ws</sub>/Fe<sub>Tot</sub>\*100, where Fe<sub>ws</sub> is water-soluble fraction of Fe<sub>Tot</sub>) varied from 60 to 1144 ng m<sup>-3</sup> and from 6.7 to 26.5%, respectively. A striking similarity in the temporal variability of total inorganic acidity (TIA = NO<sub>3</sub><sup>-</sup> + nss-SO<sub>4</sub><sup>2-</sup>) and Fe<sub>ws</sub> (%) provides evidence for acid processing of mineral dust (alluvium) during atmospheric transport from the IGP. Contribution of TIA to water-soluble inorganic species [(nss-SO<sub>4</sub><sup>2-</sup> + NO<sub>3</sub><sup>-</sup>)/ΣWSIS], mass ratios of Ca/Al and Fe/Al, abundance of dust (%) and Fe<sub>ws</sub> (%) in the IGP-outflow are similar to the aerosol composition over the Bay of Bengal. With the rapid increase in anthropogenic activities over south and south-east Asia, the enhanced fractional solubility of aerosol iron (attributed to acid processing of mineral dust) has implications to further increase the air-sea deposition of Fe to the surface ocean.

**(B. Srinivas, M.M. Sarin and R. Rengarajan)**

### **Aerosol organic carbon-to-organic mass conversion factor in the continental outflow**

Based on quantitative assessment of individual components of PM<sub>2.5</sub> [mineral dust, organic carbon and elemental carbon (OC and EC), water-soluble organic carbon (WSOC) and inorganic species (WSIS)], we have assessed aerosol organic carbon-to-organic mass (OC to OM) conversion factor centring at 1.5 ± 0.2 (range: 1.3 – 2.7) in the atmospheric outflow from the Indo-Gangetic Plain (IGP). Diagnostic ratios of carbonaceous species [OC/EC ≈ 7.0 ± 2.2, WSOC/OC ≈ 0.52 ± 0.16, and K<sup>+</sup>/EC ≈ 0.48 ± 0.17] suggest dominant impact from biomass burning emissions (wood-fuel and post-harvest agricultural-waste burning). Although aerosol composition over the Bay of Bengal shows striking similarity with diagnostic ratios documented for the IGP-outflow, relatively high conversion factor (Range: 1.1 – 3.7) for organic aerosol mass over the oceanic region provide evidence for oxidation during long-range atmospheric transport.

**(B. Srinivas and M.M. Sarin)**

### **Atmospheric deposition of phosphorus to the Northern Indian Ocean**

Air-sea deposition of phosphorous is an important external source of this macro-nutrient for ocean primary productivity. Although global budgets have shown that atmospheric input of phosphorous is comparable to its riverine supply, studies on regional scale are rather limited. Our case study of the Northern Indian Ocean summarizes sources and atmospheric pathway of phosphorous to the surface ocean. The water-soluble aerosol phosphorous (P<sub>1<sub>org</sub></sub>) concentration is significantly high over Bay of Bengal (BoB) compared to that over the Arabian Sea (ARS). Relative increase in the supply of aerosol-P over BoB is attributed to acid-processing of mineral dust during long-range atmospheric transport in addition to its supply from anthropogenic sources. Our estimate of P-deposition to the Northern Indian Ocean (~ 1.2 Gmol-P yr<sup>-1</sup>) is comparable to its atmospheric deposition over other oceanic regions (North Atlantic: ~ 0.2 Gmol-P yr<sup>-1</sup> by Baker et al., 2010; ~ 0.22 Gmol-P yr<sup>-1</sup> by Mahowald et al., 2008), and is consistent with the model based projections for the Northern Indian Ocean (~ 1.2 Gmol-P yr<sup>-1</sup> by Duce et al., 1991; ~ 1.4 Gmol-P yr<sup>-1</sup> by Okin et al., 2010; ~ 0.4 Gmol-P yr<sup>-1</sup> by Mahowald et al., 2008). These results highlight the importance of atmospheric source in influencing the biogeochemical cycle of phosphorous in the Northern Indian Ocean.

**(B. Srinivas and M.M. Sarin)**

# SCIENCE at PRL

## Theoretical Physics

### Top polarisation measurement and anomalous Wtb couplings

Kinematical distributions of the decay products of the top quark carry information on the polarisation of the top as well as on any possible new physics in the decay of the top quark. In this work, observables were constructed in the form of asymmetries in the kinematical distributions to probe their effects. Charged-lepton angular distributions in the decay are insensitive to anomalous couplings and are a sensitive measure of top polarisation. However, these are difficult to measure in the case of highly boosted top quarks as compared to energy distributions of decay products. These are then sensitive, in general, to both top polarisation and top anomalous couplings. Various asymmetries are compared for their sensitivities to the polarisation of the top quark as well as to possible new physics in the Wtb vertex, paying special attention to the case of highly boosted top quarks. A  $\chi^2$  analysis is performed to determine the regions in the polarisation of the top quark and the couplings of the Wtb vertex constrained by different combinations of the asymmetries.

*This work was done in collaboration with Arun Prasath and R.M. Godbole of CHEP, Indian Institute of Science, Bengaluru.*

(S.D. Rindani)

### Contact fermion-Higgs interactions at an $e^+e^-$ collider with polarized beams

The possibility is considered that new physics can be represented by contact interactions giving rise to interaction vertices of the form  $e^+e^-Hf\bar{f}$ , where  $f$  represents a charged lepton  $\ell$  or a (light) quark  $q$ , and  $H$  the recently discovered Higgs boson. Such vertices would give contributions beyond the standard model to the Higgs production processes  $e^+e^- \rightarrow H\ell^+\ell^-$  and  $e^+e^- \rightarrow Hq\bar{q}$  at a future  $e^+e^-$  collider. Writing the most general form for these vertices allowed by Lorentz symmetry, and assuming that such contact interactions contribute in addition to the standard model production processes, where the final-state fermion pair comes from the decay of Z boson, several observables with differing CP and T properties in the process  $e^+e^- \rightarrow H\ell^+\ell^-$  are proposed. These, if measured, can be used to constrain the couplings occurring in contact interaction vertices. Limits on these couplings that may be obtained at a collider with centre-of-mass energy of 500 GeV and an integrated luminosity of 500 fb<sup>-1</sup> are obtained, assuming that both electron positron beams can be longitudinally polarized, and find that the sensitivity can be improved by a specific choice of the signs of the polarizations of the electron and positron beams.

*This work was done in collaboration with K. Huitu of the University of Helsinki, Finland, K. Rao of IIT Bombay, Mumbai and Pankaj Sharma of the University of Adelaide, Australia.*

(S.D. Rindani)

### New Physics in $e^+e^- \rightarrow Z\gamma$ at the ILC with polarized beams: Explorations beyond conventional anomalous triple gauge boson coupling

One of the most-studied signals for physics beyond the standard model in the production of gauge bosons in electron-positron collisions is that due to the anomalous triple gauge boson couplings in the  $Z\gamma$  final state. In this work, we study the implications of this at the ILC with polarized beams for signals that go beyond traditional anomalous triple neutral gauge boson couplings. Attention is drawn to a dimension-8 CP-conserving  $Z\gamma Z$  vertex that has not found mention in the literature. A systematic study of the anomalous couplings in general terms was carried out and a classification was arrived at. Further, linear-order distributions with and without CP violation were obtained. A correspondence is set up between the triple gauge boson couplings and the four-point contact interactions. Also presented are sensitivities on these anomalous couplings, which will be achievable at the ILC with realistic polarization and luminosity.

*This work was done in collaboration with B. Ananthanarayan and J. Lahiri of CHEP, IISc, Bengaluru, and M. Patra of TIFR, Mumbai.*

(S.D. Rindani)

### Flavour antisymmetry

Consequences of assuming (i) that the (Majorana) neutrino mass matrix  $M_\nu$  displays flavour antisymmetry,  $S_\nu^T M_\nu S_\nu = -M_\nu$  with respect to some discrete symmetry  $S_\nu$  contained in  $SU(3)$  and (ii)  $S_\nu$  together with a symmetry  $T_l$  of the Hermitian combination  $M_l M_l^\dagger$  of the charged lepton mass matrix forms a finite discrete subgroup  $G_f$  of  $SU(3)$  whose breaking generates these symmetries. Assumption (i) leads to at least one massless neutrino and allows only four textures for the neutrino mass matrix in a basis with a diagonal  $S_\nu$  if it is assumed that the other two neutrinos are massive. Two of these textures contain a degenerate pair of neutrinos. Assumption (ii) can be used to determine the neutrino mixing patterns. We work out these patterns for two major group series  $\Delta(3N^2)$  and  $\Delta(6N^2)$  as  $G_f$ . It is found that all  $\Delta(6N^2)$  and  $\Delta(3N^2)$  groups with even  $N$  contain some elements which can provide appropriate  $S_\nu$ . Mixing patterns can be determined analytically for these groups and it is found that only one of the four allowed neutrino mass textures is consistent with the observed values of the mixing angles  $\theta_{13}$  and  $\theta_{23}$ . This texture corresponds to one massless and a degenerate pair of neutrinos which can provide the solar pair in the presence of some perturbations. The well-known groups  $A_4$  and  $S_4$  provide examples of the groups in respective series allowing correct  $\theta_{13}$  and  $\theta_{23}$ . An explicit example based on  $A_4$  and displaying a massless and two quasi degenerate neutrinos is discussed.

(A. S. Joshipura)

### Generalized mu tau symmetry

The generalized mu tau interchange symmetry in the leptonic mixing matrix  $U$  corresponds to the relations  $|U_{\mu i}| = |U_{\tau i}|$  with  $i = 1, 2, 3$ . It predicts maximal atmospheric mixing and maximal Dirac CP violation given  $\theta_{13} \neq 0$ . We show that the generalized  $\mu$ - $\tau$  symmetry can arise if the charged lepton and neutrino mass matrices are invariant under specific residual symmetries contained in the finite discrete subgroups of  $O(3)$ . The groups  $A_4$ ,  $S_4$  and  $A_5$  are the only such groups which can entirely fix  $U$  at the leading order. The neutrinos can be (a) non-degenerate or (b) partially degenerate depending on the choice of their residual symmetries. One obtains either vanishing or very large  $\theta_{13}$  in case of (a) while only  $A_5$  can provide  $\theta_{13}$  close to its experimental value in the case (b). We provide an explicit model based on  $A_5$  and discuss a class of perturbations which can generate fully realistic neutrino masses and mixing maintaining the generalized mu-tau symmetry in  $U$ . Our approach provides generalization of some of the ideas proposed earlier in order to obtain the predictions,  $\theta_{23} = \pi/4$  and  $\delta_{CP} = \pm\pi/2$ .

*This work is done in collaboration with Ketan M. Patel from INFN, Padova, Italy.*

(A. S. Joshipura)

### Thawing quintessence from the inflationary epoch to today

By considering observational constraints from the recent Union2.1 Supernova type Ia data, the baryon acoustic oscillations data, the cosmic microwave background shift parameter measurement by Planck and the observational Hubble parameter  $H(z)$  data we obtain a lower bound on the initial value of the quintessence field in thawing quintessence models of dark energy. For potentials of the form  $V(\phi) \sim \phi^{\pm 2}$  we find that the initial value  $|\phi_i| > 7 \times 10^{18} \text{ GeV}$ . Also, for other monomial potentials we obtain  $|\phi_i| > O(M_{Pl})$ , the reduced Planck mass. We relate  $\phi_i$  to the duration of inflation by assuming that the initial value of the quintessence field is determined by quantum fluctuations of the quintessence field during inflation. From the lower bound on  $\phi_i$  we obtain a lower bound on the number of e-foldings of inflation, namely,  $N > 2 \times 10^{11}$ .

*This work was done in collaboration with Anjan A. Sen of Jamia Milia Islamia, New Delhi.*

(G. Gupta and R. Rangarajan)

### Revisiting a pre-inflationary radiation era and its effect on the CMB power spectrum

We revisit the scenario where inflation is preceded by a radiation era by considering that the inflaton too could have

been in thermal equilibrium early in the radiation era. Hence we take into account not only the effect of a pre-inflationary era on the inflaton mode functions but also that of a frozen thermal distribution of inflaton quanta. We discuss the issues relevant to our scenario of a pre-inflationary radiation dominated era and obtain the scalar power spectrum for this scenario. We find that the power spectrum is free from infrared divergences. We use the WMAP and Planck data to determine the constraints on the inflaton comoving 'temperature' and on the duration of inflation. We find that the best fit value of the duration of inflation is less than 1 e-folding more than what is required to solve cosmological problems, while only an upper bound on the inflaton temperature can be obtained.

*This work was done in collaboration with Suratna Das of IIT Kanpur and Jayanti Prasad of IUCAA, Pune.*

**(G. Goswami and R. Rangarajan)**

### Nonthermal CP Violation in Soft Leptogenesis

Soft leptogenesis is a mechanism which generates the matter-antimatter asymmetry of the Universe via the out-of-equilibrium decays of heavy sneutrinos in which soft supersymmetry breaking terms play two important roles: they provide the required CP violation and give rise to the mass splitting between otherwise degenerate sneutrino mass eigenstates within a single generation.

This mechanism is interesting because it can be successful at a lower temperature regime  $T \lesssim 10^9 \text{ GeV}$  in which the conflict with the overproduction of gravitinos can possibly be avoided. In earlier works the leading CP violation is found to be nonzero only if finite temperature effects are included. By considering generic soft trilinear couplings, we find two interesting consequences: 1) the leading CP violation can be nonzero even at zero temperature realizing nonthermal CP violation and 2) the CP violation is sufficient even far away from the resonant regime allowing soft supersymmetry breaking parameters to assume natural values at around the TeV scale. We discuss phenomenological constraints on such scenarios and conclude that the contributions to charged lepton flavor violating processes are close to the sensitivities of present and future experiments.

*This work was done in collaboration with Rathin Adhikari and Arnab Dasgupta of Jamia Millia Islamia, New Delhi, and Chee Sheng Fong of Universidade de Sao Paulo, Brazil.*

**(R. Rangarajan)**

### Explaining the CMS $eejj$ and $e\phi_T jj$ Excess and Leptogenesis in Superstring Inspired $E_6$ Models

We show that superstring inspired  $E_6$  models can explain both the recently detected excess  $eejj$  and  $e\phi_T jj$  signals at CMS, and also allow for leptogenesis. Working in a R-parity

conserving low energy supersymmetric effective model, we show that the excess CMS events can be produced via the decay of exotic sleptons in Alternative Left-Right Symmetric Model of  $E_6$ , which can also accommodate leptogenesis at a high scale. On the other hand, either the  $eejj$  excess or the  $e\phi_T jj$  excess can be produced via the decays of right handed gauge bosons, but some of these scenarios may not accommodate leptogenesis as there will be strong  $B - L$  violation at low energy, which, along with the anomalous fast electroweak  $B + L$  violation, will wash out all baryon asymmetry. Baryogenesis below the electroweak scale may then need to be implemented in these models.

**(M. Dhuria, C. Hati, R. Rangarajan and U. Sarkar)**

### The $eejj$ Excess Signal at the LHC and Constraints on Leptogenesis

We review the non-supersymmetric (Extended) Left-Right Symmetric Models (LRSM) and low energy  $E_6$ -based models to investigate if they can explain both the recently detected excess  $eejj$  signal at CMS and leptogenesis. The  $eejj$  excess can be explained from the decay of the right-handed gauge bosons ( $W_R$ ) with mass  $\sim \text{TeV}$  in certain variants of the LRSM (with  $g_L \neq g_R$ ). However such scenarios can not accommodate high-scale leptogenesis. Other attempts have been made to explain leptogenesis while keeping the  $W_R$  mass almost within the reach of the LHC by considering the resonant leptogenesis scenario in the context of the LRSM for relatively large Yukawa couplings. However this may not be feasible due to washout of the lepton asymmetry by certain processes. Therefore we consider three effective low energy subgroups of the superstring inspired  $E_6$  model having a number of additional exotic fermions which provides a rich phenomenology to be explored. We however find that these three effective low energy subgroups of  $E_6$  too cannot explain both the  $eejj$  excess signal and leptogenesis simultaneously.

**(M. Dhuria, C. Hati, R. Rangarajan and U. Sarkar)**

### Falsifying leptogenesis for a TeV scale $W_R^\pm$ at the LHC

We study the left-right symmetric extensions of the Standard Model (LRSM) and point out that the discovery of a right-handed charged gauge boson  $W_R^\pm$  with mass in the TeV range will have profound consequences for leptogenesis. We consider the LRSM with both triplet and doublet Higgs scalars, and in both the cases we find that if the  $W_R^\pm$  with mass of around a few TeV is found, for example through a signal of two leptons and two jets that has been reported by CMS to have a  $2.8\sigma$  local excess over the Standard Model background at the LHC, then it will rule out all possibilities of leptogenesis. In that case, the baryon asymmetry of the universe has to be generated after the electroweak phase transition and from the baryon number violation that can give rise to neutron-antineutron oscillation or  $(B - L)$  violating proton decay.

**(M. Dhuria, C. Hati, R. Rangarajan and U. Sarkar)**

### Identifying and resolving the degeneracies in neutrino oscillation parameters in current experiments

The three major unknown neutrino oscillation parameters at the present juncture are the mass hierarchy, the octant of the 2-3 mixing angle and the CP phase. It is well known that the presence of hierarchy-CP and octant degeneracies affects the unambiguous determination of these parameters. In this paper we show a comprehensive way to study the remaining parameter degeneracies in the form of generalized hierarchy-  $\theta_{23} - \delta_{CP}$  degeneracy. This is best depicted as contours in the test  $\theta_{23} - \delta_{CP}$  plane for different representative true values of parameters. We show that depending on whether the wrong-hierarchy and/or wrong-octant solutions occur in this plane with wrong or right value of  $\delta_{CP}$  a total of eight different possibilities can exist. These multiple solutions, apart from affecting the determination of the true hierarchy and octant, also affect the accurate estimation of  $\delta_{CP}$ . We identify which of these eight different degenerate solutions can occur in the test  $\theta_{23} - \delta_{CP}$  parameter space, taking the long-baseline experiment  $\text{NO}\nu\text{A}$  running in the neutrino mode as an example. Inclusion of the  $\text{NO}\nu\text{A}$  antineutrino run removes the wrong-octant solutions appearing with both right and wrong hierarchy. Adding T2K data to this resolve the wrong hierarchy – right octant solutions to a large extent. The remaining wrong hierarchy solutions can be removed by combining  $\text{NO}\nu\text{A} + \text{T2K}$  with atmospheric neutrino data. We demonstrate this using ICAL@INO as the prototype atmospheric neutrino detector. We find that the degeneracies can be resolved at the  $2\sigma$  level by the combined data set, for the true parameter space considered in the study.

*This work was done in collaboration with Pomita Ghosal from LNM IIT Jaipur and Sushant Raut from Royal. Inst. Tech. Stockholm.*

(S. Goswami, M. Ghosh and N. Nath)

### Economizing the LBNE configuration with current experiments

The LBNE superbeam experiment in Fermilab (renamed recently as DUNE) is one of the proposed next generation neutrino facilities. Its aims include measuring the unknown neutrino oscillation parameters – the neutrino mass hierarchy, the octant of the mixing angle  $\theta_{23}$  and the CP violating phase  $\delta_{CP}$ . The current and upcoming experiments T2K,  $\text{NO}\nu\text{A}$  and ICAL@INO will also be collecting data for the same measurements. In this paper, we explore the sensitivity reach of LBNE in combination with these other experiments. We evaluate the least exposure required by LBNE to determine the above three unknown parameters with reasonable confidence. We find that for each case, the inclusion of data from T2K,  $\text{NO}\nu\text{A}$  and ICAL@INO help to achieve the same sensitivity with a reduced exposure from LBNE thereby helping to economize the configuration. We also quantify the effect of the proposed near detector on systematic errors and study the consequent improvement in sensitivity. We also examine the role played by the

second oscillation cycle in furthering the physics reach of LBNE. Finally, we optimize the neutrino-antineutrino running of LBNE.

*This work was done in collaboration with Sushant Raut from Royal. Inst. Tech. Stockholm.*

(S. Goswami and M. Ghosh)

### Can the hint of $\delta_{CP}$ indicate the neutrino mass hierarchy and the octant of 2-3 mixing angle ?

The T2K experiment running in the neutrino mode has already provided a hint for the best-fit value of -90 degrees for the leptonic CP phase. We show that if this is confirmed by future neutrino runs of T2K then that will simultaneously indicate the mass hierarchy to be normal and the octant of the 2-3 mixing angle to be higher, i.e. a value greater than 45 degrees. This is due to the fact that with only neutrino data the other combinations of hierarchy and octant admit degenerate solutions at other CP values as well, thus precluding an unambiguous hint for CP phase = -90 degree. We also show that the main role of antineutrino data in improving CP sensitivity is to remove the degenerate solutions with the wrong octant of the 2-3 mixing angle. Thus the antineutrino run will be useful for those hierarchy and octant combinations where this degeneracy is present. If this degeneracy is absent then better sensitivity is obtained from only neutrino run due to higher statistics.

*This work was done in collaboration with Sushant Raut from Royal. Inst. Tech. Stockholm.*

(S. Goswami and M. Ghosh)

### TeV Scale Left-Right Symmetry and Large Mixing Effects in Neutrinoless Double Beta Decay

We revisit various contributions to neutrinoless double beta decay ( $0\nu\beta\beta$ ) in a TeV-scale left-right symmetric model (LRSM) for type-I seesaw dominance. We show that the momentum-dependent effects due to  $W_L - W_R$  exchange ( $\lambda$  diagram) and  $W_L - W_R$  mixing ( $\eta$  diagram) could give dominant contributions to the  $0\nu\beta\beta$  amplitude in a wide range of the LRSM parameter space with large left-right neutrino mixing. In particular, for a relatively large  $W_L - W_R$  mixing, the  $\eta$  contribution by itself could saturate the current experimental limit on the  $0\nu\beta\beta$  half-life, thereby providing stringent constraints on the relevant LRSM parameters, complementary to the indirect constraints derived from lepton-flavor-violating observables. In a simplified scenario parametrized by a single light-heavy neutrino mixing, the inclusion of the  $\lambda$  and  $\eta$  contributions leads to significantly improved  $0\nu\beta\beta$  constraints on the light-heavy neutrino mixing as well as on the  $W_L - W_R$  mixing parameters. We also present a concrete TeV-scale LRSM setup, where the mixing

effects are manifestly enhanced, and discuss the interplay between  $0\nu\beta\beta$ , lepton flavor violation, and electric dipole moment constraints.

*This work was done in collaboration with Manimala Mitra from University of Durham and P.S.B. Bhupal Dev from University of Manchester.*

(S. Goswami)

### Looking for hints of a reconstructible seesaw model at the Large Hadron Collider

We study the production of heavy neutrinos at the Large Hadron Collider through the dominant  $\gamma$ -channel production mode as well as the vector boson fusion process. We consider the TeV scale minimal linear seesaw model containing two heavy singlets with the opposite lepton number. This model is fully reconstructible from oscillation data apart from an overall normalization constant which can be constrained from the metastability of the electroweak vacuum and bounds coming from lepton flavor violation searches. The Dirac nature of heavy neutrinos in this model implies suppression of the conventional same-sign-dilepton signal at the Large Hadron Collider. We analyze the collider signatures with the trilepton final state and missing transverse energy as well as vector boson fusion type signals which are characterized by two additional forward tagged jets. Our investigation reveals that due to stringent constraints on light-heavy mixing coming from lepton flavor violation and metastability bounds, the model can be explored only for a light to moderate mass range of heavy neutrinos. We also note that in case of a positive signal, flavor counting of the final trilepton channel can give information about the mass hierarchy of the light neutrinos.

(S. Goswami, G. Bambhaniya, S. Khan, P. Konar and T. Mondol)

### Boundedness of scalar potential utilising copositivity

To understand physics beyond the standard model it is important to have the precise knowledge of Higgs boson and top quark masses as well as strong coupling. A recently discovered new boson which is likely to be the standard model Higgs with mass 123-127 GeV has a submissive impact on the stability of the new physics beyond standard model. The beyond standard model scenarios that include many scalar fields possess scalar potential with many quartic couplings. Due to the complicated structures of such scalar potentials it is indeed difficult to adjudicate the stability of the vacuum. Thus one needs to formulate a proper prescription for computing the vacuum stability criteria. In this work we have used the idea of copositive matrices to deduce the conditions that guarantee the boundedness of the scalar potential. We have discussed the basic idea behind the copositivity and then used that to determine the vacuum stability criteria for the left-right

symmetric models with doublet and triplet scalars and Type-II seesaw. As this idea is based on the strong mathematical arguments, it helps to compute simple and unique stability criteria embracing the maximum allowed parameter space. Let us consider a symmetric matrix of order three:

$$S_3 = \begin{pmatrix} \lambda_{11} & \lambda_{12} & \lambda_{13} \\ & \lambda_{22} & \lambda_{23} \\ & & \lambda_{33} \end{pmatrix}$$

This matrix copositive if and only if,

$$\lambda_{ii} \geq 0, \quad \lambda_{ij} + \sqrt{\lambda_{ii}\lambda_{jj}} \geq 0, \\ \sqrt{\prod_{i=1,2,3} \lambda_{ii} + \sum_{i,j,k} \lambda_{ij} \sqrt{\lambda_{kk}} + \sqrt{2 \prod_{i,j,k} (\lambda_{ij} + \sqrt{\lambda_{ii}\lambda_{jj}})}} \geq 0,$$

where  $\{i, j, k\} = \text{Permutation of } \{1, 2, 3\}$  with  $i < j$ .

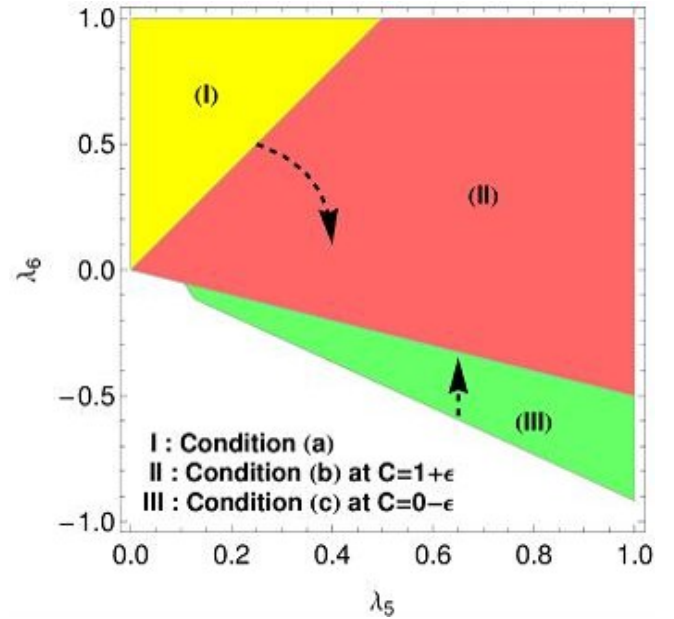


Figure 1 : Demonstration how the unphysical parameters are eliminated requiring maximisation on parameters space. This is shown with an order three field direction for an L-R symmetric model with triplet scalar.

*This work was done in collaboration with J. Chakraborty of IIT Kanpur.*

(P. Konar and T. Mondal)

### Semi-invisible production at Large Hadron Collider exploring with constrained variables

Mass variable  $S_{min}$  and its variants were constructed by minimising the parton level center of mass energy that is consistent with all inclusive measurements. They were proposed to have the ability to measure mass scale of new physics in a fully model independent way. In this work

we relax the criteria by assuming the availability of partial informations of new physics events and thus constraining this mass variable even further. Starting with two different classes of production topology, i.e. antler and non-antler, we demonstrate the usefulness of these variables to constrain the unknown masses. This discussion is illustrated with different examples, from the standard model Higgs production and beyond standard model resonance productions leading to semi-invisible production. We also utilise these constrains to reconstruct the semi-invisible events with the momenta of invisible particles and thus improving the measurements to reveal the properties of new physics.

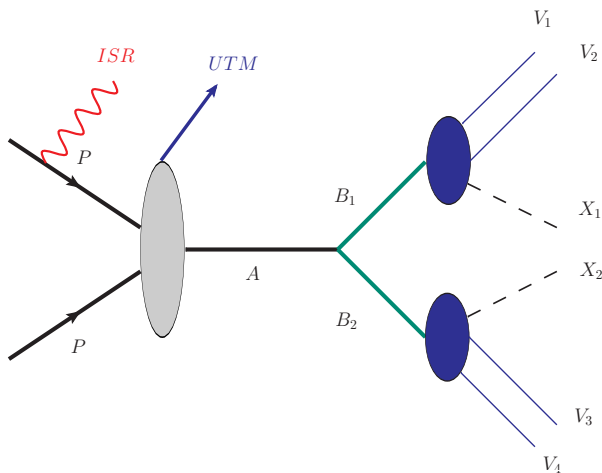


Figure 2 : Representative for a simple antler topology produced at the large hadron collider.

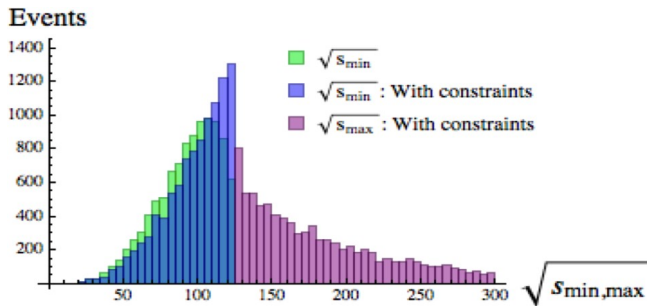


Figure 3 : Shows the distribution of two constrained variables having sharp endpoint/ threshold at true resonant mass.

(P. Konar and A.K. Swain)

### Permanent electric dipole moments of closed-shell atoms

Electric dipole moment (EDM) of a closed-shell (diamagnetic) system arises predominantly due to the parity (P) and time-reversal (T) violating (P,T-odd) electron-nucleus tensor-pseudotensor (T-PT) and nuclear Schiff moment (NSM) interactions. Measurements of EDMs of the  $^{223}\text{Rn}$ ,  $^{199}\text{Hg}$  and  $^{225}\text{Ra}$  atoms have been reported so far, among

which the  $^{199}\text{Hg}$  result is the most precise. By employing a number of relativistic many-body methods and combining the calculations with the measurements we determine the limits on the T-PT coupling constant  $C_T < 2.09 \times 10^{-9}$  and the NSM  $S < 1.45 \times 10^{-12} |e|fm^3$  respectively. Using the nuclear models and from the above limit on NSM, we further yield limits on the strong CP-violating parameter  $\theta_{QCD} < 1.1 \times 10^{-9}$  and the combined up and down quark chromo-EDMs  $(d_u - d_d) < 2.8 \times 10^{-26} |e|cm$  respectively.

*This work is done in collaboration with B. P. Das of Indian Institute of Astrophysics, Bangalore.*

(Y. Singh and B. K. Sahoo)

### Relativistic Equation of Motion Coupled-cluster Method for Excited States of the Closed-shell Systems

We have implemented the equation-of-motion coupled-cluster (EOMCC) method in the four-component relativistic framework with the spherical atomic potential to generate the excited states for the closed-shell atomic systems. This development will be very useful to carry out the required theoretical study in many systems where high precision results are in demand. We have applied the method to calculate the excitation energies of many low-lying states in a few Ne-like highly charged ions, such as Cr XV, Fe XVII, Co XVIII and Ni XIX, and compare them against their corresponding experimental values to demonstrate the successful implementation of the method. The considered ions are apt to substantiate accurate inclusion of the relativistic effects in the evaluation of the atomic properties that are interesting for the astrophysical studies.

(D. K. Nandy, Y. Singh and B. K. Sahoo)

### Precise estimate of quadrupole shifts for the $Yb^+$ atomic clock transitions

Quadrupole shifts for three prominent clock transitions,  $[4f^{14}6s]^2S_{1/2} \rightarrow [4f^{14}5d]^2D_{3/2}$ ,  $[4f^{14}6s]^2S_{1/2} \rightarrow [4f^{14}5d]^2D_{5/2}$  and  $[4f^{14}6s]^2S_{1/2} \rightarrow [4f^{13}6s^2]^2F_{7/2}$ , in the  $Yb^+$  ion are investigated by calculating the quadrupole moments ( $\Theta_s$ ) of the  $5d_{3/2,5/2}$  and  $4f_{7/2}$  states using the relativistic coupled-cluster (RCC) methods. We find an order difference in the  $\Theta$  value of the  $4f_{7/2}$  state between our calculation and the experimental result, but our result concurs with the other calculations that are carried out using different many-body methods than ours. However, our  $\Theta$  value of the  $5d_{3/2}$  state is in good agreement with the available experimental result and becomes more precise till date to estimate the quadrupole shift of the  $[4f^{14}6s]^2S_{1/2} \rightarrow [4f^{14}5d]^2D_{3/2}$ , clock transition more accurately. To justify the accuracies in our calculations, we have also evaluated the hyperfine structure constants of the  $6s_{1/2}$ ,  $5d_{3/2,5/2}$  and  $4f_{7/2,5/2}$  states of  $^{171}\text{Yb}^+$  ion using the same RCC methods

and compare the results with their experimental values. We also determine the lifetime of the  $5d_{3/2}$  state to eradicate the disagreement between two different experimental results.

(D. K. Nandy and B. K. Sahoo)

### Alkali-atom and alkaline-earth-metal ion long range interactions for collision studies

Accurate knowledge of interaction potentials among the alkali atoms and alkaline earth ions is very useful in the studies of cold atom physics. Here we carry out theoretical studies of the long-range interactions among the Li, Na, K, and Rb alkali atoms with the  $\text{Ca}^+$ ,  $\text{Ba}^+$ ,  $\text{Sr}^+$ , and  $\text{Ra}^+$  alkaline earth ions systematically which are largely motivated by their importance in a number of applications. These interactions are expressed as a power series in the inverse of the inter-nuclear separation  $R$ . Both the dispersion and induction components of these interactions are determined accurately from the algebraic coefficients corresponding to each power combination in the series. Ultimately, these coefficients are expressed in terms of the electric multipole polarizabilities of the above mentioned systems which are calculated using the matrix elements obtained from a relativistic coupled-cluster method and core contributions to these quantities from the random phase approximation. We also compare our estimated polarizabilities with the other available theoretical and experimental results to verify accuracies in our calculations. In addition, we also evaluate the lifetimes of the first two low-lying states of the ions using the above matrix elements. Graphical representation of the dispersion coefficients versus  $R$  are given among all the alkaline ions with Rb.

*This work is carried out in collaboration with J. Kaur and B. Arora of Department of Physics, Guru Nanak Dev University, Punjab, India.*

(D. K. Nandy and B. K. Sahoo)

### Thermal dispersion interactions of the alkali metal-atoms with graphene in the Dirac model

Using accurate dynamic polarizabilities of the Li, Na, K and, Rb atoms, we scrutinize the thermal Casimir-Polder interactions of these atoms with a single layered graphene. Considering the modified Lifshitz theory for material interactions, we reanalyze the dispersion coefficient ( $C_3$ ) values of the above atoms with graphene as functions of separation distance, gap parameter and temperature among which some of them were earlier studied by estimating the dynamic polarizabilities of the above atoms using the single oscillator model. All these  $C_3$  coefficients have been evaluated in the framework of the Dirac model. The interactions are described for a wide range of distances and temperatures to demonstrate the changes in behavior with the varying

conditions of the system. Also, sensitivities of the interactions with the gap parameters are analyzed explicitly. From these analyses, we find a suitable region where measurements of interaction potentials can be carried out so that a justifiable value for the gap parameter can be surmised.

*This work is carried out in collaboration with K. Kaur, J. Kaur and B. Arora of Department of Physics, Guru Nanak Dev University, Punjab, India.*

(B. K. Sahoo)

### van der Waal interactions between the alkali atoms with a graphene layer and with a carbon nanotube

We have studied the interaction coefficients of the Li, Na, K and Rb atoms with a graphene layer and with a single walled carbon nanotube (CNT) using the hydrodynamic and Dirac models. The results from both the models are evaluated using accurate values of the dynamic polarizabilities of the above alkali atoms. Accountability of accurate dynamic polarizabilities of the alkali atoms to determine the above coefficients are accentuated by comparing the obtained coefficients using the precise values of the dynamic dipole polarizabilities against the values estimated from the single oscillator approximation that are generally used in the earlier calculations. These coefficients are given for a wide range of separation distances between the considered ground states of the atoms and the wall surfaces and also for different nanotube radii. The coefficients for the graphene layer are fitted to a logistic function of the separation distance. For CNT, we find a paraboloid kind of fit dependent both on the separation distances and radii of the CNT.

*This work is carried out in collaboration with H. Kaur and B. Arora of Department of Physics, Guru Nanak Dev University, Punjab, India.*

(B. K. Sahoo)

### Experimental and theoretical investigation of lifetime of the $3d^2D_{5/2}$ state in $^{40}\text{Ca}^+$

There have been diverse range of the values for the lifetimes of the metastable states of  $^{40}\text{Ca}^+$  reported by both the theoretical and experimental studies. To remove this ambiguity, we have carried out afresh both the measurement and theoretical investigation to confirm the lifetime of its  $3d^2D_{5/2}$  state ( $\tau_{3d^2D_{5/2}}$ ). A high-efficiency quantum state detection method by monitoring the quantum jumps of a laser-cooled single  $\text{Ca}^+$  ion in a miniature ring Paul trap was employed in the measurement. Also, sophisticated calculations were performed considering higher order non-linear terms in the relativistic coupled-cluster (RCC) method with all possible single and double excitations, but accounting only the important triple excitations from both the core and valence

orbitals. Systematic factors affecting the measurement, such as the collision with background gases, heating effects, the power of the 866-nm laser, and the state detection errors were carefully analyzed. Our observational and theoretical values for  $\tau_{3d5/2}$  are 1174(10) ms and 1172(3) ms, respectively, which agree well with two of the earlier experimental and theoretical results. The present theoretical analysis demonstrates that the contributions from the core triples and Breit interaction are notable to estimate the theoretical results very precisely.

*This work has been carried out in collaboration with H. Guan, H. Shao, Y. Qian, Y. Huang, P. L. Liu, W. Bian, C. B. Li, and K. L. Gao, State Key Laboratory of Magnetic Resonance and Atomic and Molecular Physics, Wuhan Institute of Physics and Mathematics, Chinese Academy of Sciences, Wuhan 430071, China.*

(B. K. Sahoo)

### **Spectroscopy of Plasma Embedded Li-like Systems with the Screening Effects in the Two-body Debye Potentials**

The spectroscopic properties of Li atom and Li-like Ca and Ti ions in the plasma environment are investigated using a relativistic coupled-cluster (RCC) method. Assuming the plasma is of low density and very hot, we consider the Debye model with two approximations to account for the screening effects: (i) in the nuclear potential alone and (ii) in both the nuclear and the electron-electron interaction potentials. Also, calculations for the energies and the lifetimes of the atomic states are carried out for the plasma free systems in order to check their accuracies following which they are investigated in the plasma environment. It is observed that screenings in the electron-electron interaction potentials stabilize the systems more than the case when the screenings present only in the nuclear potential. Similarly, the blue and red shifts in the  $\Delta n = 0$  and  $\Delta n \neq 0$  transition lines (with the principal quantum number  $n$ ) of the Li-like ions observed in the (i) approximation alter in the case of (ii) approximation. The level-crossings among the energy levels are observed for the large screening effects and found to be prominent in the states of higher orbital angular momentum. The lifetimes of many low-lying states of the allowed transitions are estimated by considering different plasma screening strengths.

*This work has been carried out in collaboration with M. Das and S. Pal, National Chemical Laboratory, Pune, India.*

(B. K. Sahoo)

### **Relativistic equation-of-motion coupled-cluster method for the double ionization potentials of the atoms**

Equation-of-motion coupled-cluster method in the relativistic framework has been developed to calculate double ionization spectra (DI-EOMCC) of the closed-shell atomic systems.

This method is employed to calculate the principal valence double ionization potential values of He and alkaline earth metal (Be, Mg, Ca, Sr and Ba) atoms. Our results are compared with the results available from the national institute of standards and technology (NIST) database and other ab initio calculations. We have achieved an accuracy of  $\sim 0.1\%$ , which is an improvement over the first principles T-matrix calculations available earlier. We also present results using the second-order many-body perturbation theory and the random-phase approximation in the equation-of-motion framework and these results are compared with the DI-EOMCC results.

*This work has been carried out in collaboration with H. Pathak, A. Ghosh, N. Vaval and S. Pal, National Chemical Laboratory, Pune, India and B. P. Das, Indian Institute of Astrophysics, Bangalore, India.*

(B. K. Sahoo)

### **Statistical properties of spectral fluctuations of $N$ interacting bosons in an harmonic trap**

Spectral fluctuations of a system of  $N$  weakly interacting bosons in an isotropic harmonic trap are studied, with the focus on the deviations from Poisson spectral statistics, typical of a quantum integrable systems. In this work utilized are the ideas formulated by Makino et al. [Phys. Rev. E 67, 066205 (2003)] who have extended the approach of Berry and Robnik [J. Phys. A 17, 2413 (1984)]. Earlier investigations of the Berry conjecture [Proc. R. Soc. London, Ser. A 356, 375 (1977)] of Poisson spectral statistics mainly considered quantum systems whose classical counterparts are integrable. However, the system of  $N$  weakly interacting bosons in the external trap has no classical counterpart. Also, it is a realistic and experimentally achievable system with close relation to Bose-Einstein condensation. Thus, a stringent analysis of the applicability of the Berry conjecture to this kind of systems is indeed required. We observe that for small boson number, the system is close to integrability and the nearest-neighbor level spacing distribution and the level number variance exhibit deviations from Poisson statistics similar to those of rational rectangular billiards.

*This work was done in collaboration with Dr (Mrs) Barnali Chakrabarti (Presidency University, Kolkata).*

(V.K.B. Kota)

### **Random Matrix Theory for Transition Strength Densities in Finite Quantum Systems: Results from Embedded Unitary Ensembles**

Embedded random matrix ensembles are generic models for describing statistical properties of finite isolated interacting quantum many-particle systems. For the simplest spinless

fermion (or boson) systems, with say  $m$  fermions (or bosons) in  $N$  single particle states and interacting via  $k$ -body interactions, one has EGUE( $k$ ) [embedded GUE of  $k$ -body interactions] with GUE embedding and the embedding algebra is  $U(N)$ . A finite quantum system, induced by a transition operator, makes transitions from its states to the states of the same system or to those of another system. Examples are electromagnetic transitions (then the initial and final systems are same), nuclear beta and double beta decay (then the initial and final systems are different), particle addition to or removal from a given system and so on. Towards developing a complete statistical theory for transition strength densities (transition strengths multiplied by the density of states at the initial and final energies), derived are formulas for the lower order bivariate moments of the strength densities generated by a variety of transition operators. Firstly, for a spinless fermion system, using EGUE( $k$ ) representation for a Hamiltonian that is  $k$ -body and an independent EGUE( $t$ ) representation for a transition operator that is  $t$ -body and employing the embedding  $U(N)$  algebra, finite- $N$  formulas for moments up to order four are derived, for the first time, for the transition strength densities. Secondly, formulas for the moments up to order four are also derived for systems with two types of spinless fermions and a transition operator similar to beta decay and neutrinoless beta decay operators. In addition, moments formulas are also derived for a transition operator that removes  $k_0$  number of particles from a system of  $m$  spinless fermions. In the dilute limit, these formulas are shown to reduce to those for the EGOE version derived using the asymptotic limit theory of Mon and French. Numerical results obtained using the exact formulas for two-body ( $k = 2$ ) Hamiltonians (in some examples for  $k = 3$  and 4) and the asymptotic formulas clearly establish that in general the smoothed (with respect to energy) form of the bivariate transition strength densities take bivariate Gaussian form for isolated finite quantum systems. Full extensions of these results to bosonic systems and EGUE ensembles with further symmetries are for future.

*This work was done in collaboration with Dr (Mrs) Manan Vyas (Instituto de Ciencias Físicas, UNAM, Cuernavaca, México).*

(V.K.B. Kota)

### Shape effects on double beta decay in deformed shell model: $^{70}\text{Zn}$ and $^{150}\text{Nd}$ examples

Using deformed shell model based on Hartree-Fock intrinsic states with  $^{70}\text{Zn}$  as an example and employing two realistic effective interactions in ( $^2p_{3/2}$ ,  $^1f_{5/2}$ ,  $^2p_{1/2}$  and  $^1g_{9/2}$ ) space with  $^{56}\text{Ni}$  core, namely jj44b that produces deformed shape and JUN45 that generates spherical shape, deformation dependence of the  $0\nu$  and  $2\nu$  nuclear transition matrix elements (NTME) for double beta decay has been investigated. All the past studies on this question used phenomenological interactions. With jj44b interaction, the NTME  $M^{0\nu}$  for neutrinoless double beta decay (NDBD) comes out to be 1.99 and for JUN45 interaction the value is 4.32. Thus, there is a reduction by a factor 2 in  $M^{0\nu}$

as we go from spherical to deformed shape. This result is further substantiated by using  $^{150}\text{Nd}$  as another example and employing the Kuo-Herling interaction with  $^{132}\text{Sn}$  core. This interaction produces deformed shape and by artificially reducing its strength produces spherical shape. The nuclear structure matrix element  $M^{0\nu}$  here changes from 1.26 to 3 as we go from deformed to spherical shape. Thus, spherical shape or pairing correlations enhance NTME for NDBD and deformation reduces NTME. Similar results are also obtained for NTME for  $2\nu$  DBD. These explain the NTME given by various nuclear models.

*This work was done in collaboration with R. Sahu (Berhampur University, Berhampur, Odhisa).*

(V.K.B. Kota)

### Shell model and deformed shell model spectroscopy of $^{62}\text{Ga}$

A comprehensive analysis has been carried out of the recently available experimental data [H.M. David et al., Phys. Lett. B 726, 665 (2013)] for high-spin states up to  $J^\pi = 17^+$  with isospin  $T = 0$  in the odd-odd  $N = Z$  nucleus  $^{62}\text{Ga}$  using shell model calculations within the full  $f_{5/2}pg_{9/2}$  model space and deformed shell model based on Hartree-Fock intrinsic states in the same space. The calculations have been performed using the jj44b effective interaction developed recently by B.A. Brown and A.F. Lisetskiy for this model space. The results obtained with the two models are similar and they are in reasonable agreement with experimental data. In addition to the  $T = 0$  and  $T = 1$  energy bands, band crossings and electromagnetic transition probabilities, calculated are also the  $T = 0$  and  $T = 1$  pairing energies in the shell model states. Important findings are: (i) the calculations predict band crossing starting at  $J = 13^+$  for the lowest  $T = 0$  band; (ii) for the lowest  $T = 0$  band, the contributions from isoscalar and isovector pairing are approximately equal for  $J > 5^+$  while for  $J < 5^+$ , isovector pairing plays a larger role; (iii) calculations correctly predict six  $1^+$  levels with  $T = 0$  as reported in a recent experiment; (iv) calculated low level-density at low-energies is in agreement with experiment.

*This work was done in collaboration with R. Sahu (Berhampur University, Berhampur, Odhisa) and P.C. Srivastava (IIT Roorkee, Roorkee).*

(V.K.B. Kota)

### Review of electronic transport in the underdoped cuprates

A review of our recent investigations related to the ac transport properties in the pseudogapped state of cuprate high temperature superconductors is presented. For our theoretical calculations we use a phenomenological Greens

function proposed by Yang, Rice and Zhang (YRZ). This is based upon the renormalized mean-field theory of the Hubbard model and takes into account the strong electron-electron interaction present in Cuprates. The pseudogap is also taken into account through a proposed self energy. We have tested the form of the Greens function by computing ac conductivity of cuprates and then compared with experimental results. We found agreement between theory and experiment in reproducing the doping evolution of ac conductivity but there is a problem with absolute magnitudes and their frequency dependence. This shows a partial success of the YRZ ansatz. The ways to rectify it are suggested and worked out.

*This work was done in collaboration with Prof. Raman Sharma of HP University, Shimla, HP.*

(N. Singh)

### Yang, Rice, and Zhang ansatz and the antiferromagnetic spin waves

In the underdoped regime of the cuprate phase diagram, the modified version of the Resonance Valence Bond (RVB) model by Yang, Rice and Zhang (YRZ) captures the strong electronic correlation effects very well as corroborated by the ARPES and many other experiments. However, under a non-equilibrium transport setting, YRZ says nothing about the scattering mechanisms of the charge carriers. In the present investigation we include, in a very simplified way, the scattering of charge carriers due to antiferromagnetic type spin waves (ASW). The effect of ASW excitations on conductivity has been studied by changing combined life times of the included process. It has been found that there is a qualitative change in the conductivity in the right direction. The theoretical conductivity reproduces qualitatively the experimental one.

*This work was done in collaboration with Prof. Raman Sharma of HP University, Shimla, HP.*

(N. Singh)

### Impurity induced resistivity upturns in underdoped cuprates

Impurity induced low temperature upturns in both the ab-plane and the c-axis dc-resistivities of cuprates in the pseudogap state have been observed in experiments. We provide an explanation of this phenomenon by incorporating impurity scattering of the charge carriers within a phenomenological model by Yang-Rice-Zhang in this regime. The scattering between charge carriers and the impurity atom is considered within the lowest order Born approximation. Resistivity is calculated within Kubo formula using the impurity renormalized spectral functions. Using physical parameters for cuprates, we describe qualitative features of the upturn phenomena and its doping evolution that coincides with the experimental findings and we stress the role of strong electronic correlations.

(N. Das and N. Singh)

### Charged Higgs contribution to neutrinoless double beta decay

The singly charged Higgs boson contribution to the neutrinoless double beta decay is neglected on grounds of couplings involving very small masses and smaller nuclear matrix elements. Such contributions are reconsidered, but now in the light of QCD corrections and renormalization group evolution. It is found that the charged Higgs contribution is at least as large as the other contributions. Moreover, there can be large cancellations between contributions coming from different sources. This observation has an important impact on the phenomenology.

(N. Mahajan)

### Non Bunch-Davies states and entanglement in the light of BICEP2 results

The BICEP collaboration result on the tensor to scalar ratio  $r$  indicates a blue tilt in the primordial gravitational wave spectrum. This blue tilt and the observed large value  $r = 0.2$  are difficult to accommodate within the single field inflationary scenarios under standard conditions. Non Bunch-Davies vacuum states have been proposed as a possibility. Such vacua are known to lead to pathologies. It is proposed to interpret them as excited/squeezed states built over the standard Bunch-Davies vacuum. The associated entanglement properties due to de Sitter horizon, and how such an approach may be more natural in the context of inflation is discussed.

(N. Mahajan)

### $B \rightarrow K^* l^+ l^-$ : Zeroes of angular observables as test of standard model

The LHCb collaboration has found deviations in some of the angular observables in the semi-leptonic process  $B \rightarrow K^* l^+ l^-$ . For a long time, it is known that the position of the zero of the lepton forward-backward asymmetry in this decay mode is a clean probe of physics beyond the standard model. The zeroes of some more angular observables are studied and interesting correlations between various zeroes are found. A new observable is proposed, which has the potential to probe the primed operators in a way complementary to the existing methods. The precise values of the zeroes along with the tight correlations among them then becomes a litmus test of the standard model.

(G. Kumar and N. Mahajan)

**Acoustic radiation from vortex - barrier interaction in atomic Bose-Einstein condensate**

We examine the dynamics of a vortex dipole in the Bose-Einstein condensates of trapped dilute atomic gases at zero temperature in the presence of a Gaussian barrier potential. The density anisotropy induced by the barrier enhances the acoustic radiation from the vortex dipole. This is due to the deviation of the condensate density from the equipotential curves and variation in the curvature of the vortex dipole trajectory. Due to the acoustic radiation, the vortex dipole dissipates energy and spirals towards the edge of the condensate. As a result, we observe an increase in the vortex-antivortex annihilation events. To examine the effect of the Gaussian barrier, we estimate the correction to the Thomas-Fermi condensate density using the perturbation expansion method and the results are in very good agreement with the numerical results.

**(K. Suthar, A. Roy, and D. Angom)**

**Fluctuation - and interaction - induced instability of dark solitons in single and binary condensates**

We show that the presence of a soliton in a single-species condensate, at zero temperature, enhances the quantum depletion sufficiently enough to induce dynamical instability of the system. We also predict that for two-species condensates, two Goldstone modes emerge in the excitation spectrum at phase separation. Of these, one is due to the presence of the soliton. We use Hartree-Fock-Bogoliubov theory with Popov approximation to examine the mode evolution, and demonstrate that when the anomalous mode collides with a higher energy mode it renders the solitonic state oscillatory unstable. We also report a soliton-induced change in the topology of the density profiles of the two-species condensates at phase separation.

**(A. Roy and D. Angom)**

# SCIENCE at PRL

## Atomic, Molecular and Optical Physics

### **Accurate multipixel phase measurement with classical-light Interferometry**

We demonstrate accurate phase measurement from experimental low photon level interferograms using a constrained optimization method that takes into account the expected redundancy in the unknown phase function. This approach is shown to have significant noise advantage over traditional methods, such as balanced homodyning or phase shifting, that treat individual pixels in the interference data as independent of each other. Our interference experiments comparing the optimization method with the traditional phase-shifting method show that when the same photon resources are used, the optimization method provides phase recoveries with tighter error bars. In particular, rms phase error performance of the optimization method for low photon number data (10 photons per pixel) shows a  $> 5\times$  noise gain over the phase-shifting method. In our experiments where a laser light source is used for illumination, the results imply phase measurement with accuracy better than the conventional single-pixel-based shot-noise limit that assumes independent phases at individual pixels. The constrained optimization approach presented here is independent of the nature of the light source and may further enhance the accuracy of phase detection when a non-classical light source is used.

*This work was done in collaboration with Mandeep Singh, Kedar Khare from IIT Delhi and Anand Kumar Jha from IIT Kanpur.*

**(S. Prabhakar and R. P. Singh)**

### **Higher order optical vortices and formation of speckles**

We have experimentally generated higher order optical vortices and scattered them through a ground glass plate that results in speckle formation. Intensity autocorrelation measurements of speckles show that their size decreases with an increase in the order of the vortex. It implies an increase in the angular diameter of the vortices with their order. The characterization of vortices in terms of their annular bright ring also helps us to understand these observations. The results may find applications in stellar intensity interferometry and thermal ghost imaging.

**(S. G. Reddy, S. Prabhakar, A. Kumar, J. Banerji and R. P. Singh)**

### **Propagation of an arbitrary vortex pair through an astigmatic optical system**

We embed a pair of vortices with different topological charges in a Gaussian beam and study its evolution through an astigmatic optical system, a tilted lens. The propagation dynamics are explained by a closed-form analytical expression. Furthermore, we show that a careful examination of the intensity distribution at a predicted position past the lens can determine the charge present in the beam. To the best of our knowledge, our method is the first noninterferometric technique to measure the charge of an arbitrary vortex pair. Our theoretical results are well supported by experimental observations.

**(S. G. Reddy, S. Prabhakar, A. Aadhi, J. Banerji and R. P. Singh)**

### Entanglement measure using Wigner function

We study the entanglement present between the two modes of a bipartite system using the Wigner function. The Wigner function stands out among all (quasi) probability distributions in quantum mechanics because it is real, non-singular, yields correct quantum mechanical operator averages in terms of phase space integrals and possesses definite marginal distributions. The negativity of the Wigner function is discussed as a measure of the non-classicality and the quantum interference pattern obtained therein as a possible measure of the entanglement between the two modes of the vortex states. This measure of entanglement is compared with the results obtained from concurrence.

*This work was done in collaboration with A. Banerji and A. Bandyopadhyay of Hooghly Engineering and Technology College, Hooghly.*

(R. P. Singh)

### Violation of Bell's inequality for phase singular beams

We have considered optical beams with phase singularity and experimentally verified that these beams, although being classical, have properties of two mode entanglement in quantum states. We have observed the violation of Bell's inequality for continuous variables using the Wigner distribution function (WDF) proposed by Chowdhury et al. [Phys. Rev. A 88, 013830 (2013)]. Our experiment establishes a new form of Bell's inequality in terms of the WDF which can be used for classical as well as quantum systems.

(S. Prabhakar, S. G. Reddy, A. Aadhi, P. Chithrabhanu, G. K. Samanta and R. P. Singh)

### High-power, continuous-wave, solid-state, single-frequency, tunable source for the ultraviolet

We report the development of a compact, high-power, continuous-wave, single-frequency, ultraviolet (UV) source with extended wavelength tunability. The device is based on single-pass, intracavity, second-harmonic-generation (SHG) of the signal radiation of a singly resonant optical parametric oscillator (SRO) working in the visible and near-IR wavelength range. The SRO is pumped in the green with a 25-mm-long, multigrating, MgO doped periodically poled stoichiometric lithium tantalate (MgO:sPPLT) as nonlinear crystal. Using three grating periods, 8.5, 9.0, and 9.5  $\mu\text{m}$  of the MgO:sPPLT crystal and a single set of cavity mirrors, the SRO can be tuned continuously across 710.7-836.3 nm in the signal and corresponding idler across 2115.8-1462.1 nm with maximum idler power of 1.9 W and maximum out-coupled signal power of 254 mW. By frequency-doubling the intracavity signal with a 5-mm-long bismuth borate (BIBO) crystal, we can further tune the SRO continuously over 62.8 nm across 355.4-418.2 nm in

the UV with maximum single-frequency UV power, as much as 770 mW at 398.28 nm in a Gaussian beam profile. The UV radiation has an instantaneous line-width of  $\sim 14.5\text{MHz}$  and peak-peak frequency stability of 151 MHz over 100 s. More than 95% of the tuning range provides UV power  $>260\text{mW}$ . Access to lower UV wavelengths can in principle be realized by operating the SRO in the visible using shorter grating periods.

(A. Aadhi, A. N. Chaitanya, R. P. Singh and G. K. Samanta)

### Type-I frequency-doubling characteristics of high-power, ultrafast fiber laser in thick BIBO crystal

We report on experimental realization of optimum focusing condition for type-I second-harmonic generation (SHG) of high-power, ultrafast laser in "thick" nonlinear crystal. Using single-pass, frequency doubling of a 5 W Yb-fiber laser of pulse width  $\sim 260\text{fs}$  at repetition rate of 78 MHz in a 5-mm-long bismuth triborate (BIBO) crystal we observed that the optimum focusing condition is more dependent on the birefringence of the crystal than its group-velocity mismatch (GVM). A theoretical fit to our experimental results reveals that even in the presence of GVM, the optimum focusing condition matches the theoretical model of Boyd and Kleinman, predicted for continuous-wave and long-pulse SHG. Using a focusing factor of  $\xi = 1.16$  close to the estimated optimum value of  $\xi = 1.72$  for our experimental conditions, we generated 2.25 W of green radiation of pulse width 176 fs with single-pass conversion efficiency as high as 46.5%. Our study also verifies the effect of pulse narrowing and broadening of angular phase-matching bandwidth of SHG at tighter focusing. This study signifies the advantage of SHG in "thick" crystal in controlling SH-pulse width by changing the focusing lens while accessing high conversion efficiency and broad angular phase-matching bandwidth.

(A. N. Chaitanya, A. Aadhi, R. P. Singh and G. K. Samanta)

### All-periodically poled, high-power, continuous-wave, single-frequency tunable UV source

We report on experimental demonstration of an all-periodically poled, continuous-wave (CW), high-power, single-frequency, ultra-violet (UV) source. Based on internal second-harmonic-generation (SHG) of a CW singly resonant optical parametric oscillator (OPO) pumped in the green, the UV source provides tunable radiation across 398.94-417.08 nm. The compact source comprising of a 25-mm-long MgO-doped periodically poled stoichiometric lithium tantalate (MgO:sPPLT) crystal of period  $\Lambda_{\text{SLT}}=8.5\mu\text{m}$  for OPO and a 5-mm-long, multi-grating ( $\Delta\text{KTP}=3.3, 3.4, 3.6$  and  $3.8\mu\text{m}$ ), periodically poled potassium titanium phosphate (PPKTP) for intra-cavity SHG, provides as much as 336 mW of UV power at 398.94 nm, corresponding to a green-to-UV conversion efficiency of  $\sim 6.7\%$ . In addition, the singly resonant

OPO (SRO) provides 840 mW of idler at 1541.61 nm and substantial signal power of 108 mW at 812.33 nm transmitted through the high reflective cavity mirrors. UV source provides single-frequency radiation with instantaneous line-width of  $\sim 18.3\text{MHz}$  and power  $>100\text{mW}$  in Gaussian beam profile (ellipticity  $> 92\%$ ) across the entire tuning range. Access to lower UV wavelengths requires smaller grating periods to compensate high phase-mismatch resulting from high material dispersion in the UV wavelength range. Additionally, we have measured the normalized temperature and spectral acceptance bandwidth of PPKTP crystal in the UV wavelength range to be  $\sim 2.25^\circ\text{C}\cdot\text{cm}$  and  $\sim 0.15\text{nm}\cdot\text{cm}$ , respectively.

(A. Aadhi, A. N. Chaitanya, R. P. Singh and G. K. Samanta)

**Solar wind particle experiment payload ASPEX for ADITYA-L1 mission: Design, Development and Experimental results**

A sub payload of ASPEX, Solar Wind Ion Spectrometer (SWIS) comprising of a top hat analyser (THA) and a magnetic mass analyser (MMA) is being designed and developed. The SWIS is capable of analyzing the energy of solar ions in the range of 200 eV to 20 keV with  $\sim 10\%$  resolution. Post energy analysis, a magnetic mass analyser is used to detect the alpha-particles and protons present in the solar wind. This instrument has  $2\pi$  angular measurement capability along the solar elevation and  $\pm 26^\circ$  angular resolution in the ecliptic plane. The instrument will be mounted on the 3-axis stabilized satellite deck, always viewing sun.

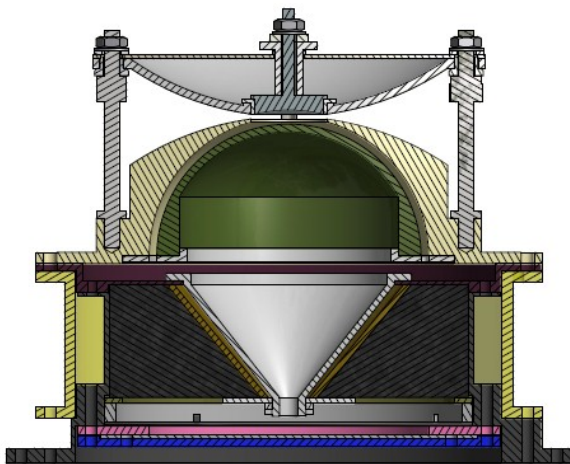


Figure 1 : Cross section of the final 3D model of the SWIS payload.

The lab model was designed and fabricated at the Space Application Center, Ahmedabad to demonstrate the “proof of concept” for SWIS payload (Figure 1). A 80 mm diameter MCP with a delay line detector (DLD) as anode was used for position encoding of the ion arrival on detector after energy analysis, followed by mass separation. The mass separator uses 16 NdFeB magnets arranged circularly. The separation

of  $N_2^+$ ,  $Ar^+$ ,  $Kr^+$  and  $Xe^+$  was obtained and is shown in Figure 2.

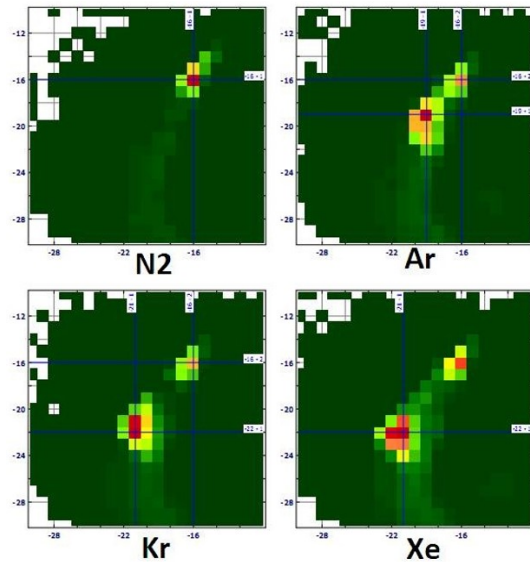


Figure 2 : Appearance of peak corresponding to different mass of ions. Note the relative position of  $Ar^+$ ,  $Kr^+$  and  $Xe^+$  with respect to  $N_2^+$ .

Trajectories of ions of various mass and energy are simulated inside the SWIS instrument and designed parameters are fine-tuned for the flight model. The fabrication of the flight model is underway.

(P. Kumar, B. Bapat, S. B. Banerjee and K. P. Subramanian)

**Development of resistive encoder anode for SWIS payload**

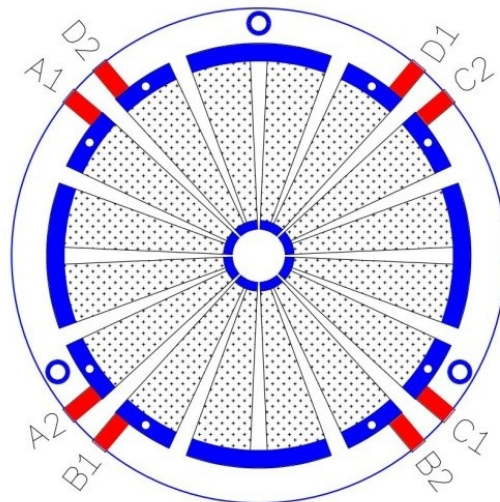


Figure 3: Ge coated RAE: The area marked with black dots is Ge coated. Four pair of readout are marked in red and blue color shows gold coated region for contacts.

Resistive anode encoder (RAE) which is to be used for position detection instead of DLD in the final flight model is also being developed in collaboration with RRCAT, Indore. RAE consist of specific pattern coated with germanium (Ge) on a sapphire substrate, Figure 3. Necessary electronics involving charge sensitive preamplifiers, shaping amplifiers, peaking ADCs etc. are used for extracting the position information of the signal on the detector. To test and the electronics, synthetic resistive anodes were made using PCBs with segmented tracks with soldered resistances between segments. These anodes were used in experiments for testing the performance of top-hat analyser with magnetic mass analyser. The results obtained in these experiments matched well with the results from earlier studies, where a delay-line detector was used for position encoding of ion arrival on the large area detector. The development flight model RAE is currently under progress. They are being developed by coating patterns of germanium resistive tracks on a 100 mm diameter sapphire plate. Ends of the tracks are appropriately metalized using gold deposition in order to form the Ge films as a continuous resistive chain.

*This work is in collaboration with RRCAT.*

**(P. Kumar, B. Bapat, K. Baladaniya, P. Adhyaru, S.B. Banerjee and K.P. Subramanian)**

### Ion Optic simulation for SWIS

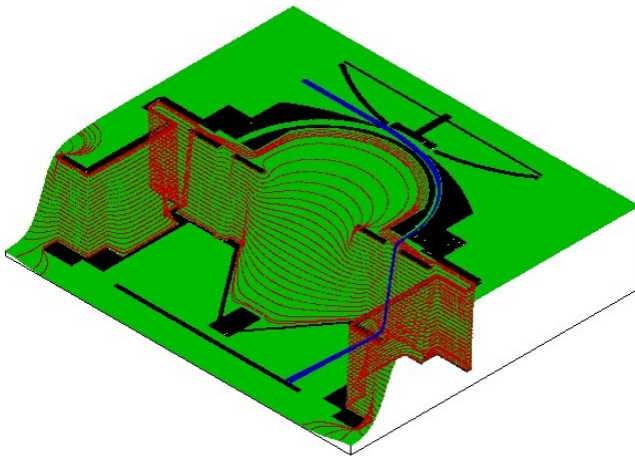


Figure 4 : Potential energy view of the ESA with equipotential lines marked in red. A typical ion trajectory through the ESA is shown in blue.

Electrostatic Energy Analyser(ESA): Ion trajectory simulations for the electrostatic energy analyser were performed using SIMION package. This package employs finite difference method to solve the electrostatic field equations for a particular configuration of electrode potentials. Hence, particle trajectories are calculated using the field solution and particle initial condition, Figure 4. Different potential arrays were created in SIMION and an optimum configuration for the ESA was obtained based on the field analysis.

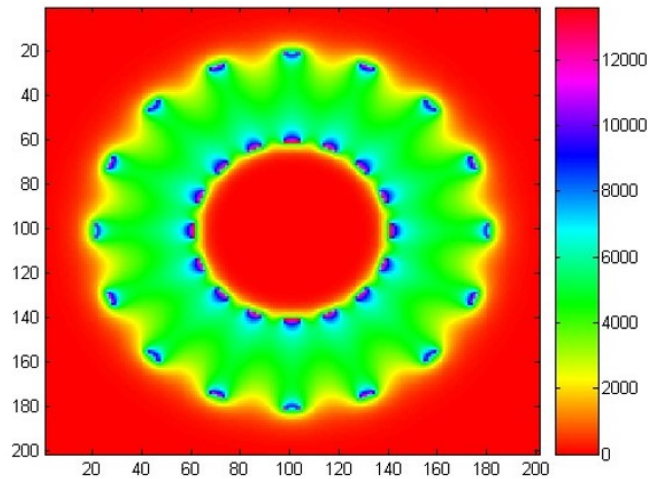


Figure 5 : Field generated due to 16 thin permanent magnets arranged in circular fashion at plane Z = 0.

Magnetic Mass Analyser(MMA): Field simulation to study and optimise the MMA parameters was performed in MATLAB through an in-house developed code. This code incorporates the exact analytical solution of the field generated by 16 permanent magnets arranged in a circular fashion, Figure 5. Variation of magnetic field in the gap between magnet pair and along the height were also estimated to obtain correct dimension of the magnet length and pole strength. Based on the field simulations for ESA and MMA we have obtained a final configuration of Top hat analyser.

**(P. Kumar, S. B. Banerjee and K. P. Subramanian)**

### Study of the dependence of dissociation kinematics on impact energy in electron-ionization

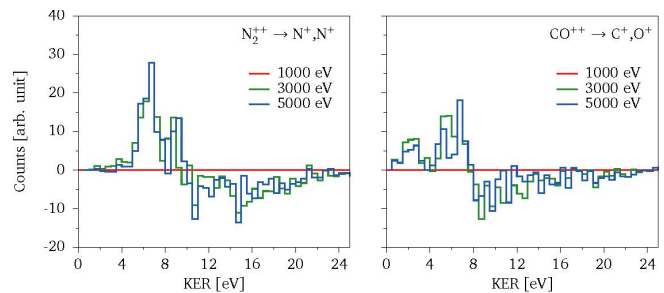


Figure 6 : Cross sections of KER spectra of dissociation channel  $N_2^{++} \rightarrow N^+, N^+$  [left] and  $CO^{++} \rightarrow C^+, O^+$  [right] observed at electron impact energies 3 and 5 KeV are compared with KER spectra observed at 1 KeV. If excitation probability is an uni-parameter function of transition energy, no change would be observed. Observed common trend in dissociation kinematics suggests that excitation probability is also a function of the impact energy.

We have performed a comparative study of dissociative ionization of doubly-ionized  $N_2^+$  and CO molecular ions created upon high energy electron impact at three energies viz 1,3 and 5 keV in order to investigate the role of impact

energy on the dissociation kinematics. We have analyzed and compared KER distributions of Charge Symmetric Dissociation (CSD) of doubly-ionized  $N_2^{++}$  and CO molecules. A common trend in the KER spectra for these two dissociation channels has been found and is attributed to the variation of the impact energy. We reason that such features that remain valid and appear in comparing the kinematics must be arising from the properties of ionization. The observed nature suggests that the excitation probability is also a function of impact energy that previously only assumed as an uni-parameter function of the transition energy.

(A. Pandey, P. Kumar, S. B. Banerjee, K. P. Subramanian and B. Bapat)

### Study of energy selected states of charge symmetric dissociation in photo-ionization

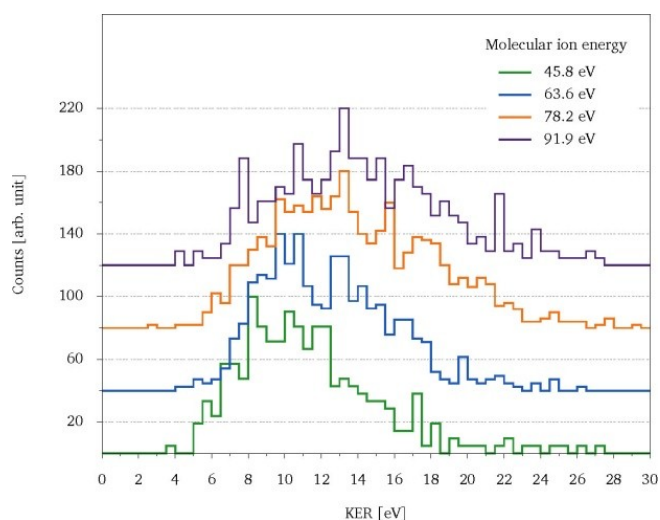


Figure 7 : KER spectra of dissociation channel  $N_2^{++} \rightarrow N^+, N^+$  [left] and  $CO^{++} \rightarrow C^+, O^+$  [right] at different molecular ion energies for 155 eV photon impact are shown. Molecular ion energy refers the remaining energy available to the system after ionization: difference of photon energy from energy of electron ejected in ionization. It represents upper bound of the total energy available to molecular ion after ionization. CSD channel starts appearing when molecular ions have more than 45.8 eV energy for  $N_2$  and 34.5 eV in case of CO. As available energy increases, it is evident from the plots, KER range widen and extends to the higher side.

A set of experiments on  $N_2$  and CO have been performed for 155 eV photon impact at INDUS-1 to study dissociative ionization processes of these molecules upon photo-excitation. Experiments are performed to make a comparative study between dissociative ionization channels for different excitation processes. In experiments performed at INDUS-1, we have measured complete kinematics of the ionic products produced in fragmentation. In addition, we have also recorded energy spectrum of the electron ejected in ionization of molecules. A single pass Cylindrical Mirror Analyzer (CMA) has been used to record and energy analyze the ejected electrons. CMA and Ion momentum spectrometer are coupled on a common axis, facing the ionization point in order to collect the ions and electrons from ionization region. Energy analyzed electrons observed from CMA

identify the electronic decay processes and measurement of correlated momentum of ions obtained from RIMS provides the corresponding dissociation kinematics.

From many results that have been obtained in analysis, one result is very significant in the study of nature of highly excited states. We have observed that excitation in highly unstable states will preferably decay to its corresponding asymptotic limits. The down-conversion process is established to be not a prominent decay mechanism involved in dissociation after ionization.

(A. Pandey, K. Saha, P. Kumar, S. B. Banerjee, B. Bapat and K. P. Subramanian)

### Study of charge asymmetric dissociation in electron and photo-ionization

Charge Asymmetric Dissociation (CAD) channels have been quite extensively studied in electron impact as well as photon impact processes. Study of CAD channels are relevant because of the fact that they access further higher excited states of dications and for the same reason are scarcely studied in comparison to CSD channels. KER distributions calculated from TOF distribution for  $C^{++} : O$  channel is found to be 15.7 eV, for  $N^{++} : N$  18.2 eV and for  $O^{++} : C$  25.5 eV at 1000 eV electron impact energy. This trend reflects the same order as of the ionization potentials of participating dications as well as of their lowest asymptotic limits with respect to their ground (initial) states : 46.4, 53.5 and 59.4 eV (written in the same order). Width of KER distribution reflects the energy span of involved PECs in dissociation for a given target energy. This observation suggests that PECs increasingly go steeper with the transition energy.

Kinematical study of photo-impact case reveals more about CAD channels as in this case kinematics is recorded at different molecular ion energies. In this case, observation of the fact that increase in KER width is not same as the change in molecular energy in a given CAD channel indicates that either coupling of states are involved or excited molecular ions would be decaying to their excited asymptotic limits. We infer that the second scenario is more probable because of the fact that though KER widths don't increase in same proportion, their increase is linear.

(A. Pandey, K. Saha, P. Kumar, S. B. Banerjee, B. Bapat and K. P. Subramanian)

### New 10 K astrochemical ices experimental facility at PRL

A new experimental chamber was set up for studying low temperature Astrochemistry at Physical Research Laboratory (PRL), India. An Ultra-High Vacuum (UHV) chamber, that can reach base pressures up to  $10^{-10}$  mbar, containing a cold head with Zinc Selenide (ZnSe) substrate that can be cooled down to 10 K. An all metal leak valve is used to introduce the gases to condense and form molecular ices on to the cooled

ZnSe substrate at 10 K. The morphology of the ices will be probed by FTIR operating at Mid-IR region ( $4000\text{--}400\text{ cm}^{-1}$ ), with a resolution of  $2\text{ cm}^{-1}$ .

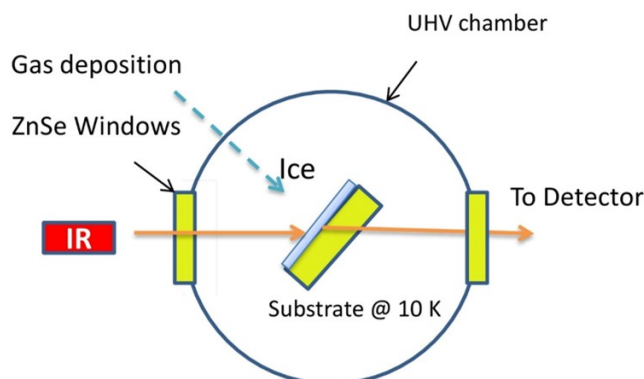


Figure 8 : Schematic of the experimental setup that can simulate astrochemical ices at 10 K.

(B. Sivaraman, S.P. Murali Babu and S. Pavithraa)

#### Lately exposed amorphous water ice on Comet 49P/Arend-Rigaux

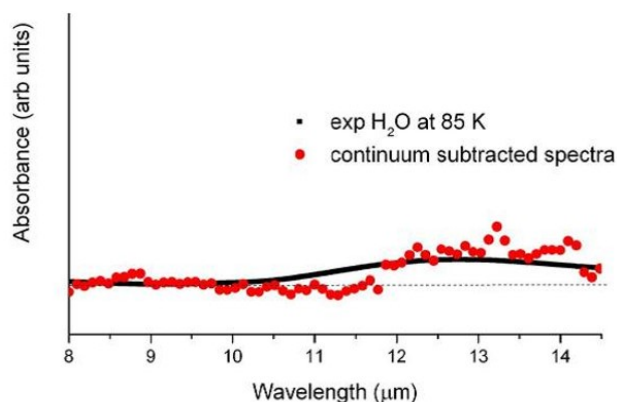


Figure 9 : IR spectra recorded by depositing water molecules at 85 K compared with the continuum subtracted spectra obtained from Spitzer observation in 2006. Dotted lines indicate zero in the absorbance scale for the experimental spectrum.

Comet 49P/ Arend-Rigaux, thought to be a low activity comet since the 1980's was found to be active in its recent apparitions. Analysis of the data obtained from Spitzer observation of the comet in 2006 compared with laboratory spectra has revealed amorphous water ice on the surface. In addition, in 2012 a jet was found to appear during its subsequent perihelion passage as witnessed during an observation carried out on 26th March 2012 using the PRL telescope at Mt. Abu. This confirms recent activity of Comet 49P/Arend-Rigaux due to the volatile subsurface materials exposed after several passages close to the Sun.

(B. Sivaraman, V. Venkataraman, A. Kalyan, S. Arora and S. Ganesh)

#### Inorganic residue from thermal processing of cometary ices : A case study using carbon disulfide - ammonia ices

We have carried out, for the first time, experimental investigation on binary ice mixture containing carbon disulfide ( $CS_2$ ) and ammonia ( $NH_3$ ) ices formed at 10 K. Icy films were formed in various combinations to investigate the reactivity of  $CS_2$  and  $NH_3$  molecules on icy mantles. Phase transition was found to take place as the 10 K ice was warmed to higher temperatures and the phase transition temperature was found to be 5 K higher for the mixed ice in comparison to the layered deposits. In the case of  $NH_3$  ices, deposition carried out at 10 K was found to contain  $NH_3$  homo-dimers that was found to reorient upon annealing to 40 K. Thermal processing of the mixed deposition of  $CS_2$ - $NH_3$  ice was found leave residue, could be ammonium dithiocarbamate, which was even found to be present even at 340 K.

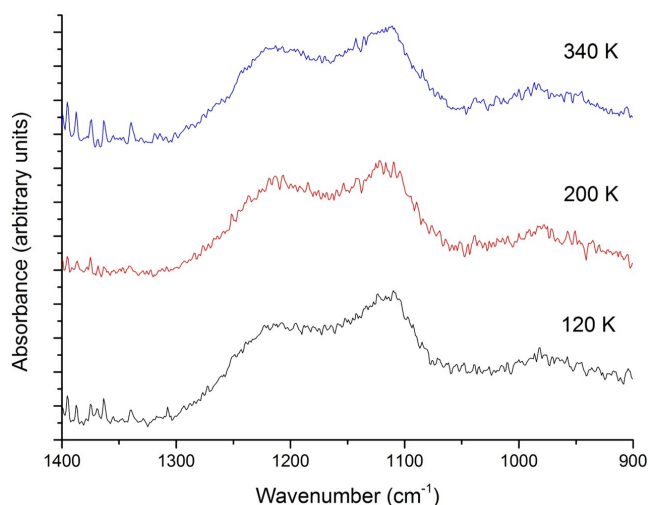


Figure 10 : IR spectra recorded at various temperatures after  $NH_3$  -  $CS_2$  ice sublimation revealed formation of ammonium dithiocarbamate from thermal processing of the ices formed at 10 K to higher temperatures.

(S. Pavithraa, T. Kaur, S.P. Murali Babu and B. Sivaraman)

#### Interstellar icy thiols: only amorphous ethanethiol exists in icy grains

Following the recent identification of ethanethiol in the interstellar medium (ISM) we have carried out Vacuum UltraViolet (VUV) spectroscopy studies of ethanethiol ( $CH_3CH_2SH$ ) from 10 K until sublimation in an ultrahigh vacuum chamber simulating astrochemical conditions. These results are compared with those of methanethiol ( $CH_3SH$ ), the lower order thiol also reported to be present in the ISM. VUV spectra recorded at higher temperature reveal conformational changes in the ice and phase transitions whilst evidence for dimer production is also presented. We also recorded the Infrared spectra of Ethanethiol in our 10 K system at PRL which revealed that the Phase transition

temperature is higher than 180 K. We also conclude that only amorphous Ethanethiol can exist in ISM.

The VUV part of this work was done in collaboration with Dr. B M Cheng, NSRRC, Taiwan and Prof. N. J. Mason, The Open University, UK.

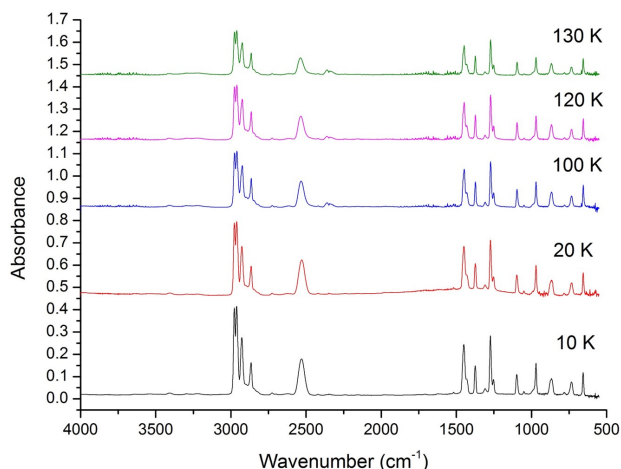
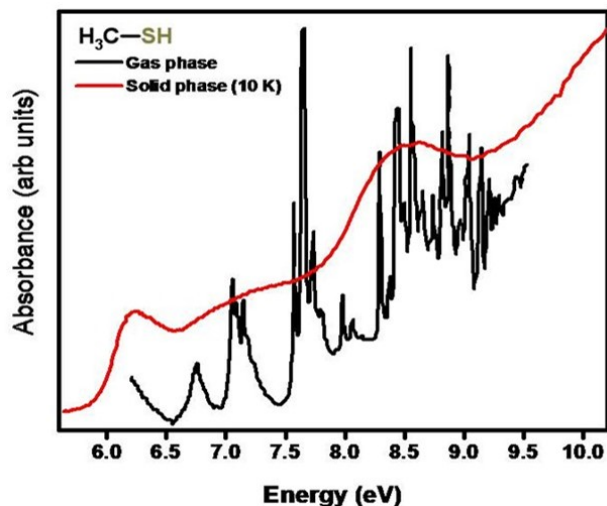


Figure 11 : (Top) VUV spectrum of methanethiol ice, formed at 10 K, compared with the gas phase spectrum. (Bottom) IR spectra of ethanethiol ices formed at 10 K and annealed until sublimation.

(B. Sivaraman and S. Pavithraa)

### Infrared spectra of fibrous nanosilica, KCC-1

We carried out an experiment in order to obtain the infrared (IR) spectra of fibrous nanosilica, KCC-1, at astrochemical conditions. Solid samples of KCC-1, obtained from Dr Vivek, TIFR, was coated on to a zinc Selenide (ZnSe) substrate. At UHV conditions, KCC-1 samples were then cooled down to 10 K to simulate dust grains in dense clouds. After cooling down IR spectra were recorded at temperatures starting from 10 K and up to room temperature. Spectra thus recorded will be used to discover fibrous silica in the interstellar medium (ISM).

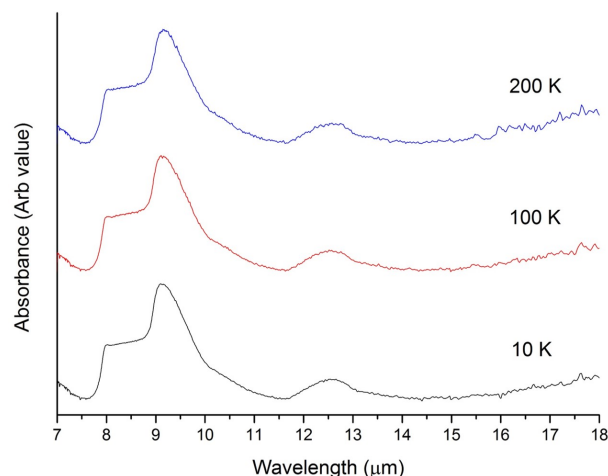


Figure 12 : Temperature dependent Infrared spectra of KCC-1 at astrochemical conditions.

(B. Sivaraman, S. Pavithraa and V. Venkataraman)

### Morphology of propargyl containing molecules

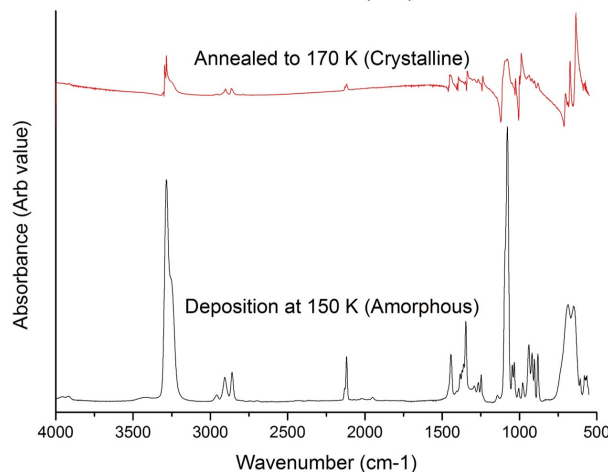
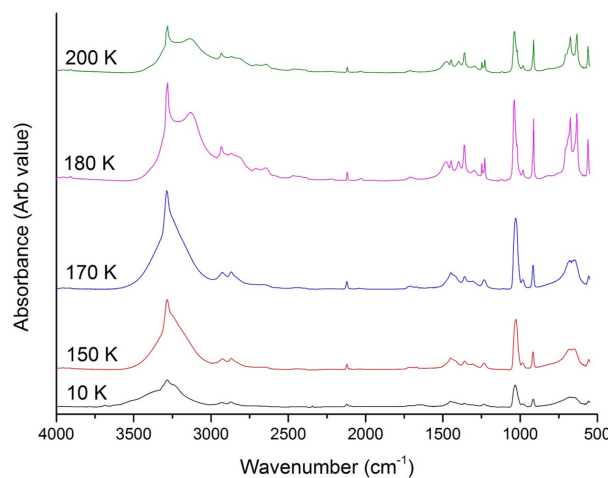


Figure 13 : Infrared spectra of amorphous and crystalline propargyl alcohol (top), propargyl ether (bottom).

There are two experimentally proven pathways to synthesize the six member, benzene ( $C_6H_6$ ), one by the addition of three acetylene ( $C_2H_2$ ) molecules and then other via the recombination of two propargyl radical ( $C_3H_3$ ). The second pathway was predicted in 1992 that could efficiently synthesize the basic PAH unit. This was demonstrated recently using propargyl alcohol ( $CHCCH_2OH$ ). Propargyl Alcohol is a known stable isomer of the propenal ( $CH_2CHCHO$ ) molecule that was discovered in the ISM in 2004 hence the isomer Propargyl Alcohol would be present in those regions where Propenal was found.  $C_6H_6$  synthesis from PA in fact had opened the possibility of an entirely new reaction network on the icy mantles of cold dust grains; the “propargyl channel to PAH” on dust grains at low temperature. Therefore two propargyl containing molecules (propargyl alcohol and propargyl ether) on cold dust grains in the dense medium were studied in order to understand their morphology. This was carried out at the low temperature astrochemistry facility operating at conditions of 10 K and  $10^{-10}$  mbar pressure simulating astrochemical conditions and the morphology changes was probed by Fourier Transform Infrared (FTIR) spectrometer. The first spectrum of amorphous propargyl ether at 10 K was recorded, which upon annealing turned crystalline at 170 K. A significant variation in absorbance and peak position of the spectra was observed, which shows that propargyl ether ices turn opaque at 170 K.

(T. Kaur, S. Pavithraa and B. Sivaraman)

### Spatial and temporal variability of Monsoon and Westerlies from Glacial deposits in Himalaya

Relict glacier sediments provide information about the temporal and spatial variability of past glaciations which are driven by two major weather systems viz. the Indian Summer Monsoon (ISM) and the mid-latitude westerlies. The influence of these weather systems varies spatially, such that most of the southern and eastern part of Himalaya experiences more of summer precipitation (ISM) and Mid-latitude westerlies provide the winter precipitation at the western regions of the Himalaya, Trans-Himalaya and Tibet. There is a continuing debate on the relative role of Indian Summer Monsoon (ISM) and the mid-latitude westerlies in driving the glaciation in Himalaya. Most studies suggest that on multi-millennial time scales, Himalayan glaciers responded to the enhanced ISM. This led to the suggestion that compared to the northern latitude glaciers; the Himalayan glaciers advanced and receded asynchronously with glaciations in Northern Hemisphere.

To understand the spatial variability of the ISM and the mid-latitude westerlies in driving the glaciation during the late Quaternary period, we have undertaken studies in three climatic domains viz. central Himalaya (monsoon dominated), eastern Zaskar Himalaya (transitional climatic zone) and the Ladakh Himalaya (westerlies dominated).

**Central Himalaya:** The glacial and paraglacial landforms in the Trans Himalayan region of the Dhauliganga valley (in Utrakhnad Himalaya between latitude  $30^{\circ}45' - 30^{\circ}55'$  N and longitude  $79^{\circ}35' - 79^{\circ}47'$  E) is located between the

dry steppe of the Tibetan plateau in the north and the sub-humid Himalayan climate in the south. East Kamet is a major glacier. Detailed field mapping of landforms along with optical and radiocarbon dating indicated four events of glaciations with decreasing magnitude. These were termed as East Kamet Stage -Ia (EKS-Ia), EKS-Ib, EKS-II, EKS-III and EKS-IV respectively. The oldest EKS-Ia and Ib were dated to Marine Isotopic Stage-3 (MIS-3), the EKS-II to the Last Glacial Maximum (MIS-2), EKS-III was dated to  $7.9 \pm 0.7$  ka, and the EKS-IV occurred during  $3.4 \pm 0.3$  ka and  $1.9 \pm 0.2$  ka.

Maximum valley glaciations viz. the EKS-Ia occurred during the strengthened Indian Summer Monsoon (ISM) during MIS-3. The recessional moraines (EKS-Ib) reflected gradual decline in ISM towards the later part of MIS-3. The valley responded to the global Last Glacial Maximum (LGM) with the deposition of EKS-II moraine. This implied that the terrain responded to strengthened mid-latitude westerlies during the LGM. The early Holocene EKS-III glaciation occurred around  $7.9 \pm 0.7$  ka which broadly corresponds to the early Holocene cooling event (8.2 ka), whereas the EKS-IV was attributed to a cool and moist climate.

Four distinct outwash gravel terraces constitute a major landform in the study area and represent the post LGM deglaciation events that are associated with the re-establishment of Indian Summer Monsoon (ISM). Stratified scree deposits and alluvial fan are the youngest paraglacial landforms developed during between 5.5 ka and 3 ka. Although glaciers respond to a combination of temperature and precipitation changes, however during the Holocene it seems that temperature played a limiting role in modulating glaciers and their spatial extent.

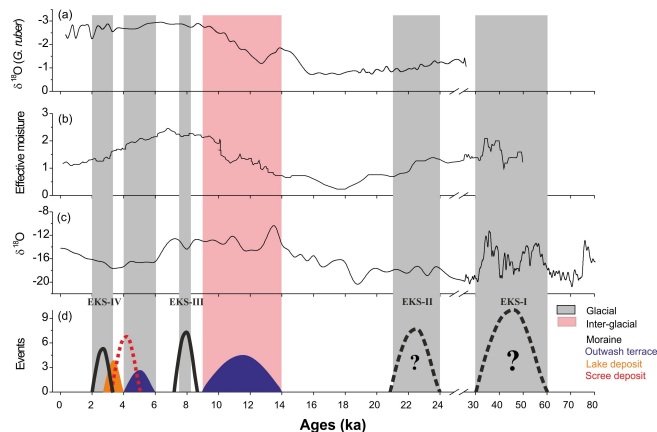


Figure 14 : Time span of gravel terraces (d) are compared with the global climatic events which have been reconstructed from oxygen isotope composition in foraminifera and ice cores (a, b and c).

The oldest glaciation (EKS-Ia and Ib) occurred during the relatively wetter condition corresponding to the MIS-3 core. The second major glacial advance occurred during the Global LGM (MIS-2) and attributed to the enhanced mid-latitude westerlies in the region. This was followed by a major deglaciation event dated to 14 ka and 9 ka indicates gradually strengthening of the ISM in the region after the LGM. The third glacial advance (EKS-III) though limited in extent

becomes important because this event occurred during the early Holocene cooling dated to 8.2 ka, thus indicating the sensitivity of Himalaya glaciers to short-term global climatic perturbations. Onset of early mid-Holocene warming in the valley is represented by the second deglaciation event. Following this, a fluctuating climatic condition prevailed in the region which led to the stratified scree fan aggradations and development of peat deposits between 5 ka to 3 ka. Finally the glacier receded to its present position after a minor advance during cool and moist late Holocene (Figure 14).

*This work was done in collaboration with Pinky Bisht, Sunil Negi, Y.P. Sundriyal of HNB Garhwal University and S. Nawaz Ali of BSIP Lucknow.*

**(A. D. Shukla, M. G. Yadava and N. Juyal)**

### Eastern Zaskar Himalaya

Recently, by virtue of their locations, Zaskar and Ladakh Himalaya have become areas of active glaciological research. Zaskar lies in the transitional climatic zone between the Indian Summer Monsoon (ISM) and mid Latitude westerlies. In view of this, chronologically constrained glacial deposits can inform on temporal changes in the two weather systems. The study is undertaken in the Sarchu plain which is located in the eastern Zaskar Himalaya. The terrain lies in Tethyan sedimentary domain in which a broad "U"-shaped valley, with elevation ranging between 4200 to 6000 m asl, is carved on an anticline. The southern end of the valley is demarcated by a north dipping Lingti-Sarchu fault. Presently mid-latitude westerlies accounts for  $\sim 64.4\%$  precipitation and the ISM contributes  $\sim 35.6\%$ . Presently the glaciers are located on the northern slopes of the Sarchu plain above 5500 m.

The study focused on the (i) temporal evolution of various landforms in Sarchu plain and (ii) the relative roles of ISM and mid- Westerlies in driving the glaciation. This work involved detailed geomorphological mapping of landforms and sedimentary sequences and Optical dating. The style of landform occurrences suggested that the "U"- shaped valley of Sarchu plain was carved by an older glacial event; termed as Sarchu Glacial Stage-I (SGS-I). This was followed by a phase of deglaciation that led to a valley- fill aggradation. Subsequently, a phase of glacial advance was inferred from sharp crested lateral moraine ridges, termed Sarchu Glacial Stage-II (SGS-II). The third Sarchu Glacial Stage-III (SGS-III) was inferred by drumlins and ground moraine which are preferentially preserved the upper reaches of the Sarchu plain and directly overlies the outwash glacio-fluvial terraces. The moraine dammed lake is located in the upstream gorge section and is overlain by well- rounded and imbricated outwash fluvial gravel.

The lateral moraine was optically dated to  $19.6 \pm 1.3$  ka and  $19.8 \pm 1.8$  ka; the drumlins are date to  $6.9 \pm 0.6$  ka to  $2.6 \pm 0.2$  ka; the outwash gravel above the moraine dammed lake gave an optical age of  $4.7 \pm 0.3$  ka. These ages enable a tentative scenario of landform evolution and contemporary climate. Based on regional evidences, the

oldest glaciation (SGS-I) is placed at the cold and wet Marine Isotopic Stage-4 (MIS-4;  $\sim 60$  ka). This was followed by a phase of deglaciation ascribed to the pluvial MIS-3 (5030 ka). SGS-II advance is dated to the LGM, during which the tributary glaciers from southern and western flanks descended down to  $\sim 4200$  m. SGS-III was dated to the early to mid-Holocene. This was followed by a phase of incision that was initiated  $\sim 5$  ka and has continued till date. The study indicates that the glacial responded more to the strengthened mid-latitude westerlies and the glacio-fluvial processes were accentuated during the intensified ISM. Quantification of Ice volume and corresponding temperature changes during the late Quaternary period are under process.

*This work is undertaken in collaboration with Shubhra Sharma and S.K. Bhartarya of WIHG, Pinky Bisht and Y.P. Sundriyal of HNB Garhwal University, Pritam Chand of JNU.*

**(A.D. Shukla and N. Juyal)**

### Ladakh Himalaya

Glaciers in Ladakh ranges provide unique opportunity to understand the past climate history particularly the temporal changes in the mid-latitude westerlies. We examined a spectacular glaciated Ganglas valley, in the north of Leh town. This valley was carved by the Puche and its tributary glaciers during the late Quaternary. Presently the glacier has withered towards the northwest and occupies a small area around the headwall of the Khardung ridge (Ladakh Batholith) at an elevation of  $\sim 5400$  m.

Based on detailed field mapping supported by total station survey, two generations of lateral moraines were identified. The older event, marked as the Puche Glacial Advance-I (PGA-I), descended down to a distance of  $\sim 14$  km and terminated at 3783 m, near Ganglas villege. This advance left a distinct latero-frontal moraine ridge traceable upstream up to  $\sim 4000$  m. The younger PGA-II advance terminated around South Pullu at 4507 m and left degraded and dissected lateral moraine ridge overlain by the frost shattered debris flow fans.

Multiple samples for optical dating were collected from cryoturbated sand bodies embedded within the moraines. Three samples from PGA-I were bracketed between  $35 \pm 5$  ka to  $24 \pm 2$  ka. Younger PKGA-II was dated to between  $21 \pm 3$  ka and  $18 \pm 3$  ka (Figure 15). This chronology indicates that the Puche glacier responded to the winnowing phase of the humid Marine Isotopic Stage-3 (MIS-3) and the expansion persisted during the early part of the MIS-2. Interestingly, the younger advance (PGA-II) broadly corresponds to the Global Last Glacial Maximum (LGM). The chronometric evidence indicate that the glaciation around Leh responded to a combination of the Indian Summer Monsoon (ISM) and the mid-latitude westerlies. Our results are at variance with the earlier studies (based on exposure age dating) and suggest that the Trans Himalayan glaciers responded synchronously with the global LGM.

Summarizing the results from the above study, indicate that the mid-latitude westerlies were the major source of moisture

in driving the late Quaternary glaciation in Ladhak and Zanskar region. Whereas in the monsoon dominated Central Himalaya, glaciers responded to a combination of the ISM and mid-latitude westerlies. Our results are at variance with the earlier study in which ISM was implicated for late Quaternary glaciation in the Himalayan region.

*This work was done in collaboration with Naresh Rana, Pinky Bisht, Y.P. Sundriyal of HNB Garhwal university, Pradeep Srivastava, J. Perumal from WIHG and Umesh Sharma of DST.*

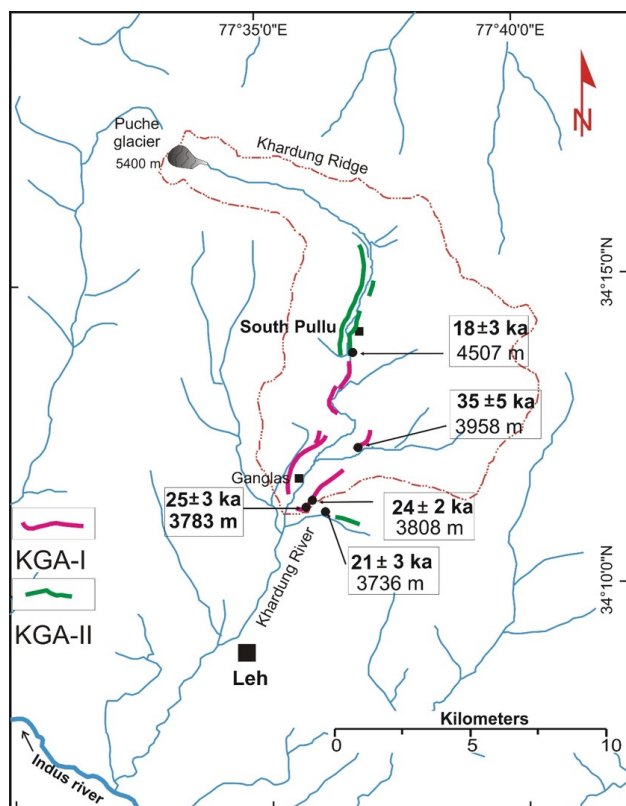


Figure 15 : Map showing Khardung valley (dotted line), PGA-I (red line), PGA-II (green line).

(A. D. Shukla and N. Juyal)

### Decoding sensitivity variation in Quartz

Quartz is amongst the more abundant minerals on Earth and is found in most geological systems. Luminescence sensitivity (photon flux/mg.Gy) of quartz can vary over ten orders of magnitude or even more. Various factors such as the origin, radiation, thermal and optical history of quartz have been used to explain such a large variation in luminescence sensitivity, but a thorough insight was still awaited. Recent developments in instrumentation permitted measurement of luminescence yields of single 100  $\mu\text{m}$  size grains. Variation in sensitivity of quartz of natural quartz grains was measured and analyzed these using photoluminescence (PL),

time-resolved luminescence and Fourier transform infra-red (FTIR) techniques. Luminescence sensitivity and integrated intensity of normalized FTIR signal in  $3000 - 3600\text{cm}^{-1}$  region were anti-correlated, such that, for a sensitivity variation of about 5 orders of magnitude was anti correlated to five fold change in the integrated water absorption signal. This was explained on the basis of formation of silica-water-impurity complexes (aqua-complexes). Given that OH - defects in detrital quartz grains have recently been considered as a potential tool for provenance analysis, the present study suggests an even larger potential of luminescence sensitivity for easy and rapid estimation of sediment provenance.

*This work was done in collaboration with Dr. S. Chawla, National Physical Laboratory, Delhi, Dr. M.D. Sastry, Gemmological Institute, Mumbai and Dr. V. Balaram, National Geophysical Research Institute, Hyderabad.*

(S.K. Sharma and A.K. Singhvi)

### Past High energy Events on the Western Indian Coast

The 2004 tsunami event informed on possible amplitudes of marine inundations in eastern coasts of India. Similar inferences on the western coast were however lacking. The work of Dr. N. Bhatt of M.S. University, Baroda, provided the first geological evidences of high energy wave events from the coastline of Gujarat in western India. He inferred that in the region between Mundra and Bhadreshwar of the Kachchh coast, a tsunami event in form of sand layer sandwiched between mud layers and we dated this to have been deposited a millenium ago. Further, large boulders occur in as imbricates in sandy matrix in scattered and embedded manner in the coastline between Madhavpur and Chorwad. Our chronometric work provided an age of  $6.6 \pm 0.7$  ka. A tsunamite at Ratiya, north of Madhavpur yielded OSL date of  $35.4 \pm 4.3$  ka. Field evidences suggest that the energy source of palaeo tsunami sand layers was the Strait of Hormoz and the boulders of Ratiya-Madhavpur-Chorwad segment were driven by waves from the Chagos Archipelago.

*This work was done in collaboration with Prof. N. Bhatt of M.S. University of Baroda, Vadodara and Dr. M. K. Murari of University of Cincinnati, USA.*

(A.K. Singhvi)

### Barite as a radiation dosimeter

We explored the possible use of Barite ( $\text{BaSO}_4$ ) for radiation dosimetry and for geochronology using both TL and OSL techniques. Natural barite has a glow peak at 608 K and has a minimum detectable dose of  $1.45 \pm 0.12\text{mGy}$ . This peak shows  $\sim 35\%$  fading after 30 days of storage. We examined sensitivity variation, reproducibility and linearity upon  $\beta$ -irradiation and infer that the signal can be used to date geological events in the range 15-20ka.

(S.K. Sharma and A.K. Singhvi)

**Chronology of large floods in the Ping river, Thailand**

As a part of a international consortium reconstruction of the flood history of the Ping River for over 1500 years was reconstructed using documentary evidence, gauged records, tree rings, speleothems, flood sediments and morphostratigraphy, hydraulics, geochronology, geochemistry, and modern climatology. This study used luminescence ages of over 40 samples. Combination of documentary evidence with flood and flow proxies (sedimentary, speleothem, tree rings) and gauged records provided a long and robust reconstructed of floods in the past. It was inferred that there have been three channel and floodplain reconfiguring floods in a period of ca. 600 years which, when

repeated, had devastating impacts on the people of northern Thailand. The long record of floods reaching Bangkok is non-stationary and the flood history is best understood by reference to ENSO, the IOD and cyclone frequency and trajectories. The studies do-not support the role for Greenhouse warming but predicted increased frequency of extreme *LaNiña* events that are likely to increase flooding in cases of the right conditions of the IOD. Land-use does did not play a role in the flood history.

*This work was in collaboration with Prof. R. J. Wasson and Prof. A. Zeigler of Singapore National University, Singapore.*

**(A. K. Singhvi)**

# PUBLICATIONS

## Publication in Journals

### Astronomy and Astrophysics

1. Amanullah R., Goobar, A., Johansson, J., Banerjee, D.P.K., Venkataraman, V., Joshi V., Ashok N.M. et al (total 13 authors), 2014, "The peculiar extinction law of SN2014J measured with The Hubble Space Telescope", ApJ Letters, v. 788, p. L21, pp. 1-6.
2. Baug, T., Chandrasekhar, T., Ganesh, S., 2014, "Possible spatial asymmetry in semiregular variable UZ Arietis", MNRAS, v. 443, p. 3624-3630.
3. Bisoi, S.K., Janardhan, P., Ingale, M., Subramanian, P., Ananthakrishnan, S., 2014, "A study of density modulation index in the inner solar wind during solar cycle 23", ApJ., v. 795, p. 69-76.
4. Chandra, S., Baliyan, K.S., Ganesh, S., Foschini, L., 2014, "Understanding the Nature of the Blazar CGRaBS J0211+1051", ApJ., v. 791, p. 85-94.
5. Chattopadhyay, T., Vadawale, S.V., Rao, A.R., Sreekumar, S., Bhattacharya, D., 2014, "Prospects of hard X-ray polarimetry with Astrosat-CZTI", Experimental Astronomy, v. 37, p. 555-577.
6. Chattopadhyay, T., Vadawale, S.V., Shanmugam, M., Goyal, S.K., 2014, "Measurement of Low Energy Detection Efficiency of a Plastic Scintillator: Implications on the Lower Energy Limit and Sensitivity of a Hard X-Ray Focal Plane Compton Polarimeter", Astrophysical Journal Supplement, v. 212, p. 1-12.
7. Chaturvedi, P., Deshpande, R., Dixit, V., Roy, A., Chakraborty, A., Mahadevan, S., Anandarao, B.G., Leslie, H., Janardhan, P., 2014, "Determination of mass and orbital parameters of a low-mass star HD 123597B", MNRAS, v. 442, p. 3737-3744.
8. Chesneau, O., Millour, F., De Marco, O., Bright, S.N., Spang, A., Banerjee, D.P.K., Ashok, N.M., Kamiski, T., Wisniewski, J.P., Meilland, A., Lagadec, E., 2014, "V838 Monocerotis: the central star and its environment a decade after outburst", A&A Letters, v. 569, p. L3, pp. 1-5.
9. Das, R., Banerjee, D.P.K., Arpita, N., Mondal, S., 2015, "Near-infrared studies of V5558 Sgr: an unusually slow nova with multiple outbursts", MNRAS, v. 447, p. 810, pp. 1-12.
10. Jaisawal, G.K., Naik, S., 2014, "Investigation of iron emission lines in the eclipsing high mass X-ray binary pulsar OAO 1657-415", Bull. Astr. Soc. India, v. 42, p. 147-164.
11. Jaisawal, G.K., Naik, S., 2015, "Broadband spectroscopy of the eclipsing high mass X-ray binary 4U 1700-37 with Suzaku", MNRAS, v. 448, p. 620-628.
12. Joshi, V., Banerjee, D.P.K., Ashok, N.M., 2014, "Infrared studies of recurrent nova T Pyxidis during its 2011 outburst", MNRAS, v. 443, p. 559-567.
13. Marion, G.H., Sand, D.J., Hsiao, E.Y., Banerjee, D.P.K., Joshi, V., Venkataraman, V., Ashok, N.M. et al. (total 26 authors), 2015, "Early Observations and Analysis of the Type Ia SN 2014J in M82", ApJ., v. 798, p. 39, pp. 1-12.
14. Mathew, B., Varricatt, W., Subramanian, A., Ashok, N.M., Banerjee, D.P.K., 2014, "Optical/IR studies of Be stars in NGC 6834 with emphasis on two specific stars", Research in Astronomy and Astrophysics, v. 14, p. 1173-1192.
15. Mercier, C., Subramanian, P., Gilbert, C., Janardhan,

- P., 2015, "The Structure of Solar Radio Noise Storms", *A&A*, v. 576, p. A136, pp. 1-10.
16. Millour, F., Lagadec, E., De Marco, O., Banerjee, D.P.K., Mékarnia, D., Spang, A., Chesneau, O., 2014, "Catching Stellar Mergers at Work with the Very Large Telescope Interferometer", *The Messenger*, v. 158, p. 35-38.
17. Munari, U., Henden, A., Banerjee, D.P.K., Ashok, N.M., Righetti, G.L., Dallaporta, S., Cetrulo, G., 2015, "The hybrid, coronal lines nova V5588 Sgr (2011 N.2) and its six repeating secondary maxima", *MNRAS*, v. 447, p. 1661-1672.
18. Naik, S., Jaisawal, G.K., 2015, "Suzaku observation of Be/X-ray binary pulsar EXO 2030+375", *Research in Astronomy and Astrophysics*, v. 15, p. 537-548.
19. Raj, A., Ashok, N.M., Rudy, R.J. et. al. (a total of 10 authors), 2015, "IR study of Nova V2468 Cygni from early decline to coronal phase", *Astron. J.*, v. 149, p. 136-149.
20. Rao, A.R., Vadawale, S.V., 2015, "Variation of the inner disk radius during the onset of the 2010 outburst of MAXI J1659-152", *Research in Astronomy and Astrophysics*, v. 15, p. 45-54.
21. Schaefer, G.H., Brummelaar, T., Gies, D.R., Banerjee, D.P.K., Ashok, N.M., Joshi, V., et al. (total of 35 authors), 2015, "Imaging the Expanding Fireball of Nova Delphini 2013", *Nature*, v. 515, p. 234, pp. 1-32.
22. Singal, A.K., 2014, "Comment on Cosmic radio dipole from NVSS and WENSS", *Astr. Astrophys.*, v. 568, p. A63, pp. 1-2.
23. Singal, A.K., 2014, "Discordance of the unified scheme with observed properties of quasars and high-excitation galaxies in the 3CRR sample", *Astr. J.*, v. 148, p. 16, pp. 1-6.
24. Singal, A.K., Rajpurohit, K., 2014, "Fanaroff-Riley dichotomy of radio galaxies and the Malmquist bias", *Mon. Not. R. Astro. Soc.*, v. 42, p. 1656-1660.
25. Singal, A.K., Rajpurohit, K., 2014, "Dependence of Fanaroff-Riley break of radio galaxies on luminosity and redshift", *Astrphys. Sp. Sc.*, v. 353, p. 233-240.
29. Kushwaha, U., Joshi, B., Veronig, A., Moon Y.J., 2015, "Large-scale contraction and subsequent disruption of coronal loops during various phases of the M6.2 flare associated with the confined flux rope eruption", *ApJ.*, v. 807, p. 101-118.
30. Louis, R.E., Beck, C., Mathew, S.K., Venkatakrisnan, P., 2014, "Anomalous flows in a sunspot penumbra", *A&A*, v. 570, p. 92-100.
31. Mishra, W., Srivastava, N., 2014, "Morphological and kinematic evolution of three interacting coronal mass ejections of 2011 February 13-15", *ApJ.*, v. 794, p. 64-79
32. Mishra, W., Srivastava, N., Chakrabarty, D., 2015, "Evolution and consequences of interacting CMEs of 2012 November 9-10 using STEREO/SECCHI and in situ observations", *Solar Physics*, v. 290, p. 527-552
33. Bayanna, R.A., Mathew, S.K., Venkatakrisnan, P., Srivastava, N., 2014, "Narrow-Band imaging system for the Multi-Application Solar Telescope at Udaipur Solar Observatory: Characterization of Lithium Niobate etalons", *Solar Physics*, v. 289, p. 4007-4019
34. Bayanna, R.A., Mathew, S.K., Kumar, B., Louis, R.E., Venkatakrisnan, P., 2014, "A study of the relation between intensity oscillations and magnetic field parameters in a sunspot: Hinode observations", *Research in Astronomy and Astrophysics*, v. 14, p. 1458-1468
35. Bayanna, R.A., Louis, R.E., Chatterjee, S., Mathew, S. K., Venkatakrisnan, P., 2015, "Membrane-based deformable mirror: intrinsic aberrations and alignment issues", *Applied Optics*, v. 54, p. 1727-1736
36. Suthar, Y., Venkatakrisnan, P., Ravindra, B., Jaffrey, S.N.A., 2014, "The evolution of the net twist current and the net shear current in Active Region NOAA 10930", *Solar Physics*, v. 289, p. 2459-2471
37. Vemareddy, P., Wiegmann, T., 2014, "Quasi-static three-dimensional magnetic field evolution in solar active region NOAA 11166 associated with an X1.5 Flare", *ApJ.*, v. 792, p. 40-52
38. Vemareddy, P., Zhang, J., 2014, "Initiation and eruption process of magnetic flux rope from solar active region NOAA 11719 to Earth-directed CME", *ApJ.*, v. 797, p. 80-91

### Solar Physics

26. Kumar, D., Bhattacharyya, R., Smolarkiewicz, P.K., 2015, "Repetitive formation and decay of current sheets in magnetic loops: An origin of diverse magnetic structures", *Physics of Plasmas*, v. 22, p. 012902, pp. 1-14.
27. Kumar, S., Bhattacharyya, R., Smolarkiewicz, P.K., 2014, "Formation of magnetic discontinuities through viscous relaxation", *Physics of Plasmas*, v. 21, p. 052904, pp. 1-13
28. Kushwaha, U., Joshi, B., Cho, K.S., Veronig, A., Tiwari, S.K., Mathew, S.K., 2014, "Impulsive energy release and non-thermal emission in a confined M4.0 flare triggered by rapidly evolving magnetic structures", *ApJ.*, v. 791, p. 23-38

### Planetary Sciences and PLANEX Program

39. Banerjee, R., Ray, D., 2014, "Disseminated sulphides in basalts from the northern Central Indian Ridge: implications on late-stage hydrothermal activity.", *Geo-Marine Letters*, v. 35, p. 91-103.
40. Bhandari, N., Srivastava, N., 2014, "Active moon: evidences from Chandrayaan-1 and the proposed Indian missions", *Geoscience Letters*, v. 1, p. 11, pp. 1-12.
41. Chattopadhyay, T., Vadawale, S.V., Shanmugam, M., Goyal, S.K., 2014, "Measurement of low energy detection efficiency of a plastic scintillator: Implications on the low energy limit and sensitivity of a Hard X-ray

- focal plane Compton polarimeter*", The Astrophysical Journal Supplement Series, v. 212, p. 12, pp. 1-12.
42. Chauhan, P., Kaur, P., Srivastava, N., Sinha, R., Jain, N., Murty, S.V.S., 2015, "*Hyperspectral remote sensing of planetary surfaces: an insight into composition of inner planets and small bodies in the solar system*", Curr. Sci., v. 108, 5, p. 1041-1046.
  43. Desai, A.J., Shiv, M., Murty, S.V.S., 2014, "*Lunar crater ejecta distribution and characterization using Mini-RF and LROC-WAC data*", Current Science , v. 107, p. 824-831.
  44. Gupta, R.P., Srivastava, N., Tiwari, R.K., 2014, "*Evidences for relatively new volcanic flows on the Moon.*", Curr. Sci., v. 107, 3, p. 454-460.
  45. Mishra, R.K., Goswami, J.N., 2014, "*Fe-Ni and Al-Mg isotope records in UOC chondrules: Plausible stellar source of 60 Fe and other short-lived nuclides in the early Solar System*", Geochimica et Cosmochimica Acta , v. 132, p. 440-457.
  46. Murty, S.V.S., 2014, *Book Review "Planetary Climates"*, Curr. Sci., v. 106, p. 1018-1019.
  47. Patel, V., Pabari, J., Patel, J., 2014, "*Revisiting Lunar Water Ice Content Retrieval Using Lunar Remote Sensing Data*", IOSR Journal of Electrical and Electronics Engineering, v. 9, p. 14-18.
  48. Ray, D., Ghosh, S., Murty, S.V.S., 2015, "*Evidence of shock pressure above 600 kb and post shock annealing in Nyaung IIIAB Octahedrite*", Journal of Geological Society India, v. 85, p. 153-162.
  49. Ray, D., Misra, S., 2014, "*Contrasting aerodynamic morphology and geochemistry of impact spherules from Lonar crater, India: Some insights into their cooling history*", Earth, Moon and Planets, v. 114, p. 59-86.
  50. Shanmugam, M., Acharya, Y.B., Vadawale, S.V., Mazumdar, H.S., 2015, "*A new technique for measuring the leakage current in Silicon Drift Detector based X-ray spectrometer- Implications for on-board calibration*", JINST, v. 10 , p. 02009, pp. 1-18.
  51. Sinha R.K., Murty, S.V.S., 2015, "*Amazonian modification of Moreux crater: Record of recent and episodic glaciation in the Protonilus Mensae region of Mars*", Icarus, v. 245, p. 122-144.
  52. Varatharajan, I., Srivastava, N., Murty, S.V.S., 2014, "*Mineralogy of young lunar mare basalts: Assessment of temporal and spatial heterogeneity using M<sup>3</sup> data from Chandrayaan-1*", Icarus, v. 236, p. 56-71.
  53. Vijayan, S., Mohan, S., Murty, S.V.S., 2015, "*Lunar regolith thickness estimation using dual frequency microwave brightness temperature and influence of vertical variation of FeO+TiO<sub>2</sub>*", Planetary and Space Science, v. 105, p. 123-132.
- Space and Atmospheric Sciences**
54. Abdu, M.A., de Souza, J R., Batista, I.S., Santos, A.M., Sobral, J.H.A., Rastogi, R.G., Chandra, H., 2014, "*The role of electric fields in sporadic E layer formation over low latitudes under quiet and magnetic storm conditions*", J. Atmos. Sol. Terr. Phys., v. 115-116, p. 95-105.
  55. Bagiya, M.S., Sridharan, R., Sunda, S., Jose, L., Pant, T.K., Choudhary, R., 2014, "*Critical assessment of the forecasting capability of L-band scintillation over the magnetic equatorial region Campaign results*", J. Atmos. Sol. Terr. Phys., v. 110-111, p. 15-22.
  56. Bagiya, M.S., Hazarika, R., Laskar, F.I., Sunda, S., Gurubaran, S., Chakrabarty, D., Bhuyan, P.K., Sridharan, R., Pallamraju, D., 2014, "*Effects of prolonged southward interplanetary magnetic field on low latitude ionospheric electron density*", J. Geophys. Res. Space Phys., v. 119, p. 5764-5776.
  57. Chakrabarty, D., Fejer, B.G., Gurubaran, S., Pant, T.K., Abdu, M.A., Sekar, R., 2014, "*On the pre-midnight ascent of F-layer in the June solstice during the deep solar minimum in 2008 over the Indian sector*", J. Atmos. Sol. Terr. Phys., v. 121, p. 177-187.
  58. Haider, S.A., Mahajan, K.K., 2014, "*Lower and upper ionosphere of Mars*", Space Sci. Rev., v. 182, p. 19-84.
  59. Kanawade, V.P., Shika, S., Phlker, C., Rose, D., Suman, M.N.S., Gadhavi, H., Kumar, A., Shiva N.S.M., Ravikrishna, R., Yu, H., Sahu, L.K., Jayaraman, A., Andreae, M.O., Pschl, U., Gunthe, S.S., 2014, "*Infrequent occurrence of new particle formation at a semi-rural location, Gadanki, in tropical Southern India*", Atmos. Environ., v. 94, p. 264-273.
  60. Kedia, S., Ramachandran, S., Holben, B.N., Tripathi, S.N., 2014, "*Quantification of aerosol type, and sources of aerosols over the Indo-Gangetic Plain*", Atmos. Environ., v. 98, p. 607-619.
  61. Kulkarni, P., Ramachandran, S., 2015, "*Comparison of aerosol extinction between lidar and SAGE II over Gadanki, a tropical station in India*", Annales Geophysicae, v. 33, p. 351-362.
  62. Lal, S., Venkataramani, S., Chandra, N., Cooper, O.R., Brioude, J., Naja, M., 2014, "*Transport effects on the vertical distribution of tropospheric ozone over western India*", J. Geophys. Res. Atmos., v. 119, p. 10012-10026.
  63. Laskar, F.I., Pallamraju, D., 2014, "*Does sudden stratospheric warming induce meridional circulation in the mesosphere thermosphere system?*", J. Geophys. Res. Space Phys., v. 119, p. 10133-10143.
  64. Laskar, F.I., Pallamraju, D., Veenadhari, B., 2014, "*Vertical coupling of atmospheres: Dependence on strength of sudden stratospheric warming and solar activity*", Earth, Planets and Space, v. 66, p. 1-10.
  65. Laskar, F.I., Pallamraju, D., Veenadhari, B., Vijaya L.T., Reddy, A.M., Chakrabarti, S., 2015, "*Gravity waves in the thermosphere: Solar activity dependence*", Adv. Space Res., v. 55, p. 1651-1659.
  66. Mallik, C., Ghosh, D., Ghosh, D., Sarkar, U., Lal, S., Venkataramani, S., 2014, "*Variability of SO<sub>2</sub>, CO and light hydrocarbons over a megacity in Eastern India: effects of emissions and transport*", Environ. Sci. Pollut. Res., v. 21, p. 8692-8706.

67. Manju, G., Haridas, M.K.M., Ramkumar, G., Pant, T.K., Sridharan, R., Sreelatha, P., 2014, "Gravity wave signatures in the dip equatorial ionosphere thermosphere system during the annular solar eclipse of 15 January 2010", J. Geophys. Res. Space Phys., v. 119, p. 4929-4937.
68. Naja, M., Mallik, C., Sarangi, T., Sheel, V., Lal, S., 2014, "SO<sub>2</sub> measurements at a high altitude site in the central Himalayas: Role of regional transport", Atmos. Environ., v. 99, p. 392-402.
69. Ojha, N., Naja, M., Sarangi, T., Kumar, R., Bhardwaj, P., Lal, S., Venkataramani, S., Sagar, R., Kumar, A., Chandola, H.C., 2014, "On the processes influencing the vertical distribution of ozone over the central Himalayas: Analysis of yearlong ozonesonde observations", Atmos. Environ., v. 88, p. 201-211.
70. Pallamraju, D., Gurubaran, S., Venkat Ratnam, M., 2014, "A brief overview on the special issue on CAWSES-India Phase II program", J. Atmos. Sol. Terr. Phys., v. 121, p. 141-144.
71. Pallamraju, D., Baumgardner, J., Singh, R. P., Laskar, F. I., Mendillo, C., Cook, T., Lockwood, S., Narayanan, R., Pant, T. K., Chakrabarti, S., 2014, "Daytime wave characteristics in the mesosphere lower thermosphere region: Results from the Balloon-borne Investigations of Regional-atmospheric Dynamics experiment", J. Geophys. Res. Space Physics, v. 119, p. 2229 - 2242.
72. Pandey, K., Sahu, L.K., 2014, "Emissions of volatile organic compounds from biomass burning sources and their ozone formation potential over India", Curr. Sci., v. 106, p. 1270-1279.
73. Pandya, B.M., Haider, S.A., 2014, "Numerical simulation of the effects of meteoroid ablation and solar EUV/X-ray radiation in the dayside ionosphere of Mars: MGS/MEX observations", J. Geophys. Res. Space Phys., v. 119, p. 9228-9245.
74. Pramitha, M., Venkat Ratnam, M., Taori, A., Krishna Murthy, B.V., Pallamraju, D., Bhaskar, R.S.V., 2015, "Evidence for tropospheric wind shear excitation of high-phase-speed gravity waves reaching the mesosphere using the ray-tracing technique", Atmos. Chem. Phys., v. 15, p. 2709-2721.
75. Rastogi, R.G., Chandra, H., Janardhan, P. Shah R., 2014, "Equatorial and mid-latitude ionospheric currents in India based on 40 years of data at Trivandrum and Alibag", Ind. J. Radio and Space Phys., v. 43, p. 274-283.
76. Rastogi, R.G., Chandra, H., Janardhan, P., Hoang, T.L., Condori, L., Pant, T.K., Prasad, D.S.V.V.D., Reinisch, B., 2014, "Ionospheric spread-F during the magnetic storm of 22 January 2004 at stations in Asian zone", J. Earth Syst. Sci., v. 123, p. 1273-1285.
77. Russell, P.B., Kacenelenbogen, M., Livingston, J.M., Hasekamp, O.P., Burton, S.P., Schuster, G.L., Johnson, M.S., Knobelspiesse, K.D., Redemann, J., Ramachandran, S., Holben, B.N., 2014, "A multi-parameter aerosol classification method and its application to retrievals from spaceborne polarimetry", J. Geophys. Res. Atmos., v. 119, p. 9838-9863.
78. Sahu L.K., 2014, "Reactive halogens and their measurements in the troposphere", Ind. J. Marine Sci., v. 43, p. 1-8.
79. Sarkhel, S., Mathews, J.D., Raizada, S., Sekar, R., Chakrabarty, D., Guharay, A., Jee, G., Kim, J.H., Kerr, R.B., Ramkumar, G., Sridharan, S., Wu, Q., Mlynczak, M.G., Russell III, J.M., 2015, "A case study on the occurrence of an unusual structure in the sodium layer over Gadanki, India", Earth, Planets and Space, v. 67, p. 19, pp. 1-15.
80. Sekar, R., Gupta, S.P., Chakrabarty, D., 2014, "Characteristics of E-region background ionosphere and plasma waves measured over the dip equator during total solar eclipse campaign", J. Atmos. Sol. Terr. Phys., v. 114, p. 58-65.
81. Sekar, R., Gupta, S.P., Chakrabarty, D., 2014, "On the altitude of initiation of the gradient drift waves at different longitude sectors in the vicinity of the dip equator", J. Atmos. Sol. Terr. Phys., v. 121, p. 59-62.
82. Selvaraj, D., Patra, A.K., Chandra, H., Sinha, H.S.S., Das, U., 2014, "Scattering cross section of mesospheric echoes and turbulence parameters from Gadanki radar observations", J. Atmos. Sol. Terr. Phys., v. 119, p. 162-172.
83. Sheel, V., Sahu, L.K., Kajino, M., Deushi, M., Stein, O., Nedelec, P., 2014, "Seasonal and inter-annual variability of CO based on MOZIC observations, MACC reanalysis and model simulations over an urban site in India", J. Geophys. Res. Atmos., v. 119, p. 9123-9141.
84. Sridharan, R., Bagiya, M.S., Sunda, S., Choudhary, R., Pant, T.K., Jose, L., 2014, "First results on forecasting the spatial occurrence pattern of L-band scintillations and its temporal evolution", J. Atmos. Sol. Terr. Phys., v. 119, p. 53-62.
85. Sunda, S., Sridharan, R., Vyas, B.M., Khekale, P.V., Parikh, K.S., Ganeshan, A.S., Sudhir, C.R., Satish, S.V., Bagiya, M.S., 2015, "Satellite Based Augmentation Systems A Novel and Cost Effective Tool For Ionospheric and Space Weather Studies", Space Weather, v. 13, p. 6-15.
86. Thampi, S.V., Bagiya, M.S., Chakrabarty, D., Acharya, Y.B., Yamamoto, M., 2014, "An ensemble average method to estimate absolute TEC using radio beacon based differential phase measurements: Applicability to regions of large latitudinal gradients in plasma density", Radio Sci., v. 49, p. 1153-1161.
87. Thampi, S.V., Sridharan, R., Das, T.P., Ahmed, S.M., Kamalakar, J.A., Bhardwaj, A., 2015, "The spatial distribution of molecular Hydrogen in the lunar atmosphere New results", Planet. Space Sci., v. 106, p. 142-147.
88. Yadav, R., Sahu, L.K., Jaaffrey, S.N.A., Beig, G., 2014, "Distributions of ozone and related trace gases at an urban site in western India", J. Atmos. Chem., v. 71, p. 125-144.
89. Yadav, R., Sahu, L.K., Jaaffrey, S.N.A., Beig, G., 2014, "Temporal Variation of Particulate Matter (PM) and Potential Sources at an Urban Site of Udaipur in

Western India", *Aerosol and Air Quality Res.*, v. 14, p. 1613-1629.

### Geosciences

90. Akhtar, U.S., Rastogi, N., McWhinney, R.D., Bruce, U., Chow, C-W., Evans, G. J., Scott, J. A., 2014, "The combined effects of physicochemical properties of size-fractionated ambient particulate matter on in vitro toxicity in human A549 lung epithelial cells", *Toxicology Reports*, v. 1, p. 145-156
91. Awasthi, N., Ray, J.S., Pande, K., 2015, "Origin of the Mile Tilek Tuff, South Andaman: evidences from  $^{40}\text{Ar}$ - $^{39}\text{Ar}$  chronology and geochemistry", *Curr. Sci.*, v. 108, p. 205-210.
92. Awasthi, N., Ray, J.S., Singh, A.K., Band, S.T., Rai, V.K., 2014, "Provenance of the Late Quaternary sediments in the Andaman Sea: Implications for monsoon variability and ocean circulation", *Geochem. Geophys. Geosys.*, v. 15, p. 3890-3906.
93. Bohra, A., Kotlia, B.S., Laskar, A.H., Yadava, M.G., 2014, "Evidence of late quaternary palaeoseismicity from Yunam Tso, Lahaul and Spiti, NW Himalaya, India", *J. Earth Syst. Sci.*, v. 123, p. 606-613.
94. Bose, T., Chakraborty, S., Borgaonkar, H., Sengupta, S., Ramesh, R., 2014, "Estimation of past atmospheric carbon dioxide levels using tree-ring cellulose  $\delta^{13}\text{C}$ ", *Curr. Sci.*, v. 107, p. 971-982.
95. Goodbred Jr. S.L., Paolo, P.M., Ullah, M.S., Pate, R.D., Khan, S.R., Kuehl, S.A., Singh, S.K., Rahaman, W., 2014, "Piecing together the Ganges-Brahmaputra-Meghna River delta: Use of sediment provenance to reconstruct the history and interaction of multiple fluvial systems during Holocene delta evolution", *Geol. Soc. Am. Bull.*, v. 126, p. 1495-1510.
96. Goswami, V., Singh, S.K., Bhushan, R., 2014, "Impact of water mass mixing and dust deposition on Nd concentration and  $\epsilon_{\text{ND}}$  of the Arabian Sea water column", *Geochim. Cosmochim. Ac.*, v. 145, p. 30-49.
97. Kiran, R., Krishna, V. V.J., Naik, B. G., Mahalakshmi, G., Rengarajan, R., Mazumdar, A., Sarma, N.S., 2015, "Can hydrocarbons in coastal sediments be related to terrestrial flux? A case study of Godavari river discharge (Bay of Bengal)", *Curr. Sci.*, v. 108, , p. 96-100.
98. Lekshmy, P.R., Mudhun, M., Ramesh, R. Jani, R.A., 2014, " $^{18}\text{O}$  depletion in monsoon rain relates to large scale organized convection rather than the amount of rainfall", *Scientific Reports (Nature)*, v. 4, p. 56-61.
99. Prakash, S., Ramesh, R., Sheshshayee, M.S., Mohan, R., Sudhakar, M., 2015, "Nitrogen uptake rates and f-ratios in the Equatorial and Southern Indian Ocean", *Curr. Sci.*, v. 108, p. 239-245.
100. Rahaman, W., Singh, S.K., Rai, V.K., 2014, "Molybdenum isotopes in two Indian estuaries: Mixing characteristics and input to oceans," *Geochim. Cosmochim. Ac.*, v. 141, p. 407-422.
101. Rajput, P., Sarin, M.M., Sharma, D., Singh, D., 2014, "Organic aerosols and inorganic species from post-harvest agricultural-waste burning emissions over northern India: Impact on mass absorption efficiency of elemental carbon", *Environ. Sci.: Processes & Impacts*, v. 16, p. 2371-2379.
102. Ram, K., Sarin, M.M., 2015, "Atmospheric carbonaceous aerosols from Indo-Gangetic Plain and Central Himalaya: Impact of anthropogenic sources", *J. Environ. Manage*, v. 148, p. 153-163.
103. Rengarajan, R., Sarma, V.V.S.S., 2015, "Submarine groundwater discharge and nutrient addition to the coastal zone of the Godavari estuary", *Mar. Chem.*, v. 172, p. 57-69.
104. Sati, S. P., Ali, S. N., Rana, N., Bhattacharya, F., Bhushan, R., Shukla, A. D., Sundriyal, Y. P., Juyal, N., 2014, "Timing and extent of Holocene glaciations in the monsoon dominated Dunagiri valley (Bangni glacier), Central Himalaya, India", *J. Asian Earth Sci.*, v. 91, p. 125-136.
105. Singh, A., Ramesh, R., 2015, "Environmental controls on new and primary production in the northern Indian Ocean", *Prog. Oceanogr*, v. 131, p. 138-145.
106. Singh, A., Gandhi, N., Ramesh, R., Prakash, S., 2015, "Role of cyclonic eddy in enhancing primary and new production in the Bay of Bengal", *J. Sea Res.*, v. 97, p. 5-13.
107. Singh, A., Rastogi, N., Sharma, D., Singh, D., 2015, "Inter and intra-annual variability in aerosol characteristics over northwestern Indo-Gangetic Plain", *Air. Qual. Res.*, v. 15, p. 376-386.
108. Singh, A., Mohiuddin, A., Ramesh, R., Raghav, S., 2014, "Estimating the Loss of Himalayan Glaciers under Global Warming Using the  $\delta^{18}\text{O}$ -Salinity Relation in the Bay of Bengal", *Environ. Sci. Tech. Lett.*, v. 1, p. 249-253.
109. Singh, P., Yadava, M.G., Ahmad, M.Z., Mohapatra, P.P., Laskar, A.H., Doradla, S., Saravanavel, J., Kumanan, C.J., 2014, "Fertile farmlands in Cauvery delta: evolution through LGM", *Curr. Sci.*, v. 108, p. 218-225.
110. Singh, S.P., Singh, S.K., Bhushan, R., 2014, "Dissolved boron in the Tapi, Narmada and the Mandovi estuaries, the western coast of India: Evidence for conservative behavior", *Estuar. Coast*, v. 37, p. 1017-1027.
111. Singh, S.P., Singh, S.K., Bhushan, R., Rai, V.K., 2015, "Dissolved silicon and its isotopes in water column of the Bay of Bengal: Internal cycling versus lateral transport", *Geochim. Cosmochim. Ac.*, v. 151, p. 172-191.
112. Singh, S. P., Singh, S. K., Bhushan, R., 2013, "Internal cycling of dissolved barium in water column of the Bay of Bengal", *Mar. Chem.*, v. 154, p. 12-23.
113. Srinivas, B., arin, M.M., 2014, " $\text{PM}_{2.5}$ , EC and OC in atmospheric outflow from the Indo-Gangetic Plain: Temporal variability and aerosol organic carbon-to-organic mass conversion factor", *Sci. of the Total Environ.*, v. 487, p. 196-205.

114. Srinivas, B., Sarin, M. M., Rengarajan, R., 2014, "Atmospheric transport of mineral dust from the Indo-Gangetic Plain: Temporal variability, acid processing and iron solubility", *Geochem. Geophys. Geosyst.*, v. 15, p. 3226-3243.
115. Srinivas, B., Sarin, M. M., Sarma, V. V. S. S., 2014, "Atmospheric outflow of nutrients to the Bay of Bengal: Impact of anthropogenic sources," *Jour. Marine Systems*, v. 141, p. 34-44.
116. Srivastava, R., Ramesh, R., Rao, T.N., 2015, "Stable isotopic differences between summer and winter monsoon rains over southern India", *J. Atmos. Chem*, v. 71, p. 321-331.
117. Sudheer, A.K., Rengarajan, R., Sheel, V., 2015, "Secondary organic aerosol over an urban environment in a semi-arid region of western India", *Atmos. Pollution Res.*, v. 6, p. 11-20.
118. Sudheer, A.K., Rengarajan, R., Deka, D., Bhushan, R., Singh, S.K., Aslam, M. Y., 2014, "Diurnal and Seasonal Characteristics of Aerosol Ionic Constituents over an Urban Location in Western India: Secondary Aerosol Formation and Meteorological Influence", *Aerosol Air Qual. Res.*, v.14, p. 1701-1713.
119. Viladkar, S.G., Ramesh, R., 2014, "Stable Isotope geochemistry of some Indian Carbonatites: Implications for magmatic processes and post-emplacement hydrothermal alteration", *Comunicaciones Geológicas*, v. 101, p. 55-62.
120. Yadava, M.G., Dayal, A. M., Ramesh, R., 2014, "Effects of dead carbon fraction and the mineralogy of speleothems on their stable carbon and oxygen isotopic variations", *Gond. Geol. Mag.*, v. 29, p. 53-59.
127. Das, M., Sahoo, B.K., Pal, S., 2014, "Relativistic Spectroscopy of Plasma Embedded Li-like Systems with the Screening Effects in Two-body Debye Potentials", *J. Phys. B*, v. 47, p. 175701, pp. 1-13.
128. Dhuria, M., Hati, C., Rengarajan, R. Sarkar, U., 2015, "Explaining the CMS  $eejj$  and  $e$  missing  $p_T jj$  excess and leptogenesis in superstring inspired  $E_6$  models", *Phys. Rev. D*, v. 91, p. 055010, pp. 1-9.
129. Deppisch, F. F., Gonzalo, T. E., Patra, S., Sahu, N., Sarkar, U., 2015, "Signal of Right-Handed Charged Gauge Bosons at the LHC?", *Phys. Rev. D*, v. 90, p. 053014, pp. 1-5.
130. Deppisch, F. F., Gonzalo, T. E., Patra, S., Sahu, N., Sarkar, U., 2015, "Double beta decay, lepton flavor violation, and collider signatures of left-right symmetric models with spontaneous D-parity breaking", *Phys. Rev. D*, v. 91, p. 015015, pp. 1-18.
131. Guan, H., Shao, H., Qian, Y., Huang, Y., Liu, P.L., Bian, W., Li, C.B., Sahoo, B.K., Gao, K.L., 2015, "Combined experimental and theoretical probe of the lifetime of the  $3d\ 2D5/2$  state in  $40Ca^+$ ", *Phys. Rev. A*, v. 91, p. 022511 (1-7).
132. Kadam, G.P., Mishra, H., 2014, "Bulk and shear viscosities of hot and dense hadron gas", *Nucl.Phys.*, v. A934, p. 133-147.
133. Kadam, G.P., 2015, "Transport properties of hadronic matter in magnetic field", *Mod. Phys. Lett.*, A30, 10, p. 1550031, pp. 1-11.
134. Bambhaniya, G., Goswami, S., Khan, S., Konar, P., Mondal, T., 2015, "Looking for hints of a reconstructible seesaw model at the Large Hadron Collider", *Phys. Rev. D*, v. 91, p. 075007, pp. 1-8.
135. Joshipura, A.S., Patel, K.M., 2014, "Discrete flavour symmetries for degenerate solar neutrino pair and their predictions", *Phys. Rev. D*, v. 90, p. 036005, pp. 1-15.
136. Roy, K., Chakrabarti, B., and Kota, V.K.B, 2014, "Statistical properties of spectral fluctuations of  $N$  interacting bosons in an harmonic trap", *Phys. Rev. E*, v. 90, p. 052137, pp. 1-8.
137. Kaur, J., Nandy, D.K., Arora, B., Sahoo, B.K., 2015, "Properties of alkali-atoms and alkaline-earth-metal ions for an accurate estimate of their long-range interactions", *Phys. Rev. A*, v. 91, p. 012705, pp. 1-11.
138. Kaur, K., Kaur, J., Arora, B., Sahoo, B.K., 2014, "Emending thermal dispersion interactions of Li, Na, K and Rb the alkali atoms with graphene in the Dirac model", *Phys. Rev. B*, v. 90, p. 245405, pp. 1-7.
139. Mahajan, N., Rengarajan, R., Sarkar, A., 2014, "Supersymmetric flat directions and resonant gravitino production", *Phys. Rev. D*, v. 90, p. 023522, pp. 1-6.
140. Ghosh, M., Ghoshal, P., Goswami, S., Raut, S.K, 2014, "Evidence for leptonic CP phase from  $NO\nu A$ ,  $T2K$  and  $ICAL$ : A chronological progression", *Nucl. Phys. B*, v. 884, p. 274-304.
141. Mahajan, N., 2014, "Charged Higgs contribution to  $0\nu 2\beta$  decay", *Phys.Rev. D*, v. 90, p. 035015, pp. 1-5.

### Theoretical Physics

121. Arora, B., Kaur, H., Sahoo, B.K., 2014, "Dispersion  $C3$  coefficients for the alkali atoms interacting with a graphene layer and with a carbon nanotube", *J. Phys. B*, v. 47, p. 155002, pp. 1-9.
122. Ananthanarayan, B., Lahiri, J., Patra, M., Rindani, S.D., 2014, "New physics in  $e^+e^- \rightarrow Z\gamma$  at the ILC with polarized beams: explorations beyond conventional anomalous triple gauge boson couplings", *JHEP*, v. 8, p. 124, pp. 1-28.
123. Kumar, A., Bhatt, J.R., Kaw, P.K., 2014, "Instabilities in Anisotropic Chiral Plasmas", *arXiv:1405.2865*, v. 2, pp. 1-19.
124. Prasanna, A.R., 2015, "On photon trajectories and electromagnetics near strongly gravitating cosmic sources, *Journal of Electromagnetic Waves and Applications*", *Journal of Electromagnetic Waves and Applications*, v. 29:3, p. 283-330
125. Chatterjee, B., Mishra, H., Mishra, A., 2015, "CP violation and chiral symmetry breaking in hot and dense quark matter in the presence of a magnetic field", *Phys. Rev. D*, v. 91, p. 034031, pp. 1-14.
126. Chakraborty, J., Konar, P., Mondal, T., 2014, "Copositive Criteria and Boundedness of the Scalar Potential", *Phys.Rev. D*, v. 89, p. 095008, pp. 1-23.

142. Mahajan, N., 2014, "Some remarks on nonminimal coupling of the inflaton", *Int.J.Mod.Phys. D*, v. 23, p. 1450076, pp. 1-10
143. Nandy, D.K., Singh, Y., Sahoo, B.K., 2014, "Implementation and applications of the relativistic equation-of-motion coupled-cluster method for the excited states of closed-shell atomic systems", *Phys. Rev. A*, v. 89, p. 062509, pp. 1-6.
144. Nandy, D.K., Sahoo, B.K., 2014, "Quadrupole shifts for the  $171\text{Yb}^+$  ion clocks: Experiments versus theories", *Phys. Rev. A*, v. 90, p. 050503(R), pp. 1-5.
145. Nandy, D.K., Sahoo, B.K., 2015, "Relativistic calculations of radiative properties and fine structure constant varying sensitivity coefficients in astrophysically relevant Zn II, Si IV and Ti IV ions", *MNRAS*, v. 447, p. 3812-3823.
146. Singh, N., 2014, "A generalization of the two-dimensional Ising model and the Bragg-Williams meanfield theory", *Phys. Scr.*, v. 89, p. 095204-095210.
147. Singh, N., 2014, "Optical conductivity of cuprates from Yang-Rice-Zhang ansatz: Comparison with experiment", *Physics Letters A*, v. 378, p. 2795-2800.
148. Chavda, N.D., Deota, H.N., Kota, V.K.B., 2014, "Poisson to GOE transition in the distribution of the ratio of consecutive level spacings", *Phys. Lett. A*, v. 378, p. 3012-3017.
149. Bhalla, P., Singh, N., 2014, "Infrared properties of cuprates in the pseudogap state: A study of Mitrovic-Fiorucci and Sharapov-Carbotte scattering rates", *Eur. Phys. J. B*, v. 8, p. 213, pp. 1-13.
150. Pathak, H., Ghosh, A., Sahoo, B.K., Das, B.P., Vaval, N., Pal, S., 2014, "Relativistic Equation of Motion Coupled-cluster Method for the Double Ionization Potentials of the Closed-shell Atoms", *Phys. Rev. A*, v. 90, p. 010501(R), pp. 1-7.
151. Pathak, H., Sahoo, B.K., Das, B.P., Vaval, N., Pal, S., 2014, "Relativistic Equation of Motion Coupled-cluster Method: Application to the closed-shell atomic systems", *Phys. Rev. A*, v. 89, p. 042510, pp. 1-7.
152. Srivastava, P.C., Sahu, R., Kota, V.K.B., 2015, "Shell model and deformed shell model spectroscopy of  $62\text{Ga}$ ", *Eur. Phys. J. A*, v. 51, p. 3, pp. 1-9.
153. Dev, P.S.B., Goswami, S., Mitra, M., 2015, "TeV Scale Left-Right Symmetry and Large Mixing Effects in Neutrinoless Double Beta Decay", *Phys. Rev. D*, v. 91, p. 113004, pp. 1-17.
154. Sahu, R., Kota, V.K.B., 2015, "Deformed shell model results for neutrinoless double beta decay of nuclei in  $A=60-90$  region", *Int. J. Mod. Phys. E*, v. 24, p. 1550022, pp. 1-21.
155. Sahoo, B.K., Singh, Y., Das, B.P., 2014, "Relativistic many-body analysis of the electric dipole moment of  $223\text{Rn}$ ", *Phys. Rev. A*, v. 90, p. 050501(R), pp. 1-4.
156. Sahoo, B.K., 2014, "Role of the multipolar black-body radiation shifts in the atomic clocks at the 10-18 uncertainty level", *Pramana-J. Phys.*, v. 83, p. 255-263.
157. Singh, Y., Sahoo, B.K., 2014, "Correlation trends in the polarizabilities of atoms and ions in the boron, carbon and zinc homologous sequences of elements", *Phys. Rev. A*, v. 90, p. 022511, pp. 1-8.
158. Singh, Y., Sahoo, B.K., 2015, "Rigorous limits on the hadronic and semileptonic CP-violating coupling constants from the electric dipole moment of  $199\text{Hg}$ ", *Phys. Rev. A*, v. 91, p. 030501(R), pp. 1-5.
159. Swain, A.K., Konar, P., 2015, "Constrained  $\sqrt{s}_{min}$  and reconstructing with semi-invisible production at hadron colliders", *Journal of High Energy Physics*, v. 1503, p. 142, pp. 1-22.
160. Goswami, S., Khan, S., Mishra, S., 2014, "Threshold effects and renormalization group evolution of neutrino parameters in TeV scale seesaw models", *Int. J. Mod. Phys. A*, v. 29, p. 1450114, pp. 1-30.
161. Haldar, S.K., Chakrabarti, B., Chavda, N.D., Das, T.K., Canuto, S., Kota, V.K.B., 2014, "Level-spacing statistics and spectral correlations in diffuse van der Waals clusters", *Phys. Rev. A*, v. 89, p. 043607, pp. 1-11.
162. Suthar, K., Roy, A., Angom, D., 2014, "Acoustic radiation from vortex-barrier interaction in atomic Bose-Einstein condensate", *J. Phys. B*, v. 47, p. 135301, pp. 1-9.
163. Roy, A., Angom, D., 2014, "Fluctuation- and interaction-induced instability of dark solitons in single and binary condensates", *Phys. Rev. A*, v. 90, p. 023612, pp. 1-9.
164. Tomar, G., Mohanty, S., 2014, "Muon anomalous magnetic moment and positron excess at AMS-02 in a gauged horizontal symmetric model", *JHEP*, v. 2014, p. 133, pp. 1-15.

### Atomic, Molecular and Optical Physics

165. Aadhi, A., Chaitanya, A.N., Jabir, M.V., Singh, R.P., Samanta, G.K., 2015, "All-periodically poled, high-power, continuous-wave, single-frequency tunable UV source", *Optics letters*, v. 40(1), p. 33-36.
166. Aadhi, A., Chaitanya, A.N., Singh, R.P., Samanta, G.K., 2014, "High-power, continuous-wave, solid-state, single-frequency, tunable source for the ultraviolet", *Optics letters*, v. 39 (12), p. 3410-3413.
167. Aadhi, A., Chaitanya, A.N., Singh, R.P., Samanta, G.K., 2014, "Type-I frequency-doubling characteristics of high-power, ultrafast fiber laser in thick BIBO crystal", *Optics Letters*, v. 39 (18), p. 5419-5422
168. Banerji, A., Singh, R.P., Bandyopadhyay, A., 2014, "Entanglement measure using Wigner function: Case of generalized vortex state formed by multiphoton subtraction", *Optics Communications*, v. 330, p. 85-90.
169. Sivaraman, B., Radhika, N., Das, A., G. Gopakumar, Majumdar, L., Chakrabarti, S.K., Subramanian, K.P., Raja Sekhar, B.N., Hada, M., Mont. Notic. Roy, 2015, "Infrared spectra and chemical abundance of methyl propionate in icy astrochemical conditions", *Astro. Soc.*, v. 448, p. 13721377.

170. DeSarkar, S., Mathew, G., Pande, K., Phukon, P., Singhvi, A.K., 2014, "Drainage Migration and out of sequence thrusting in Bhalukpong, Western Arunachal Himalaya", *J. Geodynamics*, v. 81, p. 1-16.
171. Chauhan, N., Adharyu, P., Vaghela, H., Singhvi, A.K., 2014, "EMCCD based luminescence imaging system for spatially resolved geo-chronometric and radiation dosimetric applications", *J. Instruments*, v. 9, P11016, pp. 1-22.
172. Samanta, G.K., Kumar, S.C., Aadhi, A., Ebrahim-Zadeh, M., 2014, "Yb-fiber-laser-pumped, high-repetition-rate picosecond parametric oscillator tunable in the ultraviolet", *Optics express*, v. 22 (10), p. 11476-11487.
173. Kadlac, J., Kocurek, G., Mohrig, D., Shinde, D.P., Murari, M.K., Varma, V., Stehlik, F., Benes, V., Singhvi, A.K., 2015, "Response of fluvial, aeolian and lacustrine systems to Late Pleistocene to Holocene climate change, Lower Moravian Basin, Czech Republic", *Geomorphology*, v. 232, p. 193-208.
174. McKenna-Lawlor, S., Tomi, L., Yinghui, L., Reitz, G., Straube, U., Bhardwaj, A., Lal, A.K., Singhvi, A.K., Nagamatsu, A., Muszaphar Shukor, S., Ferrari, F., Zagreev, B., Petrov, Z., Panasyuk, M., Nymmik, N., Kuznetsov, N., Townsend, N., Lawrence, P., 2014, "Feasibility study of Astronaut Standardized Career Dose Limits in LEO and the outlook for BLEO: the Biological Responses of Humans to Energetic Particle Radiation under microgravity conditions", *Acta Astronautica*, v. 104, p. 565-573.
175. Pandey, A.K., Pandey, P., Singh, G.D., Juyal N., 2014, "Climate footprints in the Late-Quaternary-Holocene landforms of Dun Valley, NW Himalaya, India", *Current Science*, v. 106, p. 245-253.
176. Prabhakar, S., Reddy, S.G., Aadhi, A., Kumar, A., Chithrabhanu, P., Samanta, G.K., Singh, R.P., 2014, "Spatial distribution of spontaneous parametric down-converted photons for higher order optical vortices", *Optics Communications*, v. 326, p. 64-69.
177. Gobinda, R.B., Sivaraman, B., Jen-lu Lo, Sekhar, R.B.N., Bing-Ming Cheng, Pradeep T., Mason N.J., 2014, "Vacuum ultraviolet photoabsorption of interstellar icy thiols", *J. Chem. Phys.*, v. 141, p. 231101, pp. 1-4.
178. Reddy, S.G., Prabhakar, S., Aadhi, A., Banerji, J., Singh, R.P., 2014, "Propagation of an arbitrary vortex pair through an astigmatic optical system and determination of its topological charge", *Journal of the Optical Society of America A*, v. 31, p. 1295-1302.
179. Reddy, S.G., Prabhakar, S., Kumar, A., Banerji, J., Singh, R.P., 2014, "Higher order optical vortices and formation of speckles", *Optics Letters*, v. 39, p. 4364-4367.
180. Kar, R., Chakraborty, T., Chakraborty, C., Ghosh, P., Tyagi, A., and Singhvi, A.K., 2014, "Morpho-sedimentary characteristics of the Quaternary Matiali fan, Jalpaiguri, India: implications for tectonoclimatic controls", *Geomorphology*, v. 227, p.137-154.
181. Sati, S.P., Ali, S.N., Rana, N., Bhattacharya, F., Bhushan, R., Shukla, A.D., Sudriyal, Y., Juyal, N., 2014, "Timing and extent of Holocene glaciations in the monsoon dominated Dunagiri valley (Bangni glacier), Central Himalaya, India", *Journal of Asian Earth Sciences*, v. 91, p. 125-136.
182. Simores, M., Chen, Y.G., Shinde, D.P., Singhvi, A.K., 2015, "Lateral Variations in the long term slip rate of the Chelungpu fault Central Taiwan, from the analysis of the deformed fluvial terraces", *J. Geophys. Res. Solid Earth*, v. 119, p. 3740-3766.
183. Sivaraman, B., Mukherjee, R., Subramanian, K.P., Banerjee, S.B., 2015, "Benzene formation on interstellar icy mantles containing propargyl alcohol", *The Astrophysical Journal*, v. 798:72, p. 1-4.
184. Sivaraman, B., Mukherjee, R., Subramanian, K.P., and Banerjee, S.B., 2014, "Electron impact dissociation of amorphous cis-methyl acetate ice analogs", *Chem. Phys. Lett.*, v. 609, p.167-171.
185. Sivaraman, B., Nair, B.G., Sekhar, R.B.N., Jones, N.C., Hoffmann, S.V., Mason, N.J., 2014, "Electron impact dissociation and VUV photoabsorption of frozen formamide", *Chem. Phys. Lett.*, v. 608, p. 404-407.
186. Sivaraman, B., Nair, B.G., Sekhar, R.B.N., Lo J.I., Sridharan, R., Cheng, B.M., Mason, N.J., 2014, "Vacuum ultraviolet photoabsorption of pure solid ozone and its implication on the identification of ozone on Moon", *Chem. Phys. Lett.*, v. 603, p. 33-36.
187. Prabhakar, S., Reddy, S.G., Aadhi, A., Kumar, A., Chithrabhanu, P., Samanta, G.K., Singh, R.P., 2014, "Spatial distribution of spontaneous parametric down-converted photons for higher order optical vortices", *Optics Communications*, v. 326, p. 64-69.
188. Ziegler, A.D., Wasson, R.J., Bhardwaj, A., Sundriyal, Y.P., Sati, S.P., Juyal, N., Nautiyal, V., Srivastava, P., Gillen, J., Saklani, U., 2014, "Pilgrims, progress, and the political economy of disaster preparedness the example of the 2013 Uttarakhand flood and Kedarnath disaster", *Hydrological Processes*, v. 28, p. 5985-5990.

#### Computer Centre

189. Shah, N.N., Raval, J.A., Gardas, N.K., 2015, "A Review of Data Confidentiality in Removable Media and Symmetric Key Encryption Algorithms", *International Journal of Engineering Research & Technology*, V.3, I.11, 1224-1228.
190. Jivani, J., Johnson, S., Pandi, G., 2015, "A Review of USB Encryption Techniques & Algorithms for Data Confidentiality", *International Journal of Advanced Research in Computer Science and Software Engineering*, V.5, I.4., 825-830.

#### Library & Information Services

191. Nishtha, A., 2014, "Identification of Research Trends at Physical Research Laboratory (PRL), Ahmedabad, India", *Library Philosophy and Practice*, Paper 1152, p. 1-20.

# Publications in Proceedings of Conferences / Symposia/ Workshops

## Astronomy and Astrophysics

1. Bisoi, S.K., Janardhan, P., Ananthakrishnan, S., 2014, "Decline in solar polar magnetic fields and heliospheric micro-turbulence levels: Are we headed towards a Maunder minimum?", Proceedings of the XXXI, URSI General Assembly and Scientific Symposium (URSI GASS), pp 1-4.
2. Janardhan, P., Bisoi, S.K., Ananthakrishnan, S., 2014, "Declining solar polar fields and heliospheric micro-turbulence: Implications for the next solar cycle and beyond ", Contributed Talk at the 40<sup>th</sup> COSPAR Scientific Assembly, Moscow, Russia, 2 10 August 2014.
3. Bisoi, S.K., Janardhan, P., Ananthakrishnan, S., 2014, "The deepest solar minima in the past 100 years: Steady decline in solar polar fields and heliospheric microturbulence levels", Contributed Talk at 32<sup>nd</sup> ASI Scientific meeting, Mar 20-22, 2014, Mohali.
4. Bisoi, S.K., Janardhan, P., Ananthakrishnan, S., 2014, "A study of density modulation index in the inner heliospheric solar wind", Contributed Talk at 40<sup>th</sup> COSPAR meeting, Moscow, Russia, 02-10 August, 2014.
5. Bisoi, S.K., Janardhan, P., Ananthakrishnan, S., 2014, "Steady decline in solar polar magnetic fields and heliospheric microturbulence levels: Are we headed towards a Maunder minimum?", Contributed Talk at

40<sup>th</sup> URSI GASS meeting, Beijing, China, 16-23 August, 2014.

6. Bisoi, S.K., Janardhan, P., Ananthakrishnan, S., 2014, "A study of density modulation index in the inner heliospheric solar wind", Poster presentation at 40<sup>th</sup> URSI GASS meeting, Beijing, China, 16-23 August, 2014.
7. Bisoi, S.K., 2015, "Solar and solar wind studies using ground and space based observations", Thesis presentation at 33<sup>rd</sup> ASI Scientific meeting, Pune, 17-20 February, 2015.
8. Singh, K.P. et al. including Vadawale, S.V. 2014, "ASTROSAT Mission", Proceedings of the SPIE, v. 9144, p. 91441S, pp. 1-15.
9. Singal, A.K., 2014, "A discrepancy observed in the dipole anisotropy in the radio sky at 1.4 GHz and that in the CMBR – A threat to the cosmological principle?", National conference on contemporary issues in high energy physics and cosmology, Journal of Physics - Conference Series, 481, 012007.

## Solar Physics

10. Srivastava, N., Crosby, N., Veronig, A., Robrecht, E., Vrsnak, B., Vennerstrom, S., Malandraki, O., Dalla, S., Rodriguez, L., Hesse, M., Odstrcil, D., 2013, "Solar eruptive filament studies at USO for the COMESEP project", Proceedings of the International Symposium

on Solar Terrestrial Physics (ISSTP), ASI conference series, v. 10, p. 67-71.

### Planetary Sciences and PLANEX Program

11. Banerjee, D., Panda, D.K., 2014, "The source of infrared stimulated luminescence signals from potassium and soda feldspars.", Abstracts of the 14<sup>th</sup> International Conference on Luminescence and ESR Dating, Montreal, 2014.
12. Basu, S.A., 2015, "Petrographical and mineralogical diversity between fresh and impact-melted domains of a Martian meteorite, Tissint.", 46<sup>th</sup> Lunar and Planetary Science Conference, Houston, Texas, USA. Abstract 1456.
13. Basu, S.A., Sisodia, M.S. Bhandari, N., 2015, "Geochemistry of texturally different fractions of Piplia Kalan Euclite and Lohawat Howardite", 46<sup>th</sup> Lunar and Planetary Science Conference, Houston, Texas, USA. Abstract 1464.
14. Bhattacharya, S., Basu, S.A., Chauhan, M., Sisodia, M. S., Le Corre, L., Reddy, V., Chauhan, P., 2015, "Spectral characterization of Piplia-Kalan meteorite in visible/near infrared spectral region.", 46<sup>th</sup> Lunar and Planetary Science Conference, Houston, Texas, USA. Abstract 1437.
15. Bose, S., Vijayan, S., Sinha, R.K., Murty, S.V.S., 2015, "Estimation of thermal inertia, sensible heat and latent heat over three landing sites on Mars", 46<sup>th</sup> Lunar and Planetary Science Conference, 16-20<sup>th</sup> March, 2015.
16. Prasad, D.K., Maniteja, V., Murty, S.V.S., 2014, "A novel approach for precise temperature measurement by planetary thermal probes.", 2<sup>nd</sup> International Workshop on Instrumentation for Planetary Missions, 1014.
17. Prasad, D.K., Rai, V.K., Murty, S.V.S., 2015, "A thermal model to study the effect of top porous layer on subsurface heat flow of Moon.", 46<sup>th</sup> Lunar Planet. Sci. Conf. 1768.
18. Ghosh, S., Ray, D., 2015, "Piplia Kalan: Is it a fragment of deep seated crust of 4 vesta asteroid?", 46<sup>th</sup> Lunar and Planetary Science Conference, abstract 1064.
19. Groopman, E., Zinner, E., Gyngard, F., Amari, S., Hoppe, P., Jadhav, M., Lin, Y., Marhas, K., Nittler, L.R., Xu, Y., 2015, "Mg-Al Isochrons in presolar grains: 26 Al/27 Al ratios are higher than previously estimated.", 46<sup>th</sup> LPSC, March 16-20, The Woodlands, Texas, Epoter 1559.
20. Mahajan, R.R., 2015, "Martian rocks that reached to Earth were ejected in 10 possible ejection events.", 46<sup>th</sup> Lunar Planetary science conference, 1166.
21. Mahajan, R.R., 2015, "Calibration of noble gas mass spectrometer: sensitivity and the long term stability.", 29<sup>th</sup> ISMAS international symposium on Mass spectrometry, pp 121-123.
22. Mahajan, R.R., 2015, "Martian meteorites: Constraint on ejection events of rocks from Mars.", 29<sup>th</sup> ISMAS international symposium on Mass spectrometry, pp 118-120.
23. Mishra, R.K., Simon, J.I., Ross, D.K., Needham, A.W., Messenger, S., Keller, L.P., Han, J., Marhas, K.K., 2015, "Na, K-rich rim around a chondrule in unequilibrated ordinary chondrite LEW 86018 (L3.1).", 46<sup>th</sup> LPSC, March 16-20, The Woodlands, Texas, 2994.
24. Murty, S.V.S., Ghosh, S., Ray, D., 2014, "Cosmic ray exposure age of Raghunathpura (IIAB) Iron meteorite.", 77<sup>th</sup> Annual Meeting of the Meteoritical Society, abstract 5135.
25. Pabari, J.P., Banerjee, D., Kanada, A., Goyal, S.K., Bhattacharya, A., Varma, P., Kumar, A., Upadhyay, R.B., 2015, "Moon Electrostatic Potential and Dust Analyser (MESDA) for future lunar mission", 46<sup>th</sup> Lunar and Planetary Science Conference, The Woodlands, Texas, Abstract 1167, 16-20 March, 2015.
26. Ray, D., Misra, S., Newsom, H., Upadhyay, D., 2015, "LA-ICP-MS trace element geochemistry of Sub-mm sized impact spherule from Lonar crater, India", 46<sup>th</sup> Lunar and Planetary Science Conference, abstract 1071.
27. Ray, D., Ghosh, S., Goswami, T., 2015, "Dergaon (H4-5) Chondrite: Diverse chondrule morphology and evidences of shock induced melting", 46<sup>th</sup> Lunar and Planetary Science Conference, abstract 1063.
28. Shukla, A.D., Ray, D., Pande, K., Shukla, P.N., 2014, "Formation of paleosol (fossil soil) in Deccan Continental flood basalt: alteration style and implications towards aqueous environment of early mars.", 8<sup>th</sup> International Conference on Mars, abstract 1190.
29. Shukla, A.D., Ray, D., Bhandari, N. 2015, "Basaltic eucrites similar to terrestrial MORBs: A geochemical approach", 46<sup>th</sup> Lunar and Planetary Science Conference, abstract 1356.
30. Shukla, A.D., Ray, D., Bhattacharya, S., Chauhan, P., 2015, "Hematite concretions from Jhuran formation (Upper Jurassic) of Kutch, India: Possible terrestrial analogue to Martian Blueberries", 46<sup>th</sup> Lunar and Planetary Science Conference, abstract 1366.
31. Sikdar, J., Rai V.K. 2015, "New chromatographic technique for simultaneous extraction of Si and Mg for their isotopic determination using MC-ICPMS", 29<sup>th</sup> ISMAS Symposium on Mass Spectrometry, Jodhpur, Rajasthan, 2-6 February, 2015.
32. Sisodia, M.S., Basu, S.A., Mahajan, R.R., 2015, "Hydrated minerals and carbonaceous chondrite fragments in Lohawat Howardite : Astrobiological implications.", Astrobiology Science Conference, p. 7069.
33. Vijayan S., Sinha, R.K., Murty, S.V.S., 2015, "Glacial environment between the interval of concentric crater fill and gully formation on Mars: Insights from lobate flow features in Alba Patera craters.", 46<sup>th</sup> Lunar and Planetary Science Conference, The Woodlands, Texas, 16-20 March, 2015.
34. Toyoda, S., Banerjee, D., Kumagai, H., Miyazaki, J-i, Ishibashi, J-i, Mochizuki, N., Kojima, S., 2014, "Gamma Ray Doses in water around sea floor hydrothermal area in the Southern Mariana Trough, in J. Ishibashi et al.

(ed.), *Sub seafloor Biosphere Linked to Hydrothermal Systems: TAIGA Concept.*, Springer.

### Geosciences

35. Bhavya, P.S., Kumar, S., Gupta, G.V.M., Sudheesh, V., Sudharma, K.V., 2015, "Carbon Uptake Mechanism in the Cochin Estuary and the Coastal Arabian Sea", World Ocean Science Congress, Cochin, India.
36. Narayana, A.C., Ramesh, R., 2014, "Climate change and its impact on coastal-marine ecosystem: Special reference to coral reefs Paleoclimates of Peninsular India", Climate Change and Marine Ecosystems: Proc. of the National Seminar on Climate Change and Marine Ecosystems, Cochin, India (eds. Hatha A.A.M., et al.). p. 24-31.
37. Rastogi, N., Patel, A., Singh, A., Singh, D., 2014, "Semi-continuous measurements of water-soluble organic carbon (WSOC): Implications to secondary organic aerosol formation", IASTA-Bulletin (ISSN 0971 4510), v. 21, p. 30-32.
38. Shukla, A.D., Srivastava, P., Rana, N., Bisht, P., Kumar, A., Jayangondaperumal, R., Sundriyal, Y., Sharma, U., Juyal, N., 2014, "Optical chronology suggests Trans Himalayan glaciers responded to the enhanced mid-latitude westerly during the last 30 ka", National Conference on Himalayan Geology-2014, Shimla, p.61.
39. Shukla, A.D., Ray, D., Pande, K., Shukla, P.N., 2014, "Formation of paleosol (Fossil Soil) in Deccan Flood Basalt: Alteration style and implications towards aqueous environment of early Mars", 8<sup>th</sup> International Conference on Mars, Pasadena, California. LPI Contribution No.1791, p.1194.
40. Shukla, A.D., Bhattacharyya, F., Rastogi, B.K., 2014, "Chronology and geochemistry of dry land fluvial system, western India", LED 2014, Montreal, Canada.
41. Rastogi, N., Patel, A., Singh, A., Singh, D., 2014, "Secondary organic aerosol formation over Indo-Gangetic Plain during winter using first PILS-WSOC measurement in India", International Aerosol Conference-2014, Busan, South Korea.
42. Rastogi, N., Singh, A., Singh, D., 2014, "Seasonal variability in secondary aerosol formation over Indo-Gangetic Plain", IGBP symposium on Geosphere-Biosphere Interactions in a Future Earth, Bengaluru, India.
43. Sudheer, A.K., Rengarajan, R., Bhushan, R., Singh, S. K., Upadhyay, M., Rathore, J.S., 2014, "Organic Aerosol over Western Region of India: Characteristics and Heterogeneity in Source", IASTA BULLETIN, v. 21, issue 1 & 2, p. 358-359.
44. Singh, A., Rastogi, N., Singh, D., 2014, "Size segregated carbonaceous aerosols over the source region of biomass burning in the Indo-Gangetic Plain", IASTA-Bulletin, v.-21, p. 23-25.

### Theoretical Physics

45. Bastero-Gil, M., Berera, A., Mahajan, N., Rangarajan, R., 2014, "Resolving the Inflationary Power Spectrum", Proceedings of CosPA 2013 - Symposium on Cosmology and Particle Astrophysics, Hawaii, e-published at <http://www.slac.stanford.edu/conf/C131112/>.
46. Mahajan, N., Rangarajan, R., 2014, "Remarks on non-Gaussian fluctuations of the inflaton and constancy of  $\zeta$  outside the horizon", J. Phys. Conf. Ser., v. 484, p. 012066, pp. 1-4.
47. Kota, V.K.B., 2014, "Lie algebra Symmetries and Quantum Phase Transitions in Nuclei", Proceedings of the National Conference on Nuclear Physics, Edited by K.C. Panda and Z. Naik, Pramana-J. Phys. 82, 743-755.
48. Sahu, R., Kota, V.K.B., 2014, "Deformed shell model studies of spectroscopic properties of  $^{64}\text{Zn}$  and  $^{64}\text{Ni}$  and the positron double beta decay of  $^{64}\text{Zn}$ ", Proceedings of the National Conference on "Nuclear Physics", Edited by K.C. Panda and Z. Naik, Pramana-J. Phys. 82, 757-767.
49. Kota, V.K.B., Vyas, M., 2014, "Embedded Random Matrix Ensembles with Lie Symmetries: Results from  $U(\Omega)$  Wigner-Racah algebra", Proceedings of International Symposium on "Symmetries in Science XVI", Edited by D. Schuch and M. Ramek, J. Phys.: Conf. Ser. 538, 012011/1-12.
50. Kota, V.K.B., 2015, "Group Theory for Embedded Random Matrix Ensembles", Proceedings of the 30th International Colloquium on Group Theoretical Methods in Physics, Edited by F. Brackx, H. De Schepper and J. Van der Jeugt, J. Phys.: Conf. Ser. 597, 012050/1-11.
51. Singh, N., Sharma, R., 2015, "Optical conductivity of cuprates in the pseudogap state: Yang-Rice-Zhang model and antiferromagnetic spin waves", AIP Conf. Proc. 1661, 110025 (2015).

### Atomic, Molecular and Optical Physics

52. Reddy, S.G., Prabhakar, S., Ali Anwar, M.A., Banerji, J., Singh, R.P., 2014, "Propagation of an arbitrary vortex pair through an astigmatic optical system", National Laser Symposium, Sri Venkateswara University, Tirupathi, India, p. CP-04-56, 03-06 December.
53. Chithrabhanu, P., Reddy, S.G., Aadhi A., Prabhakar, S., Ali Anwar, M. A., Singh, R.P., 2014, "Scattering of non-separable light beams", National Laser Symposium, Sri Venkateswara University, Tirupathi, India, p. CP-04-09, 03-06 December.
54. Aadhi, A., Chithrabhanu, P., Reddy, S.G., Prabhakar, S., Jabir, M.V., Samanta, G.K., Singh, R.P., 2014, "Non-interferometric method to measure the Pancharatnam phase using non-separable states", National Laser Symposium, Sri Venkateswara University, Tirupathi, India, p. CP-04-59, 03-06 December.

55. Reddy, S.G., Prabhakar, S., Ali Anwar, M.A., Banerji, J., and Singh, R.P., 2014, "*Modelling of scattered optical vortices*", Photonics, IIT Kharagpur, India, p. S5A.32, 13-16 December, 2014
56. Reddy, S.G., Chithrabhanu, P., Prabhakar, S., Ali Anwar, M.A., Singh, R.P., 2014, "*Recovery of orbital angular momentum states after scattering*", Photonics, IIT Kharagpur, India, p. S4C.4, 13-16 December, 2014.
57. Chithrabhanu, P., Aadhi, A., Reddy, S.G., Prabhakar, S., Ali Anwar, M.A., Singh, R.P., 2014, "*Construction of Coherent and Partially Coherent Orbital Angular Momentum Poincare Sphere*", Photonics, IIT Kharagpur, India, p. M4A.82, 13-16 December, 2014.
58. Prabhakar, S., Reddy, S.G., Chithrabhanu, P., Aadhi, A., Samanta, G.K., Singh, R.P., 2014, "*Continuous-variable Entanglement in Optical Vortex Beams*", Photonics, IIT Kharagpur, India, p. M4A.83, 13-16 December, 2014.
59. Reddy, S. G., Chithrabhanu, P., Prabhakar, S., Ali Anwar, M. A., Singh, R.P., 2015, "*Divergence of optical vortex beams with measurable parameters*", International conference on optics and photonics (ICOP 2015), Calcutta University, Kolkata, India, p. 274, 20-22 February, 2015.
60. Chithrabhanu, P., Reddy, S.G., Ali Anwar, M.A., Aadhi, A., Prabhakar, S., Singh, R.P., 2015, "*Generalized orbital angular momentum Poincare sphere*", International conference on optics and photonics (ICOP 2015), Calcutta University, Kolkata, India, p. 271, 20-22 February, 2015.
61. Aadhi, A., Chithrabhanu, P., Reddy, S.G., Chaitanya, A., Samanta, G.K., Singh, R.P., 2015, "*Superposition of polarization singularity*", International conference on optics and photonics (ICOP 2015), Calcutta University, Kolkata, India, p. 336, 20-22 February, 2015.

## Books Edited/ Review Articles/Technical Notes

### Books Edited

1. Juyal, N., Kale, V. S., 2014, "*Ladakh: The High-Altitude Indian Cold Desert, In Landscapes and Landforms of India (ed)*", Springer Dordrecht Heidelberg, p. 115-124.
2. Juyal, N. and Kale, V. S., 2014, "*The Great Rann of Kachchh: The Largest Saline Marshland in India. In Landscapes and Landforms of India (ed)*", Springer Dordrecht Heidelberg p. 231-238.
3. Singhvi, A. K., Krishnan, R. and Kale, V. S., 2014, "*Climates of India: Past and Present,. In Landscapes and Landforms of India (ed)*", Springer Dordrecht Heidelberg p. 15-24.
4. Haider, S.A., 2015, "*Upper ionosphere of Mars during solar quiet and disturbed conditions*", Planetary Exploration and Science: Recent Results and Advances, Eds. Shuanggen Jin and Wing Huen Ip, Springer Heidelberg, p. 119-146.

### Review Articles

1. Singh, N., and Sharma, R., 2015, "*Infrared conductivity of cuprates using Yang-Rice-Zhang ansatz: Review of our recent investigations*", AIP Conf. Proc., v. 1661, p. 030004.

### Technical Reports

1. Rajesh, T. A., Manke, A. A., and Ramachandran, S., 2014, "Real time data acquisition and visualization software package for aerosol size spectrometer", PRL Technical Note, PRL-TN-2014-106.
2. Phadke, K. A., Narayanan, R., Singh, R. P., and Pallamraju, D., 2014, "An Automated CCD-based Multi-wavelength Airglow Photometer (CMAP) for Optical Aeronomy Studies", PRL-TN-2014-107.

# Promotion of Basic Sciences, Official Language and Outreach Activities

## Vikram Jayanti Celebration at PRL 12 August, 2014

The birth anniversary of Prof. Vikram A. Sarabhai was celebrated at Physical Research Laboratory (PRL), Ahmedabad on 12<sup>th</sup> August 2014 by having a Tree Plantation ceremony in the morning, followed by the Awards Presentation ceremony where six distinguished scientists were bestowed the Hari Om Ashram Prerit Dr. Vikram Sarabhai Research Awards and PRL Award for the year 2013. On this occasion one of the distinguished alumni of PRL, Prof. P. D. Bhavsar, former Director of Space Applications Centre, Ahmedabad was felicitated with a memento, shawl and a citation for his outstanding contributions in his field of scientific research, Space Sciences.

The Hari Om Ashram Prerit Dr. Vikram Sarabhai research award in the field of Space Sciences was awarded to Dr. Tarun Kumar Pant from the Space Physics Laboratory, Thiruvananthapuram, for his significant contributions towards understanding atmospheric coupling processes, in particular, the association of electro-jet and counter electro-jet with neutral atmospheric dynamics.

Shri Joji J. Chaman from ISRO Inertial Systems Unit, Thiruvananthapuram received the Hari Om Ashram Prerit Dr. Vikram Sarabhai research award in the field of Space Application for his innovative and outstanding contributions in inertial navigation system for spacecrafts deployed for terrestrial and planetary missions.

In the field of Electronics, Informatics, Telematics and Automation, the Hari Om Ashram Prerit Dr. Vikram Sarabhai research award was conferred jointly to Prof. Souvik Mahapatra from the Indian Institute of Technology Bombay,

Mumbai for his significant contribution and development of Negative Bias Temperature Instability tolerant CMOS devices and to Prof. Ranjan Bose from the Indian Institute of Technology, Delhi, New Delhi for his outstanding contributions in the area of coding for secure communication.



Dignitaries from the left (seating): Prof. Utpal Sarkar, Prof. U. R. Rao, Prof. J. N. Goswami  
Dignitaries from the left (Standing): Shri J. J. Chaman, Dr. T. K. Pant, Dr. N. V. C. Rao,  
Prof. R. Bose, Dr. J. S. Ray and Prof. S. Mahapatra

The recipients of the PRL Award were Dr. N. V. Chalapathi Rao from the Banaras Hindu University, Varanasi for his pioneering contributions on Indian kimberlites and mantle processes influencing their evolution and Dr. J. S. Ray from Physical Research Laboratory, Ahmedabad for his significant contributions on the origin and evolution of Indian carbonatites and the Andaman subduction zone.

Each award carried a Medal and a Cash Prize of Rs.50,000/-. The Vikram Sarabhai Research Awards were instituted from funds provided by Pujya Shri Mota of Hari Om Ashram, Nadiad, and the PRL Award is supported by the Aruna Lal Endowment Fund established by late Prof. Devendra Lal, former Director of PRL.

## PLANEX Programme

With the aim of creating awareness amongst students and research scholars particularly in the Universities and other Laboratories and Academic Institutions and to attract bright talented students to take up research work in the challenging area of Planetary Science and Exploration, the PLANEX programme of ISRO has been organizing periodic workshops and training programmes. Following 'Outreach Activities' were organized by PLANEX group during the year 2014-2015.



Participants of the 15<sup>th</sup> PLANEX Workshop on "Mars and Moon: Remote Sensing and Analogue Studies", 4-10 January 2015.

- Twelve PLANEX supported projects are presently ongoing, and have resulted in 14 peer reviewed publications in national and international journals. Results have been presented in various national and international conferences.
- PLANEX national facilities have been used by PLANEX PIs, PRL scientists and other visitors.
- Four issues of the PLANEX newsletter have been published in this year.

## RESPOND Programme

The Indian Space Research Organization (ISRO) has evolved a programme through which financial support is provided to academia in India for conducting research and development activities related to Space Science (PRL), Space Technology and Space Application. This programme is called RESPOND. In special cases research and development projects proposed by non-academic R & D laboratories can also be supported through this programme. The aim of RESPOND is to encourage quality research in areas of relevance to the Indian space programme.

The annual RESPOND (Space Science) review meeting was held on 12-13 March 2015 at the Physical Research Laboratory to monitor the progress of ongoing projects. Reports on 17 projects were presented by investigators (PIs/Co-PIs/research students of PIs) working in different fields in space sciences and hailing from universities from different part of our country. The subjects of the proposals

encompass Astronomy and Astrophysics, Physics of the Earth atmosphere/ionosphere, Solar Physics, Space Weather, and the Space Plasma Physics.

## Activities on the promotion of Basic Sciences



PRL Exhibit in Vibrant Gujarat Global Trade Show 2015.

PRL participated in the Vibrant Gujarat Global Trade Show 2015 as a part of the Vibrant Gujarat Summit 2015. As a part of this trade show an "Education Pavilion" was set up and PRL presented exhibits which included info-sheets on various research activities carried out in PRL and live models on Optical Tweezer, Mars Orbiter Mission and Exoplanets. The exhibits received overwhelming response from the visitors which included top officials from the State Government, executives of various educational organizations, Universities, academic institutes, young students and the general public.

PRL has been organizing popular lectures by eminent scientists open to the public. In this series the following popular lectures were organized during the this year.

- "Galactic Neutrino Communication and Search for Extra Terrestrial Intelligence (SETI)", Prof. Sandip Pakvasa, University of Hawaii, Honolulu.
- "The Impacts of Extreme Space Weather on Society and the Economy", Prof. Daniel N. Baker, Director, Laboratory for Atmospheric and Space Physics, University of Colorado, Boulder, USA & Vikram Professor, PRL.

## Science Day Celebration and PRL Scholarship

As has been the practice for several years, a day-long celebration was held at the Physical Research Laboratory,

Ahmedabad to mark the National Science Day. The celebrations aim to attract young minds and motivate them to take up science as one of their career options. National Science Day is also observed to spread the message of the importance of science and its application among the people and to accelerate the pace of development among them.



Glimpses of various activities during National Science Day Celebration.

PRL Scholarships from the Aruna Lal Endowment Fund, established by late Prof. Devendra Lal, former Director, were awarded to five students on this occasion. The selection was done on the basis of their performances in the state level screening test, poster competition and oral interview. All the five students are to receive Rs. 10,000/- per year for two consecutive years and for the third year provided the students continue to study in the science stream with high academic record.

In addition to the Aruna Lal scholarship, other prizes were awarded like center wise top students (13) in the state level screening test held in February 2015 and poster/model competitions (12). Most students were accompanied by their teachers. Teachers and students had close interaction with PRL scientists and the judges of the poster/model competition throughout the day. Also, to give an impetus to young students about the various scientific research being done at PRL, a small science exhibition was organized. All the students and teacher participants visited the exhibits and interacted with PRL scientists. A unique panel discussion for teachers and parents on "Frontiers of basic research in India: Contributions of PRL and emerging opportunities" was also organized on this day. An interactive lecture with live demonstrations on "Fun with Experiments" was also delivered.

## Activities on the Promotion of Official Language

- A 5-day Translation Programme was organized by Income Tax Office, during May 05-09, 2014 in Ahmedabad which was attended by Shrimati Rumkee Dutta, Hindi Translator.
- PRL Official Language Implementation Committee meeting was held on June 26, 2014.
- A Hindi workshop was conducted in IR Observatory, Mt. Abu on June 26, 2014.
- PRL started in-house classes of Hindi Bhasha Training in June, 2014.
- PRL has been awarded Second Prize for implementation of Rajbhasha by Town Official Language Implementation Committee (TOLIC) in July, 2014.
- Hindi Technical Seminar was organized by Space Applications Centre on July 25, 2014 which was attended by all the staff and official of Hindi Section.
- Hindi magazine Vikram was inaugurated on August 15, 2014.
- As a part of implementation and progressive use of Hindi in PRL, the Hindi Pakhwada was celebrated at PRL from September 14 - 28, 2014. The highlights of the celebrations included word quiz, Hindi typing, essay, elocution, Hamara Karya, self written poetry competition, hand writing competition. This time students from schools were invited to the scientific presentation and a question-answer round was conducted. Three best questions received awards.
- PRL Official Language Implementation Committee meeting was held on September 22, 2014 in USO, Udaipur.
- A Hindi workshop was conducted in USO, Udaipur on September 22, 2014.
- Translation/publication of PRL Annual Report in October, 2014.
- An Orientation Programme for Hindi Officials and Staff was organized by Department of Space in October, 2014 in Tirupati which was attended by Hindi Officer-II & OSD.
- In the month of November, 2014 a workshop was conducted by Hindi Section of PRL regarding working on computer using Unicode. Administrative glossary in Hindi was distributed to the staff members.
- The meeting of Town Official Language Implementation Committee (TOLIC) with the Central Government Offices of Ahmedabad was hosted by PRL on December 22, 2014.
- PRL Official Language Implementation Committee meeting was held on December 24, 2014 in Thaltej, Ahmedabad.
- A Hindi workshop was conducted in Thaltej, Ahmedabad on December 24, 2014.
- The inspection of all the sections was completed by December, 2014.

- The departmental inspection was also done by Hindi Officer-II and O.S.D. in December, 2014.
- Vishwa Hindi Divas was celebrated in PRL on January 09, 2015 and an essay competition was organized on the topic Contribution of Hindi and other Indian languages in the progress of the country.
- PRL Official Language Implementation Committee meeting was held on March 18, 2015 in PRL, Ahmedabad.
- A Hindi workshop was conducted in PRL, Ahmedabad on March 18, 2015.
- Shri R.S. Gupta, Hindi Officer-II & OSD delivered lectures in Hindi at workshops held by various Departments like BSNL, Airport Authority, Food Corporation of India, Income Tax, Doordarshan, ONGC on different topics including various applications of computers in Hindi.
- The newly appointed employees have successfully completed in-house training of Hindi Typing and got cash prize/increment as personal pay and few staff are undergoing the training process presently.

# Facilities and Services

## Computer Centre

### Virtual Private Network (VPN) connectivity

VPN server is configured to provide secure access of PRL computational facilities over the Internet. The server is configured to allow access to authorized users with user digital certificate and Time based One Time Password (TOTP). To use this facility, users need smart phone to generate TOTP. Using this connectivity, user's device will be part of PRL Intranet (LAN) over secure tunnel via Internet. User can access PRL subscribed Library Journals, run network licensed software on their machine, can access available PRL Intranet web sites or any other websites which were previously only accessible from PRL LAN. Users should install OpenVPN client on their Laptop, PC, or Smart Phone to avail PRL VPN connectivity.

### 'Gagan' - ownCloud File Sync and Storage Access

Access and Share your data from anywhere using Laptops, PCs, or Smartphones. The server is configured to allow access to authorized users with Time based One Time Password (TOTP). To avail this facility, user need smart phone for generating TOTP. User needs to install ownCloud client applications on Laptops, PCs, or Smartphones for file sync. To implement this service open source software is used with few in-house customizations similar to other solutions like Dropbox, Google drive, Skydrive, etc.

## Server Virtualization

Computer Centre has started to leverage benefit of the virtualization technology for server consolidation. Internet Servers (DNS, Web, Mail, Library, Proxy, VPN, EGPS, etc.) and Intranet Servers (EDMS, DNS, Network Software License Server etc.) are migrated to virtual environment. Open Source (KVM) and Commercial (VMware vSphere) software are used to setup the virtual environment. This setup also provides redundancy as now services are no longer tied to a specific physical server. In case of a scheduled or unscheduled downtime, virtual machines can be manually or automatically migrated from one physical machine to another.

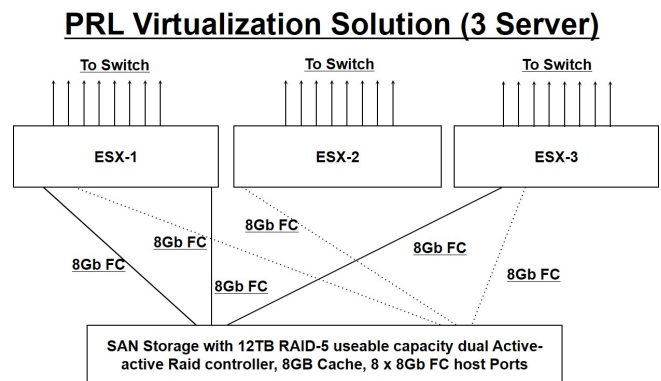


Figure 1: PRL Virtualization Solution.

### **'Tarang' - A Secure Wireless Network Access**

Secure Wireless network access within PRL campuses to allow access of PRL network and computing facilities using Laptops, PC with wireless card, and Smart Phones is deployed using 45 Access Points (APs) managed through centralized hardware controller. The controller only manages access points and APs to client communication. A separate software is developed to register the Physical /Hardware/ MAC address of users' Wi-Fi enabled devices, Only authorized/registered devices can get access to PRL wireless network. At present, wi-fi network access in the Eight-storey building in the Main Campus, Students' Hostel and PDF Blocks at Navrangpura campus, Students' hostel and Transit Accommodation in Thaltej Campus, Auditorium in Nanosims Building, Ramanathan Auditorium and Computer Centre are operational. In house developed software also manages PRL Guests' devices registration and auto de-activation when they leave PRL.

### **Video Conference (VC) over NKN Internet**

It is now possible to establish Video Conferencing over Internet on 1 Gbps NKN link. User has to provide the details like IP address and Contact information of the Person managing remote VC station. This enables us to test the connectivity and keep the setup ready for a hassle free VC at the scheduled time.

### **Telephone System**

Telephone System is being used to store the details of Incoming/Outgoing calls within PRL. Employees can submit their telephone details online using this software. Every month the system automatically generates email bills for each employee with URL to submit their telephone bills.

### **PRL File System Replication at Thaltej**

PRL's primary file system resides in 30 TB SGI storage server at Navrangpura campus in Computer Centre, where all users mail and other important files are stored. We have now deployed a similar storage server to Thaltej campus where we replicate this data on a daily basis as a disaster recovery measure.

### **NKN failsafe for servers**

Earlier, all PRL's Internet services (Mail, Web, DNS, etc) were running on BSNL provided 30 Mbps link without redundancy. Computer Centre has now configured these essential services to also run on 1 Gbps NKN network so that in case BSNL is down, our services will not halt.

### **Library and Information Services**

During 2014-15, two hundred and eleven (211) scientific and general books, 59 hindi books and 87 CDs/DVDs were added in the Main, Thaltej and USO libraries. Subscription of two journals has been added to the existing library collection of 165 journals. During this period, number of visitors, visiting the library was 3807 and number of documents issued was 2279. Forty five (45) book grant requests were processed to assist the students this year. Number of photocopies made, in house were 33822 and by outside agency were 47224. In 2014, the Library Management System LibSys was shifted to cloud and is working smoothly.

PRL Library continues to subscribe to full-text databases like AGU Digital Library, GSA Archive, Nature archive (access from 1987), PROLA, SPIE Digital Library and Science Archive. As no library can be completely self-sufficient, the Library also provides document delivery service through ILL. The number of ILL requests for articles from other institutes fulfilled by PRL Library was 264 and that of requests of PRL staff fulfilled by other libraries was 272. The articles received from other sources were being organized using Endnote Software which is a reference management software. This was done to avoid duplication of effort and time spent on tracing the articles again if requested by other students or scientists. This year the collection of articles was migrated to Zotero which is an open source reference management software.

The Library homepage acts like a window through which it is possible to access the digital content subscribed by PRL as well as open access content. Primarily, it gives links to 159 online journals out of the 167 journals subscribed by the library. The Library Blog gives information about the trials set by the Library for its users. Last year free trial was set up for GeoScience World (GSW) and EBSCO Discovery Service (EDS). Depending on the users feedback, EDS was subscribed by the Library. EDS is a single window search of academic content for the students and scientists. The blog also gives easy access to the video lectures in subject areas relevant to PRL research.

The PRL institutional repository consisting of journal articles published by the PRL authors from 1994 to present is also linked through the Library homepage. More than 3300 articles by PRL authors are now part of the repository. All the PRL theses from 1952 onwards (367) are now available full text for PRL users. All the Technical Notes since 1977, published by PRL have been digitized (105) and are available full text for PRL users. E-books page has been redesigned so as give access to the collection by subject, alphabetical and publisher wise lists. These collections can be accessed from library homepage (<http://www.prl.res.in/~library>). The Library has taken up the digitization of the photographs archive. Scanning of the photographs of about 170 albums is completed. Tagging of the photographs for retrieval, will start soon.

**Workshop**

**Moon Electrostatic Potential and Dust Analyser (MESDA) for Future Lunar Lander**

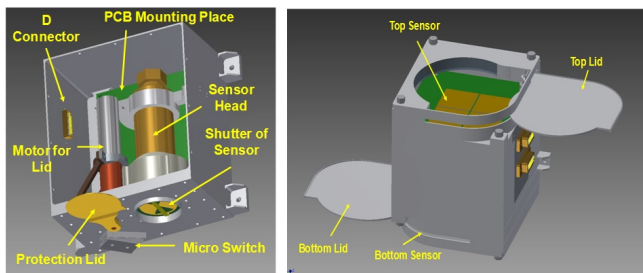


Figure 1: Mechanical package of LSPD (left) and LDD (right) payload.

To study the lunar electrostatic and dust environment, a Moon Electrostatic Potential and Dust Analyzer (MESDA) payload has been proposed for future lunar lander. There are two independent instruments in the MESDA payload viz., Lunar Surface Potential Detector (LSPD) and Lunar Dust Detector (LDD). The LSPD will measure lunar electrostatic surface potential at ~50 mm from the lunar surface, whereas the LDD will detect the presence of charged dust particles at a similar altitude using an IDT (Inter Digitated Transducer) dust sensor. Design and development of sensors and front end electronics for both the instruments have been initiated. A prototype of the LSPD (90 mm (L) × 60 mm (W) × 100 mm (H)) has been developed and initial measurements have been carried out in the laboratory. Mechanical package of LSPD is shown in Figure 1. For the LDD (100 mm (L) × 80 mm (W) × 80 mm (H)), an IDT dust sensor with one micron inter-electrode spacing has been tested using one micron dust (Figure 1). Further work on MESDA is underway. All the mechanical components were made with the precision by using Aluminium alloy material of AL-6061-T6 Grade.

**GEOTRACES Clean Van Niskin Bottle stand Modification**



Figure 2: Clean van with Niskin sampling bottles.

GEOTRACES project was initiated to study the trace elements

and its isotopes in the seawater. Therefore, clean sampling technique is the utmost requirement to accomplish purpose. Towards this clean van and the clean CTD was procured under this project. The clean van is used for the sample collection and filtration purpose with Niskin bottles attached to the stand for the filtration including other processing and packing was carried out in the clean van itself. However, during the sampling it was observed that wherever, the Niskin bottles attached to the stand were not designed properly thus hanging in unbalanced position. The Niskin sampling bottle stand was modified appropriately to the Niskin bottles which required redesigning of the stand as suitable for perfect mounting of the Niskin Bottle. The designing, re-fabrication of the stand and assembly was done at PRL workshop successfully.

**Telescope and laser mount for micro pulse Lidar**



Figure 3: Portable micro pulse Lidar.

A portable single wavelength (532 nm) micro pulse Light Detection and Ranging (LIDAR) system (height 1200 mm and diameter 220 mm) is being designed and under development at workshop. A highly precise and accurate mounting assembly has been developed to mount cassegrain telescope, diode pumped solid state laser along with various laser optics using vertical machining center VMC-850. The system is under alignment operation and further integration of detector, control electronics and various other sub system is in process.

**Spectral Sun photometer**



Figure 4: Spectral Sun photometer (left) and photometer mounted on Sun tracker (right).

Spectral Sun photometer for the measurement of aerosol optical properties has been designed and developed at Workshop. The state-of-the-art Sun photometer and DC geared motorised shutter mechanism is mounted inside PVC tube along with system control and various signal processing circuits. The water & dust proof Sun photometer is made of aluminium cylinder of diameter 45 mm and length 90 mm, housed inside a PVC tube of diameter 110 mm and length 250 mm. The aluminium cylinder is designed to mount six photodiode detectors with respective 12.5 mm six optical interference filters and baffles assembly is made using vertical machining center VMC 850. The system has been mounted on a dual axis active Sun tracker POM01. The system is working satisfactorily at Aerosol Monitoring Laboratory, PRL.

**Mechanical design of Compton X ray Polarimeter**

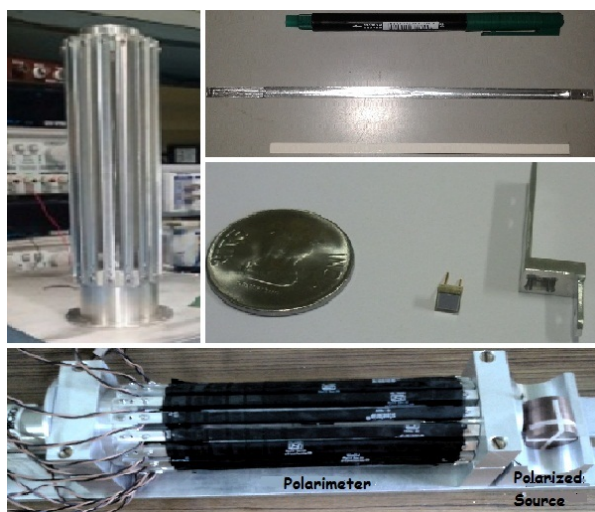


Figure 5: Mechanical design of Compton X ray Polarimeter (top left), A single CsI(Tl) and its holder (top right), single Si Photomultiplier and its holder (middle right), and Polarization experiment with the fully integrated Compton Polarimeter with polarized source kept outside the Polarimeter (bottom).

Mechanical design and development of Compton X ray

Polarimeter has been successfully accomplished at PRL Workshop. The Polarimetric structure is made of Aluminium (Al), it has 16 CsI(Tl) scintillator holders which are kept in an cylindrical array using two ~ 40 mm diameter Al made hollow cylinders at the top and the bottom. The holder is made of Al, it encloses the CsI scintillator from all sides except the side facing the plastic scatterer and the lower end of the scintillator for read out. The holder is 5 mm thick on the backside and 1 mm thick on other 2 sides. Each of the CsI(Tl) scintillators is read out by a single Si Photomultiplier (SiPM) at its end. SiPM is 3 mm × 3mm in dimension and is kept in an Al holder with a groove of 3 mm × 3 mm and 2 mm thick from all sides. Arrangement is made to couple the SiPM holder to the CsI(Tl) scintillator holder using screws, such that the SiPM surface touches the CsI back end surface properly. The plastic scintillator is kept at the centre of the polarimeter configuration using a separate Al block. All the parts were machined accurately to the requirement as per the dimensions and assembled in a sequence with electronics hardware for testing.

**Fabrication of table structure made of aluminum profiles for the clean room laboratory**



Figure 6: Tables using Aluminium profiles for optics laboratory.

Three robust tables of dimension 4.6 m (L) × 1.5 m (w) × 1.8 m (h) using aluminium profiles for our clean room has been developed and integrated at PRL Workshop. The various inter connecting couplers and connectors also have been designed and developed. The tables have been successfully assembled, installed and in operational at the clean room for optics laboratory.

**Multi-Pixel Photo Counter (MPPC)**



Figure 7: MPPC assembly.

A sub system for multi-pixel photo counter used with optical polarimeter has been successfully designed and developed at PRL Workshop. To test and calibrate module in laboratory we mounted the module into light-proof black anodized box so that stray light noise is minimized. The Hamamatsu MPPC module is mounted inside the fabricated box. Source end (Collimator end) LED PCB is mounted inside the box and light incidents on detector window of MPPC module. Rare side has electrical connections for power supply and oscilloscope. The fabricated box has substantially reduce stray light noise so calibration of MPPC is being done comfortably.

**RA and DEC Encoders mounting on CDK 20 inch telescope**

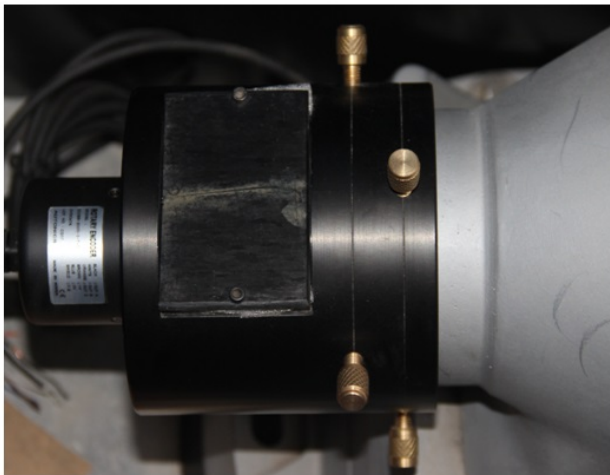


Figure 8: Encoder mount assembly.

RA & DEC encoder mounting has been designed for CDK 20 inch telescope and it has been integrated with the CDK 20 inch telescope drive system. Due to this it has become easy to get proper position of the telescope on computer and one can easily position the telescope at correct position.

**CCD focuser for NICMOS**

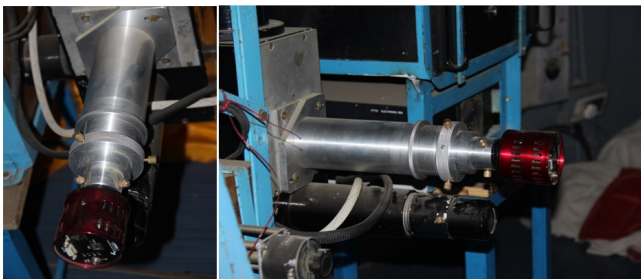


Figure 9: CCD mount focuser assembly.

Aluminium alloy based high precise and accurate CCD mount focuser was design and fabricated in PRL workshop for NICMOS camera for 1.2 m telescope. It has the facility to adjust the CCD camera for guiding the telescope in X, Y and Z directions.

**CCD-based Multi-wavelength Airglow Photometer (CMAP)**

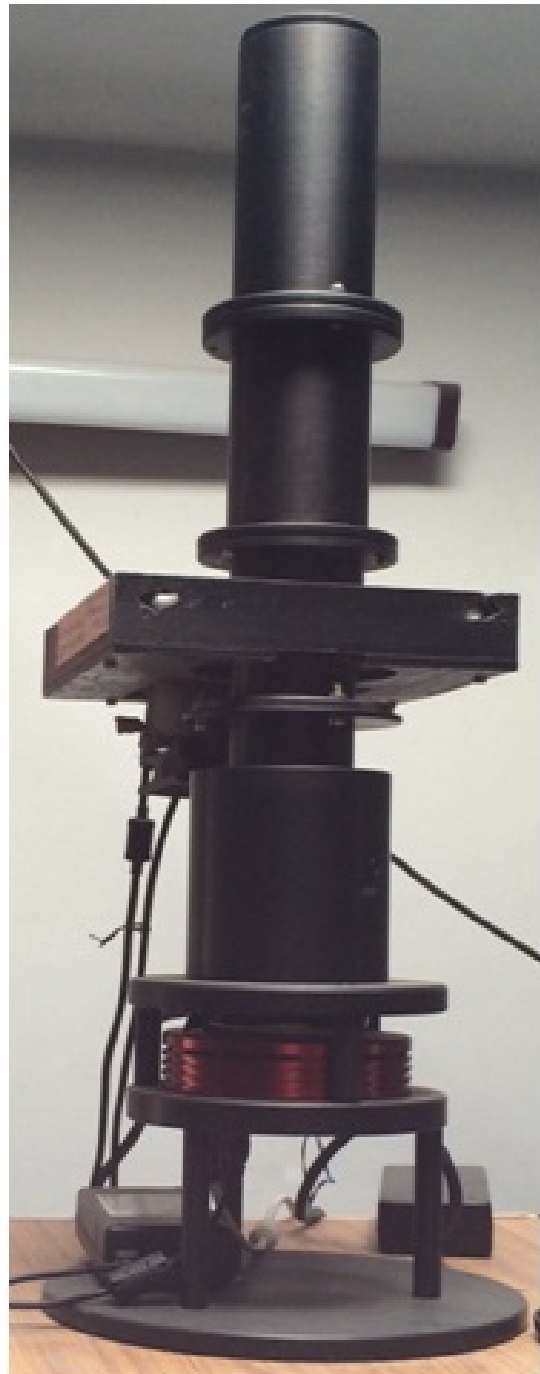


Figure 10: CMAP assembly.

An Automated CCD-based Multi-wavelength Airglow Photometer (CMAP) for optical aeronomy studies was designed and fabricated in PRL. Augmentation of filter wheel and CCD to conventional airglow photometer enables investigation of the dynamics of upper atmosphere at multiple emission wavelengths nearly simultaneously. CMAP consists of aluminium pipes of optimised dimensions to hold various

optical elements. All the pipes have fine threading on the inside to enable accurate focussing of optical rays in the system. One of the major components of CMAP is the temperature controlled filter wheel chamber, for which peltier elements were mounted on a commercially available filter wheel along with temperature sensor to control and monitor

the temperature of the filter wheel. The filter wheel was then encompassed in a Delrin box to insulate the filters from the external environment. All the mechanical components were made by using aluminium alloy material with high accuracy. CMAP is in continuous operation at the Optical Aeronomy Observatory, Gurushikhar.

# Honorary Fellows

A. Hewish

J. E. Blamont

K. Kasturirangan

M. G. K. Menon

P. Crutzen

U. R. Rao

# Honorary Faculty

A. Ambastha

A. Singal

A. C. Das

A. K. Singhvi  
FNA, FASc, FNASc, FTWAS

A. R. Prasanna

A. S. Joshipura  
FNA, FASc, FNASc

B. G. Anand Rao

D. P. Dewangan  
FNASc

H. Chandra

H. O. Vats

H. S. S. Sinha

J. Banerji

J. N. Goswami  
FNA, FASc, FNASc, FTWAS

M. M. Sarin  
FNA, FASc, FNASc

N. Bhandari  
FNA, FASc, FNASc, INSA Honorary Scientist

R. G. Rastogi  
FNA, FASc, FNASc

R. Sridharan  
FASc, FNASc, CSIR Emeritus Scientist

Shyam Lal  
FNA, FASc, FNASc

S. Krishnaswami\*  
FNA, FASc, FNASc, FTWAS, INSA Senior Scientist  
*\*Deceased on 20 July, 2015.*

S. K. Gupta  
FNASc

S. P. Gupta

S. V. S. Murty  
FASc

T. Chandrasekhar

U. C. Joshi

V. K. B. Kota

Y. B. Acharya

# Academic Faculty

---

Name	Designation	Specialization	Academic Qualification
Sarkar U. <i>FNA, FASc, FNASc</i>	Director	Particle Physics	Ph.D., Calcutta Univ.(1984)
Ashok N. M.	Senior Professor	Close Binary Stars, Novae/IR spectroscopy	Ph.D., PRL, Gujarat Univ. (1983)
Baliyan K. S.	Professor	AGNs, Comets, Atomic Physics, Milky Way	Ph.D., Roorkee Univ. (1986)
Banerjee D.	Associate Professor	Thermoluminescence & Planetary Physics	Ph.D., PRL, Gujarat Univ. (1997)
Banerjee D. P. K.	Senior Professor	Novae, Be Stars, Planetary Nebulae, IR and Optical Studies	Ph.D., PRL, Gujarat Univ. (1990)
Banerjee S. B.	Scientist - SE	Experimental Molecular Physics	Ph.D., Saurashtra Univ. (2011)
Basu Sarbadhikari A.	Scientist-SE	Petrology & Geochemistry	Ph.D., IIT, Khargpur (2009)
Bhatt J. R.	Associate Professor	Astrophysics	Ph.D., IPR, M.S. Univ.(1992)
Bhattacharyya R.	Reader	Plasma Physics	Ph.D., Jadavpur Univ., (2006)
Bhushan R.	Scientist-SF	Oceanography and Paleoclimatology	Ph.D., PRL, M.S. Univ. (2009)
Chakrabarty A.	Associate Professor	Extra-solar planets, Star Formation & Instrumentation	Ph.D., PRL, Gujarat Univ. (1999)

---

Name	Designation	Specialization	Academic Qualification
Chakrabarty D.	Reader	Upper Atmosphere and Geomagnetic storm	Ph.D., PRL, M.L.S Univ.(2008)
Deshpande R. D.	Scientist-SF	Application of Environmental Tracers in Hydrology	Ph.D., PRL, M.S. Univ. (2007)
Ganesh S.	Scientist-SE	Milky Way, Comets, AGN, Astronomical polarimetry	Ph.D., PRL, Gujarat Univ.(2010)
Goswami S.	Professor	High Energy Physics	Ph.D., Calcutta Univ. (1998)
Haider S. A. <i>FASc, FNA, FNASc</i>	Senior Professor	Planetary and Cometary Atmospheres	Ph.D., Banaras Univ. (1984)
Janardhan P.	Professor	Solar Radio Astronomy & Space Weather	Ph.D., PRL, Gujarat Univ. (1991)
Joshi B.	Reader	Solar Physics,Astronomy	Ph.D., ARIES, Kumaun Univ.(2007)
Juyal N.	Scientist-SF	Quaternary Geology & Paleoclimate	Ph.D., PRL, M.S. Univ.(2004)
Konar P.	Reader	Particle Physics	Ph.D.,HRI, Allahabad Univ.(2005)
Kumar B.	Reader	Solar Physics	Ph.D., PRL, M.L.S Univ.(2007)
Kumar S.	Reader	Aquatic and Terrestrial Biogeochemistry	Ph.D., PRL, M.S. Univ., (2004)
Mahajan N.	Associate Professor	Particle Physics	Ph.D., Delhi Univ.(2004)
Marhas K. K.	Associate Professor	Solar System studies	Ph.D., PRL, D.A.V.V Indore (2001)
Mathew S. K.	Associate Professor	Solar Magnetic & Velocity Fields	Ph.D., PRL, Gujarat Univ. (1999)
Mishra H.	Professor	Strong Interaction Physics & Nuclear Astrophysics	Ph.D., IOP, Utkal Univ. (1994)
Mohanty S.	Senior Professor	Astroparticle Physics	Ph.D., Wisconsin Univ. (1989)
Naik S.	Associate Professor	High Energy Astro- physics, X-ray Binaries	Ph.D., TIFR, Bombay Univ.(2003)
Pallamraju D.	Professor	Space Weather and Atmospheric coupling processes	Ph.D., PRL, D.A.V.V Indore(1997)
Rai V.	Associate Professor	Stable Isotope Cosmochemistry	Ph.D., PRL, M.S Univ. (2001)
Ramachandran S.	Professor	Aerosols, Radiation & Chemistry-Climate Interactions	Ph.D., PRL, M.S Univ. (1996)
Ramesh R. <i>FNA, FASc, FNASc, FTWAS</i>	Outstanding Scientist	Paleoclimatology, Oceanography & Modelling	Ph.D., PRL, Gujarat Univ. (1984)
Rangarajan R.	Professor	Particle Physics & Cosmology	Ph.D., Univ. of California, Santa Barbara (1994)

Name	Designation	Specialization	Academic Qualification
Rastogi N.	Reader	Atmospheric & Aerosol Chemistry	Ph.D., PRL, M.L.S Univ. (2005)
Ray J. S.	Professor	Isotope Geochemistry	Ph.D., PRL, M.S Univ. (1998)
Ray D.	Scientist-SD	Marine Geology & Igneous Petrology	Ph.D., Jadavpur Univ. (2009)
Rengarajan R.	Scientist-SF	Atmospheric aerosols & aqueous geochemistry	Ph.D., PRL, M.L.S Univ.(2004)
Rindani S. D. <i>FNA, FASc, FNASc</i>	Senior Professor-H	Particle Physics	Ph.D., IIT, Bombay (1976)
Sahoo B. K.	Associate Professor	Atomic Physics	Ph.D., IIA, Mangalore Univ.(2006)
Sahu L. K.	Reader	Atmospheric Science, Trace gases	Ph.D., PRL, M.L.S.Univ., (2005)
Samanta G. K.	Reader	Laser and Nonlinear optics	Ph.D., Universitat Politecnica de Catalunya Uni., Barcelona, (2009)
Sekar R.	Senior Professor	Upper Atmospheric & Ionospheric Physics	Ph.D., PRL, Gujarat Univ.(1991)
Sharma S. K.	Reader	Middle Atmosphere & Long Term Atmospheric Changes	Ph.D., PRL, Gujarat Univ.(2010)
Sheel V.	Associate Professor	Modelling of Lower Atmosphere	Ph.D., PRL, Gujarat Univ.(1996)
Shukla A. D.	Scientist-SE	Geochemistry & Cosmochemistry	Ph.D., PRL, M.S. Univ. (2012)
Singh A. D.	Professor	Atomic Physics	Ph.D., IIA, Bangalore Univ.(1998)
Singh N.	Reader	Theoretical condensed matter and Statistical physics	Ph.D., RRI, Bangalore (2006)
Singh R. P.	Professor	Laser Physics	Ph.D., J.N.U., New Delhi.(1994)
Singh S. K.	Professor	Isotope Geochemistry	Ph.D., PRL, M.S. Univ.(1999)
Sivaraman B.	Reader	Low Temperature Astrochemistry	Ph.D., The Open University, UK (2008)
Srivastava M.	Scientist - SD	Astronomical Instrumentation	Ph.D., Univ. of Pune (2012)
Srivastava N.	Professor	Solar Physics	Ph.D., PRL, Ravi Shankar Shukla Univ.(1994)
Subramanian K. P.	Professor	Experimental Atomic and Molecular Physics	Ph.D., PRL, Gujarat Univ.(1987)
Vadawale S. V.	Associate Professor	High Energy Astrophysics and X-Ray Spectroscopy	Ph.D., T.I.F.R, Bombay Univ. (2003)
Venkatakrishnan P.	Senior Professor-H	Solar Physics	Ph.D., IIA, Bangalore Univ.(1984)
Yadava M. G.	Scientist-SF	Palaeoclimate, Radiocarbon dating and stable isotopes	Ph.D., PRL, D.A.V.V., Indore (2003)

# Technical Faculty

<b>Name</b>	<b>Designation</b>
Adhyaru P. R.	Engineer-SE
Bayanna A. R.	Scientist-SE
Mahajan R.R.	Scientist-SE
Narayanan R.	Scientist-SF
Nishtha A.	Librarian-SE
Pabari J.	Engineer-SE
Rajesh T. A.	Scientist-SE
Rao D. K.	Scientist-SE
Raval J.	Engineer-SE
Panda D.	Scientist-SE
Shah A. B.	Engineer-SF
Shah R. R.	Engineer-SF
Shanmugam M.	Engineer-SE
Singh M.	Sci./Eng.-SF
Singh R. P.	Scientist-SE
Sudheer A. K.	Scientist-SE
Ubale G. P.	Engineer-SF
Vaghela H. R.	Engineer-SE
Venkataraman V.	Scientist-SE
Venkataramani S.	Scientist-SF
Wairagade S.	Engineer-SE

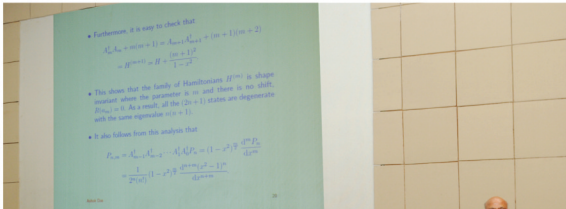


# पी.आर.एल. में गतिविधियां Events at PRL





# पी.आर.एल. में गतिविधियां Events at PRL





# पी.आर.एल. में गतिविधियां Events at PRL

